

---

# **Numerical Simulation of Dynamic Stall for Heaving Airfoils Using Adaptive Mesh Techniques**

**Wided Medjroubi**

---

Von der Fakultät für Physik  
der Carl von Ossietzky Universität Oldenburg  
zur Erlangung des Grades und Titels eines

**DOKTORS DER NATURWISSENSCHAFTEN  
DR. RER. NAT.**

angenommene Dissertation

von Frau Wided Medjroubi  
geboren am 11.10.1979 in Constantine, Algerien

Gutachter: Prof. Dr. Joachim Peinke  
Zweitgutachter: Prof. Dr. Alexander Rauh  
Tag der Disputation: 01 Juli 2011

What makes me myself rather than anyone else is the very fact that I am poised between two countries, two or three languages, and several cultural traditions. It is precisely this that defines my identity. Would I exist more authentically if I cut off a part of myself - Amin Maalouf



# Inhaltsverzeichnis

List of Tables	xv
Abstract	xvi
<b>1 Introduction</b>	<b>1</b>
1.1 Turbulence and unsteadiness . . . . .	1
1.2 Unsteady flows over airfoils . . . . .	5
1.3 Dynamic Stall . . . . .	6
1.3.1 Aerodynamics of Stall . . . . .	6
1.3.2 Literature Review on Dynamic Stall . . . . .	7
1.4 Heaving Airfoils Wakes . . . . .	11
1.4.1 Aerodynamics of Heaving Airfoils . . . . .	12
1.4.2 Literature Review on Heaving Airfoils . . . . .	14
1.4.3 Thrust Generation by Heaving Airfoils . . . . .	21
1.5 Frequency regimes in forced airfoil wakes . . . . .	21
1.6 Direct Numerical Simulations (DNS) - High Order Simulations . .	23
1.7 Objectives . . . . .	24
1.8 Outline of the Thesis . . . . .	25
<b>2 Spectral /hp Finite Element Method</b>	<b>34</b>
2.1 Introduction to Computational Fluid Dynamics (CFD) . . . . .	35
2.2 Introduction to Spectral /hp Element Methods . . . . .	39
2.3 Framework of the weighted residuals and the Galerkin formulations	40
2.4 Spectral /hp Element Discretization in two Dimensions . . . . .	42
2.5 Spectral/hp Element Discretization in three dimensions . . . . .	54
2.6 Time Discretization . . . . .	55
2.7 Airfoil motion . . . . .	55
<b>3 Validation</b>	<b>63</b>
3.1 Flow over a motionless cylinder . . . . .	64
3.2 Flow over a motionless airfoil . . . . .	70
3.2.1 $\alpha = 0^\circ$ and $Re = 500$ . . . . .	70
3.2.2 $\alpha = 10^\circ$ and $Re = 500$ . . . . .	70

3.2.3	$\alpha = 20^\circ$ and $Re = 800$ . . . . .	76
3.3	Flow over a heaving airfoil . . . . .	76
3.3.1	Wake validation . . . . .	76
3.3.2	Forces validation . . . . .	82
3.4	Conclusion . . . . .	85
<b>4</b>	<b>High-order Numerical Simulations Of The Flow Around A Heaving Airfoil</b>	<b>90</b>
4.1	Introduction . . . . .	91
4.2	The numerical method . . . . .	94
4.3	Simulations for a motionless airfoil . . . . .	103
4.3.1	Fixed airfoil at $\bar{\alpha} = 12^\circ$ . . . . .	103
4.3.2	Fixed airfoil at $\bar{\alpha} = 20^\circ$ . . . . .	107
4.4	Simulations for a heaving airfoil . . . . .	109
4.4.1	Heaving airfoil at $\bar{\alpha} = 12^\circ$ . . . . .	109
4.4.2	Heaving airfoil at $\alpha = 20^\circ$ . . . . .	116
4.5	Conclusion . . . . .	119
4.6	Acknowledgments . . . . .	120
<b>5</b>	<b>Plunging Airfoil Wakes classification Using Spectral/hp Element Method</b>	<b>125</b>
5.1	Introduction . . . . .	126
5.2	Numerical Method . . . . .	127
5.3	Results . . . . .	128
5.3.1	Constant amplitude transition . . . . .	128
5.3.2	Constant frequency transition . . . . .	131
5.3.3	Wake structures classification . . . . .	132
5.3.4	The multiple-vortices-per-half cycle mode . . . . .	137
5.4	Conclusion . . . . .	139
<b>6</b>	<b>Frequency Selection in Plunging Airfoil Wakes Using a High-Order Method</b>	<b>143</b>
6.1	Introduction . . . . .	144
6.2	The Numerical Method . . . . .	147
6.3	Results . . . . .	152
6.3.1	Unforced airfoil wakes . . . . .	154
6.3.2	Forced airfoil wakes . . . . .	155
6.3.3	Frequency regimes classifications - a frequency pattern . . . . .	163
6.4	Conclusion . . . . .	168
<b>7</b>	<b>Conclusions and Outlook</b>	<b>174</b>
7.1	Synopsis of motivation and results . . . . .	174
7.2	Future Work . . . . .	177

Danksagung	179
Lebenslauf	180
Erklärung	182
Publikationsliste	183



# Abbildungsverzeichnis

1.1	Some examples of everyday turbulent flows . . . . .	2
1.2	Transition to turbulence due to the evolution of the flow over a cylinder. . . . .	4
1.3	$C_L$ variation as a function of the AOA. . . . .	7
1.4	$C_L$ variation as a function of the instantaneous AOA. . . . .	8
1.5	Effect of the $h$ and $k$ on the aerodynamical coefficients. . . . .	10
1.6	Some examples of Micro Air Vehicles (MAV). . . . .	12
1.7	Schematic representation of the airfoil heaving and pitching motions. . . . .	13
1.8	Karman, reversed Karman and neutral vortex street. . . . .	15
1.9	Multiple-vortex-per-cycle wake. . . . .	16
1.10	Vorticity distributions of experimental simulations of drag, thrust, and neutral wakes. . . . .	17
1.11	Forces, incident and resultant velocities on the airfoil during the up- and downstroke of the heaving oscillation. . . . .	18
1.12	Comparison of Vorticity distributions obtained using experimental and computational (Navier-Stokes solver) results. . . . .	20
1.13	$C_T$ and $\eta$ as a function of $k$ . . . . .	21
1.14	Leading- and trailing-edge shedding. . . . .	22
1.15	Wakes classification as a function of $k$ and $h$ . . . . .	22
2.1	An example of a 3D structured grid and a 2D unstructured grid. . . . .	38
2.2	Standard regions for triangular and quadrilateral expansions. . . . .	43
2.3	Construction of a two-dimensional expansion basis. . . . .	44
2.4	Collapsed coordinates and the transformation from triangle to rectangle coordinates. . . . .	45
2.5	The construction of a triangular expansion of the 4 <sup>th</sup> order. . . . .	46
2.6	Schematic representation of the the moving frame of reference and the absolute frame of reference. . . . .	56
2.7	The heave motion. . . . .	57
3.1	The mesh used for the cylinder simulations. . . . .	65
3.2	Nomenclature of the geometrical parameters for the cylinder simulations. . . . .	66

3.3	$C_l$ at $Re = 200$ using $N\epsilon\kappa\tau\alpha r$ -solver compared to [14] . . . . .	67
3.4	Vorticity contours at $Re = 40, 50, 100$ and $200$ using $N\epsilon\kappa\tau\alpha r$ -solver compared to [14] . . . . .	68
3.5	Streamtracers at $Re = 20$ and $40$ using $N\epsilon\kappa\tau\alpha r$ -solver compared to [7] . . . . .	69
3.6	The numerical grid used for the airfoil simulations validation. . . . .	71
3.7	Comparison of $u$ -velocity contours from [17] and using the $N\epsilon\kappa\tau\alpha r$ -solver at $Re = 500$ and $\alpha = 0^\circ$ . . . . .	72
3.8	Comparison of $v$ -velocity contours from [17] and using the $N\epsilon\kappa\tau\alpha r$ -solver at $Re = 500$ and $\alpha = 0^\circ$ . . . . .	72
3.9	Comparison of the pressure iso-contours from [17] and using the $N\epsilon\kappa\tau\alpha r$ -solver at $Re = 500$ and $\alpha = 0^\circ$ . . . . .	73
3.10	Comparison of the surface pressure coefficient $C_p$ distribution over the airfoil upper-surface at $Re = 500$ and $\alpha = 0^\circ$ using the $N\epsilon\kappa\tau\alpha r$ -solver and from [17]. . . . .	73
3.11	Comparison of $u$ -velocity contours from [17] and using the $N\epsilon\kappa\tau\alpha r$ -solver at $Re = 500$ and $\alpha = 10^\circ$ . . . . .	74
3.12	Comparison of $v$ -velocity contours from [17] and using the $N\epsilon\kappa\tau\alpha r$ -solver at $Re = 500$ and $\alpha = 10^\circ$ . . . . .	74
3.13	Comparison of the pressure iso-contours from [17] and using the $N\epsilon\kappa\tau\alpha r$ -solver at $Re = 500$ and $\alpha = 10^\circ$ . . . . .	75
3.14	Comparison of the surface pressure coefficient $C_p$ distribution over the airfoil $Re = 500$ and $\alpha = 10^\circ$ using the $N\epsilon\kappa\tau\alpha r$ -solver and from [17]. . . . .	75
3.15	$u$ -velocity contours at (a) $t=0.1$ , (b) $t=1$ , (c) $t=2$ , (d) $t=3$ . From [17] and with the $N\epsilon\kappa\tau\alpha r$ -solver, at $Re = 800$ and $\alpha = 20^\circ$ . . . . .	77
3.16	$u$ -velocity contours at (a) $t=4$ , (b) $t=5$ , (c) $t=6$ , (d) $t=7$ . From [17] and with the $N\epsilon\kappa\tau\alpha r$ -solver, at $Re = 800$ and $\alpha = 20^\circ$ . . . . .	78
3.17	$u$ -velocity contours at (a) $t=8$ , (b) $t=9$ , (c) $t=10$ . From [17] and with the $N\epsilon\kappa\tau\alpha r$ -solver, at $Re = 800$ and $\alpha = 20^\circ$ . . . . .	79
3.18	Surface pressure distribution over the airfoil surface at (a) $t=0.5$ , (b) $t=1$ , (c) $t=2$ , (d) $t=3$ , (e) $t=4$ , (f) $t=6$ . The results are for the fixed airfoil at $\alpha = 20^\circ$ , $Re = 800$ . . . . .	80
3.19	Surface pressure distribution over the airfoil surface at (a) $t=7$ , (b) $t=8$ , (c) $t=9$ , (d) $t=10$ . The results are for the fixed airfoil at $\alpha = 20^\circ$ , $Re = 800$ . . . . .	81
3.20	Vorticity visualisation for the wake comparison of (a) experimental results [10], (b) numerical simulations [23]: using a laminar (upper frame) and a turbulent (lower frame) solver. (c) Vorticity distribution using the $N\epsilon\kappa\tau\alpha r$ -solver. The flow parameters are $Re = 2 \times 10^4$ , $\alpha = 0^\circ$ , $h = 0.0125$ and $k = 4.0$ . . . . .	83

3.21 Wake comparison of (a) experimental results [10] at  $h = 0.0125$ , (b) numerical simulations [23]: with a laminar solver (upper frame) and a turbulent solver (lower frame) at  $h = 0.025$ , and (c) (b) numerical simulations [23]: with a laminar solver (upper frame) and a turbulent solver (lower frame) at  $h = 0.02$ , and (d) using the  $N\epsilon\kappa\tau\alpha r$ -solver at  $h = 0.0125$ . For all cases  $Re = 2 \times 10^4$  and  $\alpha = 0^\circ$ . . . . . 84

4.1 The heave motion. . . . . 99

4.2 The numerical grid. . . . . 100

4.3 Mesh details. . . . . 100

4.4  $C_p$  at  $\bar{\alpha} = 20^\circ$ ,  $Re = 800$ . . . . . 101

4.5  $u$ -velocity at  $Re = 800$  and  $\bar{\alpha} = 20^\circ$ . . . . . 102

4.6 Vorticity at  $\bar{\alpha} = 12^\circ$  and  $Re = 4500$ . . . . . 104

4.7  $C_L(t)$  and  $C_d(t)$   $\bar{\alpha} = 12^\circ$ ,  $Re = 4500$  and  $Re = 8000$ . . . . . 104

4.8 Vorticity at  $\bar{\alpha} = 12^\circ$  and  $Re = 8000$ . . . . . 105

4.9 Vorticity at  $\alpha = 12^\circ$ ,  $Re = 4500$  and  $Re = 8000$ . . . . . 106

4.10 Vorticity at  $t = 9.6$ ,  $\alpha = 12^\circ$ ,  $Re = 4500$  and  $Re = 8000$ . . . . . 107

4.11 Vorticity at  $\bar{\alpha} = 20^\circ$  and  $Re = 800$ . . . . . 108

4.12  $C_D(t)$  and  $C_L(t)$  at  $\alpha = 12^\circ$ ,  $Re = 800$  and  $Re = 1600$ . . . . . 109

4.13  $C_D$  and  $C_L$  at  $Re = 1600$  and  $\bar{\alpha} = 12^\circ$ ,  $\alpha = 20^\circ$ . . . . . 110

4.14  $y(t)$  at  $f = 0.3184$  and  $a = 0.1047$ . . . . . 111

4.15 Vorticity at  $\bar{\alpha} = 12^\circ$ ,  $Re = 4500$ ,  $f = 0.3184$  and  $a = 0.1047$ . . . . 112

4.16  $C_D(t)$ ,  $C_L(t)$  for fixed & heaving airfoil at  $\bar{\alpha} = 12^\circ$ ,  $Re = 4500$ . . . 113

4.17 Vorticity and pressure at  $Re = 4500$ ,  $f = 0.3184$  and  $a = 0.1047$ . . 114

4.18 Vorticity at  $\bar{\alpha} = 12^\circ$ ,  $Re = 8000$ ,  $f = 0.3184$  and  $a = 0.1047$ . . . . 115

4.19  $C_D(t)$ ,  $C_L(t)$  at  $\bar{\alpha} = 12^\circ$ ,  $f = 0.3184$ ,  $a = 0.1047$ ,  $Re = 4500$ ,  $8000$ . 116

4.20  $y(t)$  at  $f = 0.25$  and  $a = 0.7958$ . . . . . 117

4.21 Vorticity at  $\bar{\alpha} = 20^\circ$ ,  $Re = 800$ ,  $f = 0.25$  and  $a = 0.7958$ . . . . . 118

4.22  $C_D(t)$ ,  $C_L(t)$  at  $Re = 800$ ,  $\bar{\alpha} = 20^\circ$ ,  $f = 0.25$  and  $a = 0.7958$ . . . . 119

5.1 Vorticity at  $Re = 10^4$ ,  $\bar{\alpha} = 0^\circ$ . . . . . 129

5.2  $u(y)$  at  $\bar{\alpha} = 0^\circ$  and  $Re = 10^4$ . . . . . 130

5.3 Vorticity at  $Re = 10^4$ ,  $\bar{\alpha} = 0^\circ$ ,  $k = 3.92$ ,  $h = 0.001, 0.02, 0.035, 0.05$ . 131

5.4  $u(y)$   $\bar{\alpha} = 0^\circ$ ,  $Re = 10^4$ ,  $k = 3.92$ ,  $h = 0.001, 0.02, 0.035, 0.05$ . . . . 133

5.5 Wakes classification as a function of  $h$  and  $k$ . . . . . 134

5.6 Vorticity at  $Re = 10^4$ ,  $\bar{\alpha} = 0^\circ$ , ( $k = 1.96$ ,  $h = 0.1$ ), ( $k = 1.96$ ,  $h = 0.08$ ). . . . . 134

5.7 Vorticity at  $Re = 10^4$ ,  $\bar{\alpha} = 0^\circ$ , ( $k = 4.14$ ,  $h = 0.025$ ), ( $k = 5.18$ ,  $h = 0.02$ ). . . . . 135

5.8 Vorticity at  $Re = 10^4$ ,  $\bar{\alpha} = 0^\circ$ ,  $kh = 0.08$ . . . . . 136

5.9 Vorticity at  $Re = 10^4$ ,  $\bar{\alpha} = 0^\circ$ , ( $h = 0.05$ ,  $k = 1.96$ ), ( $h = 0.05$ ,  $k = 4.14$ ). . . . . 136

5.10	Vorticity at $\bar{\alpha} = 0^\circ$ , $Re = 10^4$ , $k = 4.52$ and $h = 0.02$ . . . . .	138
6.1	Schematic representation of the absolute and moving frame of references. . . . .	151
6.2	The numerical grid. . . . .	153
6.3	Leading- and trailing-edge meshing details. . . . .	153
6.4	Vorticity distribution at $\bar{\alpha} = 0^\circ$ (a) $Re = 10^4$ and (b) $Re = 2 \times 10^4$ . 154	
6.5	Vorticity distribution close-up view of the trailing-edge region at $\bar{\alpha} = 0^\circ$ (a) $Re = 10^4$ and (b) $Re = 3 \times 10^4$ . . . . .	155
6.6	(a) Time trace of the horizontal velocity $u$ for a motionless airfoil at $Re = 10^4$ . (b) The Fast Fourier Transform of $u(t)$ for a motionless airfoil at $Re = 10^4$ . (c) Time trace of the horizontal velocity $u$ for a motionless airfoil at $Re = 2 \times 10^4$ . (d) The Fast Fourier Transform of $u(t)$ for a motionless airfoil at $Re = 2 \times 10^4$ . (e) Time trace of the horizontal velocity $u$ for a motionless airfoil at $Re = 3 \times 10^4$ . (f) The Fast Fourier Transform of $u(t)$ for a motionless airfoil at $Re = 3 \times 10^4$ . . . . .	156
6.7	(a) Time trace of the horizontal velocity $u$ and its (b) Fast Fourier Transform $h = 0.001$ , $k = 1.96$ . (c) Time trace of $u$ and its (d) Fast Fourier Transform at $h = 0.04$ , $k = 1.96$ . (e) Time trace of $u$ and its (f) Fast Fourier Transform at $h = 0.1$ , $k = 1.96$ . . . . .	158
6.8	Vorticity distribution at $\bar{\alpha} = 0^\circ$ , $Re = 10^4$ for (a) a drag-producing wake ( $k = 1.96$ , $h = 0.001$ ), (b) view of the near wake region. (c) A neutral wake ( $k = 1.96$ , $h = 0.04$ ), (d) view of the near wake region. (e) A thrust-producing wake ( $k = 1.96$ , $h = 0.1$ ), (f) view of the near wake region. . . . .	160
6.9	(a) Time trace of the horizontal velocity $u$ and its (b) Fast Fourier Transform at $k = 1.96$ , $h = 0.05$ . (c) Time trace of the horizontal velocity $u$ and its (d) Fast Fourier Transform at $k = 3.92$ , $h = 0.05$ . 161	
6.10	Vorticity contours at $\bar{\alpha} = 0^\circ$ , $Re = 10^4$ for (a) a neutral wake ( $k = 1.96$ , $h = 0.05$ ), (b) view of the near wake region. (c) A thrust-producing wake ( $k = 3.92$ , $h = 0.05$ ), (d) view of the near wake region. . . . .	162
6.11	Phase diagram of the wake-types classification as a function of the amplitude $h$ and the normalized forcing frequency $k/k_{nat}$ . . . . .	164
6.12	Vorticity contours at $\bar{\alpha} = 0^\circ$ , $Re = 10^4$ , $h = 0.05$ and $k = 3.92$ ( $k/k_{nat} = 0.5$ ) during one oscillation cycle. $y$ is the vertical position of the airfoil. (a) $y$ is at its maximum vertical position, (b) $y=0$ , (c) $y$ is at its minimum vertical position, (d) $y=0$ , and (e) $y$ is at its maximum vertical position. . . . .	165
6.13	Vorticity contours at $\bar{\alpha} = 0^\circ$ , $Re = 10^4$ , $h = 0.1$ and $k = 1.96$ during one oscillation cycle. (a) $y=0$ , (b) $y$ at its minimum vertical position, (c) $y=0$ , (d) $y$ is at its maximum vertical position, (e) $y=0$ . 166	

- 
- 6.14 Streamlines at  $\bar{\alpha} = 0^\circ$ ,  $Re = 10^4$ ,  $h = 0.1$  and  $k = 1.96$  during one oscillation cycle. (a)  $y=0$ , (b)  $y$  at its minimum vertical position, (c)  $y=0$ , (d)  $y$  is at its maximum vertical position, (e)  $y=0$ . . . . 167



# Tabellenverzeichnis

3.1	Comparison of geometrical parameters for the flow over a motionless cylinder. The comparison is between the present study and the previously published results in [4, 5, 7, 14]. . . . .	66
3.2	Comparison of the Strouhal number, the lift and drag coefficients for the unsteady flow over a motionless cylinder. The comparison is between the present study and the previously published results in [1, 7, 14, 15]. . . . .	67
3.3	Comparison of mean and standard deviations of the lift, and drag coefficients. The comparison is between the present study and the previously published results in [13, 23] for a heaving airfoil at ( $h = 0.0125, k = 4.0$ ) and ( $h = 0.025, k = 4.0$ ). . . . .	85

# Abstract

The unsteady flow over streamlined bodies is one of the most important problems in fluid dynamics. The interest for these flows is motivated by their highly non-linear and unsteady nature, which make them almost impossible to solve analytically. With the increase in computing power the use and development of high-order computational methods has become an attractive alternative for the numerical modelling of unsteady flows over streamlined configurations.

In this thesis we conduct numerical simulations of steady and unsteady flows over motionless and heaving airfoils using a high-order Spectral Element method for the first time. Our simulations confirm the suitability of this method to model and characterize in very good spatial and temporal detail the flow structures and wake transitions. The results are validated against previously published experimental and computational studies.

Heaving airfoils shed vortices as they oscillate, and these wakes are classified into *drag-*, *neutral* and *thrust-producing* wakes, depending on the nature of the force produced by the airfoil. In this investigation drag, neutral and thrust wakes are successfully simulated, and also the transitions from one wake to another. Two new modes are observed in this investigation and added to the wake classification. We question the assumption that the *Strouhal number* is the main and only parameter to characterize the wake configurations, and thus the nature of the forces produced for oscillating airfoils. Our findings show that, in order to characterize such flows one needs to consider the amplitude and frequency of oscillations as independent parameters, and that the Strouhal number alone is not sufficient to characterize oscillating airfoil wakes.

Finally, we explore the frequency regimes for oscillating airfoils. These regimes depend on the forcing frequency and the forcing amplitude and on the relation between the forcing frequency and the natural frequency of the airfoil. Three frequency regimes are defined in the literature: the natural regime, the harmonic regime and the lock-in regime. These different frequency regimes are successfully simulated in this investigation. They are related to the shedding process through which the wake undergoes a transition from a Karman street to a reversed Karman street. The transition between the different frequency regimes is simulated at both constant frequency and constant amplitude. We found that the frequency regimes are strongly related to the wake type exhibited. Wake-types with multiple-vortices-per-half-cycle of oscillation are found in harmonic regimes and wake-types with one vortex-pair shed per cycle are in the region where one distinct frequency is in control (lock-in and natural regimes). Wakes where the leading-edge vortices contribute to the shedding process are also simulated.

# Zusammenfassung

Die instationäre Strömungen über Stromlinienkörpern ist eins der wichtigsten Themen der Fluidodynamik. Das Interesse an dieser Strömung ist von ihrer Nichtlinearität und Instationarität motiviert. Die Gleichungen die diese Strömung beschreiben sind deshalb analytisch unlösbar. Mit der Zunahme der Rechenleistung von Computern, der Nutzung, und der Entwicklung von hochauflösenden Computational Fluid Dynamics Methoden, verfügt man über eine attraktive und effiziente Alternative zur Lösung der instationären Strömungsgleichungen. In dieser Arbeit führen wir numerische Simulationen von stationären sowie instationären Strömungen über unbewegten und absenkenden Flügelprofilen mit einer hochauflösende Spektralen Elemente Methode (SEM) durch. Diese Methode wird das erste Mal für die numerische Lösung solcher Strömungen benutzt. Unsere Simulationen bestätigen die Eignung dieser hochauflösenden Methode zur Lösung und Charakterisierung instationärer Strömungen über Stromlinienkörpern. Es wird eine sehr detaillierte räumliche und zeitliche Beschreibung der Strömung erreicht. Die Ergebnisse, die wir mit der hochauflösenden Spektralen Elemente Methode bekommen haben sind mit bisher veröffentlichten experimentellen und numerischen Untersuchungen in dieser Arbeit validiert.

Absenkende Flügelprofile erzeugen Wirbel im Nachlauf während ihrer Bewegung. Die Nachläufe von absenkenden Flügelprofile sind in drei Modelle bezüglich der von dem Flügelprofil erzeugten Kraft zu klassifizieren: Widerstand-Nachlauf, Neutral-Nachlauf und Schub-Nachlauf. Diese Nachläufe wurden in dieser Arbeit erfolgreich simuliert, außerdem der Übergang von einem Nachlauf-Modelle zu den anderen. Zudem haben wir zwei bisher unbekannte Modi beobachtet. Wir stellen die Annahme, die Strouhal-Zahl sei der einzige Charakterisierungsparametern von absenkenden Flügelprofilnachläufen in Frage. Unsere Ergebnisse zeigen, dass im Hinblick auf solche Strömungen auch die Amplitude und die Frequenz der Absenkung zu berücksichtigen sind.

Schließlich haben wir die verschiedenen Frequenzregime die bei absenkenden Flügelprofilen erzeugt werden untersucht. Solche Frequenzregime sind abhängig vom Verhältnis der Anregungsfrequenz zur Eigenfrequenz der Wirbelablösung. Drei Frequenzregime sind in der Literatur definiert: das Eigenfrequenz-Regime, das harmonische Regime und das Lock-in Regime. Diese Regime wurden in dieser Arbeit erfolgreich simuliert, ebenso der Übergang von einem Regime zu den anderen. Wir haben festgestellt, dass die Frequenzregime die Nachlaufstruktur bestimmen. Nachlaufmodelle mit mehr als einem abgelösten Wibel pro Absenkungsperiode sind nur im harmonischen Regime zu finden. Das Eigenfrequenz- oder Lock-in Regime erzeugen Nachlaufmodelle mit nur einem abgelösten Wirbel pro Absenkungsperiode.



# Chapter 1

## Introduction

### 1.1 Turbulence and unsteadiness

Turbulent flows are present in our everyday life, whether it is smoke from a cigarette, water running from a waterfall, or just mixing some milk in a tea cup (see Fig. 1.1). This daily encounter with turbulence offers to us an intuitive and descriptive understanding of turbulence. One can observe that the main characteristics of turbulence are unsteadiness, irregularity, randomness, chaotic behaviour, and the existence of different time and length scales. Turbulence is very important for a broad range of applications. These applications can range from turbo-machinery, flow around vehicles and buildings, mixing of fuel in engines, chemical reactions, to the wind blowing on wind turbines blades. Although turbulence is a very important issue in many domains, a watertight definition of turbulence is still not available. Turbulence is mostly defined by describing its properties. According to *Tritton* [70] "No short but complete definition of turbulence seems to be possible. One has rather to describe the features that are implied by the use of the name. One can formulate a brief summary, rather than a formal definition, that attempts to encapsulate the description. Perhaps the best is that turbulence is a 'state of continuous instability'".

Turbulence is thought to arise via the instability of laminar flows. The term *laminar* is used to indicate a flow which is not *turbulent*. When a laminar flow is subjected to strong enough perturbations (for example, increasing the flow rate in a pipe flow), *instability* occurs. The change from a laminar to turbulent flow is termed *transition* to turbulence. This transition can be controlled by many parameters. The most important of these parameters is the *Reynolds number*  $Re = U_0 D / \nu$ , where  $U_0$  is the mean-flow velocity,  $D$  is the characteristic length scale (for example, the diameter of the pipe for pipe flows), and  $\nu$  is the kinematic viscosity of the fluid. When the Reynolds number is increased, the nonlinear convective terms of the Navier-Stokes equation become very large compared to the viscous terms which act as instability dampers. Thus, large Reynolds numbers



(a)



(b)

Figure 1.1: (a) Turbulent flow in a waterfall cascade (b) the turbulent and irregular flow resulting from a cigarette smoke.

are a prerequisite for the onset of turbulence. The transition to turbulence is achieved either by a sudden change in the flow configuration when the Reynolds number reaches a critical value or it can occur as a succession of qualitative changes of the laminar flow leading at the end to a fully turbulent flow (see Fig. 1.2).

Many different techniques and methods are dedicated to study the different issues concerning turbulence and turbulent flows. It is well known that laminar and turbulent flows are governed by the Navier-Stokes equations, which have been known for more than a century. These equations are able to describe all different flows in great detail. Nevertheless, the power of the Navier-Stokes equations is transformed to a weakness when dealing with turbulent flows. The Navier-Stokes provide every detail of the flow covering the smallest time and length scales. This means that the amount of information contained in the calculated velocity field is immense and this renders a *direct* approach in solving the Navier-Stokes a very difficult one. This difficulty is further increased when considering large Reynolds numbers, as the computational cost is proportional to  $Re^3$  [60]. Therefore *indirect* methods exist in order to simulate turbulent flow. These methods are based on a statistical approach, so that the flow is not described in terms of the velocity  $U(\mathbf{x}, \mathbf{t})$  but using the mean velocity field. Such methods include turbulent viscosity models (the  $k - \epsilon$  or  $k - \omega$  models), Reynold-stress models, Large-Eddy-Simulations (LES), and models based on the Probability Density Function of the velocity (PDF) [60].

One of the most interesting examples of turbulent and unsteady flows are the flows over streamlined and/or bluff bodies. This is partly because they are important in understanding various flow problems. Some examples are dynamic response phenomena, flow detachment and reattachment, boundary-layer dynamics and transition to turbulence. A thorough study of these phenomena can in principle be achieved by performing *Direct Numerical Simulations* of the turbulent flow over streamlined and bluff bodies. However, such simulations are still computationally expensive. The use of statistical approaches like LES or RANS on the other hand, while being computationally feasible, involve approximations. These approximations do not allow for a detailed following of the flow structures and important transition features like flow attachment and re-attachment. This type of information is crucial in the study of lift and thrust generation, and power extraction under unsteady conditions.

In this study, we focus on the direct numerical study of the flow over airfoils in a mid-point of the parameter space between unsteady conditions and fully turbulent flow, at low to moderate Reynolds numbers. This allow us to study, with great spatial and temporal detail, important flow transitions which occur under unsteady conditions. Our approach is therefore based on a compromise between fully resolving important flow structures and transitions, which are not visible when using averaged-field approaches like LES or RANS, and at the same time being able to perform *Direct Numerical Simulations* of non-turbulent flow

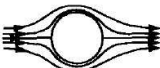
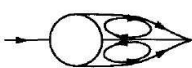
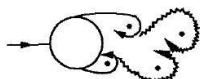
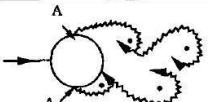
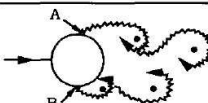
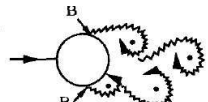
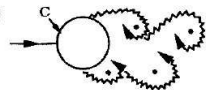
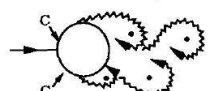
a)		No separation. Creeping flow	$Re < 5$
b)		A fixed pair of symmetric vortices	$5 < Re < 40$
c)		Laminar vortex street	$40 < Re < 200$
d)		Transition to turbulence in the wake	$200 < Re < 300$
e)		Wake completely turbulent. A: Laminar boundary layer separation	$300 < Re < 3 \times 10^5$  Subcritical
f)		A: Laminar boundary layer separation B: Turbulent boundary layer separation; but boundary layer laminar	$3 \times 10^5 < Re < 3.5 \times 10^5$ Critical (Lower transition)
g)		B: Turbulent boundary layer separation; the boundary layer partly laminar partly turbulent	$3.5 \times 10^5 < Re < 1.5 \times 10^6$ Supercritical
h)		C: Boundary layer com- pletely turbulent at one side	$1.5 \times 10^6 < Re < 4 \times 10^6$ Upper transition
i)		C: Boundary layer comple- tely turbulent at two sides	$4 \times 10^6 < Re$ Transcritical

Figure 1.2: Transition to turbulence due to the evolution of the flow over a cylinder. The Reynolds number increases from the upper to the the lower frame. (From [67].

transitions under unsteady conditions which occur in the transition from highly unsteady to fully turbulent flow.

## 1.2 Unsteady flows over airfoils

In real life applications unsteadiness is always present in the flow over streamlined bodies. Its consequences are fundamentally important problems which concern a broad range of applications. During most of the twentieth century, unsteady flows over airfoils received particularly high attention, mostly because of their impact on the design and operations of airplanes and helicopters. Other applications for unsteady flows over airfoils/streamlines bodies include turbomachinery and animal- and fish-like propulsion. Recently, there is also a large interest in unsteadiness in the field of wind turbines design and manufacturing, as unsteadiness can influence the power production of wind turbines. In this investigation we will be mainly discussing incompressible, two-dimensional, unsteady flows over motionless and oscillating airfoil wakes at low to moderate Reynolds numbers ( $Re < 10^5$ ). The term oscillating airfoils includes vertical (plunging, also called heaving and flapping) and rotational (pitching) motions. In the remainder of this investigation the term oscillating airfoils will denote the oscillatory motion of airfoils in general. The term *heaving* will be used to specify that the motion of the airfoil is vertical. This term is equal to using the terms plunging and flapping. The term *pitching* will be used to indicate the rotational motion of the airfoil.

In dealing with unsteadiness, extensive studies were concerned mainly with stall and dynamic stall, which occurs in the retreating blade of helicopters. The retreating blade stall is a dangerous flight condition which occurs in helicopters and other rotary wings [13, 44]. Helicopter stall occurs when the rotor blade rotating away from the direction of flight stalls (called retreating blade) and as a result the helicopter experiences lift loss. This is mainly resulting from the excessive angle of attack (AOA) experienced by the blade. This phenomenon constitutes a limiting factor for the maximum speed of helicopters and other flight vehicles which use rotating blades. Other undesirable effects of unsteadiness are flutter [63], vortex-induced-vibrations (VIV) [75], flow-induced-vibrations (FIV) [6, 53], buffeting and material fatigue [3, 76].

Besides these undesirable effects, unsteady flows over airfoils have also some *desirable* effects such as thrust generation by heaving airfoils. A lot of work is also dedicated to the use of *smart control systems* which use the unsteadiness in an efficient way to actively or passively control the airfoils as to reduce the vibrations [31, 51], the acoustic signature or achieve energy efficiency [54, 65]. Other beneficial aspects of unsteadiness are stall delay to higher incidences, controlled vortex generation and controlling the unsteady forces in some effective way as to permit improvements of performance.

## 1.3 Dynamic Stall

One of the most common and discussed topics in relation with unsteady flow over airfoils is the stall. Stall is an aerodynamical phenomenon which can be divided into two categories. These categories depend on whether the airfoil is static or moving and are labelled static stall and dynamic stall. Stall is extensively studied for helicopter blades, as it is associated with constraints on the helicopter speed, lift and maneuverability [33].

In the following we cite some examples where stall (dynamic and static) plays an important role. In the field of fish- and bird-like propulsion, it has been found that the proper timing of the dynamic stall vortex is crucial to the flight process [17]. On the other hand, it is clear that the limitations on the flight envelope of helicopters and other flying vehicles is caused by the onset of dynamic stall, therefore the solution to these limitations passes by a complete understanding of this phenomenon [18]. Another example where stall is to be taken into account concerns wind turbines. Wind turbines are subject to large unsteady variations in loads. This is mainly due to the unsteady nature of the inflow they are experiencing, especially in offshore locations. To predict the performance of wind turbines, the modelling should take into account the critical situation of the dynamic stall. This renders the task of the modelling of the unsteady aerodynamics a rather difficult one, as pointed out in [66]. There is an abundant literature concerned with the unsteady conditions experienced by wind turbines and their modelling. The prediction of the edgewise vibrations in the case of stall was examined by *Petersen et al.* [58]. He concluded that the use of dynamic stall models improved the level of agreement with the experimental measurements. *Schreck & Robinson* [64] emphasise that to improve the development of aerodynamical models, dynamic stall of wind turbines must be characterized and very well understood. Accounting for dynamic stall can also be achieved by using semi-empirical models, as the well known *Beddoes-Leishman* model [24].

### 1.3.1 Aerodynamics of Stall

Stall (also called static stall) occurs when the angle of attack becomes so great that the airflow is broken over the upper surface of the airfoil. The critical AOA at which the stall happens is usually in the interval 8 to 20 degrees, depending on the Reynolds number and the airfoil geometry. The variation of the lift coefficient with the angle of attack is illustrated in Fig. 1.3. The lift coefficient increases with the angle of attack until the critical value of AOA is reached. At this value the flow is massively detached from the airfoil surface and more lift can not be produced. When the angle of attack is further increased the lift drops significantly in what is called the lift-crisis or lift-stall (see Fig. 1.3).

A more complex phenomenon occurs when the airfoil stalls while the airfoil itself undergoes unsteady motion. This is called *dynamic Stall*. The dynamic

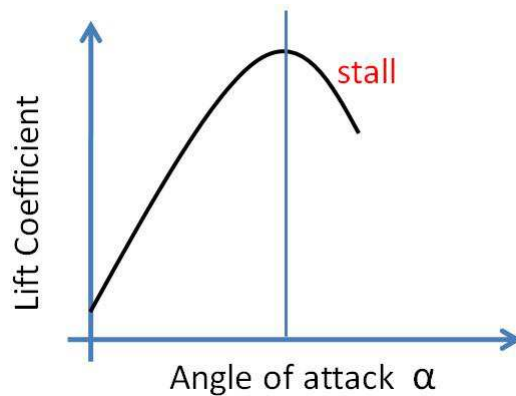


Figure 1.3: Variation of the lift coefficient as a function of the angle of attack for static stall.

stall takes place at a higher critical angle of attack as the static stall, and is characterized by a higher lift overshoot. It exhibits massive boundary-layer detachment and reattachment, separation and nonlinear effects such as one-degree of freedom instabilities. The aerodynamic forces during dynamic stall exhibit larger hysteresis with respect to the instantaneous angle of attack (see Fig. 1.4). The aerodynamical coefficients can greatly exceed the maximum values reached during static stall. Dynamic stall is characterized by the creation, the convection, and the shedding of a leading-edge vortex (LEV). As long as the LEV is on the airfoil surface, the produced lift is enhanced. However, when the LEV is swept over the airfoil surface, the aft-moving center of the pressure (ie, moving towards the trailing-edge) induces very large nose-down pitching moments. These moments are fundamentally different from their static-stall counterparts, and they can constitute high torsional dynamical loads on the airfoil. These loads may be the origin of aeroelastic problems. These problems can cause stall flutter which consequently lead to fatigue and in the long term to structural failure [44, 47].

It is clear from the previous description, and from the multitude of applications, that dynamic stall is an aerodynamic phenomenon of great importance. A better understanding of dynamic stall will allow a more realistic numerical modelling, and this in turn will enable more realistic numerical simulations of other situations where unsteadiness is involved.

### 1.3.2 Literature Review on Dynamic Stall

In this section a literature review is presented for analytical, experimental and computational studies dealing with the prediction of dynamic stall. As mentioned above, dynamical stall is of complicated nature. This mainly due to its nonlinearity and its dependence on several parameters (see Fig. 1.5 for the dependence on the frequency and amplitude for a pitching airfoil). This complexity resulted

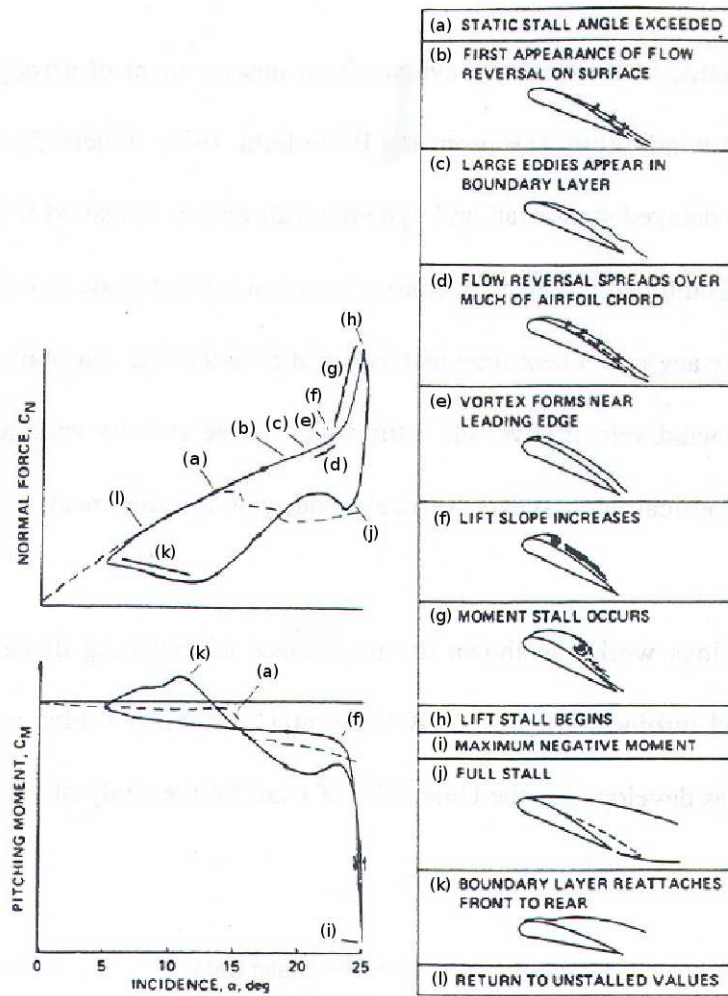


Figure 1.4: Variation of the lift (or normal forces)  $C_N$  and the pitching moment  $C_M$  as a function of the instantaneous angle of attack for a NACA0012 profile. The dashed line represents the static stall case. The solid line represents the pitching airfoil case, where the incidence angle  $\alpha$  varies as a function of time in a sinusoidal fashion (Adapted from [8]).

in the first prediction tools being mainly based on empirical and semi-empirical methods. These methods use empirical functions to fit the experimental forces data. Some examples of these methods are the Boeing-Vertol gamma function [26] and the semi-empirical method developed by ONERA [71]. It is important to note that theoretical progress is rather slow on this difficult problem, although some techniques have been developed and are still being improved and corrected. Nevertheless, these techniques are restrictive because of the assumptions and approximations that are made and deal only with a specific and limited range of flow parameters. Some of these theoretical developments are the linearized thin-airfoil method [68], the viscid-inviscid interaction method [61] and the superposition method [46].

Experimentally, most test facilities available can only produce steady flows, and the data acquisition techniques were mostly developed for steady flows. An important characteristic of the facilities used for experimental studies of dynamic stall is the ability to reproduce the frequency and amplitude parameters in their nondimensional range [17]. For example, at small reduced frequencies, the reduction of the geometric scaling of the airfoil (or model) implies very high physical frequency values. Therefore, conventional dynamic testing becomes limited to deterministically imposed unsteady motions (sinusoidal motion) or a transient motion of a specific kind (ramp motion). Experimental investigations have shown that dynamic stall depends of numerous flow parameters and on forcing conditions [17, 48, 49]. The LEV received a lot of attention and has been well documented [9, 48]. *Leishman* [43] showed that the high adverse leading-edge pressure gradients that accompany the oscillatory motion of the airfoil make it more sensitive to leading-edge separation. The author concluded that the static stall characteristics are not useful indicators of how the airfoil will behave under dynamic stall conditions. Only a limited range of test conditions have been experimentally explored and examined in detail, and much more experimental work needs to be achieved before achieving a complete understanding of dynamic stall. Further measurements are required to explain dynamic stall onset, in particular the nature of the flow in the boundary-layer region.

With the increase in computational resources and power, more computational work is dedicated to the numerical simulation and prediction of dynamic stall. In his review *McCroskey* [49] concluded that CFD research is mainly concerned with the understanding and prediction of the nonlinear phenomena of dynamic stall. These phenomena are beyond the thin-airfoil theory [68, 74]. To simulate real airfoils in real fluids the numerical methods need to account for the airfoil shape and camber, finite mean angle of attack, large amplitude motions and the boundary-layer displacement. *Giesing* [22] numerically simulates arbitrary airfoil geometries and motions, and *Desopper* [15] includes boundary-layer effects. The trend that emerges from these studies is that the individual surface pressures are affected much more than the difference in pressure across the airfoil. This explains the fluctuations observed in the lift and pitching moment. It also explains the

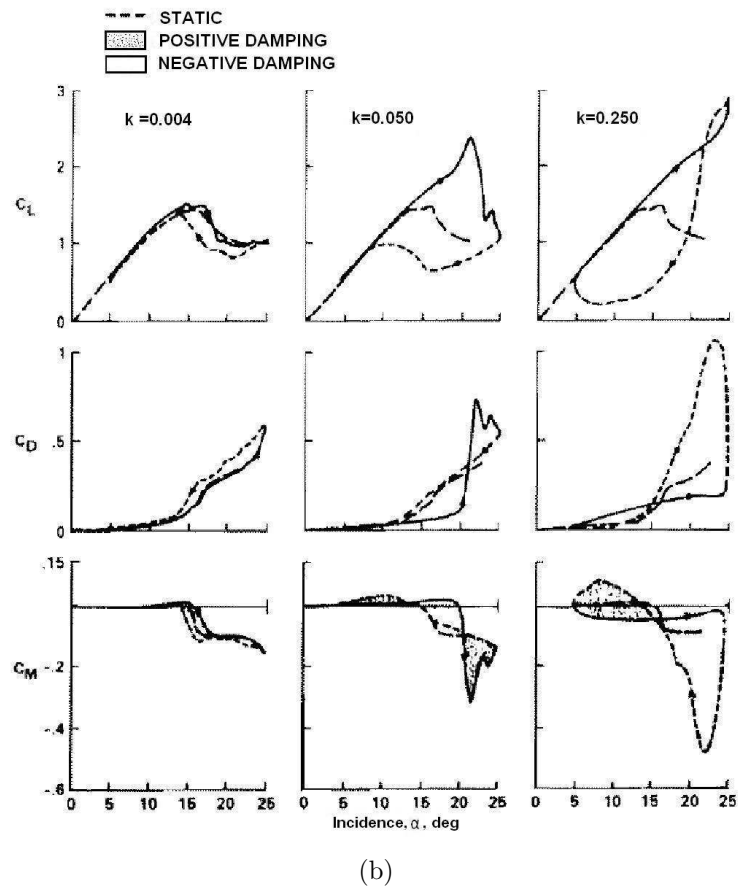
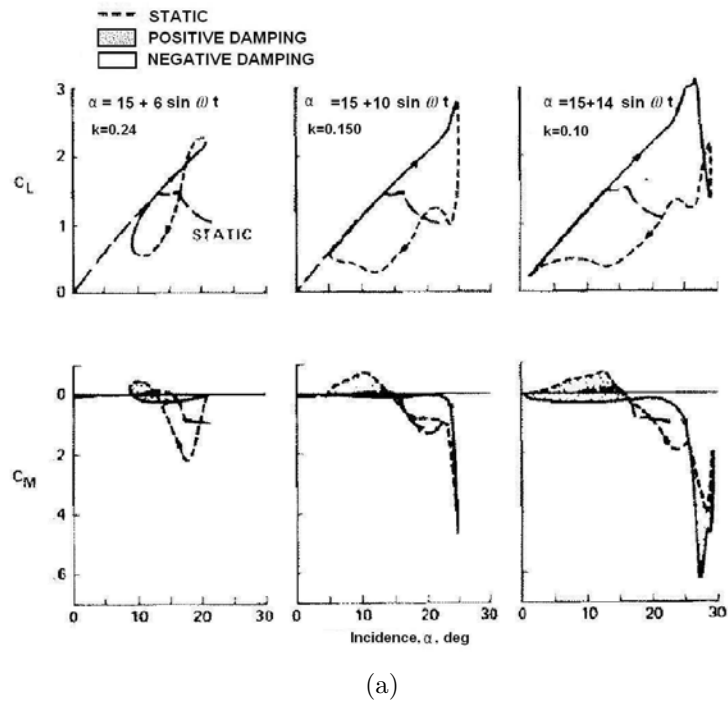


Figure 1.5: Effect of (a) the amplitude and (b) the reduced frequency of oscillations on the aerodynamical coefficients for an airfoil oscillating in pitch during dynamic stall.  $C_L$ ,  $C_D$  and  $C_M$  are the lift, drag and momentum coefficients; respectively. (Adapted from [8]).

discrepancies observed in comparing the deviations of the lift and momentum coefficients to the thin-airfoil theory and the agreement observed for the pressure coefficient. It is important to point out that if boundary-layer calculations are to be done, this requires a realistic pressure distribution to be implemented [49]. The application of the Kutta condition at the trailing-edge has been a major topic in the modelling and the computation of dynamic stall. According to *McCroskey* [49] further detailed studies are needed to clarify the conditions at the trailing-edge region, as the correct theoretical modelling of this region is particularly important to account for trailing-edge stall on heaving airfoils.

In their review *Ekaterinaris and Platzer* [16] enumerated and discussed the methods used for the numerical prediction of dynamic stall. These include mainly the unsteady panel method [77], the boundary-layer method [19] and the viscous-inviscid interaction methods [32]. The authors concluded that although in recent years significant progress has been achieved in the numerical investigation of unsteady flows (particularly dynamic stall phenomena), several issues still remain to be addressed. According to the authors the aspects which require further research are the compressibility and transonic effects at high Reynolds numbers ( $Re > 10^6$ ). Other aspects are the flow reattachment and the transitional models used to account for the transition from laminar to turbulent regimes, as a proper transition model can improve the prediction of dynamic stall forces hysteresis-loops. A challenging area for future studies and improvements are three-dimensional simulations, which are very expensive in terms of computational cost.

## 1.4 Heaving Airfoils Wakes

Small size fixed airfoils used for propulsive purposes are not efficient. This is due to the increase in the thickness of the boundary-layer which results in an increase in the viscous drag, this in turn causes lift-loss and a pressure-drag increase. On the other hand, it is well established that heaving airfoils (or oscillating airfoils in general) are more efficient than their fixed counterparts when the size and Reynolds number are decreased. Moreover, at certain combinations of frequency and amplitude of oscillations, heaving airfoils can produce lift and thrust and thus propulsion [41]. This is seen everyday in nature, as the propulsion of fish and birds and other insects relies on flapping wings for flying and flapping fins for swimming. Insects and birds not only are efficient at low Reynolds numbers but they use the heaving motion to their advantage by exploiting the aerodynamical phenomena resulting from such a motion.

The development of Micro Air Vehicles (MAVs) has motivated and stimulated the research on the subject of oscillating airfoils. MAVs are defined by the US Defence Advanced Research Project Agency (DARPA) as a class of unmanned aerial vehicles (UAV) not larger than 15 cm, and can potentially be reduced to the size

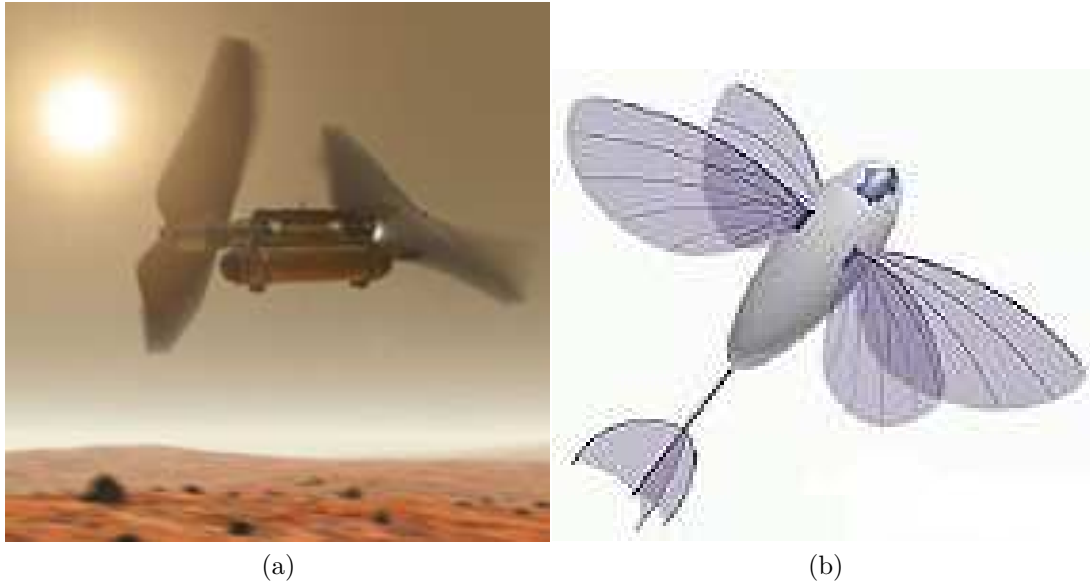


Figure 1.6: Schematic representation of Micro Air Vehicles (MAV) based on birds- and insects-like flight. (a) The *Entomopter* MAV model to be used on missions on the planet Mars [12]. (b) The Ornithopter MAV *Mentor*, designed and developed by the University of Toronto and SRI International [50].

of large insects [1]. MAVs have a broad range of applications, ranging from military to civil applications. Among these applications are rapid location of trapped persons in damaged zones, monitoring, sensor carriers, forestry and wildlife surveys. Fig. 1.6 illustrates two different kinds of MAVs. Other applications areas concerned with studying heaving airfoils are the wake vortices dynamics [42], fish and marine animals propulsion [45], flow control and the unsteady aerodynamics of blades undergoing cyclical heaving motions as helicopters and wind turbines blades [11] and generally low to moderate Reynolds numbers flows [2]. There is a need to understand heaving airfoils mechanisms which are used in nature and to adopt or change these mechanisms for the purpose of designing better and more efficient MAVs. For this end, it is necessary to predict the flow over and in the wake of these airfoils as the forces and loads on them.

### 1.4.1 Aerodynamics of Heaving Airfoils

Here we present the parameters which are important for heaving airfoils flows and expose the analysis methods and results that are currently available. Several parameters govern the heaving motion of airfoils. Among these parameters are the amplitude and the frequency of oscillations, the shape and the camber of the airfoil, and the Reynolds number.

Let us consider the airfoil motion as illustrated in Fig. 1.7. The sinusoidal

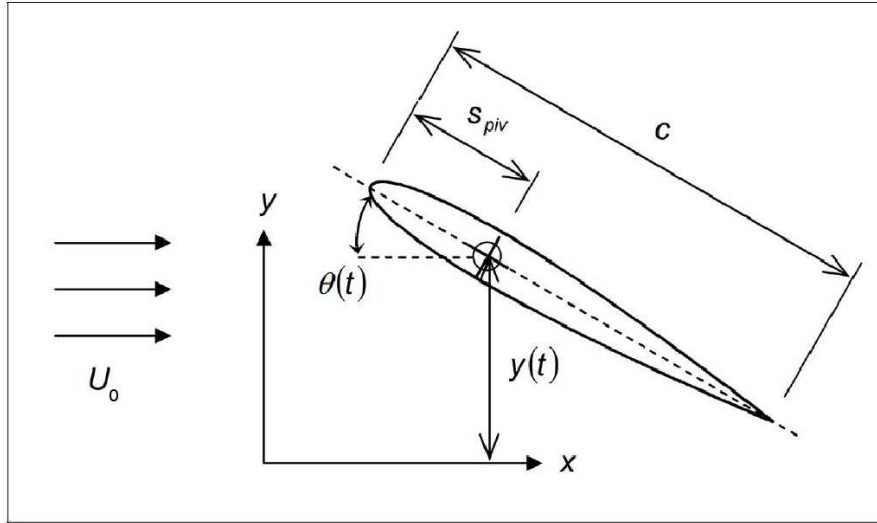


Figure 1.7: Schematic representation of the airfoil heaving and pitching motions.  $y(t)$  represents the heaving motion where the vertical coordinate of the airfoil  $y$  vary sinusoidally in time.  $\theta(t)$  represents the pitching motion of the airfoil where the angle of attack varies sinusoidally in time.  $U_0$  is the free-stream velocity and  $c$  is the airfoil chord length, and  $S_{piv}$  is the pivot-length. (Adapted from [78]).

heaving motion (not to be confused with the pitching motion where the angle of attack changes in a sinusoidal fashion, or with the hovering motion which is the combination of the pitching and heaving motion) of the airfoil is defined by

$$y(t) = h \cos(2\pi ft), \quad (1.1)$$

where  $y(t)$  represents the temporal variation of the vertical coordinate of the airfoil,  $h/c$  is the plunge amplitude normalized by the airfoil chord length  $c$ , and  $f$  is the frequency of oscillations, normalized as  $f = fc/U_0$ . Another representation of the frequency is the non-dimensional *reduced frequency* defined as  $k = \pi fc/U_0$ , where  $U_0$  is the free-stream velocity. Some investigations define the reduced frequency as  $k = 2\pi fc/U_0$ . In the reminder of this investigation, unless otherwise indicated, we use the first definition of the reduced frequency.

Numerous investigations suggest that the most important control parameter is the Strouhal number,  $St = fh/U_0 = 2kh/\pi$ , as it combines the frequency and amplitude of oscillations [35, 69]. Recent investigations show that the Strouhal number is not the only parameter that characterizes the wake and flow over the surface of the airfoil, and that the frequency and amplitude of oscillations have to be considered separately [78, 79]. The Reynolds number is also a critical parameter which influences the heaving airfoil dynamics. This is reflected by the fact that the strategies used by birds at high Reynolds number are different than those used for lower Reynolds numbers, where the leading-edge vortex is very

important. Numerous analytical and computational investigations are dedicated to study the aerodynamics of heaving airfoils. The background of these methods is discussed in the following.

If a heaving airfoil/body is exposed to an incoming flow, it will exhibit an alternate vortex shedding in the wake at a certain critical value of the Reynolds number. The alternate vortices are produced by the unsteady flow separation over the body and are called a *Karman vortex street* [21, 68, 73]. These rows are constituted of clockwise vortices on the top and anticlockwise vortices at the bottom of the vortex sheet and they are a signature that the body is producing drag (see Fig. 1.8a). The time-averaged velocity profiles for these configurations exhibit a momentum-deficit, which means that the mean velocity inside the wake is lower than the free-stream velocity. When the rows of vortices are inverted the configuration is called a reverse or inverted Karman vortex street. This is a signature of thrust production (see Fig. 1.8b), as the time-averaged velocity profiles exhibit here a momentum-jet (or excess). This means that the mean velocity inside the wake is higher than the free-stream velocity. Finally, when the rows of vortices are perfectly aligned the wake is called neutral, as the inherent drag equals the produced thrust (see Fig. 1.8c). The time-averaged velocity profiles for these configurations exhibit an equilibrium of the momentum, that is, the mean velocity is *almost* equal to the free-stream velocity.

These wakes were observed and documented experimentally and computationally [20, 41, 42, 78] (see Fig. 1.10 and Fig. 1.9). One common feature of these three wakes is that one pair of vortices is shed per cycle of oscillation of the airfoil/body. Nevertheless, some configurations exhibit more than a pair of vortices per oscillation cycle, which are called multiple-vortex-per-cycle modes (see Fig. 1.9 and Fig. 1.10). The origin of these modes is still not well understood and this will be discussed at length in Chapter 5. Using an inviscid vortex lattice method, *Hall and Hall* [28] showed that the force on the heaving airfoil is affected very little by the details of the wake vortices roll-up. The authors extended their work to  $k = 1.4$ . This means that two different wake shapes can give two different time-averaged velocity profiles but their averaged momentum excess will be the same. Therefore, the details of the wake structures are not the result of the forces distribution on the airfoil and more parameters need to be explored to explain the wake configurations obtained experimentally or computationally.

## 1.4.2 Literature Review on Heaving Airfoils

*Birnbaum* [5], was the first to analytically study the incompressible flow over a heaving airfoil, where he presented an analysis for small values of the reduced frequency. *Glauert* [23], calculated the forces on an oscillating airfoil for arbitrary oscillation frequencies. The first to state that an oscillating airfoil can produce thrust were *Knoller* [40] and *Betz* [4] in independent investigations. The thrust generation results from the fact that heaving airfoils create an effective angle of

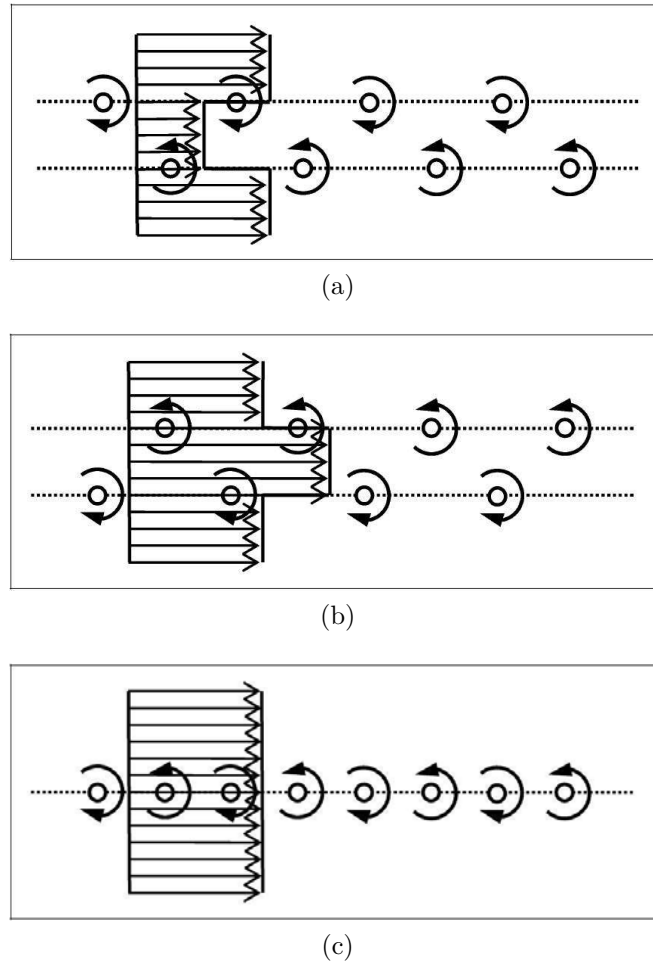
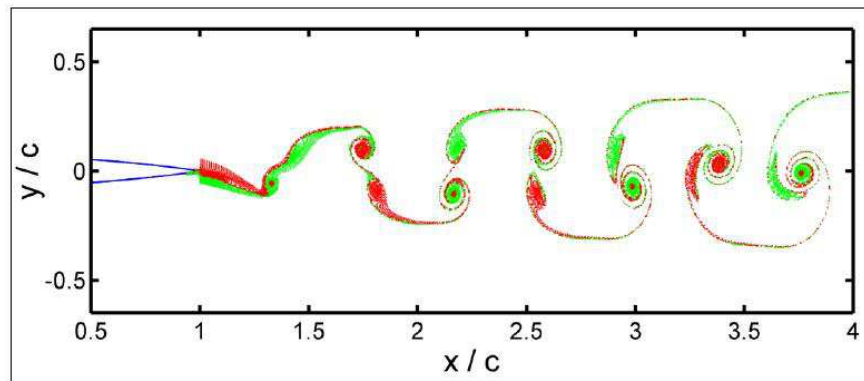
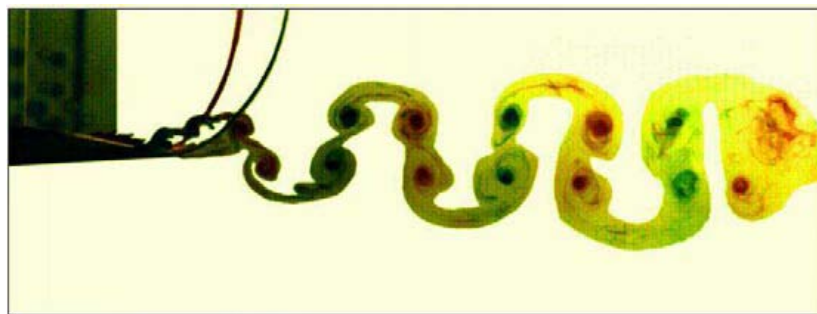


Figure 1.8: Schematic representation of: (a) Karman vortex street, the upper-row is composed of clockwise vortices and the lower-row is composed of anticlockwise vortices. This wake configuration indicates a drag-producing wake. (b) The reversed Karman vortex street, the upper-row is composed of anticlockwise vortices and the lower-row is composed of clockwise vortices. This wake configuration indicates a thrust-producing wake. Note that in the two cases there is a vertical spacing between the rows of opposite rotating vortices. The time-averaged velocity profiles are superposed on each wake, represented by the straight arrows. (c) Neutral wake, the clockwise and anticlockwise vortices are on the same row and there is no vertical spacing as in the thrust- or drag-producing wakes. This wake configuration indicates that the inherent drag is equal to the produced thrust. (From [78])

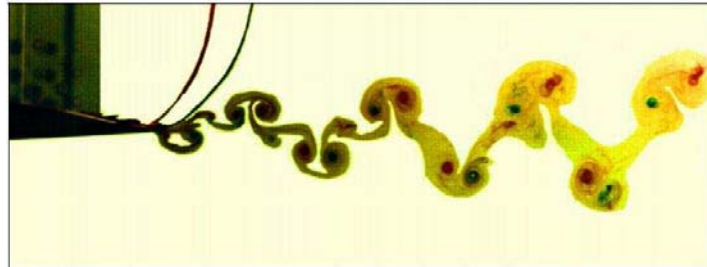


(a)

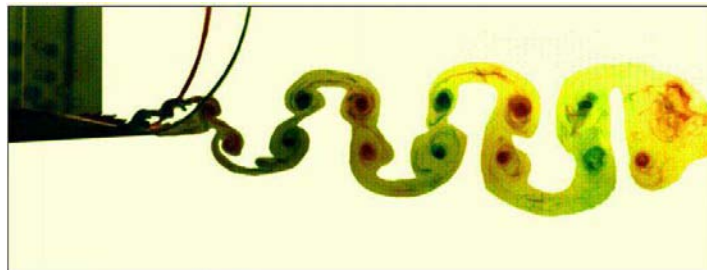


(b)

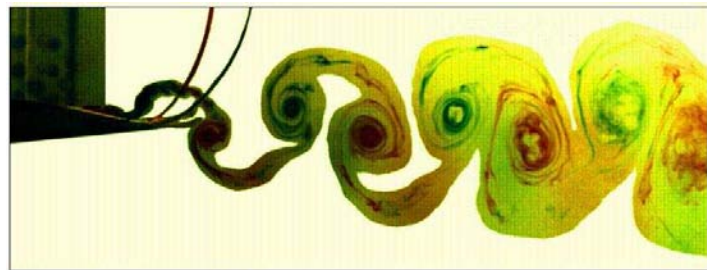
Figure 1.9: Multiple-vortex-per-cycle wake. (a) Vorticity distribution of a numerically simulated multiple-vortex-per-cycle wake. The simulation is for a heaving NACA0012 profile at  $k=4$ ,  $h=0.02$ , and  $Re = 2 \times 10^4$  using a laminar Navier-Stokes solver (from [78]). (b) Vorticity distribution of an experimentally simulated multiple-vortex-per-cycle wake (from [42]). The experiments are conducted for a heaving airfoil at the same parameters as the numerical simulation. The black box and the wires visible at the left of the experimental figure are part of the experimental apparatus used in [42].



(a)



(b)



(c)

Figure 1.10: Vorticity distributions of experimentally simulated wakes. (a) A drag-producing wake at  $k = 3.93$  and  $h = 0.0125$ . (b) A neutral wake at  $k = 3.93$  and  $h = 0.025$ . (c) A thrust-producing wake at  $k = 3.93$  and  $h = 0.05$ . The experiments are conducted for a NACA0012 profile at  $Re = 2 \times 10^4$  (from [42]). The black box and the wires visible at the left of the experimental figure are part of the experimental apparatus used in [42].

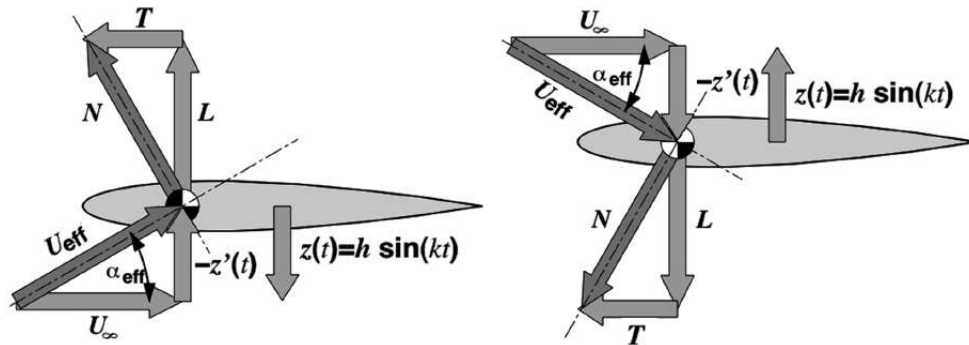


Figure 1.11: Schematic representation of incident, resultant velocities and resulting forces on the airfoil during the upstroke (right) and downstroke (left) phases of a heaving motion. (From [59]).

attack, so that an aerodynamic force is generated which decomposes into lift and thrust forces. This occurs during both the up and down strokes of the heaving motion (see Fig. 1.11). The ability of heaving airfoils to produce thrust is called the *Knoller-Betz effect*. This effect was confirmed experimentally by *Katzmayr* [39]. *Von Karman* and *Burgers* [73] showed that a wake which consists of rows of counter-rotating vortices produces thrust.

One aspect of studying heaving airfoils is to obtain expressions or predictions for the forces acting on the airfoil. *Theodorsen* [68] calculated these expressions for the time-dependent lift and momentum forces on a flat plate undergoing an oscillatory motion, as an approximation to the flow problem. The oscillations were considered to be very small in order to be able to use the linearised theory. The potential flow assumption means that the flow is considered incompressible and inviscid and that flow separation is not accounted for. *Garrick* [21] extended the analysis of *Theodorsen* by analytically calculating the thrust produced by the airfoil using the integration of the pressure over the airfoil surface and the calculation of the energy input rate into the vortex wake. *Garrick* analysis is a starting point to discuss aerodynamics of oscillating airfoils, as it is a simple method which permits the calculation of a first guess of the forces over an oscillating airfoil.

The linearized potential analysis assumes that the airfoil is treated as a flat plate, so that the thickness effects are not considered and the Kutta condition is valid. The Kutta condition states that there should be no separation at the trailing-edge of the airfoil, and this condition is likely to be violated at high amplitudes and frequencies of oscillations [38]. Another assumption of the linearised potential analysis is that the wake is considered as *frozen*, which means that it can not evolve under the action of its own induced velocity. Although this analysis showed a fair agreement at low amplitudes and frequency of oscillations, the assumptions made by these methods are very far from representing what is happening in a *real* heaving airfoil wake and is unable to explain the flow features.

Panel methods were introduced to remove some of the assumptions made by the linearised potential analysis. These methods became very popular, they assume airfoils with arbitrary sections and motions. The main idea of the Panel method is that the geometry of the airfoil is divided into *panels* and each panel induces a velocity on itself and the other panels and this can be expressed by simple equations containing geometric relations. A system of linear equations is then built up and solved for the unknown panels velocities [38]. In unsteady situations the wake must be accounted for and it is represented by a finite number of discrete panels [34]. The angle at which the wake is shed can also vary in time, as the flow over the airfoil surface varies. This renders the use of the unsteady Panel method enforcing the Kutta condition questionable.

*Young* [78] used a linearised analysis based on *Garrick* [21], an unsteady panel method code (UPM) and a Navier-Stokes solver for comparison purposes and to explore the limits of the simplifications on the flow of heaving airfoils. The author states that because the UPM code cannot account for the viscous drag from the airfoil, it predicts only thrust-producing wakes. He also found that neither the Garrick-method-based code nor the UPM code could produce the multiple-vortex-per-cycle structures observed in the experiments [42], while the Navier-Stokes solver on the other hand successfully reproduced these results. This implies that the UPM and the Garrick method were not able to capture the physics of the problem and this is probably due to the simplifications and the low-order resolution of these methods. As an example, see Fig. 1.12, where an unsteady panel code is unable to reproduce the results obtained experimentally by *Lai & Platzer* [42]. Note that the turbulent Navier-solver used by *Young* in [78] (also plotted in Fig. 1.12) could not also reproduce the experimental results. This can be attributed to the inefficiency of the turbulent model used. Or this can also mean that the flow is laminar. The laminar Navier-Stokes solver, on the other hand reproduced the experimental results. In conclusion, one can state that there is a need for a *high-order method* in space and in time, with *no simplifications* in order to be able to grasp all the aerodynamic features and flow transition details. Such a method is used in this investigation.

The choice of using the Spectral Element /hp Method is motivated by the fact that such method allows a very high spatial resolution without an exceedingly high computational cost. Additionally, there is no need for remeshing operations, since convergence can be achieved by increasing the order of the polynomial approximation in all or some regions of the computational domain. As remeshing is a very time consuming operation, obtaining convergence without remeshing allows a substantial reduction of computational time when using Spectral /hp Element Methods. Moreover, this method allows to perform a Direct Numerical Simulation (DNS) and therefore no assumptions are made about the laminar or turbulent nature of the flow. Additionally, there is no need for a turbulence model (LES or RANS) or a transition-to-turbulence model.

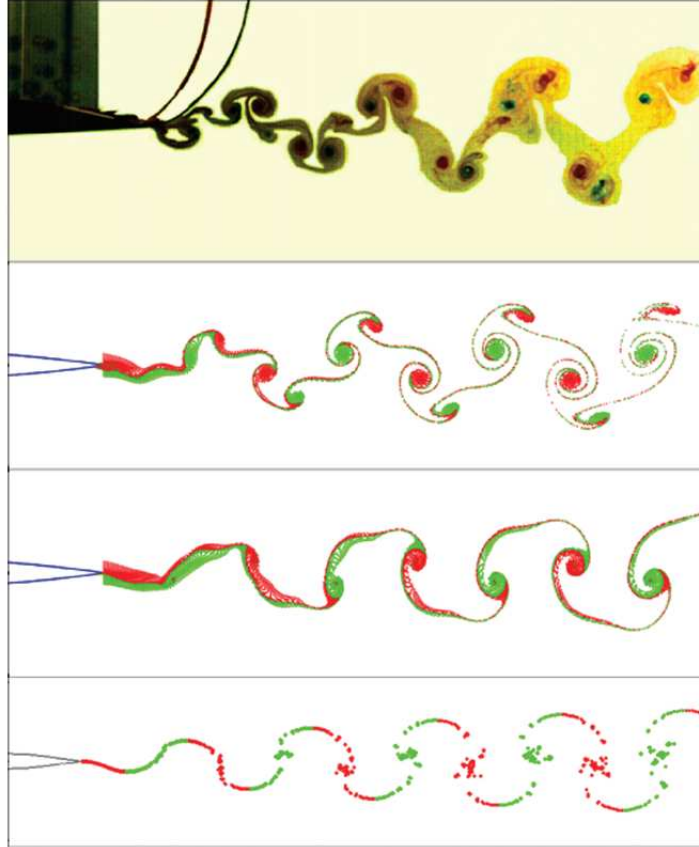


Figure 1.12: Comparison of vorticity distributions obtained using the experimental results of *Lai & Platzer* [42] and the numerical simulation results of *Young* [78]. The top frame represent the experimental simulations of the near wake obtained by dye injection at the trailing-edge of the airfoil [42]. The second and third frames from the top show the vorticity distribution obtained using numerical simulations [78], where scalar particles representing the dye in the experiments were released from a vertical plane at the trailing-edge of the airfoil. The numerical simulations were obtained a Navier-Stokes solver which is laminar for the second frame and a turbulent solver for the third frame. The fourth frame from the top is obtained numerically using an Unsteady Panel Method (UPM), presented in [78]. All cases shown in this figure are for a NACA0012 profile which is heaving at  $Re = 2 \times 10^4$ ,  $k = 8$  and  $h = 0.0125$ . From this figure it is clear that the laminar Navier-Stokes solver is able to reproduce the experimental results. The turbulent Navier-Stokes solver and the unsteady panel method are not able to reproduce the experimental results.

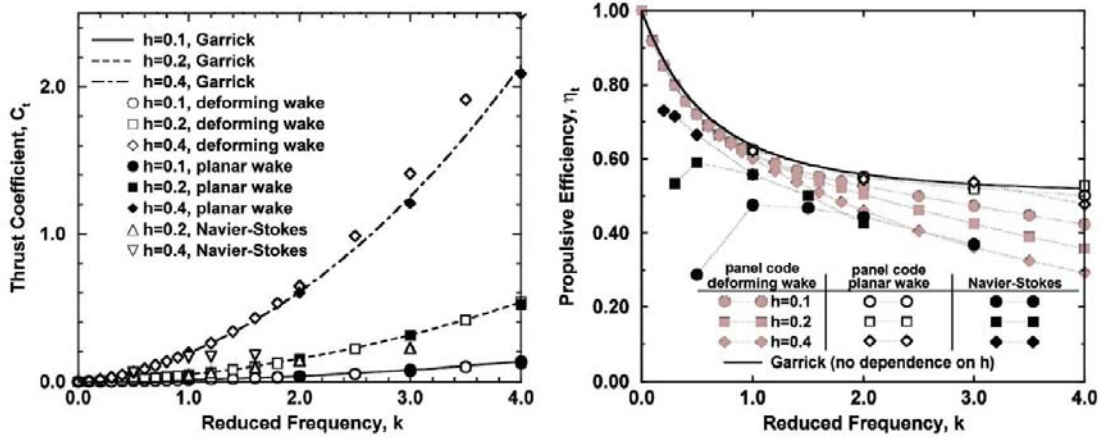


Figure 1.13: Thrust coefficient  $C_T$  (left) and propulsive efficiency  $\eta$  (right) as a function of the reduced frequency  $k$  (from [59]).

### 1.4.3 Thrust Generation by Heaving Airfoils

The transition from a drag- to a thrust-producing wake occurs when increasing the frequency of oscillations at constant amplitude, and vice versa (see Fig. 1.15). Thrust increases when the frequency and amplitude of oscillation increases. Nevertheless, the propulsive efficiency  $\eta$ , defined as the ratio of thrust times the flight velocity divided by the power needed to set the airfoil in an oscillatory motion, does not follow this trend. Indeed, it decreases as the frequency of oscillation increases (see Fig. 1.13). On the other hand, the efficiency increases when the amplitude of oscillations increases (see Fig. 1.13). This indicates the complex nature of the mechanism that leads to thrust production by heaving airfoils. It is clear that the thrust production (or the transition from a drag-producing wake to a thrust-producing wake) occurs at a critical value of the Strouhal number (and the parameter  $kh$ ). At high Reynolds numbers ( $Re > 4 \times 10^4$ ) efficient thrust production is obtained by the shedding of the vortices at the trailing-edge (they constitute the reversed Karman street). At high Reynolds numbers the thrust efficiency is obtained near the dynamic stall boundary for a constant value of Strouhal number [59]. For low Reynolds numbers  $1 \times 10^4 < Re < 3 \times 10^4$  (which are of interest for this investigation and for MAVs applications) the flow is much more complex. This is reflected in the fact that efficiency is achieved by the shedding at both the trailing- and leading-edge (see Fig. 1.14).

## 1.5 Frequency regimes in forced airfoil wakes

For motionless bodies exposed to an inflow, it is well known that a Karman vortex street occurs as soon as a critical Reynolds number is reached [27, 55, 56, 72]. The natural frequency (or Strouhal frequency) is defined as the frequency of

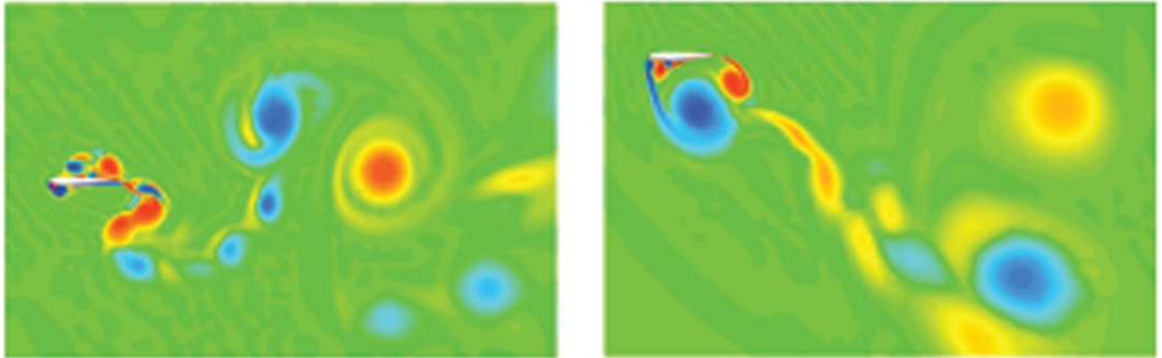


Figure 1.14: Vorticity contours representing the shedding from both the trailing and leading edge of the heaving airfoil at  $Re = 2 \times 10^4$ . The reduced frequency and the amplitude of oscillations are:  $k = 2$  and  $h = 0.75$  (left),  $k = 0.5$  and  $h = 3$  (right) (from [59]).

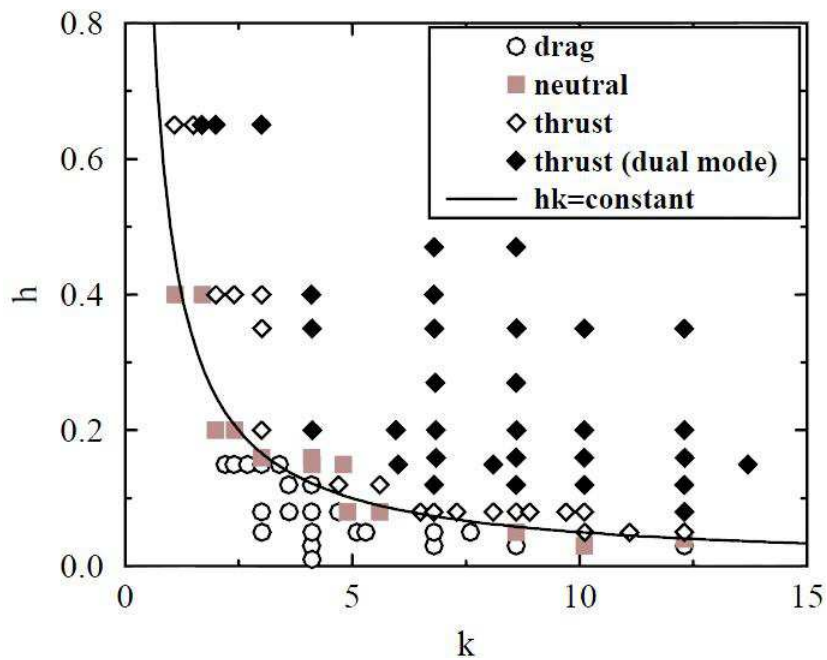


Figure 1.15: Drag- and thrust-producing wakes and neutral wakes classification as a function of the reduced frequency  $k$  and amplitude of oscillations  $h$ . This classification is obtained via experimental investigations. (From [35]).

shedding of vortices of the unforced airfoil [27, 37, 78]. On the other hand, the forced wake of the airfoil can undergo different frequency regimes depending on the forcing frequency and the forcing amplitude as on the relation between the forcing frequency and the natural frequency of the static airfoil. Three frequency regimes are defined in the literature: the natural regime, the harmonic regime and the lock-in regime [78, 79]. In the natural regime the vortex shedding frequency is equal to the natural frequency. In the harmonic regime, the vortex shedding frequency is a mixture or a combination of the natural and the forcing frequency. Finally, in the lock-in regime, the vortex shedding frequency is locked to the forcing frequency. These regimes have been studied and observed for oscillating cylinders [10, 37, 55, 56, 80] and only few studies exist for oscillating airfoils [78, 79].

## 1.6 Direct Numerical Simulations (DNS) - High Order Simulations

Most of the previously cited numerical methods used to investigate the flow over and in the wake of heaving airfoils are *low-order* numerical methods. This means that low-order spatial and temporal discretizations are used to express the unknown variable. Low-order simulations can rarely capture the *real* physics of the problem, especially when few grid points are used. In the case of unsteady flows and oscillating airfoil wakes, low-order methods can only be used in some parameters intervals. These methods fail when extreme values are considered, for example: high angles of attack, high frequency and/or amplitudes of oscillation, low Reynolds numbers, etc. As these extreme parameters values represent very interesting phenomena (which are important to the detailed understanding of the physics of the flow) high-order methods are needed. Low resolution methods can also spread the vortices, unless a very large number of grid points is used in the boundary-layer, wake and near-field region [25]. This increases dramatically the computational cost, especially for three-dimensional simulations based on these low-order methods. High-order methods are the prime choice if any modelling of the phenomenon is to be done, as all the details are to be captured for the establishment of a good model or at least to define the important parameters which are needed for the modelling.

Some high-order schemes have been developed and used in order to increase the resolution of numerical simulations. Such approaches have been especially used in the field of computational aeroacoustics. These high-order schemes which use only few mesh points per wavelength, have low numerical dissipation and dispersion. Furthermore, these schemes can solve for a wider range of wavenumbers than low-order schemes. As an example we cite the implicit compact scheme, which is widely used in acoustics [62] and the high-order McCormack

schemes [30]. On the other hand, compact high-order methods, such as spectral elements or *p-type* finite element techniques provide high accuracy, if the solution is smooth and if a suitable mapping can be defined between the local subdomains and the standard region (see Chapter 2 for more details). Highly accurate spectral methods such as the Fourier method, are very successful (when using very simple geometries) in analyzing fundamental fluid mechanics in combination with the use of Direct Numerical Simulations (DNS). For complex geometries, *Finite Volumes* and *Finite Elements* based methods are widely used, but their low accuracy makes these methods relatively inefficient in terms of accuracy per unit of computational power. By applying high-order polynomial expansions within the elements, the *Spectral /hp Element Methods* offer the high accuracy of Spectral (or Fourier) based methods and the geometric flexibility and capabilities of Finite Element Methods. This method provides an efficient tool of obtaining the highest possible accuracy for a given computational cost [36, 57].

The development of high-order methods allows their combination with DNS methods [7, 14, 29]. This combination is possible due to the high performance of modern computers capabilities. This is a very important issue, since DNS is the preferred tool for fundamental studies. This is mainly due to the absence of approximations and to the fact that all the flow is resolved at all scales. DNS allows an accurate representation of the aerodynamical phenomena encountered in unsteady flow simulations. It is also a very good tool for modelling turbulence and transition to turbulence [52]. The complex flow detachment, reattachment, and the boundary-layer unsteadiness and complex nature, in addition to the shedding which occurs at the sharp trailing-edge of the airfoil represent a considerable numerical challenge for methods using low-order accuracy spatial schemes. Therefore, in this investigation the Spectral /hp Element Method is used in an attempt to achieve highly accurate temporal and spatial simulations of the unsteady flow over a heaving airfoil.

## 1.7 Objectives

The objectives of the present investigation can be detailed as follows:

- The use of a high-order and high-accuracy direct numerical method in order to obtain highly accurate temporal and spatial simulations, and fully resolve the flow and all the scales involved without any approximation.
- To investigate the flow over motionless and heaving airfoils, and to study the dependence of the aerodynamical forces and the wake on several flow parameters.
- To investigate the specific case of drag- and thrust-producing wakes as well as neutral wakes at low Reynolds numbers, at low heaving amplitudes and

at low to high heaving frequencies. This interval is not explored so far in the literature and it has very interesting properties. These properties arise from the interaction of the natural frequency of the vortices shedding and the frequency imposed by the heaving motion.

- To investigate the process of thrust generation by heaving airfoils at low to moderate Reynolds numbers ( $Re < 10^5$ ) in order to provide an explanation for the experimentally observed heaving airfoil wakes.
- To determine the dependence of thrust production and the wake modes on the governing parameters such as the amplitude and frequency of the heaving motion. Most of the investigations in the literature deal with the pitching motion and there are only very few studies dedicated to the heaving motion.
- To explore the relation between the observed wakes and the shedding from the leading- and trailing-edge, especially the multiple-vortices-per-cycle mode.
- To verify the validity of the single parameter characterization of the thrust production and the observed wakes.
- To explore the different frequency regimes exhibited by the heaving airfoils and link these regimes to the wake types and the aerodynamical forces.
- To validate the simulations obtained by the *Nektar*-solver used in combination with the moving frame of reference technique. This validation is achieved for motionless cylinders as for motionless and for oscillating airfoils.

## 1.8 Outline of the Thesis

This thesis is divided into six chapters. In Chapter 2 we introduce the Spectral /hp Element Method and its mathematical background. In Chapter 3 the *Nektar*-solver is validated for a motionless cylinder and a motionless and heaving airfoil. In Chapter 4 we explore the unsteady flow over motionless and heaving airfoils and the aerodynamical coefficients generated by these flows. The effect of varying the flow parameters on the flow over the airfoil surface, the near wake configuration, and the aerodynamical forces is also addressed. Chapter 4 is based on a paper submitted to *Computers and Fluids* and is currently under review. In Chapter 5 we study the specific case of heaving airfoils. The wakes exhibited by heaving airfoils are explored, and also the transition between these wakes as a function of the amplitude and frequency of oscillations. The dependence of the wake types on several parameters is investigated, along with some new

features about the shedding of vortices at the leading and trailing-edge. The origin of the multiple-vortex-per-cycle mode is discussed. Chapter 5 is based on a paper submitted to *Journal of Computational and Applied Mathematics* and is currently under review. In Chapter 6 we investigate the frequency selection in motionless and heaving airfoils, the different frequency regimes exhibited by the heaving airfoil, the transition between these regimes, and the relation between wake types and frequency regimes. Chapter 6 constitutes a paper submitted to *Fluid Dynamics Research* and is currently under review.

## Bibliography

- [1] Defense Advanced Research Projects Agency. Future Technology-Driven Revolutions In Military Operations. In *RAND Corporation*, 1992.
- [2] M. R. Amiralaei, H. Alighanbari, and S. M. Hashemi. Unsteady CFD of a Plunging Airfoil in Low Reynolds Number Flow Regime. In *40th Fluid Dynamics Conference and Exhibit*, Chicago-Illinois, July 2010. American Institute of Aeronautics and Astronautics.
- [3] Corporate Authors. Aircraft Stalling and Buffeting, Lecture series. Technical report, Advisory Group for Aerospace Research and Development, Paris, France, 1975.
- [4] A. Betz. Ein Beitrag zur Erkl drung des Segelflufes. *Zeitschrift f r Flugtechnik und Motorluftschiffahrt*, 3:269–272, 1912.
- [5] W. Birnbaum. Das ebene Problem des schlagenden Fl gels. *Zeitschrift f r angewandte Mathematik und Mechanik*, 4:277–292, 1924.
- [6] R. D. Blevins. *Flow-induced vibration*. New York, Van Nostrand Reinhold Co., 1977. 377 p., 1977.
- [7] B. S. Carmo, S. J. Sherwin, P. W. Bearman, and R. H. J. Willden. Wake transition in the flow around two circular cylinders in staggered arrangements. *J. Fluid Mech.*, 597(1):1–29, 2008.
- [8] L. W. Carr. Progress in Analysis and Prediction of Dynamic Stall. *Journal of Aircraft*, 25(1):6–17, 1988.
- [9] L. W. Carr, K. W. McAlister, and W. J. McCroskey. Analysis of the Development of Dynamic Stall Based on Oscillating Airfoil Experiments. In *NASA Institute for Advanced Concepts Project TN D-8382*, 1977.
- [10] M. Cheng, Y. T. Chew, and S. C. Luo. Numerical Investigation of a Rotationally Oscillating Cylinder in Mean Flow. *J. Fluid Struct.*, 15(7):981–1007, 2001.
- [11] P. G. Choudhuri, D. D. Knight, and M. R. Visbal. Two-Dimensional Unsteady Leading-Edge Separation on a Pitching Airfoil. *AIAA J.*, 32(4):673–680, 1994.
- [12] A. Colozza and R. C. Michelson. Planetary Exploration Using Biomimetics: An Entomopter for Flight on Mars: Phase II Final Report. In *NASA Institute for Advanced Concepts Project NAS5-98051*, 2002.

- [13] A. T. Conlisk. Modern helicopter rotor aerodynamics. *Progress in Aerospace Sciences*, 37(5):419–476, 2001.
- [14] R. Darekar and S. J. Sherwin. Flow Past a Square-Section Cylinder With a Wavy Stagnation Face. *J. Fluid Mech.*, 426:263–295, 2001.
- [15] A. Desopper. Influence of the Laminar and Turbulent Boundary Layers in Unsteady Two-Dimensional Viscous-Inviscid Coupled Calculations. In *Proc. IUTAM Colloq. Unsteady Turbulent Shear Flows, Toulouse, France*, 1981.
- [16] J. A. Ekaterinaris and M. F. Platzer. Computational Prediction of Airfoil Dynamic Stall. *Prog. Aerosp. Sci.*, 33:759–846, 1997.
- [17] J. A. Ekaterinaris, M.S. Chandrasekhara, and M.F. Platzer. Recent Developments in Dynamic Stall Measurements, Computations and Control. In *43rd AIAA Aerospace Sciences Meeting and Exhibit*, Reno-Nevada, 10-13 January 2005. AIAA.
- [18] C. P. Ellington. The Aerodynamics of Hovering Insect Flight. *Philos T. Roy. Soc. A*, 305, 1984.
- [19] L. E. Ericsson and J. P. Reding. Fluid Dynamics of Unsteady Separated Flow. PartII: Lifting Surfaces. *Prog. Aerosp. Sci.*, 24:249–356, 1987.
- [20] P. Freymuth. Propulsive vortical signature of plunging and pitching airfoils. *AIAA J.*, 26:881–883, 1988.
- [21] I. E. Garrick. Propulsion of a Flapping and Oscillating Airfoil. Report 567, NACA, 1937.
- [22] J. P. Giesing. Nonlinear Two-Dimensional Unsteady Potential Flow with Lift. *J. Aircraft*, 5:135–143, 1968.
- [23] H. Glauert. The Force and Moment on an Oscillating Airfoil. *Rep. Memor. Aero. Res. Comm.*, 1242, 1929.
- [24] A. Gonzalez and X. Munduate. Unsteady Modelling of the Oscillating S809 Aerofoil and NREL phase VI parked Blade Using the Beddoes-Leishman dynamic Stall Model. In *The Science of Making Torque from Wind, Journal of Physics: Conference Series*, volume 75, 2007.
- [25] H. Gopalan. *Numerical Modeling of Aerodynamics of Airfoils of Micro Air Vehicles in Gusty Environment*. PhD thesis, University of Akron, 2008.
- [26] R.E. Gormont. A Mathematical Model of Unsteady Aerodynamics and Radial Flow for application to Helicopter Rotors. In *Eustis Directorate Report, TR-72-67*, 1973.

- [27] S. I. Green. *Fluid Vortices*. Kluwer Academic Publishers, 1995.
- [28] K. C. Hall and S. R. Hall. *A Rational Engineering Analysis of the Efficiency of Flapping Flight*. Fixed and Flapping Wing Aerodynamics for Micro Air Vehicle Applications - J.T. Mueller - AIAA - Reston - VA, 2000.
- [29] R. D. Henderson and D. Barkley. Secondary Instabilities in the Wake of a Circular Cylinder. *Physics of Fluids*, 8(6):1683, 1996.
- [30] R. Hixon and E. Turkel. High-Accuracy Compact McCormack-type Schemes for Computational Aeroacoustics. In *AIAA Aerospace Sciences Meeting and Exhibit, 36th, Reno, NV*, 1998.
- [31] D. G. Infield, J. B. Feuchtwang, and P. Fitches. Development and Testing of a Novel Self-Twisting Wind Turbine Rotor. In *European Wind Energy Conference*, pages 329–332, Nice-France, May 1999.
- [32] H. M. Jang. *A Viscous-Inviscid Interaction Method for Unsteady Flows*. PhD thesis, University of Michigan, 1990.
- [33] W. Johnson. *Helicopter Theory*. Dover Publications; Revised edition, 1994.
- [34] K. D. Jones and M. F. Platzer. Experimental Investigation of the Aerodynamic Characteristics of Flapping-Wing Micro Air Vehicles. In *41st Aerospace Sciences Meeting and Exhibit*, volume 0418, pages 1–11, Reno-Nevada, 6-9 January 2003. AIAA.
- [35] K. D. Jones, C. M. Dohring, and M. F. Platzer. Wake Structures Behind Plunging Airfoils: A Comparison of Numerical and Experimental Results. In *34th AIAA Aerospace Sciences Meeting and Exhibit*, Reno-Nevada, 15-18 January 1996. American Institute of Aeronautics and Astronautics.
- [36] G. E. Karniadakis and S. Sherwin. *Spectral/hp Element Methods for Computational Fluid Dynamics*. Oxford University Press, 2005.
- [37] G. E. Karniadakis and G. S. Triantafyllou. Frequency selection and asymptotic states in laminar wakes. *J. Fluid Mech.*, 199(1):441–469, 1989.
- [38] J. Katz and A. Plotkin. *Low Speed Aerodynamics*. McGraw-Hill Companies - Cambridge University Press, Cambridge, 2nd edition, 2001.
- [39] R. Katzmayr. Effect of Periodic Changes of Angle of Attack on Behaviour of Airfoils. Technical Report TM-147, NACA, 1992.
- [40] R. Knoller. Die Gesetze des Luftwiderstandes. *Flug- und Motortechnik*, 3 (21):1–7, 1909. Wien.

- [41] M. M. Koochesfahani. Vortical patterns in the wake of an oscillating airfoil. *AIAA J.*, 27:1200–1205, 1989.
- [42] J. C. S. Lai and M.F. Platzer. Jet Characteristics of a Plunging Airfoil. *AIAA J.*, 37(12):1529–1537, 1999.
- [43] J. G. Leishman. Dynamic stall on the NACA 23012 aerofoil. *Exp. Fluids*, 9: 49–58, 1990.
- [44] J. G. Leishman. *Principles of Helicopter Aerodynamics*. Cambridge University Press, 2000.
- [45] M. J. Lighthill. Biofluidynamics: A survey. *Contemporary Mathematics*, 141:1–32, 1993.
- [46] W. J. McCroskey. Inviscid Flowfield of an Unsteady Airfoil. *AIAA J.*, 11: 1130–1137, 1973.
- [47] W. J. McCroskey. The Phenomenon of Dynamic Stall. Technical Report 81264, NASA Technical Memorandum, 1981.
- [48] W. J. McCroskey, L. W. Carr, and K. W. McAlister. Dynamic Stall Experiments on Oscillating Airfoils. *AIAA J.*, 14:57–63, 1976.
- [49] W.J. McCroskey. Unsteady airfoils. *Ann. Rev. Fluid Mech.*, 14:285–311, 1982.
- [50] Mentor the Hovering Ornithopter, 2010. <http://www.ornithopter.org/history.mav.shtml>.
- [51] V. Middleton, P. Fitches, J. Jeronimidis, and J. B. Feuchtwang. Passive Blade Pitching for Overspeed Control of an HAWT. In *20th British Wind Energy Association Conference*, Cardiff University of Wales, September 2-4 1998.
- [52] P. Moin and K. Mahesh. Direct Numerical Simulation: A Tool in Turbulence Research. *Annual Review of Fluid Mechanics*, 30:539–578, 1998.
- [53] E. Naudascher and D. Rockwell. *Flow-Induced Vibrations: An Engineering Guide*. Rotterdam, Netherlands: Balkema, 1994.
- [54] R. C. Nelson, T. C. Corke, and H. Othman. A Smart Wind Turbine Blade Using distributed Plasma Actuators for Improved Performance. In *46th Aerospace Sciences Meeting*, Reno, Nevada, January 7-10 2008. AIAA.
- [55] A. Ongoren and D. Rockwell. Flow structure from an oscillating cylinder Part 1. Mechanisms of phase shift and recovery in the near wake. *J. Fluid Mech.*, 191(1):197–223, 1988.

- [56] A. Ongoren and D. Rockwell. Flow structure from an oscillating cylinder Part 2. Mode competition in the near wake. *J. Fluid Mech.*, 191(1):225–245, 1988.
- [57] J. Peiro, S. Giordana, C. Griffith, and S. J. Sherwin. High-Order Algorithms for Vascular Flow Modelling. *Int. J. Numer. Meth. Fl.*, 40(1-2):137–151, 2002.
- [58] J. T. Petersen, H. A. Madsen, A. Björck, P. Enevoldsen, S. Øye, H. Ganander, and D. Winkelaar. Prediction of Dynamic Loads and Induced Vibrations in Stall. Report R-1045-EN, RISØ, 1998.
- [59] M. F. Platzer, K. D. Jones, J. Young, and J. C. S. Lai. Flapping-Wing Aerodynamics: Progress and Challenges. *AIAA Journal*, 46(9):2136–2149, 2008.
- [60] S. B. Pope. *Turbulent Flows*. Cambridge University Press, 2000.
- [61] V. A. Riziotis and S. G. Voutsinas. Dynamic Stall Modelling on Airfoils Based on Strong Viscous-Inviscid Interaction Coupling. *International Journal for Numerical Methods in Fluids*, 56:185–208, 2008.
- [62] K. L. Sanjiv. Compact Finite Difference Schemes With Spectral-Like Resolution. *J. Comp. Phys.*, 103(1):16–42, 1992.
- [63] R. H. Scanlan and J. J. Tomko. Airfoil and Bridge Deck Flutter Derivatives. *Journal of the Engineering Mechanics Division ASCE*, 97:1717, 1971.
- [64] S. Schreck and M. Robinson. Blade Three-Dimensional Dynamic Stall Response to Wind Turbine Operating Condition. *Journal of Solar Energy Engineering*, 127(4):488–495, 2005.
- [65] Y. Shimizu and Y. Kamada. Studies on a Horizontal Axis Wind Turbine With Passive Pitch-Flap Mechanism: Performance and Flow Analysis Around Wind Turbine. *J. Fluid Eng.-T. ASME*, 123(3):516–522, 2001.
- [66] M. R. Soltani and F. R. Marzabadi. Effect of Plunging Amplitude on the Performance of a Wind Turbine Blade Section. *The Aeronautical Journal*, 127(4):488–495, 2007.
- [67] B. M. Sumer and J. Fredsøe. *Hydrodynamics Around Cylindrical Structures*. World Scientific, 2006.
- [68] T. Theodorsen. General Theory of Aerodynamic Instability and the Mechanism of Flutter. Technical report, NACA report, 1935.

- [69] G. S. Triantafyllou, M. S. Triantafyllou, and M. A. Grosenbaugh. Optimal Thrust Development in Oscillating Foils with Application to Fish Propulsion. *J. Fluid Struct.*, 7:205–224, 1993.
- [70] D. J. Tritton. *Physical Fluid Dynamics*. Clarendon Press, Oxford, 1988.
- [71] E. J. Tulapurkara. Turbulence Models for the Computation of Flow Past Airplains. *Prog. Aerosp. Sci.*, 28:1–95, 1996.
- [72] T. Von Karman. *Aerodynamics*. McGraw-Hill Education, 1963.
- [73] T. von Karman and J. M. Burgers. *General Aerodynamic Theory*, volume 2 of *Aerodynamic Theory: A General Review of Progress*. W.F. Durand - Springer, Berlin, 1935.
- [74] T. Von Karman and W. R. Sears. Airfoil Theory for Nonuniform Motion. *J. Aeronaut. Sci.*, 5:379–390, 1938.
- [75] C. H. K. Williamson and R. Govardhan. Vortex-Induced Vibrations. *Annu. Rev. Fluid Mech.*, 36:413–55, 2004.
- [76] J. R. Wright and J. E. Cooper. *Introduction to Aircraft Aeroelasticity and Loads*. Wiley, 2007.
- [77] Z. X. Yao, P. Garcia-Fogeda, D. D. Liu, and G. Shen. Vortex/wake Flow Studies for Airfoils in Unsteady motions. *AIAA Paper*, 89:2225, 1989.
- [78] J. Young. *Numerical simulation of the unsteady aerodynamics of flapping airfoils*. PhD thesis, School of Aerospace, Civil and Mechanical Engineering. The University of New South Wales. Australian Defence Force Academy, May 2005.
- [79] J. Young and J. C. S. Lai. Oscillation Frequency and Amplitude Effects on the Wake of a Plunging Airfoil. *American Institute of Aeronautics and Astronautics*, 42(10):2042–2052, 2004.
- [80] Z. C. Zheng and N. Zhang. Frequency effects on lift and drag for flow past an oscillating cylinder. *J. Fluid Struct.*, 24(3):382–399, 2008.



## Chapter 2

# Spectral /hp Finite Element Method

The numerical simulations presented in this investigation were performed using the *Nεκταρ* solver, which uses the Spectral /hp Element Method as a discretization method. The version of the solver that we used was provided by the group of Prof. S. Sherwin at Imperial College (London) [26] and apart from minor changes was kept in its original form. The solver was previously validated for many geometries, among these cylindrical [7], helical [9] and rectangular [22]. We chose to validate the solver for the airfoil and cylindrical geometries (see Chapters 3 and 4). The solver was used previously for the simulation of the unsteady flow over a stationary and moving airfoil [24], but using the Arbitrary Lagrangian Eulerian Method (ALE) to account for the airfoil motion. In this investigation we use a moving frame of reference method, as it offers more flexibility and converges faster than ALE. The moving frame of reference involves no actual motion of the grid, therefore no grid-update at each time step is necessary [22].

The present investigation concentrates on low to moderate Reynolds numbers ( $Re \leq 3 \times 10^4$ ) as the numerical solver being a Direct Numerical Simulation (DNS) solver is not suitable for higher Reynolds numbers. This is mainly due to the prohibitively high computational cost. Our goal in using the Spectral /hp Element Method (SEM) based *Nεκταρ*-solver is to achieve high accuracy simulations in order to characterize the highly unsteady and nonlinear flow over a motionless or oscillating airfoil at low to moderate angles of attack. The *Nεκταρ*-solver was up to now used only for very low Reynolds numbers simulations [7, 22]. Encouraged by the potential of the SEM we used the *Nεκταρ*-solver for simulations at moderate to high Reynolds numbers ( $Re \leq 3 \times 10^4$ ). The results we obtained

agree very well with previously published experimental and numerical results (see Chapter 3 for the validation simulations). Our choice in using the *NekTar*-solver is motivated by the capabilities of the Spectral /hp Element Methods in reproducing the flow dynamics with very high spatial and temporal resolutions and by its *exponential convergence* properties [10, 17–19, 27, 28].

In Section 2.1 we introduce Computational Fluid Dynamics (CFD) simulations. In Section 2.2 the Spectral /hp Element Method is briefly introduced. The framework of weighted residuals and Galerkin formulations are outlined in Section 2.3. The discretization for 2D problems is discussed in Section 2.4, along with the elemental operations on standard and general-shaped elements. The solution procedure of the global system and the global assembly method are described in Section 2.4. The extension to 3D cases is outlined in Section 2.5, and the time advancement scheme is explained in Section 2.6.

## 2.1 Introduction to Computational Fluid Dynamics (CFD)

The Navier-Stokes equations have been known for more than a century, but they can be solved analytically only for a very limited number of flows and simple geometries. The reason for this lies in the fact that these equations are nonlinear partial differential equations (PDEs) in almost every real-flow situation. In some cases, such as one-dimensional flows and Stokes flow, the PDEs can be simplified to linear equations. The nonlinearity is due to convective acceleration, which is an acceleration associated with the change in velocity over position. Hence, any convective flow, whether turbulent or not, will involve nonlinearity. The most common approach to circumvent these limitations and difficulties in the solution of the Navier-Stokes equations is based on simplifying them. This simplification is achieved using approximations, dimensional analysis, and empirical input. This approach is quite successful when the flow studied can be described by one or two parameters. Therefore, an extension of such simplifications to complex geometries or flow situations is not possible.

The non-dimensionalisation of the Navier-Stokes equations can leave the Reynolds number as the only independent parameter of the problem. This is used in practical engineering design and is a very valuable and useful method. However, many flows require several dimensionless parameters for their characterization, as it is the case for flows over airfoils.

Conducting experiments, can also be an efficient way of measuring global parameters, like drag, lift, pressure and velocity. However, in the cases where flow details are required, for example separation and boundary-layer details, ex-

perimental investigation turns out to be costly and/or time consuming and even in some cases not possible to realize. With the increase of modern computers calculation and storage capabilities an alternative to empirical, semi-empirical and experimental investigations is the numerical solution of the partial differential governing equations. The use of numerical methods to solve flow problems is known as *Computational Fluid Dynamics* (CFD). CFD nowadays represents more than a third of all research in the field of fluid mechanics and this proportion is still increasing [11].

CFD is a branch of fluid mechanics that uses numerical methods and algorithms to solve and analyze problems that involve fluid flows. As introduced earlier, CFD is born from the need to solve the governing partial differential equations (or Navier-Stokes equations) numerically, as these equations can not be solved analytically. CFD has also become a valuable design tool, as it is very attractive and cheap alternative to experiments which require big, costly and hardly adaptive wind tunnels. CFD methods are based on the idea of numerically obtaining an approximated solution of the Navier-Stokes equations. This is achieved by using a *discretization method* which will approximate the differential equations by a set of algebraic equations. The resulting algebraic equations can then be solved using different numerical methods. The approximations of the solution are obtained by applying the numerical methods to small subdomains in space and in time called sub-domains or sub-elements. The solution is then obtained at discrete points in space and time called nodes or grid points. The accuracy of the numerical method is related to the quality of the spatial and temporal discretization.

## CFD Methodology

When applying CFD methods a certain methodology is followed. The main steps for numerically solving a fluid dynamics problem are :

- The definition of the mathematical model.
- The choice of the discretization method.
- The choice and the construction of the numerical spatial grid.
- The choice of the solution method and temporal discretization.

In this section the previous points are introduced briefly.

## The mathematical model

Choosing the mathematical model which represents the flow-problem to solve is the first step of any numerical solution method. The mathematical model

is chosen depending on the problem to be solved. If the flow is compressible, inviscid, one- or two-dimensional, laminar, or turbulent, the model has to be written/chosen accordingly. The mathematical model can include simplifications of the exact conservation laws. In general, the Navier-Stokes equations are used to account for the motion of the fluid in many situations. These equations describe how the velocity, pressure, temperature, and density of a moving fluid are related. The equations are a set of coupled differential equations. In practice, these equations are too difficult to solve analytically. For a 3D case, these equations consist of a time-dependent continuity equation for conservation of mass, three time-dependent conservation of momentum equations and a time-dependent conservation of energy equation. There are four independent variables in the problem, three are the spatial coordinates of the solution domain, and the time  $t$ . There are six dependent variables; the pressure  $p$ , density  $\rho$ , and temperature  $T$  and three components of the velocity vector  $(u, v, w)$ . All of the dependent variables are functions of all four independent variables. The Navier-Stokes equations are therefore partial differential equations. In some cases one can introduce simplifications to the Navier-Stokes equations based on the flow problem properties. These simplifications result in general when the flow is incompressible, inviscid, one- or two-dimensional.

## Discretization methods

When the mathematical model is selected, one has to adopt a suitable discretization method. The discretization method is a method of approximating the differential equations by a system of algebraic equations for the solution variable. This approximation is achieved at a set of discrete locations in space and time, the nodes. Many discretization methods exist, but the most commonly used are: finite differences method (FD) [21, 29], finite volumes method (FV) [31], and finite elements method (FE) [1, 12, 16]. The choice of the discretization method depends on the nature of the flow problem and the geometry of the domain considered. For example, finite differences are suitable when simple geometries are involved and finite elements are used when the geometry considered is complex.

## Numerical grid

As mentioned above, the approximation of the solution variable is achieved at a set of discrete locations in space. To define these locations one needs a discrete representation of the geometrical domain in which the flow problem is to be solved. The solution domain is divided into a finite number of sub-domains or elements where the solution variable is to be calculated. This division results in what is referred to as the numerical or the solution grid. There are in general two grid types: structured and unstructured grids.

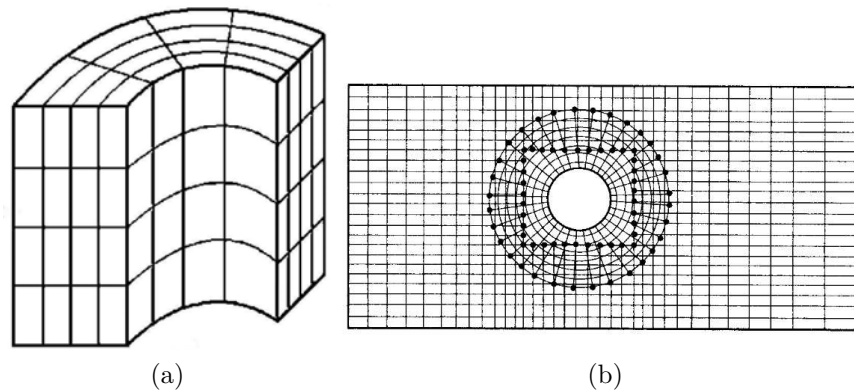


Figure 2.1: (a) A partial view of a 3D cylindrical structured grid. (From [23]). (b) A 2D unstructured grid used to calculate the flow around a circular cylinder in a channel. (From [11]).

The structured grid is a regular grid with non-overlapping sub-domains. It consists of groups of grid lines which do not cross each other and cross each member of the other groups only once. This property is very useful as it allows the lines of a given group to be numbered consecutively. Each grid point (or node) has four neighboring grid points in 2D and 6 neighboring grid points in 3D. This property also means that the matrix of the algebraic equation system (obtained after the discretization of the partial differential equations governing the flow problem) has a regular shape and can be optimally solved using efficient solvers. An example of such a grid is shown on Fig. 2.1a.

The unstructured grid, on the other hand is used for complex geometries and consists the most flexible type of grid as it can be used to fit arbitrary domains. The sub-domains of such a grid are allowed to have arbitrary shapes (see Fig. 2.1b). There is also no restrictions on the number of neighboring grid points. Unstructured grids are usually generated automatically using mesh generation algorithms, for which an extensive literature exists [8, 23, 30]. A disadvantage of the unstructured grid is that the matrix of the algebraic equation is neither regular, nor diagonal. Therefore the solvers for algebraic equation systems are slower for unstructured grids compared to the structured ones.

## Solution methods

When a grid type is used, one has to choose the approximation to be used in the discretization method. In the finite difference method, the approximations for the derivatives at the grid points are to be selected. In the finite volume method, the surface and volume integrals have to be approximated. Finally, in the finite element method one has to choose the appropriate shape functions and the weighting functions. When the governing equations are discretized, a very

large system of non-linear algebraic equations results. The solution method to be chosen to solve these equations depends on the nature of the problem at hand. For example, for unsteady flows one uses initial value problem solution methods for ordinary differential equations. Steady flow problems on the other hand, are usually solved using pseudo-time advancing schemes. Since in general the equations are non-linear, methods which use successive linearization of the equations systems are used and the resulting equations are almost always solved using iterative techniques. Efficient solvers are needed to solve the resulting algebraic equations. Their choice depends on many parameters, like the grid type and the number of grid points.

## 2.2 Introduction to Spectral /hp Element Methods

As stated above, the mathematical modelling of a flow problem gives rise to a system of partial differential equations which need to be discretized to be solved numerically. The discretization method used in this work is the Spectral /hp Element Method (SEM). In this Section a brief introduction to this method is given. Readers interested in more details about the derivation and implementation of the method can refer to the reference book by *E.M. Karniadakis* and *S. Sherwin* [18] and the following references [6, 17, 20, 27, 28].

The Spectral /hp Element Method is a discretization method derived from the Finite Element Method (FEM) [1, 12, 16] and the classic Spectral Method (SM) [2, 4, 5, 13]. The main idea of the FEM is the subdivision of the computational domain  $\Omega$  into sub-domains  $\Omega^e$  (also called elements). The solution of the differential equations is build-up as a sequence of *local* (or elemental) approximations. These local approximations are linear combinations of lower-order functions such as linear or quadratic polynomials. These functions are subjected to some conditions to ensure the continuity of the *global* approximation on  $\Omega$ . The convergence strategie in Finite Element Methods is achieved by refining the subdivisions of the computational domain  $\Omega$ , i.e, making the subdomains smaller (this is called mesh refinement). The classic Spectral Method on the other hand uses high-order functions for the approximation of the solution of the differential equations in the *whole* domain without spatial discretization. The convergence in this case is achieved by increasing the order of the approximation functions. This method stems from Fourier analysis and it is successfully used for widely diverse applications, such as wave propagation (for acoustic, elastic, seismic and electromagnetic waves), solid and structural analysis, marine engineering, biomechanics, and even financial engineering.

The Spectral /hp Element Method is based on both the Finite Element Method and the classic SM: the computational domain is discretized into sub-

domains where high-order polynomials are used for the approximation functions. Thus the Spectral /hp Element Method takes advantage of the geometrical flexibility of the Finite Element Method and the high-accuracy of Spectral Method. In SEM the mesh refinement is called *h-convergence*, and increasing the order of the approximation functions is called *p-convergence*. Thus the /hp in the name of the Spectral /hp Element Method. One of the most important advantages of the Spectral /hp Element Method is that for sufficiently smooth problems, the computational cost in obtaining an approximate solution with very small error is lower and one can achieve *spectral* or *exponential* convergence. According to Boyd [3] "a spectral series possesses the property of exponential convergence if the error decreases faster than any finite inverse power of  $N$  as  $N$ , the number of terms in the truncated series, increases".

The problem that we consider in this investigation is the incompressible, unsteady and viscous flow over stationary and moving airfoils. The governing equations for this flow are the Navier-Stokes equations, written in a non-dimensional form as follows

$$\nabla \cdot \mathbf{u} = 0, \quad (2.1)$$

$$\frac{\partial \mathbf{u}}{\partial t} + (\mathbf{u} \cdot \nabla) \mathbf{u} = -\nabla p + \frac{1}{Re} \nabla^2 \mathbf{u}. \quad (2.2)$$

$\mathbf{u}$  is the velocity vector,  $p$  the pressure,  $Re = U_0 c / \nu$  the Reynolds number,  $\nu$  the kinematic viscosity,  $U_0$  the free-stream velocity, and  $c$  the chord length of the airfoil. The chord length and the free-stream velocity are used to make the equations non-dimensional.

### 2.3 Framework of the weighted residuals and the Galerkin formulations

The Spectral /hp Element Method makes use of the weighted residuals framework. To introduce this framework we consider the following linear differential equation in a domain  $\Omega$

$$\mathbb{L}(u) = 0. \quad (2.3)$$

The solution of (2.3) is then expanded in the form

$$u^\delta(X, t) = u_0(X, t) + \sum_k^N \hat{u}_k(t) \Phi_k(X), \quad (2.4)$$

where  $\hat{u}_k$  are unknown coefficients,  $\Phi_k(X)$  are the *expansion functions*,  $k$  is the element index,  $N$  the total number of elements in the domain and  $u_0(X, t)$  satisfies the initial and boundary conditions. When (2.4) is inserted in (2.3) one obtains

a non-zero residual (since  $\Phi_k(X)$  are approximations and not exact solutions), which can be written as

$$\mathbb{L}(u^\delta) = R(u^\delta). \quad (2.5)$$

A unique solution is determined for (2.5) by placing a restriction on the residual  $R$  to obtain a system of ordinary differential equations. In the framework of weighted residuals the restriction on  $R$  is that its inner product with respect to arbitrary *weight* (or *test*) *functions*  $v(X)$  is zero

$$(v(X), R) = 0, \quad (2.6)$$

where the inner product is defined as

$$(v(X), R) = \int_{\Omega} v(X) R dX. \quad (2.7)$$

The weight functions are chosen to be approximated by a linear combination of known functions

$$v(X) = \sum_l^N a_l v_l(X), \quad (2.8)$$

where  $v_l(X)$  are known functions. Using the definition (2.7) and inserting (2.8) and (2.5) into (2.6) we obtain

$$\int_{\Omega} \sum_l^N a_l v_l(X) \mathbb{L}(u^\delta) dX = 0. \quad (2.9)$$

Using equation (2.4) in (2.9) we obtain a system of algebraic equations to determine the unknowns  $\hat{u}_k$ . Assuming that the operator  $\mathbb{L}$  is time independent and using the Equation 2.4 we can write

$$\int_{\Omega} \sum_{l=1}^{N_{dof}} a_l v_l(X) \mathbb{L} \left[ u_0(X) + \sum_{k=1}^N \hat{u}_k \Phi_k(X) \right] dX = \sum_{l=1}^{N_{dof}} a_l \left\{ \int_{\Omega} v_l(X) \mathbb{L}[u_0(X)] dx + \int_{\omega} v_l(X) \mathbb{L} \left[ \sum_{k=1}^{N_{dof}} \hat{u}_k \Phi_k(X) \right] dX \right\} = 0, \quad (2.10)$$

which can be re-written as follows

$$\sum_{k=1}^{N_{dof}} \left\{ \hat{u}_k \int_{\Omega} v_l(X) \mathbb{L}[\Phi_k(X)] \right\} dX = - \int_{\Omega} v_l(X) \mathbb{L}[u_0(X)] dx, \quad k = 1, \dots, N_{dof}. \quad (2.11)$$

Equation 2.11 can be re-arranged in matrix form as follows

$$\mathbf{A}\hat{\mathbf{u}} = \mathbf{b}, \quad (2.12)$$

where  $\hat{\mathbf{u}}$  is the vector of the unknown coefficients  $\hat{u}_k$  and there components are given as

$$A_{lk} = \int_{\Omega} v_l(X) \mathbb{L} [\Phi_k(X)] dX, \quad (2.13)$$

$$b_l = - \int_{\Omega} v_l(X) \mathbb{L} [u_0(X)] dX. \quad (2.14)$$

$$(2.15)$$

In the Galerkin formulation the test (or weighted) functions are the same as the expansion functions leading to  $v_l(X) = \Phi_j(X)$ . This formulation is chosen because it has some interesting properties, like the orthogonality of the error to the test space in the energy norm and minimisation of the energy norm of the error (for more details see [18]).

## 2.4 Spectral /hp Element Discretization in two Dimensions

In this Section, we explain the discretization in two dimensions by introducing the expansion bases used and the techniques to perform elemental operations such as integration and differentiation.

The expansion bases introduced here are considered within a standard region  $\Omega_{st}$ , which in two-dimensional simulations of the Navier-Stokes equations are triangular and/or quadrilateral regions/elements. The expansion bases used throughout this investigation are constructed from a one-dimensional modal basis, which is defined as follows

$$\phi_p(\xi) = \begin{cases} \psi_0^a = \frac{1-\xi}{2} & p = 0, \\ \psi_p^a = \frac{1-\xi}{2} \frac{1+\xi}{2} P_{p-1}^{1,1}(\xi) & 0 \leq p \leq P, \\ \psi_P^a = \frac{1+\xi}{2} & p = P, \end{cases} \quad (2.16)$$

where  $\xi$  is the one-dimensional Cartesian coordinate ( $-1 \leq \xi \leq 1$ ) and  $P_{p-1}^{1,1}(\xi)$  is a Jacobi polynomial of order  $P$ . The standard two-dimensional quadrilateral region  $\mathcal{Q}^2$  is defined as follows

$$\Omega_{st} = \mathcal{Q}^2 = \{-1 \leq \xi_1, \xi_2 \leq 1\}, \quad (2.17)$$

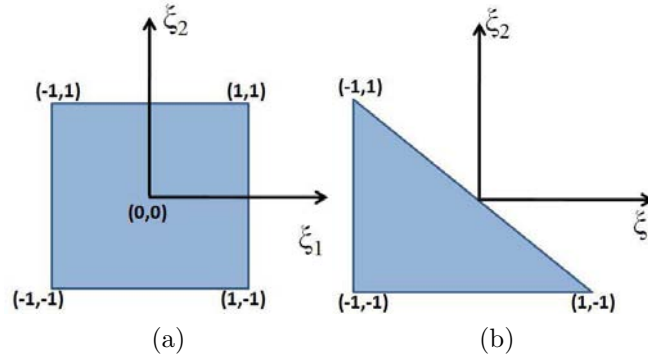


Figure 2.2: Standard regions for the (a) triangular and (b) quadrilateral expansions in the Cartesian coordinates system.

and is illustrated in Fig. 2.2a for triangular and quadrilateral standard regions. The two-dimensional base is then constructed as the product of one-dimensional bases such as in equation (2.16), as follows

$$\phi_{pq}(\xi_1, \xi_2) = \psi_p^a(\xi_1)\psi_q^a(\xi_2), \quad 0 \leq p, q, p \leq P, q \leq Q, \quad (2.18)$$

where  $P$  and  $Q$  are the order of the expansion bases  $\psi_p^a(\xi_1)$  and  $\psi_q^a(\xi_2)$ ; respectively.  $P$  and  $Q$  can take the same value or be different. In this investigation we consider  $P = Q$ . In Fig. 2.3, the construct of a two-dimensional base from the product of two one-dimensional expansions of order  $P = 4$  is illustrated. Equation (2.18) can be regarded as the tensorial product of two one-dimensional expansions defined in each Cartesian direction, namely  $\xi_1$  and  $\xi_2$ .

An important property of the modal expansions based on equation (2.18) is that they can be splitted into boundary and interior modes. The modes that are non-zero on the boundary  $\Omega_{st}$  and are zero elsewhere are called *boundary modes*, while the modes which are zero on the boundary and non-zero elsewhere are called *interior modes*. This property is very useful when a  $C^0$  global expansion is needed, since a global expansion can be created from the local ones simply by shape-matching of the boundary modes. Further use of this property is discussed in Section 2.4. In the case of a two-dimensional expansion, the boundary modes are further decomposed into two modes : *vertex modes*, having a unit value at one vertex and zero at the any other vertex, and *edge modes* having a support on one edge and zero on any other edge. This decomposition can be considered as part of the meshing procedure. Fig. 2.3 shows an example of such decomposition.

In order to obtain a generalised tensorial expansion that can be used in different domain shapes (for example triangles and quadrilaterals in two-dimensional domains) it is necessary to introduce a new coordinate system. This coordinate system is labeled *collapsed system*, and its coordinates  $\eta_1$  and  $\eta_2$  are introduced as follows

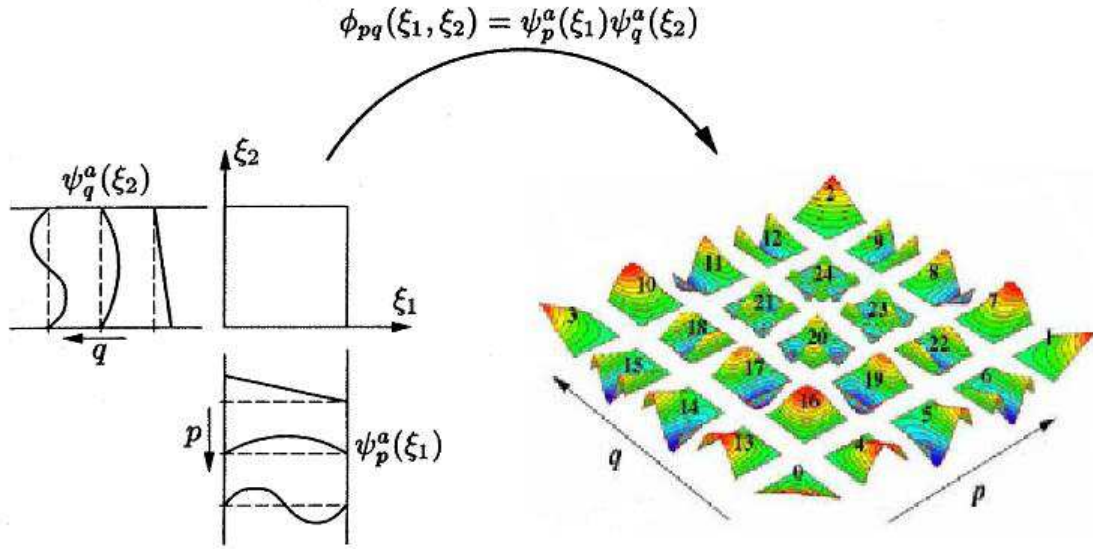


Figure 2.3: Construction of a two-dimensional expansion basis from the tensorial product of two one-dimensional expansions of order  $P = 4$  (Figure adapted from [14, 18]). The numbering of the modes is explained in Section 2.4.

$$\eta_1 = 2\frac{1 + \xi_1}{1 - \xi_2}, \eta_2 = \xi_2. \quad (2.19)$$

This collapsed coordinate system is based on a mapping from a quadrilateral to a triangular region, as in Fig.2.2, thus the name *collapsed*, as two adjacent vertices of the quadrilateral region are *collapsed* to form a triangular region (see Fig. 2.4).

The standard triangular region resulting from this transformation is

$$\Omega_{st} = \tau^2 = (\xi_1, \xi_2) \mid -1 \leq \xi_1, \xi_2, \xi_1 + \xi_2 \leq 0. \quad (2.20)$$

The coordinates  $\xi_1, \xi_2$  can be recovered using the inverse transformation

$$\xi_1 = \frac{(1 + \eta_1)(1 - \eta_2)}{2} - 1, \xi_2 = \eta_2. \quad (2.21)$$

The new triangular standard region is then defined by the coordinate system  $(\eta_1, \eta_2)$  as follows

$$\Omega_{st} = \tau^2 = \{(\eta_1, \eta_2) \mid -1 \leq \eta_1, \eta_2 \leq 0\}. \quad (2.22)$$

Note that equation (2.22) is identical to equation (2.17), which defines the standard quadrilateral region in the Cartesian coordinates system. The new collapsed coordinate system is then used to define the expansion basis  $\phi_{pq}(\xi_1, \xi_2)$  for a triangular region as

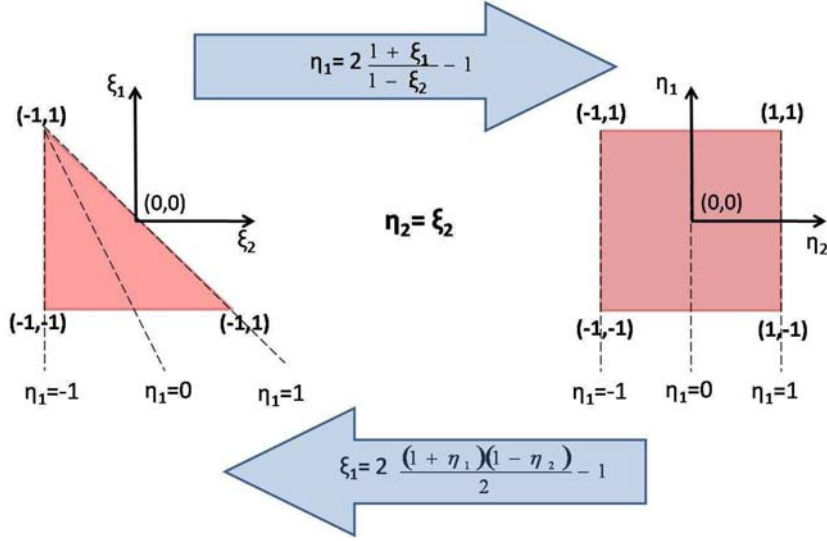


Figure 2.4: Illustration of the transformation from the triangular element to the rectangular element transformation through the collapsed coordinates. The triangular element coordinates  $(\xi_1, \xi_2)$  are related to the rectangular element coordinates  $(\eta_1, \eta_2)$  with the transformation relations written on the arrows. (Adapted from [18]).

$$\phi_{pq}(\xi_1, \xi_2) = \psi_p^a(\eta_1)\psi_{pq}^b(\eta_2), \quad (2.23)$$

where  $\psi_{pq}^b(\eta_2)$  are the modified one-dimensional expansion bases given by

$$\psi_{pq}^b(\eta) = \begin{cases} \psi_q^a(\eta) & p = 0, 0 \leq q \leq Q, \\ (\frac{1-\eta}{2})^{p+1} & 0 \leq p \leq P, q = 0, \\ (\frac{1-\eta}{2})^{p+1} \frac{1+\eta}{2} \mathcal{P}_{q-1}^{2p+1,1}(\eta) & 0 \leq p \leq P, 0 \leq q \leq Q, \\ \psi_q^a(\eta) & p = P, 0 \leq q \leq Q. \end{cases} \quad (2.24)$$

An example of such an expansion (with  $P = Q = 4$ ) is illustrated in Fig. 2.5. Expansion (2.24), as expansion (2.18), can be splitted into boundary (vortex and edge) modes and interior modes. The tensorial-product nature of the expansions simplifies the solution procedure, as many important numerical operations can be numerically evaluated with a reduced operations count compared to non-tensorial expansions [18].

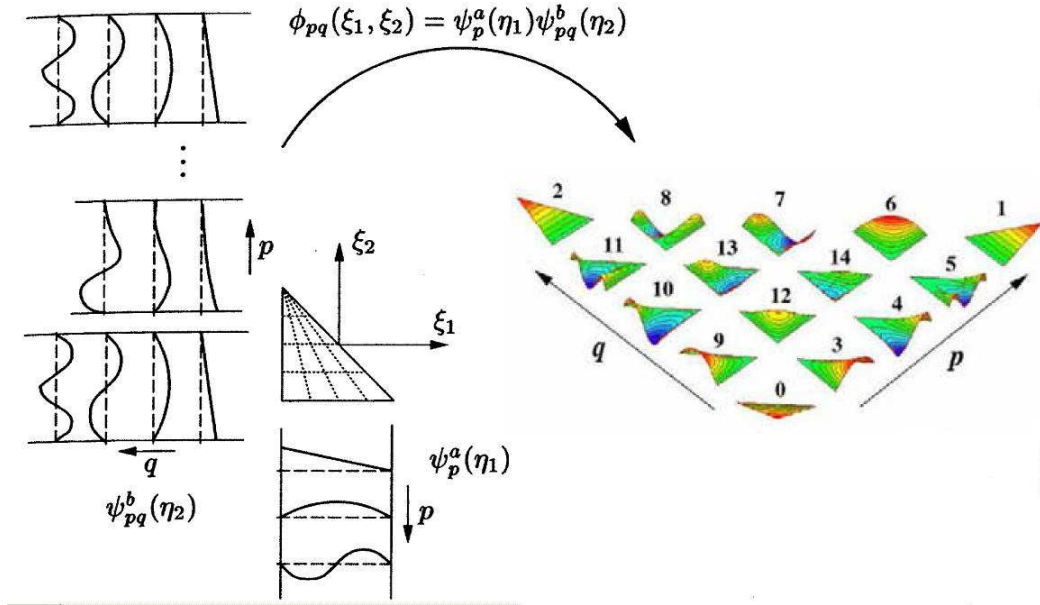


Figure 2.5: The construction of a triangular expansion of the fourth-order ( $p = 4$ ). The construction makes use of the tensorial product of two modified principal functions  $\psi_p^a(\eta_1)$  and  $\psi_p^b(\eta_2)$ . The modes are decomposed into boundary and interior modes. The boundary modes have similar shapes along each edge (Figure adapted from [14, 18]). The numbering of the modes is explained in Section 2.4.

## Elemental operations

Each element or subdomain  $\Omega_e$  from  $\Omega$  can be mapped to a standard region, where the expansion basis is defined as shown above. To obtain a  $\mathcal{C}^0$  continuous expansion on  $\Omega$ , the Galerkin formulation requires that the operations such as integration and differentiation are to be performed at a local level. This means that the contribution of each element is to be summed up to obtain a global system [18]. Local or elemental operations are outlined in this Section.

### Elemental integration : Gauss quadrature

To perform numerical integration on the elemental level, Gaussian quadrature is used. The Gaussian quadrature is an approximation of the definite integral, expressed as weighted sums of functions values at specified points within the domain of integration, called *collocation points*.

Consider the one-dimensional integral to be evaluated (expressed in Cartesian coordinates) as

$$\int_{-1}^1 u(\xi) d\xi. \quad (2.25)$$

The Gaussian quadrature approximates (2.25) by the following summation

$$\int_{-1}^1 u(\xi) d\xi \approx \sum_{i=0}^{Q-1} \omega_i u(\xi_i). \quad (2.26)$$

$\omega_i$  are weights and  $\xi_i$  are the quadrature points in the interval  $[-1, 1]$  where the integral  $\int_{-1}^1 u(\xi) d\xi$  is to be evaluated. The integrand is then represented as a *Lagrange* polynomial  $h_i(\xi)$  at the points  $\xi_i$  as follows

$$u(\xi) = \sum_{i=0}^{Q-1} u(\xi_i) h_i(\xi) + \epsilon(u), \quad (2.27)$$

where  $\epsilon(u)$  is the approximation error resulting from using the Gaussian quadrature approximation. Inserting (2.27) into (2.25) results in the following equation

$$\int_{-1}^1 u(\xi) d\xi = \sum_{i=0}^{Q-1} \omega_i u(\xi_i) + R(u), \quad (2.28)$$

where  $\omega_i$  are the weights defined as

$$\omega_i = \int_{-1}^1 h_i(\xi) d\xi, \quad (2.29)$$

and  $R(u)$  is the residual defined in terms of the integration error as

$$R(u) = \int_{-1}^1 \epsilon(u) d\xi. \quad (2.30)$$

The location of the quadrature points  $\xi_i$  (called zeroes) needs to be specified. The residual  $R(u)$  is zero if  $u(\xi)$  is a polynomial of order  $Q - 1$  or less, however one can choose the zeroes which enable the exact integration of polynomials of higher-order than  $Q - 1$ , these are the zeroes of the Jacobi polynomials [18]. Several variants of Gauss quadrature can be employed to integrate exactly polynomials of order  $2Q - 1$  (classical Gauss quadrature rule), of order  $2Q - 2$  (Gauss-Radau) and of order  $2Q - 3$  (Gauss-Lobatto). These variants depend on the nature of the points included in the integration interval (interior points only, interior points plus one interval-end point, or interior points plus the two interval-end points).

For two-dimensional standard quadrilateral regions, Gauss quadrature can be written in the Cartesian coordinates system as

$$\int_{\mathcal{Q}^2} u(\xi_1, \xi_2) d\xi_1 d\xi_2 = \int_{-1}^1 \left[ \int_{-1}^1 u(\xi_1, \xi_2) |_{\xi_2} d\xi_1 \right] d\xi_2 \quad (2.31)$$

$$\approx \sum_{i=0}^{Q_1-1} \omega_i \left[ \sum_{j=0}^{Q_2-1} \omega_j u(\xi_{1i}, \xi_{2j}) \right], \quad (2.32)$$

$$(2.33)$$

where  $\mathcal{Q}^2$  is defined in (2.17), and  $Q_1$  and  $Q_2$  are quadrature point numbers defined in the directions  $\xi_1$  and  $\xi_2$ ; respectively.

For a two-dimensional triangular region  $\tau^2 = \{-1 \leq \xi_1, \xi_2, \xi_1 + \xi_2 \leq 0\}$  a coordinate transformation is necessary to obtain constant integration bounds (as introduced earlier in Section 2.4). This yields the following expression for integrals over  $\tau^2$  in function of integrals over the collapsed domain

$$\int_{\tau} u(\xi_1, \xi_2) d\xi_1 d\xi_2 = \int_{-1}^1 u(\eta_1, \eta_2) \frac{\partial(\xi_1, \xi_2)}{\partial(\eta_1, \eta_2)} d\eta_1 d\eta_2, \quad (2.34)$$

where  $\left[ \frac{\partial(\xi_1, \xi_2)}{\partial(\eta_1, \eta_2)} \right]$  is the Jacobian of the transformation from Cartesian to collapsed coordinates. Applying the Gaussian quadrature rule results in the following approximation of the integral in the collapsed quadrilateral system of coordinates

$$\int_{-1}^1 \int_{-1}^1 u(\eta_1, \eta_2) \frac{\partial(\xi_1, \xi_2)}{\partial(\eta_1, \eta_2)} d\eta_1 d\eta_2 = \sum_{i=0}^{Q_1-1} \omega_i \left[ \sum_{j=0}^{Q_2-1} \omega_j u(\eta_{1i}, \eta_{2j}) \frac{\partial(\xi_1, \xi_2)}{\partial(\eta_1, \eta_2)} \right], \quad (2.35)$$

where  $\eta_{1i}, \eta_{2j}$  are quadrature points in the  $\eta_1, \eta_2$  directions; respectively. Replacing the Jacobian by its value  $[\partial(\xi_1, \xi_2)/\partial(\eta_1, \eta_2) = (1 - \eta_2)/(2)]$ , makes it possible to include it in the quadrature weights as follows

$$\int_{-1}^1 \int_{-1}^1 u(\eta_1, \eta_2) \frac{1 - \eta_2}{2} d\eta_1 d\eta_2 = \sum_{i=0}^{Q_1-1} \omega_i^{0,0} \left[ \sum_{j=0}^{Q_2-1} \hat{\omega}_j^{1,0} u(\eta_{1i}, \eta_{2j}) \right], \quad (2.36)$$

where  $\hat{\omega}_j^{1,0} = \omega_j^{1,0}/2$ . This results in less points needed by the Gaussian quadrature, for the triangular standard region, to reach the same accuracy as for the quadrilateral standard region.

### Elemental differentiation

Consider the following approximation of  $u^\delta(x)$

$$u^\delta(x) = \sum_{p=0}^P \hat{u}_p \phi_p(\chi^{-1}) = \sum_{p=0}^P \hat{u}_p \phi_p(\xi), \quad (2.37)$$

where  $\chi(\xi)$  is the mapping from the standard region  $\Omega_{st}$  to the region containing  $x$  in the interval  $[a, b]$ .  $u^\delta(x)$  can be differentiated using the chain rule as follows

$$\frac{du^\delta(x)}{dx} = \frac{du^\delta(\xi)}{d\xi} \frac{d\xi}{dx} = \sum_{p=0}^P \hat{u}_p \frac{d\phi_p(\xi)}{d\xi} \frac{d\xi}{dx}. \quad (2.38)$$

Considering the fact that the derivatives are always inside integrals when their evaluation is performed in the framework of the weighted residuals, and that the Gaussian quadrature is used for local integration, two approximations are introduced. The first approximation is that the derivatives are to be evaluated at the quadrature points  $\xi_i$ . The second approximation is that the expansion functions have to be represented in Lagrange polynomials (see Section 2.4). An automated technique to obtain the derivative values at the collocation points is called *collocation differentiation* [18], and it is outlined in what follows.

Consider the one-dimensional case, where  $u^\delta(\xi)$  is a polynomial of order equal or less than  $P$ , which can be exactly expressed using Lagrange polynomials  $h_i(\xi)$  using  $Q$  nodal points  $\xi_i$  as follows

$$u(\xi) = \sum_{i=0}^{Q-1} u(\xi_i) h_i(\xi), \quad (2.39)$$

where  $h_i(\xi) = \frac{\prod_{j=0, j \neq i}^{Q-1} (\xi - \xi_j)}{\prod_{j=0, j \neq i}^{Q-1} (\xi_i - \xi_j)}$ , and  $Q \geq P + 1$ .

The derivative of  $u(\xi)$  can be written as follows

$$\frac{du(\xi)}{d\xi} = \sum_{i=0}^{Q-1} u(\xi_i) \frac{dh_i(\xi)}{d\xi}. \quad (2.40)$$

The derivative at the nodal point  $\xi_i$  is then given by

$$\left. \frac{du(\xi)}{d\xi} \right|_{\xi=\xi_i} = \sum_{i=0}^{Q-1} \left. \frac{dh_i(\xi)}{d\xi} \right|_{\xi=\xi_i} u(\xi_i). \quad (2.41)$$

This collocation differentiation is then extended to two-dimensions in the following way: consider the expansion, in the standard quadrilateral region, of the form

$$u^\delta(\xi_1, \xi_2) = \sum_{p=0}^{P_1} \sum_{q=0}^{P_2} \hat{u}_{pq} \phi_{pq}(\xi_1, \xi_2), \quad (2.42)$$

$\phi_{pq}(\xi_1, \xi_2)$  is replaced by *Lagrange* polynomials, and (2.42) is re-written as

$$u^\delta(\xi_1, \xi_2) = \sum_{p=0}^{Q_1-1} \sum_{q=0}^{Q_2-1} u_{pq} h_p(\xi_1) h_q(\xi_2), \quad (2.43)$$

where

$$u_{pq} = u^\delta(\xi_{1p}, \xi_{2q}), \quad Q_1 > P_1, \quad Q_2 > P_2, \quad (2.44)$$

and  $\xi_{1p}$  and  $\xi_{2q}$  are the zeroes of the Gaussian quadrature rule. The partial derivative with respect to  $\xi_1$  is

$$\frac{du^\delta}{d\xi_1}(\xi_1, \xi_2) = \sum_{p=0}^{P_1} \sum_{q=0}^{P_2} u_{pq} \frac{dh_p(\xi_1)}{d\xi_1} h_q(\xi_2) \quad (2.45)$$

The partial derivatives, with respect to  $\xi_1$  and  $\xi_2$ , are written as follows (using the fact that for *Lagrange* polynomials  $h_p(\xi_i) = \delta_{pi}$ )

$$\frac{du^\delta}{d\xi_1}(\xi_{1i}, \xi_{2j}) = \sum_{p=0}^{P_1} u_{pj} \frac{dh_p(\xi_1)}{d\xi_1} \Big|_{\xi_{1i}}, \quad (2.46)$$

$$\frac{du^\delta}{d\xi_2}(\xi_{1i}, \xi_{2j}) = \sum_{q=0}^{P_2} u_{iq} \frac{dh_q(\xi_2)}{d\xi_2} \Big|_{\xi_{2j}}. \quad (2.47)$$

$$(2.48)$$

The derivatives in the triangular region in terms of the collapsed system are written as

$$\frac{du^\delta}{d\eta_1}(\eta_{1i}, \eta_{2j}) = \sum_{p=0}^{P_1} u_{pj} \frac{dh_p(\eta_1)}{d\eta_1} \Big|_{\eta_{1i}}, \quad (2.49)$$

$$\frac{du^\delta}{d\eta_2}(\eta_{1i}, \eta_{2j}) = \sum_{p=0}^{P_2} u_{iq} \frac{dh_p(\eta_2)}{d\eta_2} \Big|_{\eta_{2j}}, \quad (2.50)$$

$$(2.51)$$

To obtain the derivatives in the Cartesian coordinate system the chain rule is used as follows

$$\frac{\partial}{\partial \xi_1} = \frac{2}{1 - \eta_2} \frac{\partial}{\partial \eta_1}, \quad (2.52)$$

$$\frac{\partial}{\partial \xi_2} = 2 \frac{1 + \eta_1}{1 - \eta_2} \frac{\partial}{\partial \eta_1} + \frac{\partial}{\partial \eta_2}. \quad (2.53)$$

$$(2.54)$$

It is important to note that since the differentiation is performed in the physical space and the integration in the transformed space. Going backwards and forwards between these spaces is necessary to be able to evaluate the coefficients  $u_{pq}$  from the coefficients  $\hat{u}_{pq}$  and vice-versa.

## General-shaped Elements

The integration and differentiation operations as the expansion bases were introduced within the quadrilateral (and triangular) standard region  $\Omega_{st}$ . In practice the elemental regions  $\Omega^e$  can be of general shape and orientation, therefore a mapping between the Cartesian coordinates of the general-shaped regions  $(x_1, x_2)$  and the Cartesian coordinates of the standard (or local) region  $(\eta_1, \eta_2)$  is necessary. This mapping is iso-parametric (also called one-to-one mapping) and is needed for both straight-sided elements and curvilinear-sided elements.

For the case of straight-sided elements, only the coordinates of the vertices are needed as input for the mapping. Mapping a triangular region, using the global coordinates of the triangle  $\{(x_1^A, x_2^A), (x_1^B, x_2^B), (x_1^C, x_2^C)\}$  can be done with the formula

$$\begin{aligned} x_i &= \chi_1^e(\eta_1, \eta_2) \\ &= x_i^A \left( \frac{1 - \eta_1}{2} \frac{1 - \eta_2}{2} \right) + x_i^B \left( \frac{1 + \eta_1}{2} \frac{1 - \eta_2}{2} \right) + x_i^C \left( \frac{1 + \eta_2}{2} \right), \quad i = 1, 2. \end{aligned} \quad (2.55)$$

$C$  is the collapsed vertex. Using the relations (2.19) the mapping can be expressed in terms of the Cartesian coordinates of the standard region as

$$\begin{aligned} x_i &= \chi(\xi_1, \xi_2) \\ &= x_i^A \left( \frac{-\xi_2 - \xi_1}{2} \right) + x_i^B \left( \frac{1 + \xi_1}{2} \right) + x_i^C \left( \frac{1 + \xi_2}{2} \right), \quad i = 1, 2. \end{aligned} \quad (2.56)$$

Applying the same approach as for the triangular region, the mapping for the straight-sided quadrilateral region is

$$\begin{aligned} x_i &= \chi_1^e(\xi_1, \xi_2) \\ &= x_i^A \frac{1 - \xi_1}{2} \frac{1 - \xi_2}{2} + x_i^B \frac{1 + \xi_1}{2} \frac{1 - \xi_2}{2} \\ &\quad + x_i^D \frac{1 - \xi_1}{2} \frac{1 + \xi_2}{2} + x_i^C \frac{1 + \xi_1}{2} \frac{1 + \xi_2}{2}, \quad i = 1, 2. \end{aligned} \quad (2.57)$$

(2.58)

Note that to describe a straight-sided region one needs only to know the values of the vertex coordinates. In the case of a curved region one needs some information about the edge shape. Thus for these regions the expansion basis are used to map the curved edge to the standard region as follows

$$x = \chi_i(\xi_1, \xi_2) = \sum_{p=0}^{p=P_1} \sum_{q=0}^{q=P_2} \hat{x}_{pq}^i \phi_{pq}(\xi_1, \xi_2). \quad (2.59)$$

$$y = \chi_i(\xi_1, \xi_2) = \sum_{p=0}^{p=P_1} \sum_{q=0}^{q=P_2} \hat{y}_{pq}^i \phi_{pq}(\xi_1, \xi_2). \quad (2.60)$$

After defining the mappings from both straight-sided and curved general-shaped elements to the standard region, the differentiation and integration needs also to be defined for these general-shaped elements. The integration is achieved in the general-shaped element using a coordinate transformation

$$\int_{\Omega^e} u(x, y) dx dy = \int_{\Omega_{st}} u(\xi_1, \xi_2) |J| d\xi_1 d\xi_2, \quad (2.61)$$

where  $\Omega_{st}$  is the standard region,  $\Omega^e$  is the general-shaped elemental region and  $|J|$  is the Jacobian of the coordinate transformation.

To differentiate the functions within the general-shaped region  $\Omega^e$  the chain rule is applied

$$\begin{bmatrix} \partial \xi_1 \\ \partial \xi_2 \end{bmatrix} = \frac{1}{J} \times \begin{bmatrix} \frac{\partial x_2}{\partial \xi_2} & -\frac{\partial x_1}{\partial \xi_2} \\ -\frac{\partial x_2}{\partial \xi_1} & \frac{\partial x_1}{\partial \xi_1} \end{bmatrix} \times \begin{bmatrix} \partial x_1 \\ \partial x_2 \end{bmatrix}.$$

## From Elemental to Global Operations

After defining the differentiation and integration operation in each element, operations that involve the whole computational domain have to be defined. The use of a Galerkin formulation requires some form of continuity between elemental regions. In the classical Galerkin formulation this continuity is imposed by requiring that the approximations are  $\mathbb{C}^0$  continuous. To achieve a globally  $\mathbb{C}^0$  continuous expansion from elemental contributions, the global assembly process (also called *direct stiffness summation*) is used [25].

Remembering that the approximation of the solution can be written as

$$u^\delta(x) = \sum_{i=0}^{N_{dof}-1} \hat{u}_i \phi_i(x) = \sum_{e=1}^N \sum_{p=0}^P \hat{u}_p^e \phi_p^e(\xi), \quad (2.62)$$

where  $P$  is the polynomial order and  $N$  is the total number of the elements in the computational domain, and  $N_{dof}$  is the number of degrees of freedom. It is evident that there are more elemental coefficients ( $\hat{u}_p^e$ ) than global coefficients ( $\hat{u}_i$ ). Therefore, more constraints need to be imposed to relate the local and global definitions of the approximate solution  $u^\delta(x)$ . This means that each global degree of freedom (or coefficient) is related to more than one elemental degree of freedom. On the other hand, each elemental degree of freedom is related to only one global degree of freedom [15, 18, 27].

The global assembly consists in assembling (or summing) the equations for the local degrees of freedom which correspond to a single global degree of freedom. Thus a system with a degree equal to the global degrees of freedom is generated. After solving the global system, the value of the local degrees of freedom corresponding to each global degree is known using a reverse operation (explained later in this Section). The boundary-interior decomposition (introduced in Section 2.4) implies that the requirement of  $\mathbb{C}^0$  and connectivity between elements can be achieved by matching similar shaped modes on the common edge neighbour elements. This decomposition allows the use of the *static condensation* method, that permits the solution of the global system efficiently. This method can be applied to symmetric and non-symmetric problems and is based on writing the global system in a particular way. We consider here a symmetric global system of the form

$$Mx = f, \quad (2.63)$$

$x$  is the vector of the global vector expansion coefficients ( $\hat{u}_g$ ) which are unknowns,  $M$  is the global matrix and  $f$  is the vector of the known coefficients ( $\hat{u}^e$ ). The global boundary degrees of freedom are listed first, followed by the global interior degrees of freedom. This permits that the matrix  $M$  be written as follows

$$\begin{bmatrix} M_b & M_c \\ M_c^T & M_i \end{bmatrix} \times \begin{bmatrix} x_b \\ x_i \end{bmatrix} = \begin{bmatrix} f_b \\ f_i \end{bmatrix}. \quad (2.64)$$

$M_b$  is the matrix of boundary-boundary interaction modes, it is sparse and can be reordered to reduce its bandwidth.  $M_i$  is the matrix of interior-interior interaction modes and is by nature a bloc diagonal matrix. This matrix is inexpensive to evaluate since each block can be evaluated individually.  $M_c$  is the coupling matrix between boundary and interior modes and it operates only on known vectors, so it can be calculated once and stored in the form of local vectors.  $x_b$  and  $x_i$  refer to the boundary and interior components of the vector  $x$ , and  $f_b$  and  $f_i$  to the boundary and interior components of the vector  $f$ ; respectively.

The global system (2.63) can now be solved using block elimination by pre-multiplication by the matrix

$$\begin{bmatrix} I & -M_c M_i^{-1} \\ 0 & I \end{bmatrix}, \quad (2.65)$$

which results in the following matrix system

$$\begin{bmatrix} M_b - M_c M_i^{-1} M_c^T & 0 \\ M_c^T & M_i \end{bmatrix} \times \begin{bmatrix} x_b \\ x_i \end{bmatrix} = \begin{bmatrix} f_b - M_c M_i^{-1} f_i \\ f_i \end{bmatrix}, \quad (2.66)$$

where  $M_c^T$  is the transpose of the matrix  $M_c$ . This multiplication results in the following equation for the boundary unknowns ( $x_b$ )

$$(M_b - M_c M_i^{-1} M_c^T) x_b = f_b - M_c M_i^{-1} f_i, \quad (2.67)$$

and once we calculate  $x_b$  we can calculate the interior unknowns ( $x_i$ ) from the second row of the matrix system (2.66) as follows

$$x_i = M_i^{-1} f_i - M_i^{-1} M_c^T x_b. \quad (2.68)$$

The solution of the global system (2.63) consists of three operations: the evaluation of  $M_b - M_c M_i^{-1} M_c^T$ , evaluation of  $M_i^{-1}$  and finally the evaluation of  $M_c M_i^{-1}$ . The latter two operations are done at an elemental level.

## 2.5 Spectral/hp Element Discretization in three dimensions

In this investigation only two-dimensional simulations are presented, the extension of the previous analysis to three-dimensions is briefly discussed in this Section.

In a wide range of problems, there is at least one homogeneous direction, such as the flow past a cylinder and an airfoil. If we assume that the homogeneous direction is represented by the  $z$  coordinate, then a three-dimensional expansion basis can be constructed in terms of the tensorial product of a two-dimensional expansion and a one-dimensional expansion, that is

$$\phi_{pqr}(x, y, z) = \phi_{pq}(x, y) \varphi_r(z), \quad (2.69)$$

where  $\phi_{pqr}(x, y, z)$  is a three-dimensional expansion,  $\phi_{pq}(x, y)$  is a two-dimensional expansion and  $\varphi_r(z)$  is the expansion in the  $z$  direction. Because the direction  $z$  is homogeneous, there is no characteristic length scale in this direction, this favours the use of a *p-type* expansion. This expansion has the property of spanning the entire  $z$  direction rather than a multi-domain regions as it is the case if *h-type* expansions are used. This method was introduced in [17] and has many advantages, such as the fact that the FFT can be used for the transformation between the transformed and physical space. Another advantage is that solving the three-dimensional problem is reduced to solving two-dimensional problems over  $r$  Fourier planes. This can represent a significant gain in computational time [17]. When the infinite ends of the airfoil profile in the homogeneous directions are modeled in a finite computational domain, the periodicity boundary condition is used. This can be advantageously used in the choice of the *p-type* expansion that has to be used for the  $z$  direction. A natural choice is to choose *Fourier expansions* such as

$$\varphi_r(z) = e^{ir\beta z}, \quad (2.70)$$

where  $\beta = \frac{2\pi}{L_z}$  and  $L_z$  is the periodic length.

## 2.6 Time Discretization

The Navier-Stokes equations can be written in the form

$$\frac{\partial U}{\partial t} = -\nabla p + \nu \mathbb{L}(U) + \mathbb{N}(U) \quad (2.71)$$

where  $\mathbb{L}(U) \equiv \nabla^2 U$  and  $\mathbb{N}(U) \equiv -U \cdot \nabla U + F(U, t)$  are the linear and non-linear operators; respectively.  $U = (u, v, w)$  is the velocity vector,  $p$  the pressure, and  $F(U, t)$  is a forcing term. The temporal discretization is achieved via a numerical splitting scheme, as introduced in [20]. This scheme involves the propagation of  $U^n$  and  $p^n$  at a time step  $n$ , over a time step  $\Delta t$ , to determine  $U^{n+1}$  and  $p^{n+1}$  at the next time step  $n+1$ . This is achieved in three steps and expressed as follows

$$\frac{\hat{U} - U^n}{\Delta t} = \sum_{q=0}^{J_e-1} \beta_q \mathbb{N}(U^{n-q}), \quad (2.72)$$

$$\frac{\tilde{U} - \hat{U}}{\Delta t} = -\nabla \bar{p}^{n+1}, \quad (2.73)$$

$$\frac{U^{n+1} - \tilde{U}}{\Delta t} = \nu \sum_{q=0}^{J_i-1} \gamma_q \mathbb{L}(U^{n+1-q}), \quad (2.74)$$

where in the first step, the non-linear terms are advanced using a convective form which is integrated in time via a multilevel Adams-Bashforth scheme, represented by the coefficient  $\beta_q$ , (Equation (2.72)). In the second step, the time-averaged pressure term  $\bar{p}^{n+1}$  is calculated using the divergence of the equation (2.73). In the third step, the viscous term is treated implicitly via an Euler backwards (or Crank-Nicolson) scheme.

## 2.7 Airfoil motion

To implement the airfoil motion the Navier-Stokes equations and the boundary conditions are written in a moving frame of reference. The resulting system is then solved. The method is briefly described here. For further details of the solution procedure we refer the reader to [22].

Let's consider that the body is performing a translational motion  $d$  defined in the fixed or absolute frame of reference  $(X_a, Y_a)$  as  $d = (a(t), b(t))^T$ . A moving frame of reference  $(x_m, y_m)$  attached to the airfoil is defined as a function of the absolute frame as:

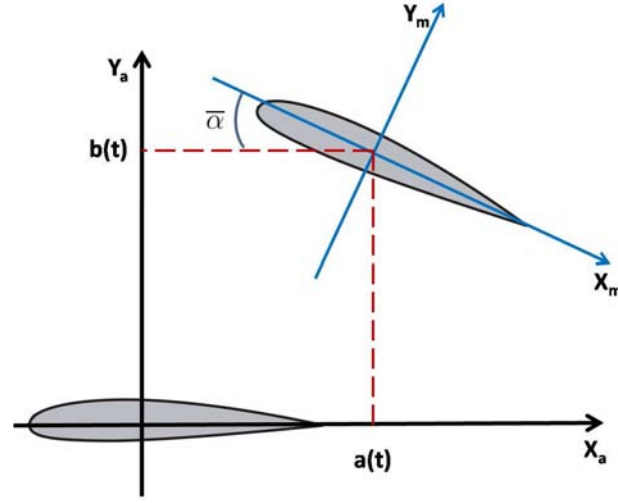


Figure 2.6: Schematic representation of moving frame of reference represented by the coordinates  $(x_m, y_m)$  and the absolute frame of reference represented by the coordinates  $(x_a, y_a)$ .  $\bar{\alpha}$  is the mean incidence (also called the initial angle of attack).  $a(t)$  and  $b(t)$  are the coordinates of the moving airfoil in the absolute frame of reference.

$$X_a = a(t) + x_m \cos \theta + y_m \sin \theta \quad (2.75)$$

$$Y_a = b(t) - x_m \sin \theta + y_m \cos \theta, \quad (2.76)$$

where  $\theta$  is the rotational angle in the moving frame of reference and  $a(t)$  and  $b(t)$  represent the coordinates of the origin of the moving frame of reference in the absolute frame of reference (see Fig. 2.6).

In the case of a plunging (non-rotating) airfoil  $\theta$  and  $a(t)$  are constant. Using matrix notation one obtains the transformation from the coordinates in the absolute frame of reference to the moving frame of reference as:

$$\mathbf{X}_a = \mathbf{d} + \mathbf{A} \mathbf{x}_m, \quad (2.77)$$

and the inverse transformation as:

$$\mathbf{x}_m = \mathbf{A}^T (\mathbf{X}_a - \mathbf{d}), \quad (2.78)$$

where  $\mathbf{d} = (a(t), b(t))^T$  and  $\mathbf{A}$  is the matrix defined as :

$$\begin{pmatrix} \cos \theta & \sin \theta \\ -\sin \theta & \cos \theta \end{pmatrix}$$

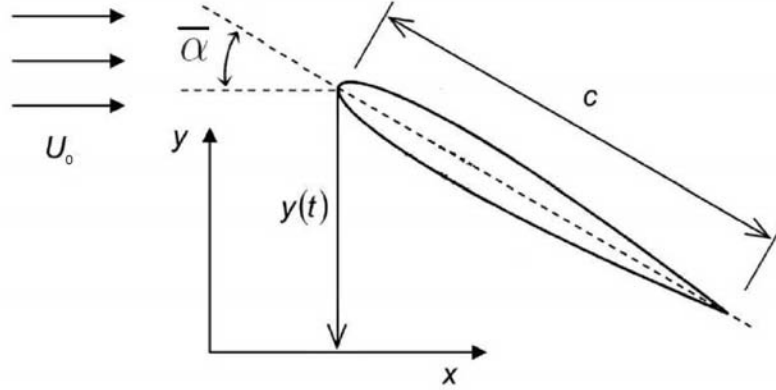


Figure 2.7: Schematic representation of the airfoil for the heave motion, where the vertical displacement  $y(t)$  varies sinusoidally.  $\bar{\alpha}$  is the mean incidence (initial angle of attack),  $U_0$  is the free-stream velocity and  $c$  the chord length.

Using the definition of the coordinates  $(x_m, y_m)$  given by the equation (2.75), the Navier-Stokes equations are re-written in the moving frame of reference as follows:

$$\nabla \cdot \mathbf{u} = 0, \quad (2.79)$$

$$\frac{\partial \mathbf{u}}{\partial t} + (\mathbf{u} \cdot \nabla) \mathbf{u} = -\nabla p + \frac{1}{\text{Re}} \nabla^2 \mathbf{u} + \mathbf{Q}(t), \quad (2.80)$$

$$Q(t) = -A^T \ddot{d}, \quad (2.81)$$

where the term  $A^T \ddot{d}$  is the result of the unsteady translational motion, in our case a plunging motion. The boundary conditions are also transformed in the moving frame of reference, and expressions are derived for Neumann and Dirichlet boundary conditions [22]. For the present simulations we have considered the body as being rigid (non-deformable) and forced to oscillate in heave (plunge) motion as illustrated in Fig. 2.7. The heave motion is defined as

$$d = y(t) = h \cos(2\pi ft). \quad (2.82)$$

where  $y(t)$  is the time-dependent vertical motion,  $h^* = h/c$  is the non-dimensional heaving frequency, and  $f^* = fc/U_0$  is the non-dimensional heaving frequency (for simplicity, the superscript  $*$  will be dropped). The airfoil is set at a constant initial angle of attack  $\bar{\alpha} = \theta$  (or mean incidence) and is forced to oscillate vertically in a sinusoidal fashion.

## Aerodynamic forces

The forces and moments are evaluated by calculating their viscous and pressure contributions. The aerodynamic force applied by the flow on the body can be expressed as the integration of local stress as:

$$F = \int_{\Omega} \sigma n_A ds_A = - \int_{\Omega} p n_A ds_A + \int_{\Omega} \tau n_A ds_A = F_{press,A} + F_{visc,A}. \quad (2.83)$$

where  $\sigma = -p\mathbf{I} + \tau$  is the stress tensor,  $\Omega$  is the airfoil surface,  $n_A$  is the unit normal on the airfoil,  $F_{press,A}$  are the pressure forces and  $F_{visc,A}$  are the viscous forces. The subscript  $A$  indicates that the quantities are expressed in the absolute frame of reference. The forces in Equation (2.83) are expressed in the moving frame of reference as follows:

$$F = F_{press,A} + F_{visc,A} = A(F_{press,m} + F_{visc,m}). \quad (2.84)$$

where  $A$  is the matrix introduced in Equation (2.78).

## Bibliography

- [1] K. J. Bathe. *Finite Element Procedures in Engineering Analysis*. Prentice-Hall, Inc., Englewood Cliffs, New Jersey, 1982.
- [2] G. Ben-Yu. *Spectral Methods and Their Applications*. World Scientific Publishing, 1998.
- [3] J. P. Boyd. *Chebyshev and Fourier Spectral Methods*. Dover Publications, 2001.
- [4] C. Canuto, M. Y. Hussaini, A. Quarteroni, and T. A. Zang. *Spectral Methods*. Springer-Verlag Berlin Heidelberg, 2006.
- [5] C. Canuto, M. Y. Hussaini, A. Quarteroni, and T. A. Zang. *Spectral Methods: Evolution to Complex Geometries and Applications to Fluid Dynamics*. Springer-Verlag Berlin Heidelberg, 2007.
- [6] B. S. Carmo. *On the Wake Interference in the Flow around Two Circular Cylinders: Direct Stability Analysis and Flow-Induced Vibrations*. PhD thesis, Department of Aeronautics, Imperial College London, 2009.
- [7] B. S. Carmo, S. J. Sherwin, P. W. Bearman, and R. H. J. Willden. Wake transition in the flow around two circular cylinders in staggered arrangements. *J. Fluid Mech.*, 597(1):1–29, 2008.
- [8] J. E. Castillo. *Mathematical Aspects of Numerical Grid Generation (Frontiers in Applied Mathematics)*. Society for Industrial Mathematics, 1987.
- [9] A. N. Cookson, D. J. Doorly, and S. J. Sherwin. Mixing Through Stirring of Steady Flow in Small Amplitude Helical Tubes. *Ann. Biomed. Eng.*, 37: 710–721, 2009.
- [10] S. Dong, D. Lucor, and G. E. Karniadakis. Flow Past a Stationary and Moving Cylinder: DNS at  $Re=10,000$ . *Department of Defense Users Group Conference*, 0:88–95, 2004.
- [11] J. H. Ferziger and M. Peric. *Computational Methods for Fluid Dynamics*. Springer, 2002.
- [12] V. Girault. *Finite Element Methods for Navier-Stokes Equations: Theory and Algorithms*. Springer, 1986.
- [13] D. Gottlieb and S. A. Orszag. *Numerical Analysis of Spectral Methods: Theory and Applications*. Society for Industrial and Applied Mathematics, 1977.

- [14] L. Grinberg and G. E. Karniadakis. A new domain decomposition method with overlapping patches for ultrascale simulations: Application to biological flows. *J. Comp. Phys.*, 229(15):5541–5563, 2010.
- [15] W. Heinrichs and B. I. Loch. Spectral Schemes on Triangular Elements. *J. Comp. Phys.*, 173(1):279–301, 2001.
- [16] C. Johnson. *Numerical Solution of Partial Differential Equations by the Finite Element Method*. Cambridge University Press, 1987.
- [17] G. E. Karniadakis. Spectral element-Fourier methods for incompressible turbulent flows. *Comput. Method Appl. M.*, 80(1-3):367–380, 1990.
- [18] G. E. Karniadakis and S. Sherwin. *Spectral/hp Element Methods for Computational Fluid Dynamics*. Oxford University Press, 2005.
- [19] G. E. Karniadakis and G. S. Triantafyllou. Frequency selection and asymptotic states in laminar wakes. *J. Fluid Mech.*, 199(1):441–469, 1989.
- [20] G. E. Karniadakis, S. A. Orszag, and M. Israeli. High-order splitting methods for the incompressible Navier-Stokes equations. *J. Comp. Phys.*, 97:414–443, 1991.
- [21] R. Leveque. *Finite Difference Methods for Ordinary and Partial Differential Equations: Steady-State and Time-Dependent Problems*. SIAM, Society for Industrial and Applied Mathematics, 2007.
- [22] L. Li, S. J. Sherwin, and P. W. Bearman. A moving frame of reference algorithm for fluid/structure interaction of rotating and translating bodies. *Int. J. Numer. Meth. Fl.*, 38:187–206, 2002.
- [23] V. D. Liseikin. *Grid Generation Methods*. Springer, 2010.
- [24] I. Lomtev, R. M. Kirby, and G. E. Karniadakis. A Discontinuous Galerkin ALE Method for Compressible Viscous Flows in Moving Domains. *J. Comp. Phys.*, 155(1):128–159, 1999.
- [25] W. McGuire, R. H. Gallagher, and R. D. Ziemian. *Matrix Structural Analysis*. John Wiley and Sons, 2000.
- [26] S. J. Sherwin. <http://www3.imperial.ac.uk/spectralhp>, 2010.
- [27] S. J. Sherwin and G. E. Karniadakis. A triangular spectral element method; applications to the incompressible Navier-Stokes equations. *Computer Methods in Applied Mechanics and Engineering*, 123(1-4):189–229, 1995.
- [28] S. J. Sherwin and J. E. Karniadakis. Tetrahedral /hp Finite Elements: Algorithms and Flow Simulations. *J. Comp. Phys.*, 124(1):14–45, 1996.

- 
- [29] J. C. Strikwerda. *Finite Difference Schemes and Partial Differential Equations*. SIAM, Society for Industrial and Applied Mathematics, 2004.
- [30] J. F. Thompson, K. S. Bharat, and N. P. Weatherill. *Handbook of Grid Generation*. CRC-Press; 1 edition, 1998.
- [31] H. K. Versteeg and W. Malalasekera. *An Introduction to Computational fluid Dynamics: The Finite Volume Method*. Longman Scientific and Technical, 1995.



# Chapter 3

## Validation

In this Chapter we validate the numerical simulations obtained using the *Nεκταρ*-solver. The validation is performed for a motionless cylinder and both motionless and heaving airfoils. The validation for the cylinder is conducted here because it is one of the most studied flow configurations in CFD, for which abundant computational and experimental data exist. The *Nεκταρ*-solver was validated for many flow geometries, among those cylindrical [2], helical [3] and rectangular [12]. It was also validated for the airfoil experiencing heaving motion against previously published numerical methods [16]. The *Nεκταρ*-solver employed by Kirby in [16] uses an *Arbitrary Lagrangian Eulerian* (ALE) framework to account for the heaving motion of the airfoil [8, 18, 21]. The author validated his 2D simulations against the numerical simulations in [22]. The *Nεκταρ*-solver we use in this investigation uses a moving frame of reference approach (previously introduced in Chapter 2) to account for the airfoil motion [12]. To the best of our knowledge, this is the first time that this version of the *Nεκταρ*-solver is used in combination with the moving frame of reference technique to simulate flows over heaving airfoils.

Note that in this investigation only 2D flows over motionless and heaving airfoils are considered. The main goal is to explore in detail the flow pattern evolution, especially in the boundary-layer region and the effects of varying the flow parameters on the flow pattern, on the aerodynamical coefficients, and on the near-wake configuration and dynamics. 2D simulations were performed as a first approach (instead of 3D simulations) due to the unsteady nature of the flow. This unsteadiness requires the use of very high spatial and temporal resolution to simulate the flow separation, the vortex shedding and the wake evolution. Simulating the 3D problem results in high computational time costs and it would be not possible to achieve, given the time frame and computational resources dedicated to this investigation. Moreover, many designs for Micro Air Vehicles use 2D motions for propulsion [6, 9]. Furthermore, Lewin & Haj-Hariri [11] simulated 2D stating that "The(ir) paper will concentrate on the heaving of a two-dimensional airfoil, since many of the phenomena of interest (e.g. thrust

generation, inversion of the vortex street, leading-edge vortex separation) can be captured with this simple motion". 2D simulations can be used as a reference to be compared to 3D simulations, and it is considered as a reliable tool in its own right.

### 3.1 Flow over a motionless cylinder

In this Section, the *Nεκταρ*-solver is used to simulate the 2D flow around a circular cylinder subjected to a uniform inflow. Our results are compared with numerical [5, 7, 14, 15] and experimental studies [1, 4] available in the literature. We present here the main features of these studies. *Dennis & Chang* [5] solved the Navier-Stokes equations in a modified polar coordinates grid using finite-difference approximations. *Liu & all.* [15] computed the Reynolds-averaged Navier-Stokes equations using a pseudo-compressibility approach on a moving grid. A high-order immersed interface method is used by *Linnick & Fasel* [14] which is presented as an alternative to lower-order methods. The same motivation is shared by *Gopalan* [7] who used a finite-difference high-order solver on a moving grid. The high spatial resolution is obtained using an implicit compact spatial differencing, which achieves a spectral-like resolution. *Berger* [1] used hotwire anemometer measurements to experimentally determine the frequency of vortex shedding the near wake of a fixed and oscillating cylinder. *Coutanceau & Bouard* [4] conducted water tank experiments to produce plane flow around a circular cylinder. Visualisations were then made by illuminating the particle seeded water tank with a sheet of intense light.

The Reynolds numbers investigated are  $Re_D = 20, 40, 50, 100, 150$  and  $200$ , where  $Re_D = \rho U_0 D / \mu$  ( $D$  is the cylinder diameter). The mesh used is an unstructured mesh composed of 1648 squares and triangles as shown in Fig. 3.1. The numerical order used for the simulations is 9 and the time step  $\Delta t = 10^{-4}$ . Note that the Spectral /hp Element Methods implemented in the *Nεκταρ*-solver permits the increase of the computational accuracy using two approaches. The first approach is to decrease the size of the sub-elements of the numerical grid (called remeshing). The second approach, which is used in this investigation, is to increase the polynomial order of the approximation used. This latter approach is preferred because it is easier and faster to implement than remeshing. We used a polynomial order of 9 and 13. As the results obtained were almost the same, we used a polynomial order of 9 for all simulations. The range of Reynolds number investigated covers the steady, steady-to-unsteady transition, and unsteady flow regimes. Experimentally, it is established that at  $40 \leq Re \leq 50$  the periodic shedding of vortices begins, whereas for lower Reynolds numbers the flow remains steady [5, 19].

For  $Re \leq 50$  the flow around the motionless cylinder is steady, and composed of two vortices or cells (called twin vortices [4]) which remain attached to the

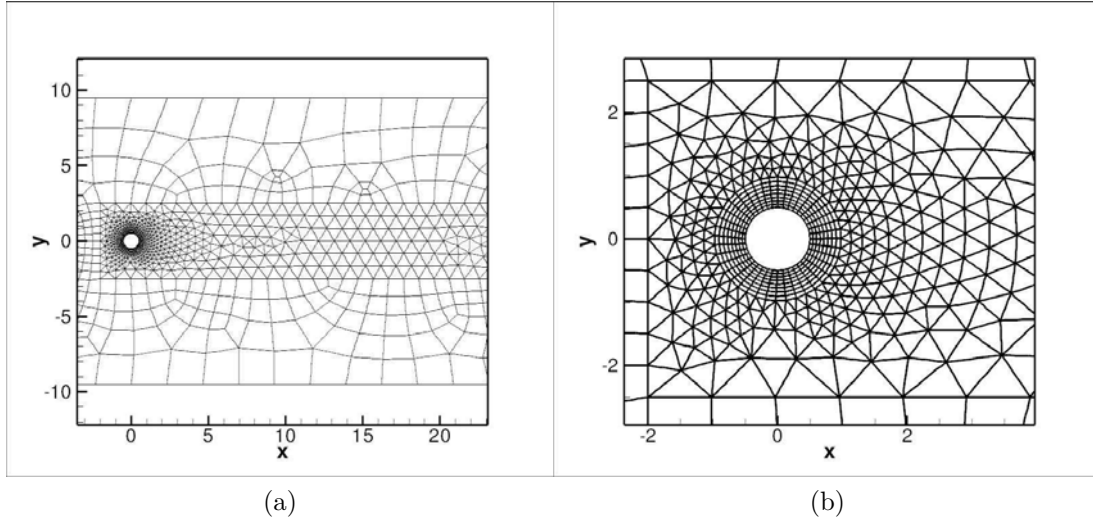


Figure 3.1: (a) The numerical mesh used for the cylinder simulations. (b) Close-up of the boundary layer region around the cylinder.

cylinder. These vortices grow in size as the Reynolds number is increased. In Table 3.1 the geometrical parameters of the steady flow structures around a motionless cylinder along with the mean value of the drag coefficient obtained using the *Nεκταρ*-solver are compared against previously published results (See Table 3.1). The meanings of the geometrical parameters are presented in Fig. 3.2.

For  $Re > 50$  the flow around the cylinder is unsteady as the twin vortices previously mentioned detach from the cylinder and are shed in the wake. The common quantity that one calculates for unsteady flow over cylinders is the Strouhal number  $St = fL U_0$  (where  $f$  is the shedding frequency of the vortices,  $L$  is the characteristic length and  $U_0$  is the free-stream velocity). Note that  $St$  is obtained from the  $C_L$  time series. We compare  $St$ , the mean values of drag and lift coefficients obtained by our simulations and simulations found in the literature (see Table 3.2). Furthermore, the time series of the lift and drag coefficients are also compared to previously published computational results [14] (see Fig.3.3).

We also compare the vorticity contours obtained numerically at  $Re = 40, 50, 100$  and  $200$  in [14] (Fig. 3.4) and the streamlines at  $Re = 20$  and  $40$  obtained numerically in [7] (Fig. 3.5) to the ones obtained using the *Nεκταρ*-solver.

Overall and for all the validation simulations conducted for the cylinder case, the results obtained using the *Nεκταρ*-solver show a very good agreement with the literature results. These results give confidence in using the solver in the determination of the natural frequency (or the frequency at which the vortices are shed).

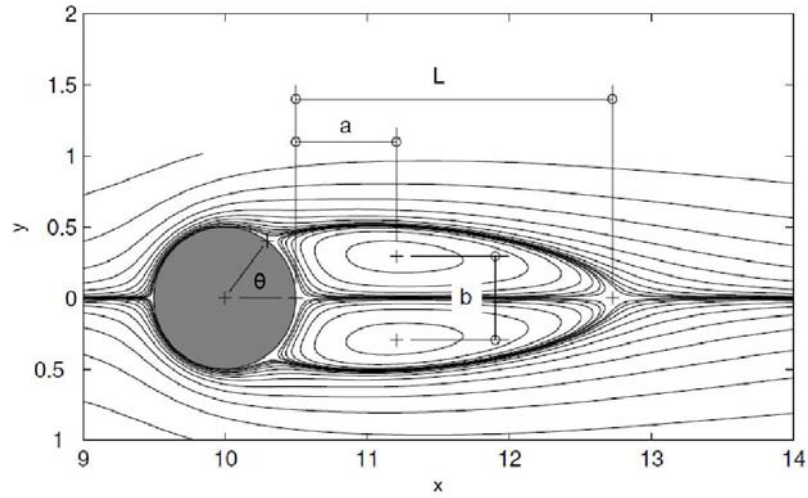


Figure 3.2: Nomenclature of the geometrical parameters to be calculated and compared for the cylinder simulation. (Adapted from [7, 14]).

	L	a	b	$\theta$	$C_D$
$Re_D = 20$					
Dennis & Chang [5]	0.94	-	-	43.7	2.05
Coutanceau & Bouard [4] *	0.93	0.33	0.46	45.0	-
Linnick [14]	0.93	0.36	0.43	43.9	2.16
Gopalan [7]	0.92	0.34	0.42	-	-
Present study	0.92	0.35	0.43	44.5	2.16
$Re_D = 40$					
Dennis & Chang [5]	2.35	-	-	53.8	1.52
Coutanceau & Bouard [4] *	2.13	0.76	0.59	53.8.0	-
Linnick [14]	2.23	0.71	0.59	53.4	1.61
Gopalan [7]	2.15	0.70	0.6	-	-
Present study	2.21	0.70	0.59	53.8	1.60

Table 3.1: Comparison of geometrical parameters for the flow over a motionless cylinder. The comparison is between the results of the the present study and previously published results in [4, 5, 7, 14]. An asterisk \* denotes experimental results and  $\theta$  denotes the flow separation angle.

	$St$	$C_D$	$C_L$
$Re_D = 100$			
Berger & Wille [1] *	0.16-0.17	-	-
Liu & al. [15]	0.165	$1.35 \pm 0.012$	$\pm 0.339$
Linnick [14]	0.166	$1.34 \pm 0.009$	$\pm 0.333$
Gopalan [7]	0.167	-	-
Present study	0.167	$1.36 \pm 0.007$	$\pm 0.336$
$Re_D = 200$			
Berger & Wille [1] *	0.18-0.19	-	-
Liu & al. [15]	0.192	$1.31 \pm 0.049$	$\pm 0.69$
Linnick [14]	0.197	$1.37 \pm 0.046$	$\pm 0.70$
Present study	0.19	$1.35 \pm 0.032$	$\pm 0.69$

Table 3.2: Comparison of the Strouhal number, the lift and drag coefficients for the unsteady flow over a motionless cylinder. The comparison is between the present study and the previously published results in [1, 7, 14, 15]. An asterisk \* denotes experimental results.  $St$  is determined from the time variation of  $C_L$ .

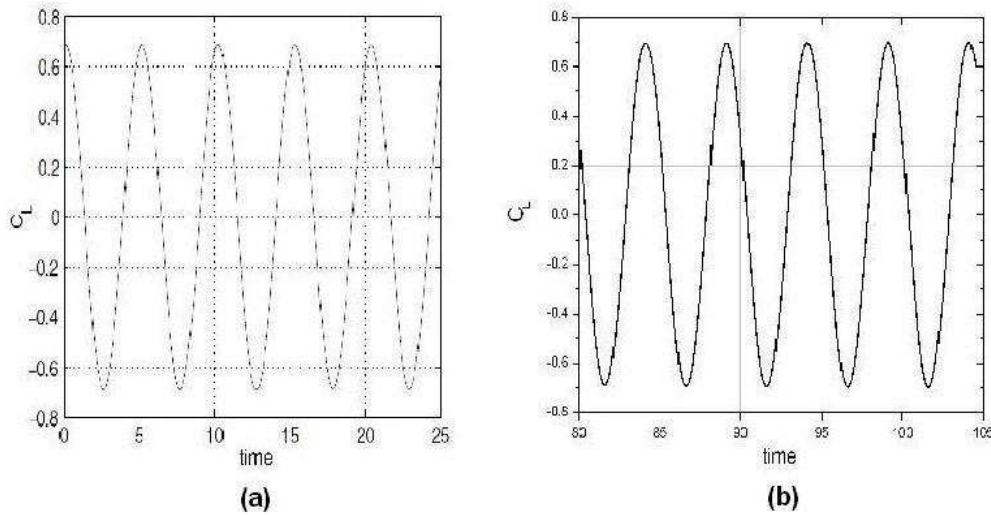


Figure 3.3: Lift coefficient time series  $Re = 200$ . (a) from [14] and (b) using the  $N\epsilon\kappa\tau\sigma R$ -solver.

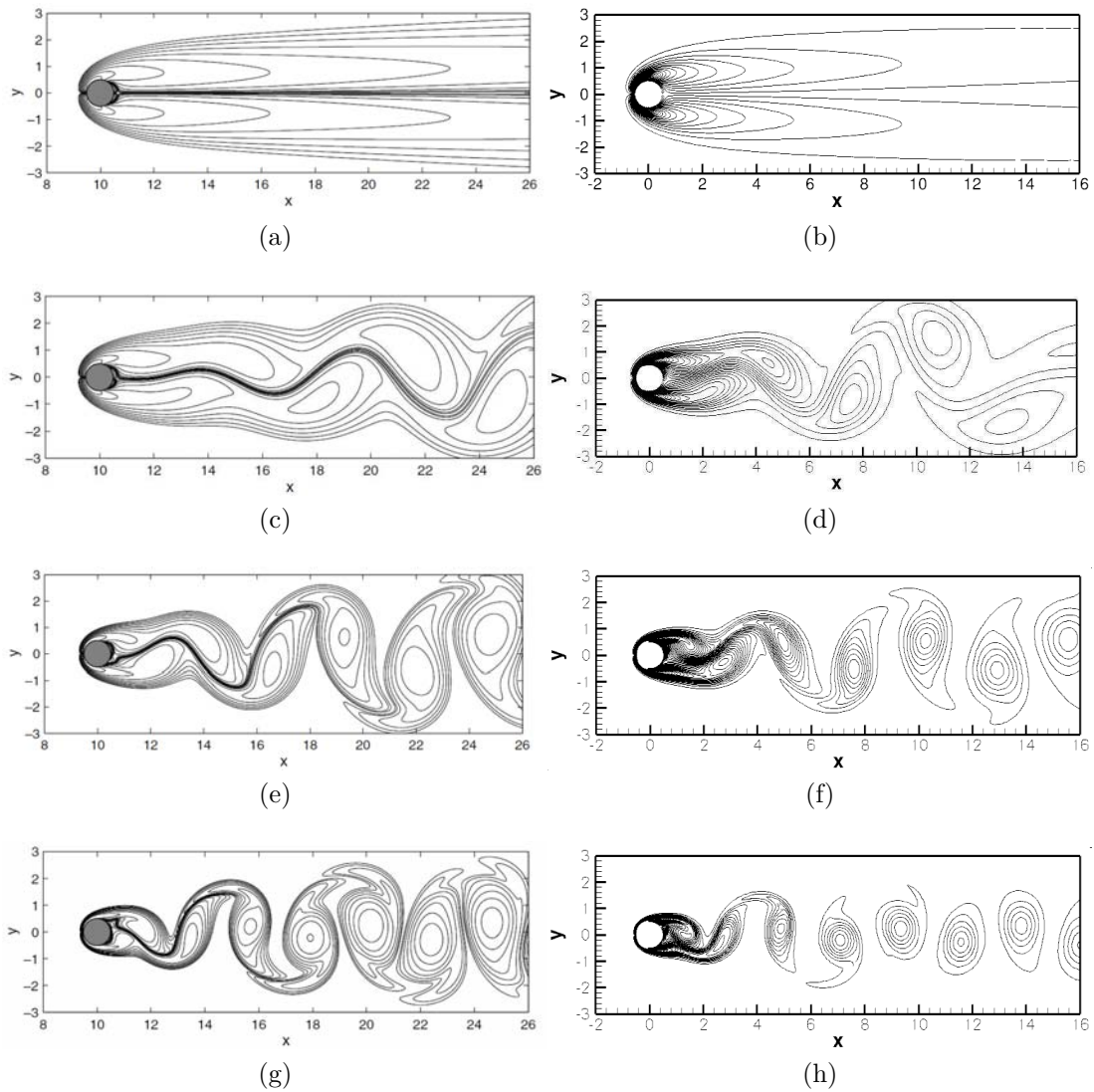
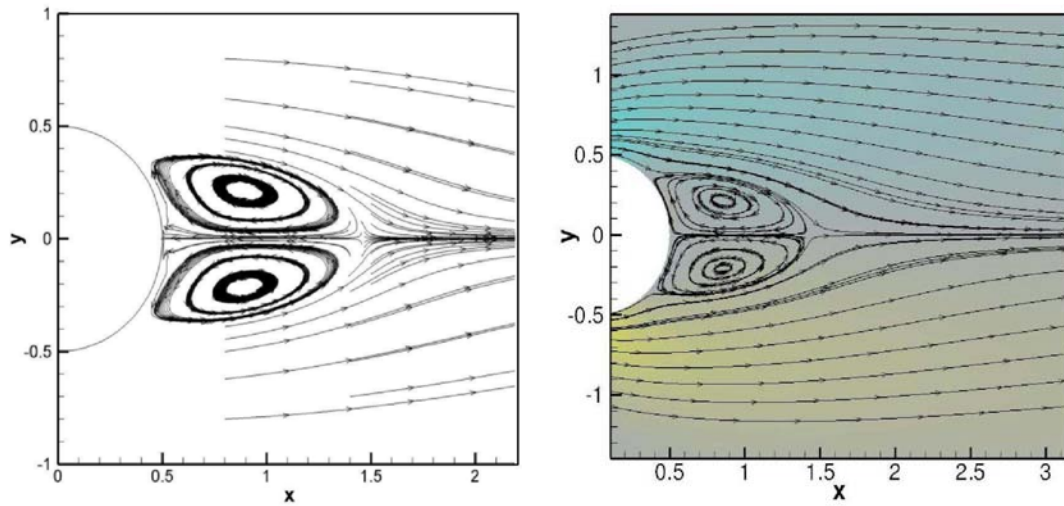
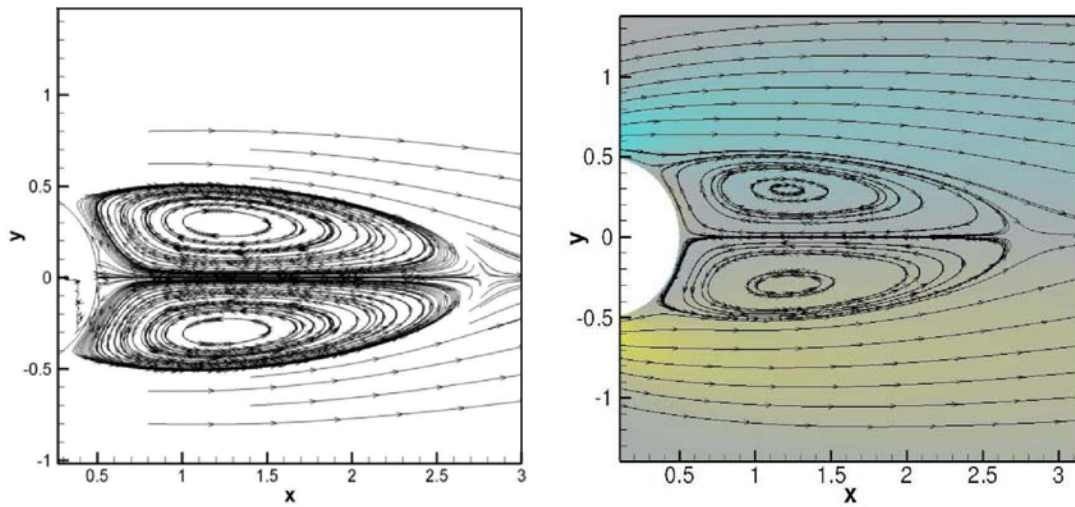


Figure 3.4: (a,b) Vorticity contours at  $Re = 40$ , (c,d)  $Re = 50$ , (e,f)  $Re = 100$ , and (g,h)  $Re = 200$ . On the left side are the results obtained in [14] and on the right side are the results obtained using the  $N\epsilon\kappa\tau\alpha r$ -solver.



(a)



(b)

Figure 3.5: Streamtraces at (a)  $Re = 20$  and (b)  $Re = 40$ . The left frames are the numerical results of Linnick [14]. The right frames are obtained using the  $N\epsilon\kappa\tau\alpha r$ -solver.

## 3.2 Flow over a motionless airfoil

Next we validate our simulations for a steady and an unsteady flow over a NACA0012 airfoil against the results obtained by *A.V. Shatalov* [17]. The author used a numerical method based on decomposing the velocity as a sum of irrotational and rotational components. The author also used a viscous-inviscid interaction method. For the purpose of comparison we simulate several flow cases at constant angles of attack ( $\bar{\alpha}$ ), as done in [17]. The numerical grid used for the *Nεκταρ* solver is composed of 4220 triangular and quadrilateral elements (see Fig. 3.6). The elements density is increased around the airfoil profile and in the wake. A polynomial order of 9 is used. We used a polynomial order of 9 and 13. As the results obtained were almost the same, we used a polynomial order of 9 for all simulations and  $\Delta t = 10^{-4}$ .

### steady flow over an airfoil

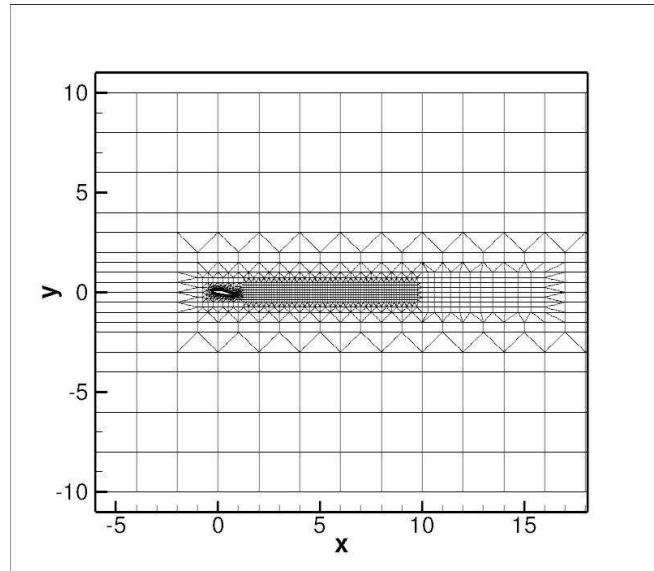
#### 3.2.1 $\alpha = 0^\circ$ and $Re = 500$

The first case simulated is the incompressible, two-dimensional viscous flow over a NACA0012 airfoil at a fixed angle of attack  $\alpha = 0^\circ$  and  $Re = 500$ . Fig. 3.7, Fig. 3.8 and Fig. 3.9 illustrate the  $u$ -velocity,  $v$ -velocity and the iso-pressure contours obtained by *A.V. Shatalov* [17]. These results compare well to our simulations using the *Nεκταρ*-solver. The dotted lines on the Figures from [17] represent the inviscid flow simulations, used by the authors for comparison, but not addressed in the present study. In Fig. 3.10 the surface pressure distribution around the airfoil upper surface is plotted for comparison. A very good qualitative and quantitative agreement is obtained when comparing to the results in [17].

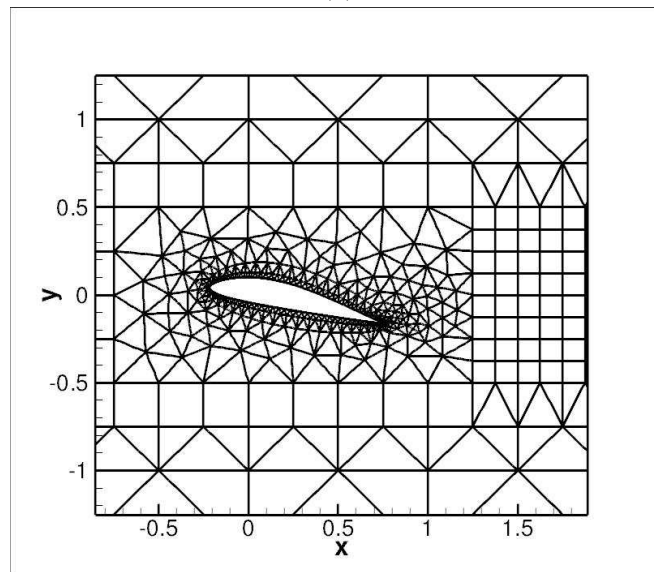
#### 3.2.2 $\alpha = 10^\circ$ and $Re = 500$

A second validation case is simulated at  $Re = 500$  and  $\alpha = 10^\circ$ . The results are presented in the form of  $u$ -velocity,  $v$ -velocity, pressure iso-contours and surface pressure coefficient  $C_p$  distributions in the Fig. (3.11-3.14); respectively. In Fig. 3.11 we note the presence of a vortex (indicated by a red arrow on the figure) which covers approximately 40% of the second half of the airfoil and is captured by both simulations. The presence of this vortex was confirmed by plotting the streamlines over the airfoil surface. On Fig. 3.11 to Fig. 3.13 from [17], the flow over the airfoil is inclined with respect to the horizontal plane due to the fact that the authors subjected the airfoil to an inclined inflow rather than to incline the airfoil itself, which is the approach used in the present study.

A very good qualitative agreement is found again between the present results and the reference, and it is confirmed by a good qualitative and quantitative



(a)



(b)

Figure 3.6: (a) The numerical grid used for the airfoil simulations validation. The resolution is increased around the airfoil surface (the boundary-layer region) and in the near wake. The mesh is composed of triangular and quadrilateral elements and the total number of elements is 4220. (b) A close-up of the grid around the airfoil surface region.

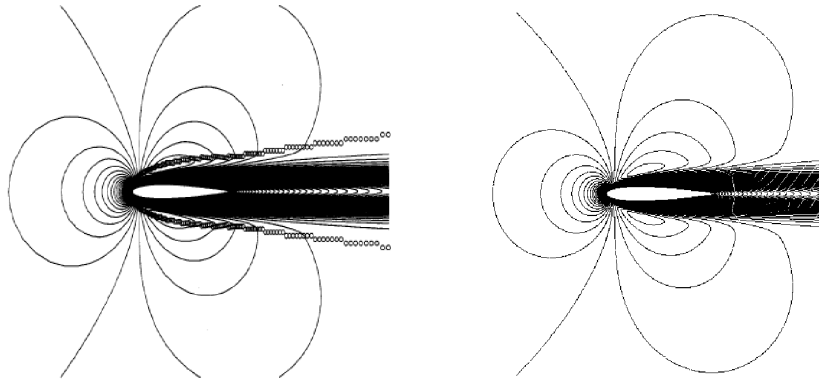


Figure 3.7:  $u$ -velocity contours, from [17] (left) and with the *NekTar* solver (right) at  $Re = 500$  and  $\alpha = 0^\circ$ .

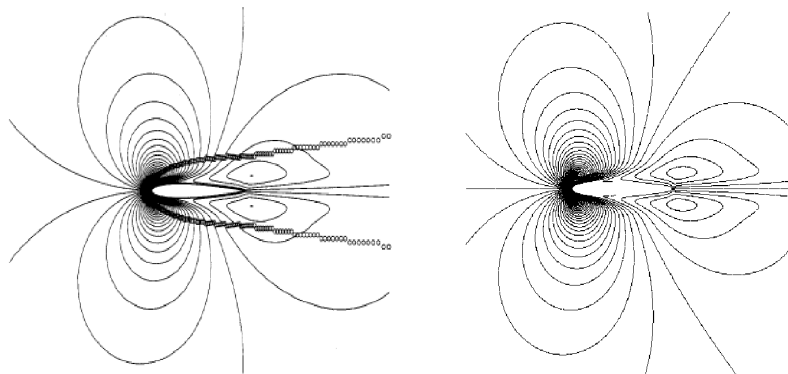


Figure 3.8:  $v$ -velocity contours, from [17] (left) and with the *NekTar* solver (right) at  $Re = 500$  and  $\alpha = 0^\circ$ .

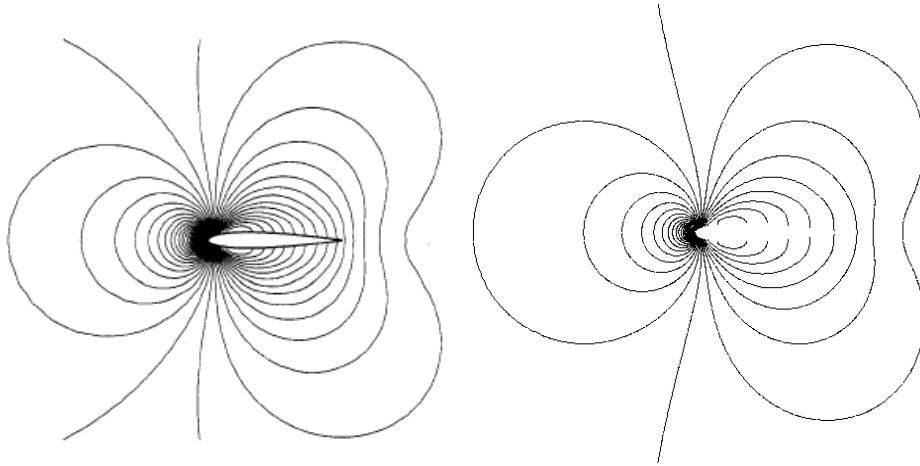


Figure 3.9: Pressure iso-contours, from [17] (left) and with the  $N\epsilon\kappa\tau\alpha r$  solver (right) at  $Re = 500$  and  $\alpha = 0^\circ$ .

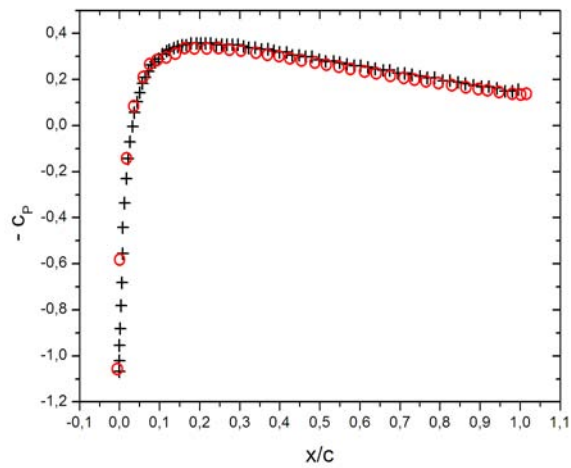


Figure 3.10: Surface pressure coefficient  $C_p$  distribution at  $Re = 500$  and  $\alpha = 0^\circ$  over the airfoil upper-surface. The open circles correspond to output from the  $N\epsilon\kappa\tau\alpha r$ -solver and the crosses are taken from [17].

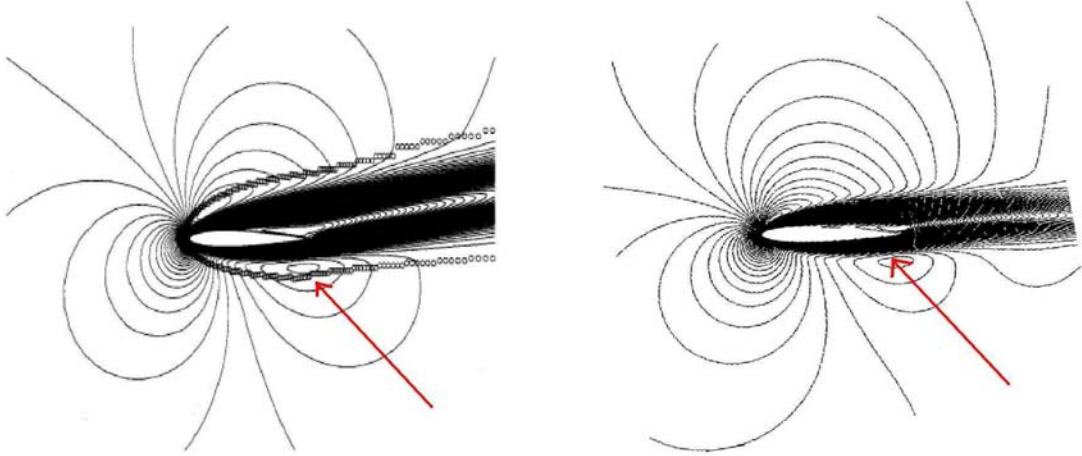


Figure 3.11:  $u$ -velocity contours, from [17] (left) and with the *Nektar* solver (right) at  $Re = 500$  and  $\alpha = 10^\circ$ . The red arrows indicate a vortex.

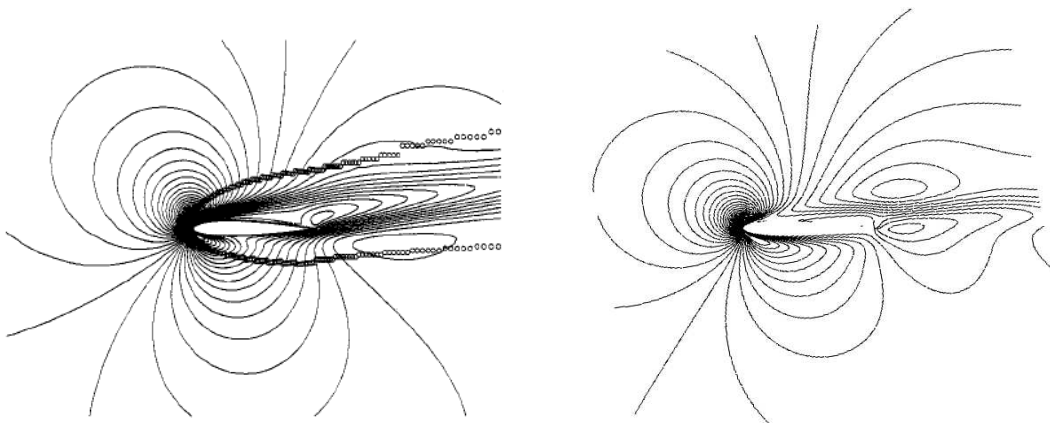


Figure 3.12:  $v$ -velocity contours, from [17] (left) and with the *Nektar* solver (right) at  $Re = 500$  and  $\alpha = 10^\circ$ .

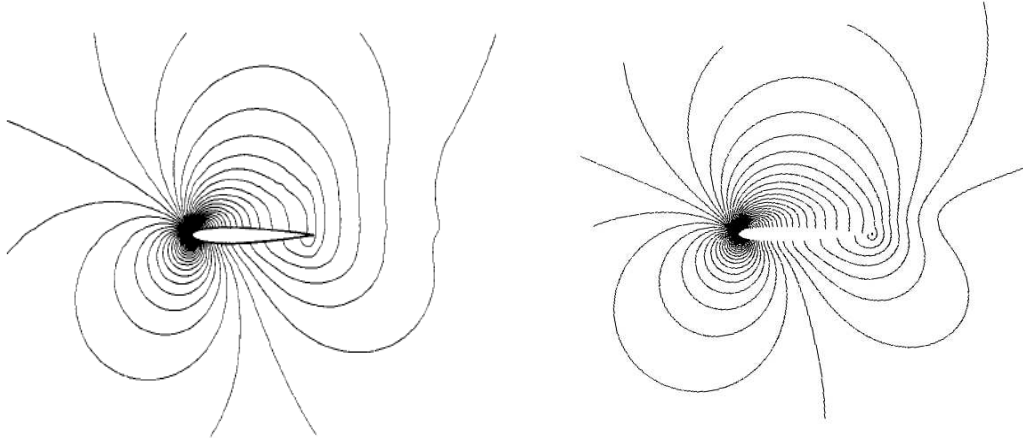


Figure 3.13: Pressure iso-contours, from [17] (left) and with the  $N\epsilon\kappa\tau\alpha r$ -solver (right) at  $Re = 500$  and  $\alpha = 10^\circ$ .

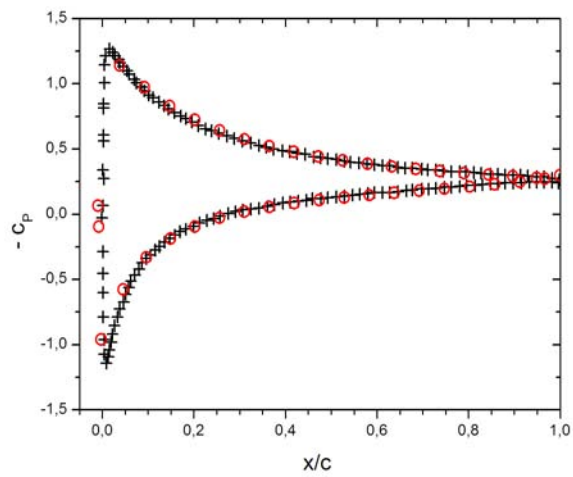


Figure 3.14: Surface pressure coefficient  $C_p$  distribution over the airfoil surface at  $Re = 500$  and  $\alpha = 10^\circ$ . The open circles are generated by the  $N\epsilon\kappa\tau\alpha r$  solver. The crosses correspond to data extracted from [17].

agreement for the surface pressure coefficient illustrated in Fig. 3.14, where our results and the results from [17] coincide.

## unsteady flow over an airfoil

To validate the code for the unsteady flow around an airfoil, we simulated three cases and validated them against the reference [17], for the following parameter combinations: ( $\alpha = 20^\circ$ ,  $Re = 800$ ), ( $\alpha = 0^\circ$ ,  $Re = 2000$ ) and ( $\alpha = 5^\circ \sin 2\pi t$ ,  $Re = 800$ ). All the simulated cases were successfully reproduced by our simulations, but for brevity we will present here only the results of one simulation case at  $\alpha = 20^\circ$  and  $Re = 800$ .

### 3.2.3 $\alpha = 20^\circ$ and $Re = 800$

The results are presented in terms of the  $u$ -velocity contours at different time steps (see Fig. 3.15 - Fig. 3.17) together with the surface pressure coefficient distributions over the airfoil surface (see Fig. 3.18 and Fig. 3.19). Comparison was also successfully achieved for the  $v$ -velocity and the iso-pressure contours (not presented here).

Our simulations shows a very good agreement with the reference [17], as they reproduced the vortices and the flow contours. Note that our simulations captured more flow details than the reference [17]. For example in Fig. 3.15d ( $t = 2$ ) more details of the flow structure, the leading- and trailing-edge vortices and the boundary layer were captured by the present study. Fig. 3.18 and Fig. 3.19 show snapshots of the surface pressure distribution at selected time steps, compared with the reference [17]. The qualitative agreement found for the  $u$ -velocity components is confirmed by a very good qualitative and quantitative agreement of the surface pressure distribution.

## 3.3 Flow over a heaving airfoil

### 3.3.1 Wake validation

Finally, we present results for the most complex flow case we used for comparison. Here we validate our results for a heaving airfoil against the experimental results in [10] and the numerical results in [23]. In [23] the author uses a Navier-Stokes code based on the work in [20]. The code solves the strong-conservation form of the non-dimensionalized 2D unsteady compressible Reynolds-Averaged Navier-Stokes equations in general coordinates. The grid used by *Young* is a C-grid and the heaving motion of the airfoil is accounted for by deforming the grid adjacent to the airfoil. The grid deformation is done as follows: the region closest to the airfoil is moved as a solid body, an intermediate region is deformed

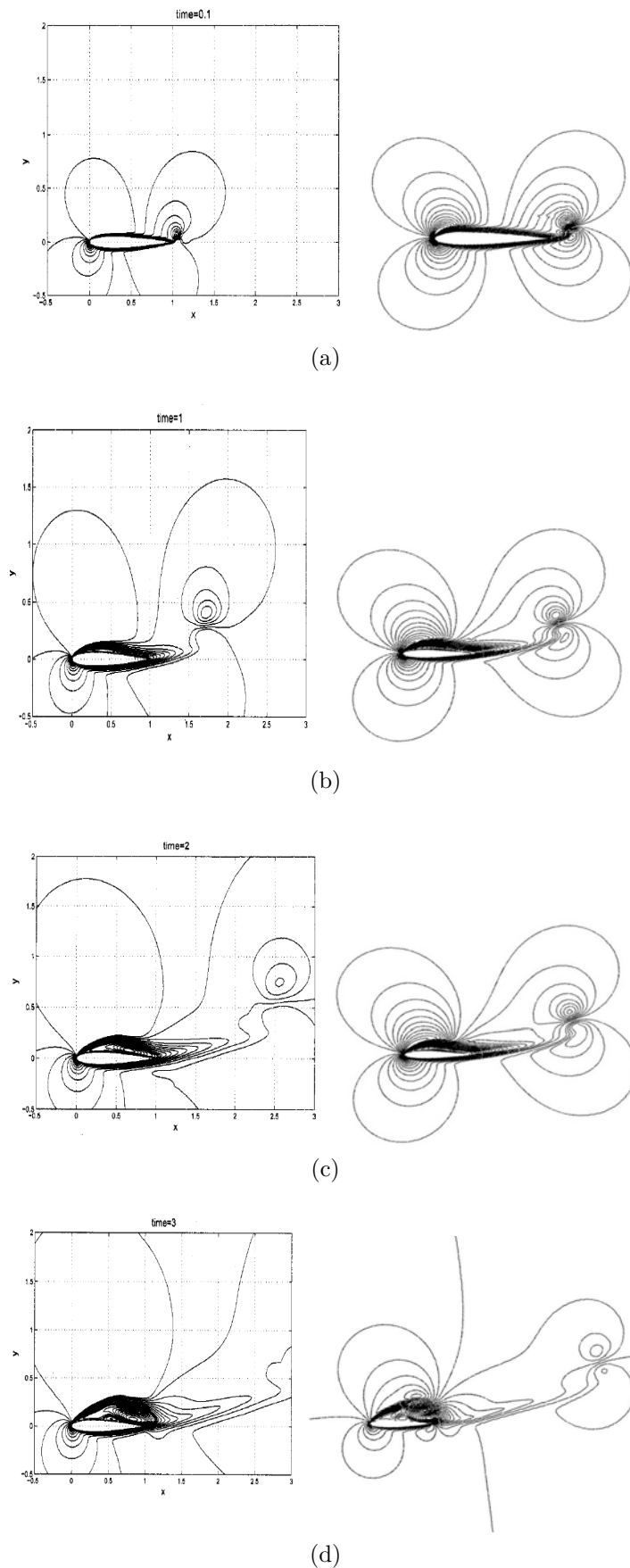


Figure 3.15:  $u$ -velocity contours at (a)  $t=0.1$ , (b)  $t=1$ , (c)  $t=2$ , (d)  $t=3$ . From [17] (left) and with the  $Nek5000$  solver (right), at  $Re = 800$  and  $\alpha = 20^\circ$ .

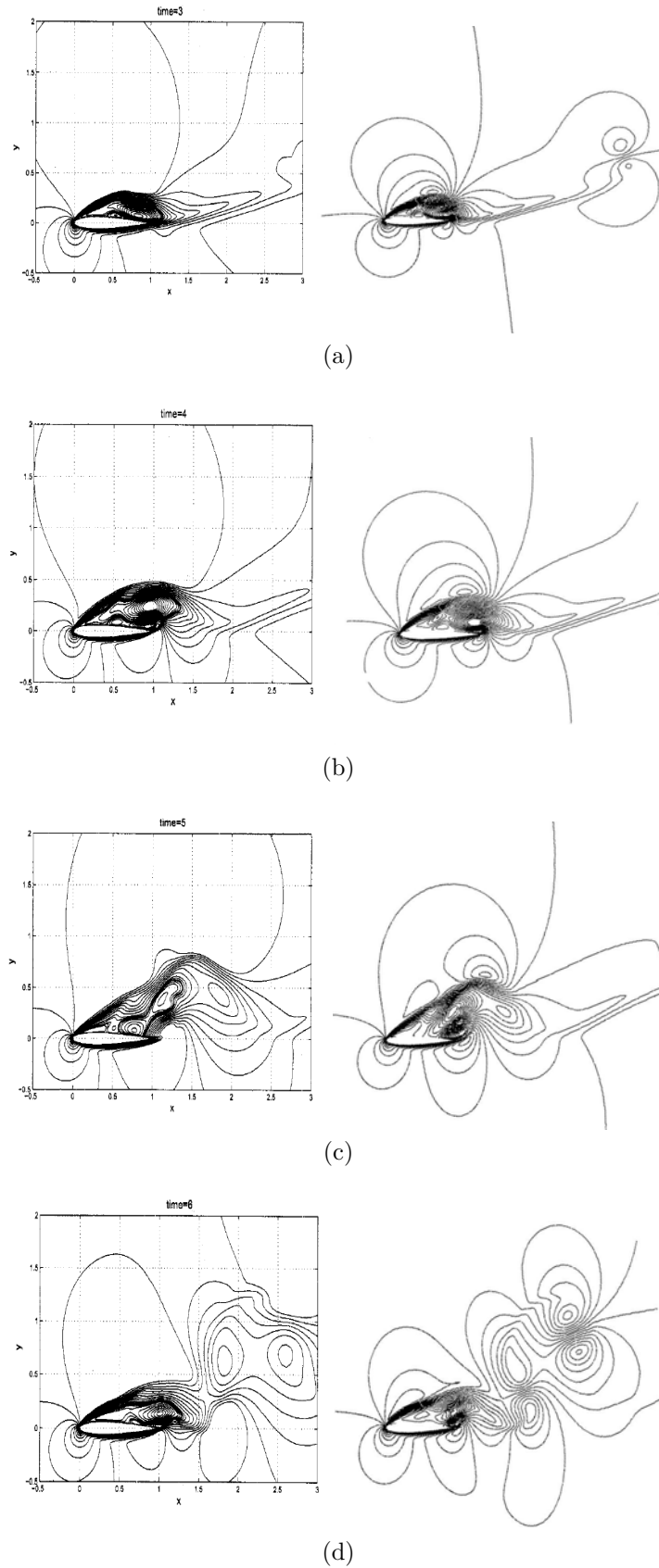


Figure 3.16:  $u$ -velocity contours at (a)  $t=4$ , (b)  $t=5$ , (c)  $t=6$ , (d)  $t=7$ . From [17] (left) and with the  $N\epsilon\kappa\tau\alpha r$  solver (right), at  $Re = 800$  and  $\alpha = 20^\circ$ .

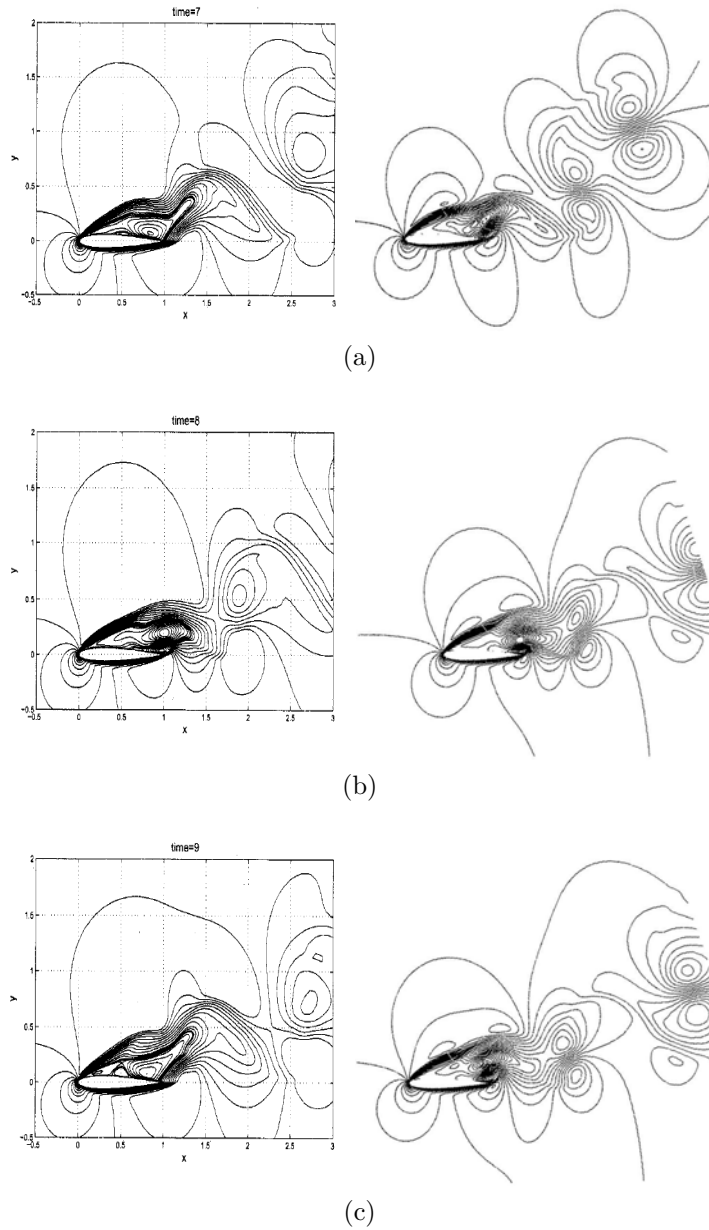


Figure 3.17:  $u$ -velocity contours at (a)  $t=8$ , (b)  $t=9$ , (c)  $t=10$ . From [17] (left) and with the *Nektar* solver (right), at  $Re = 800$  and  $\alpha = 20^\circ$ .

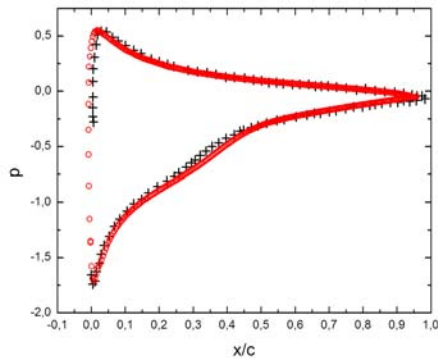
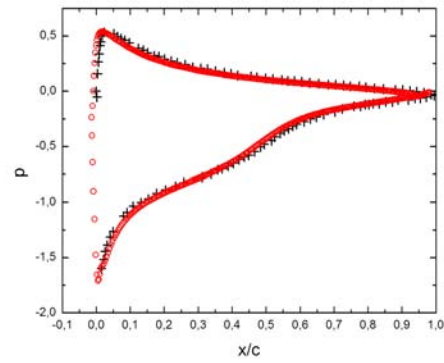
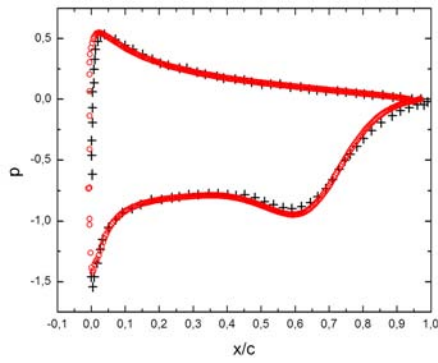
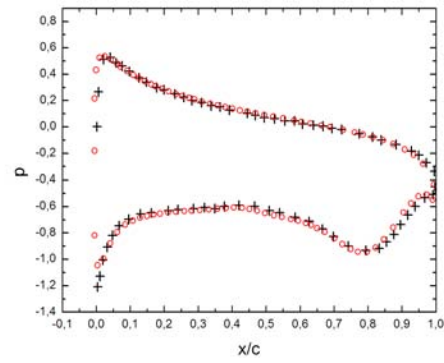
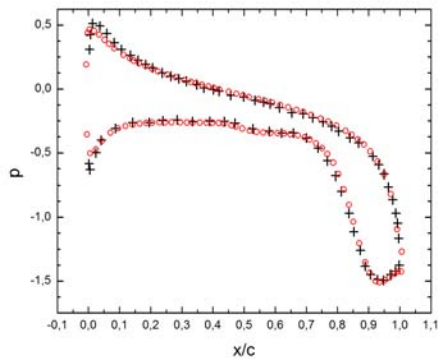
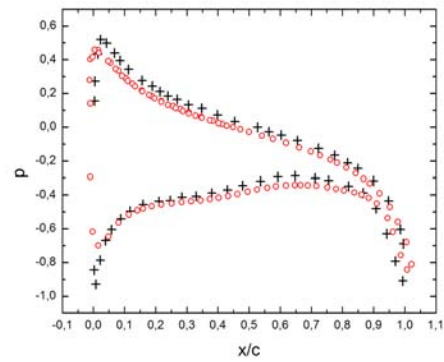
(a)  $t=0.5$ (b)  $t=1$ (c)  $t=2$ (d)  $t=3$ (e)  $t=4$ (f)  $t=6$ 

Figure 3.18: Surface pressure distribution over the airfoil surface at (a)  $t=0.5$ , (b)  $t=1$ , (c)  $t=2$ , (d)  $t=3$ , (e)  $t=4$ , (f)  $t=6$ . The results are for the fixed airfoil at  $\alpha = 20^\circ$ ,  $Re = 800$ . The open circles represent the output of the  $N\epsilon\kappa\tau\alpha r$  solver and the crosses are extracted from [17].

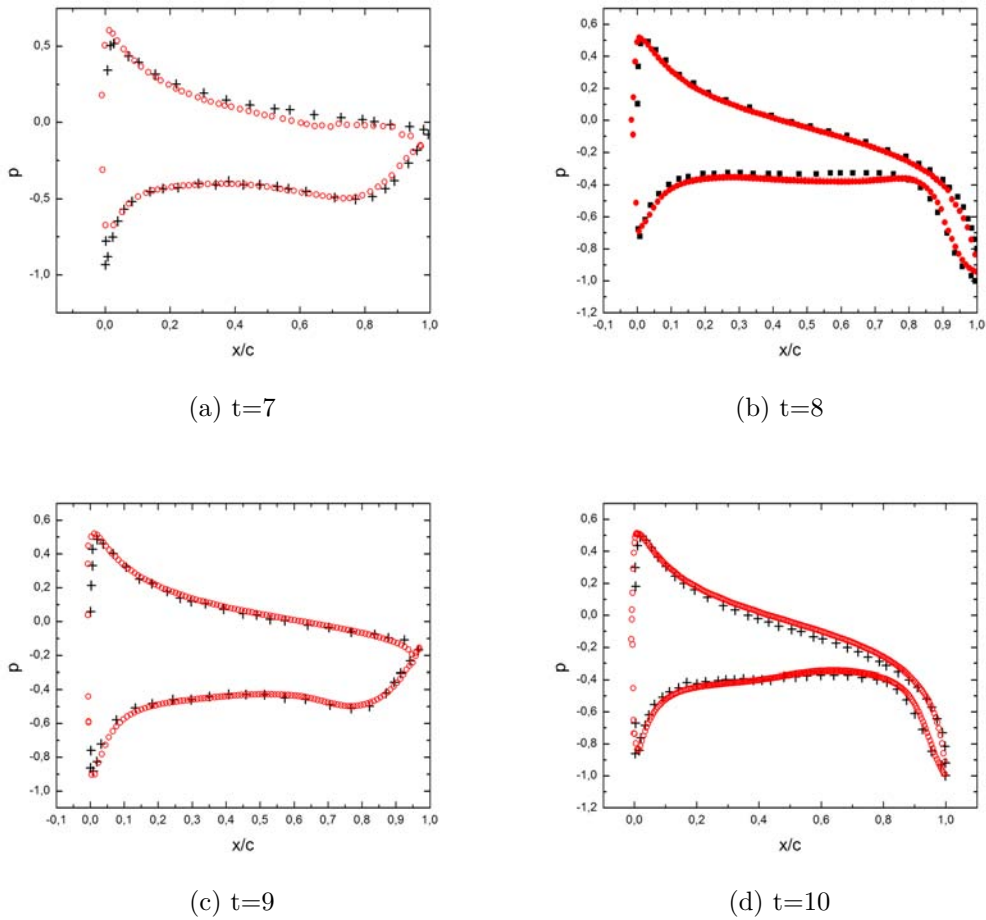


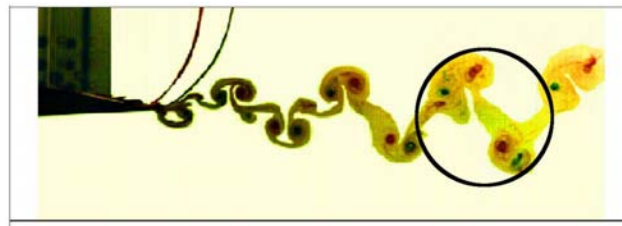
Figure 3.19: Surface pressure distribution over the airfoil surface at (a)  $t=7$ , (b)  $t=8$ , (c)  $t=9$ , (d)  $t=10$ . The results are for the fixed airfoil at  $\alpha = 20^\circ$ ,  $Re = 800$ . The open circles represent the output of the  $N\epsilon\kappa\tau\sigma r$  solver and the crosses are extracted from [17].

via a hyperbolic tangent distribution, and the outer region is left unchanged. The viscous terms of the Navier-Stokes equations are evaluated using second-order central differences in space, and the inviscid terms are evaluated using a third-order upwind scheme. The time discretization follows a second-order Crank-Nicolson scheme [23]. In the experimental study conducted by *Lai & Platzer* [10] water-tunnel tests were conducted on an airfoil forced to oscillate sinusoidally in heave for different values of frequency and amplitude. Dye flow visualization was also conducted in the midspan plane of the airfoil. The first simulation is done at  $Re = 2 \times 10^4$ , mean angle of attack  $\alpha = 0^\circ$ , heaving amplitude  $h = 0.0125$  and reduced frequency  $k = 4$ . To compare the results obtained in [10] and in [23] to the ones obtained using the *NekTar*-solver, a region of the wake is indicated by a circle in Fig. 3.20. The experimental results conducted in [10] (Fig. 3.20a) show that the wake is composed of two rows of vortices. These rows are created as the result of the shedding in the wake of two vortices per oscillation cycle. The numerical results from [23] (see Fig. 3.20b) are obtained using two solvers, a laminar one and a turbulent one. The numerical simulations of [23] show that the turbulent solver is unable to capture the experimentally obtained wake. According to *Young* [23] this may be due to the fact that the wake is generated by a laminar process. One can also argue that the turbulent solver is not efficient and is unable to reproduce the wake observed. Since *NekTar* is a DNS-solver, there are no assumptions about the nature of the flow involved in the calculations (laminar or turbulent) and the wake obtained experimentally in [10] is reproduced in all its details (see Fig. 3.20c).

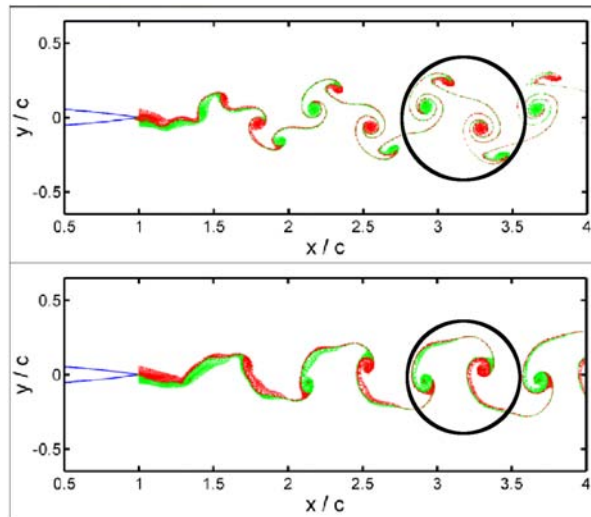
For the second simulation the heaving amplitude is increased to  $h = 0.025$  and all the other parameters are kept constant. Again we compare our simulation results to the experimental results in [10] and the computational results of [23] (see Fig. 3.21). A region of the wake is indicated by a circle in Fig. 3.21 for comparison. In [23] the author needed to run two simulations at two different heaving amplitudes  $h = 0.025$  and  $h = 0.02$  (see Fig. 3.21b and Fig. 3.21c) as the numerical code used by *Young* could not reproduce the experimental results obtained in [10] at  $h = 0.025$ . And again the turbulent solver used by *Young* could not reproduce the experimental results. Our simulations on the other hand (see Fig. 3.21d) were able to reproduce the experimentally obtained wake with the same parameters used in [10], namely  $k = 4.0$  and  $h = 0.025$  and there was no need to change the value of the heaving amplitude.

### 3.3.2 Forces validation

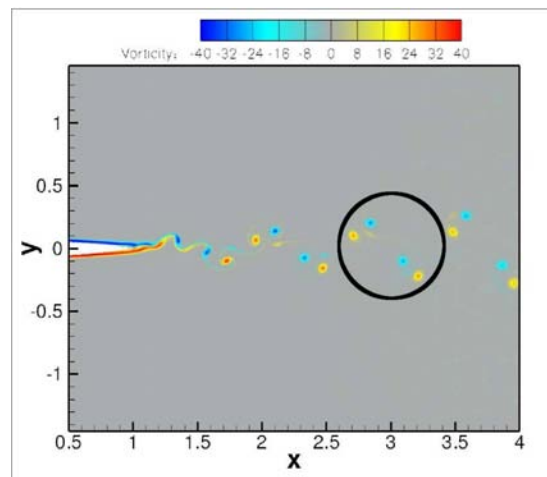
We validate the forces obtained using the *NekTar*-solver by comparing them to the computational results presented in [13, 23]. *Lian & Shyy* [13] used a pressure-based algorithm to solve the full Navier-Stokes equations in curvilinear coordinates. The convection terms are discretized using a second-order upwind scheme and the diffusion terms are discretized using a second-order central differ-



(a)



(b)



(c)

Figure 3.20: Comparison of the vorticity visualization of the wake. (a) Experimental results from [10] obtained using dye injection. Red dye was injected through the upper surface close to the trailing-edge while a green dye was injected through the lower surface close to the trailing-edge. (b) Vorticity distribution obtained using numerical simulations from [23], where scalar particles representing the dye in the experiments were released from a vertical plane at the trailing-edge of the airfoil. A laminar solver (upper frame) and a turbulent solver (lower frame) are used. (c) Vorticity distribution using the  $N\epsilon\kappa\tau\alpha R$ -solver. The flow parameters for all cases are  $Re = 2 \times 10^4$ ,  $\alpha = 0^\circ$ ,  $h = 0.0125$  and  $k = 4.0$ .

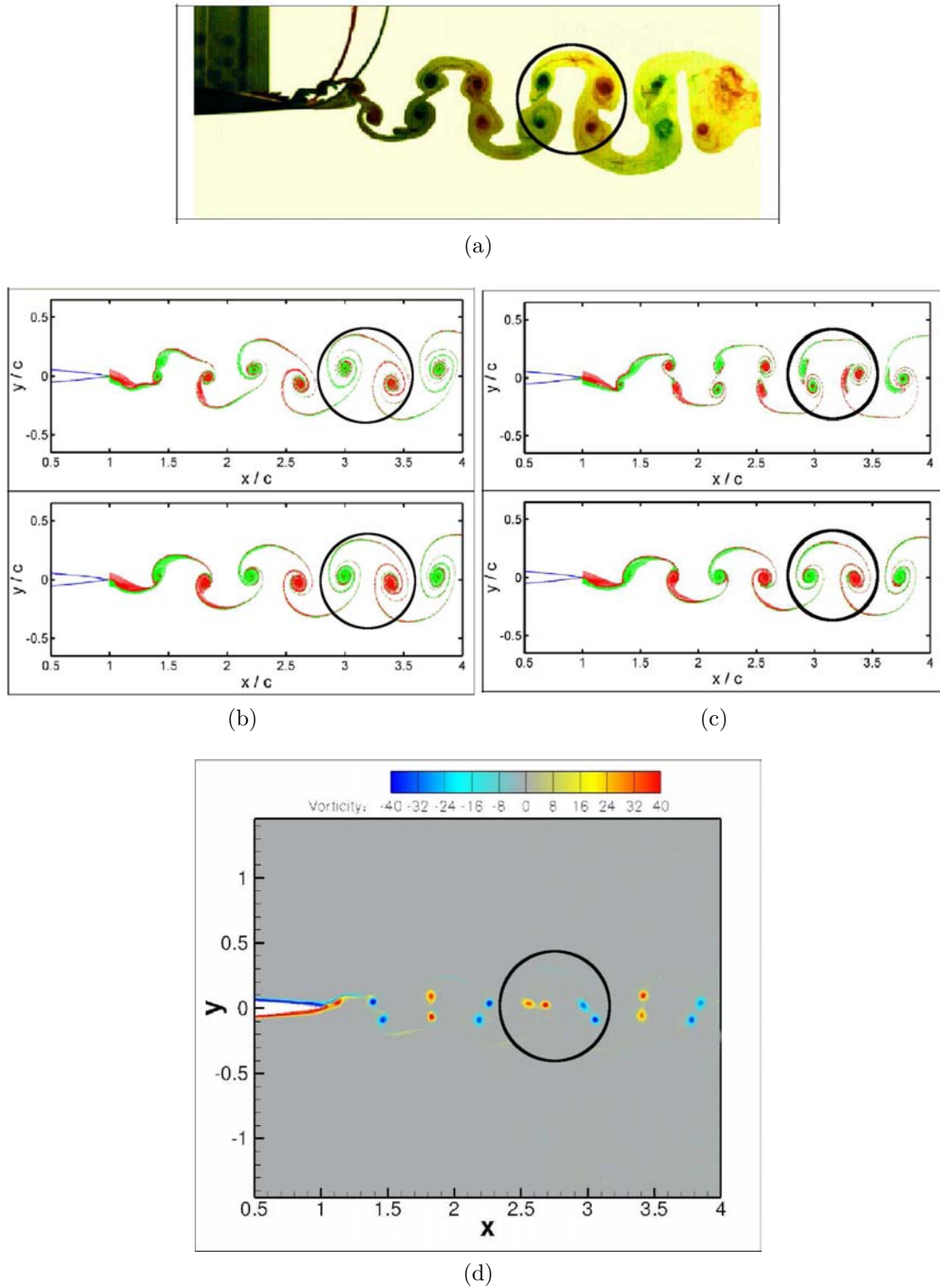


Figure 3.21: Comparison of the vorticity visualization of the wake. (a) Experimental results [10] at  $h = 0.0125$ . (b) Numerical simulations obtained using a Navier-Stokes code [23]: with a laminar solver (upper frame) and a turbulent solver (lower frame) at  $h = 0.025$ . (c) Numerical simulations from [23]: with a laminar solver (upper frame) and a turbulent solver (lower frame) at  $h = 0.02$ . (d) Vorticity distribution obtained using the *NekTar*-solver at  $h = 0.0125$ . For all cases  $Re = 2 \times 10^4$ ,  $\alpha = 0^\circ$ , and  $k = 4.0$ .

	mean $C_L$	Stdv $C_L$	mean $C_D$	Stdv $C_D$
$h = 0.0125$				
Young [23]	0.01768 *	0.75016 *	0.02252	0.00424
Lian & Shyy [13]	0.01768 *	0.75016 *	0.02338	0.00396
Present study	0.0098	0.7959	0.023	0.00436
$h = 0.025$				
Young [23]	0.0521 *	1.6229 *	0.00687	0.01645
Lian & Shyy [13]	0.0521 *	1.6229 *	0.00803	0.01624
Present study	0.04572	1.5628	0.00634	0.0186

Table 3.3: Comparison of mean and standard deviations of the lift, and drag coefficients. The comparison is between the present study and the previously published results in [13, 23] for a heaving airfoil at ( $h = 0.0125$ ,  $k = 4.0$ ) and ( $h = 0.025$ ,  $k = 4.0$ ). *Stdv* denotes the standard deviation from the mean value. \* denotes that the results concerning  $C_L$  are assumed to be identical for both references [13, 23]. This is the result from a comparison plot from [13] where the  $C_L$  values are identical to the one obtained by [23].

ence scheme. The time discretization is achieved using a second-order backward scheme. The numerical approach of *Young* [23] was introduced earlier in this chapter (Section 3.3.1). The comparison of the lift and drag mean values and standard deviations is presented in Table 3.3. The  $N\epsilon\kappa\tau\alpha r$ -solver compares very well with the numerical results obtained in [13, 23]. These good results give confidence in the ability of the  $N\epsilon\kappa\tau\alpha r$ -solver in calculating the forces over heaving airfoils.

### 3.4 Conclusion

In this Chapter, the  $N\epsilon\kappa\tau\alpha r$ -solver simulations were validated for motionless cylinders subjected to steady and unsteady flows. The results compare very well with previously published studies. The simulations were also validated for motionless airfoils with steady and unsteady flows and finally for the more complicated case of heaving airfoils. The  $N\epsilon\kappa\tau\alpha r$ -solver was able to reproduce both flow configuration and Strouhal numbers for a cylinder geometry. This gives confidence in using the solver to determine the frequency of vortex shedding. This is very important as we will use the solver in Chapter 5 and Chapter 6 to study the shedding frequency of heaving airfoils. This study requires the determination of the shedding frequency with very high precision.

The  $N\epsilon\kappa\tau\alpha r$ -solver was also validated for a motionless airfoil, with both steady and unsteady flow conditions. The solver was able to reproduce both flow configurations and surface pressure distributions over the airfoil. The results

agree qualitatively and quantitatively with previously published studies. Finally, the solver was validated for the heaving airfoil configuration at a relatively high Reynolds number ( $Re = 2 \times 10^4$ ). The solver reproduced previously published experimental and computational results with very good agreement. Moreover, the validation was also achieved for the forces produced by the airfoils and a very good agreement was found with numerical results obtained from the literature. In conclusion, the *Nεκταρ*-solver is able to reproduce experimental and computational results, both qualitatively and quantitatively, at high spatial and temporal resolution.

## Bibliography

- [1] E. Berger and R. Wille. Periodic Flow Phenomena. *Ann. Rev. Fluid Mech.*, 4:313–340, 1972.
- [2] B. S. Carmo, S. J. Sherwin, P. W. Bearman, and R. H. J. Willden. Wake transition in the flow around two circular cylinders in staggered arrangements. *J. Fluid Mech.*, 597(1):1–29, 2008.
- [3] A. N. Cookson, D. J. Doorly, and S. J. Sherwin. Mixing Through Stirring of Steady Flow in Small Amplitude Helical Tubes. *Ann. Biomed. Eng.*, 37: 710–721, 2009.
- [4] M. Coutanceau and R. Bouard. Experimental Determination of the Main Features of the Viscous Flow in the Wake of a Circular Cylinder in Uniform Translation. Part1: Steady Flow. *J. Fluid Mech.*, 79:231–256, 1977.
- [5] S. C. J. Dennis and G. Z. Chang. Numerical Solutions for Steady Flow Past a Circular Cylinder at Reynolds Numbers up to 100. *J. Fluid Mech.*, 42: 471–489, 1970.
- [6] F. E. Fish and J. Rohr. Review of dolphin hydrodynamics and swimming performance. Report 1801, SPAWARS System Center Technical Report, 1999.
- [7] H. Gopalan. *Numerical Modeling of Aerodynamics of Airfoils of Micro Air Vehicles in Gusty Environment*. PhD thesis, University of Akron, 2008.
- [8] T. J. R. Hughes, W. K. Liu, and T. K. Zimmerman. Lagrangian Eulerian finite element formulation for incompressible viscous flows. *Computer Methods in Applied Mechanics and Engineering*, 29(3):329–349, 1981.
- [9] K. D. Jones and M. F. Platzer. Experimental Investigation of the Aerodynamic Characteristics of Flapping-Wing Micro Air Vehicles. In *41st Aerospace Sciences Meeting and Exhibit*, volume 0418, pages 1–11, Reno-Nevada, 6-9 January 2003. AIAA.
- [10] J. C. S. Lai and M.F. Platzer. Jet Characteristics of a Plunging Airfoil. *AIAA J.*, 37(12):1529–1537, 1999.
- [11] G. C. Lewin and H. Haj-Hariri. Modelling thrust generation of a two-dimensional heaving airfoil in a viscous flow. *Journal of Fluid Mechanics*, 492:339–362, 2003.
- [12] L. Li, S. J. Sherwin, and P. W. Bearman. A moving frame of reference algorithm for fluid/structure interaction of rotating and translating bodies. *Int. J. Numer. Meth. Fl.*, 38:187–206, 2002.

- [13] Y. Lian and W. Shyy. Aerodynamics of low reynolds number plunging airfoil under gusty environment. In *45th AIAA Aerospace Sciences Meeting and Exhibit. 8-11 January 2007, Reno, Nevada.*, 2007.
- [14] M. N. Linnick and H. F. Fasel. A high-order immersed interface method for simulating unsteady incompressible flows on irregular domains. *Journal of Computational Physics*, 204(1):157–192, 2005.
- [15] C. Liu, X. Zheng, and C. H. Sung. Preconditional Multigrid Methods for Unsteady Incompressible flows. *J. Comput. Phys.*, 139:35–57, 1998.
- [16] I. Lomtev, R. M. Kirby, and G. E. Karniadakis. A Discontinuous Galerkin ALE Method for Compressible Viscous Flows in Moving Domains. *J. Comp. Phys.*, 155(1):128–159, 1999.
- [17] A. V. Shatalov. *Numerical Simulation of Incompressible Laminar Flows Using Viscous-Inviscid Interaction Procedure*. PhD thesis, University of California, Division Mechanical and Aeronautical Engineering, 2006.
- [18] N. Takashi and T. J. R. Hughes. An arbitrary Lagrangian-Eulerian finite element method for interaction of fluid and a rigid body. *Computer Methods in Applied Mechanics and Engineering*, 95:115–138, 1992.
- [19] D. J. Tritton. Experiments on the Flow Past a Circular Cylinder at Low Reynolds Numbers. *J. Fluid Mech.*, 6:547–567, 1959.
- [20] I. H. Tuncer and M.F. Platzer. Computational Study of Flapping Airfoil Aerodynamics. *Journal of Aircraft*, 37:514–520, 2000.
- [21] C. S. Venkatasubban. A new finite element formulation for ALE (Arbitrary Lagrangian Eulerian) compressible fluid mechanics. *International Journal of Engineering Science*, 33(12):1743–1762, 1995.
- [22] M. R. Visbal and D. V. Gaitonde. On the use of higher-order finite-difference schemes on curvilinear and deforming meshes. *J. Comput. Phys.*, 181:155–185, 2002.
- [23] J. Young. *Numerical simulation of the unsteady aerodynamics of flapping airfoils*. PhD thesis, School of Aerospace, Civil and Mechanical Engineering. The University of New South Wales. Australian Defence Force Academy, May 2005.



## Chapter 4

# High-order Numerical Simulations Of The Flow Around A Heaving Airfoil <sup>1</sup>

We simulate the incompressible, viscous flow over a two-dimensional NACA 0012 airfoil oscillating in heave at mean incidences  $12^\circ < \bar{\alpha} < 20^\circ$  and Reynolds numbers  $800 \leq Re \leq 10^4$ . The two-dimensional Navier-Stokes equations are solved using a Spectral/*hp* Element Method for the spatial discretization and a high-order splitting scheme for the evolution in time. A moving-frame of reference technique accounts for the airfoil motion. We consider the effects on the aerodynamical flow and the force coefficients caused by the variation of the mean incidence, the Reynolds number and the sinusoidal heave motion of the airfoil. The numerical simulations are in good agreement with previously published experimental and computational work, in particular the increase in the force coefficients due to the increase in the Reynolds number and/or the mean incidence are confirmed by the present study. Furthermore, we present here new details of the spatio-temporal non-linear flow pattern evolution where for the first time the Spectral/ *hp* Element Method associated with the moving frame of reference is used for this kind of flow.

---

<sup>1</sup>Submitted to publication and currently under review as W. MEDJROUBI, B. STOEVE SANDT, B. CARMO and J. PEINKE: *High-order Numerical Simulations Of The Flow Around A Heaving Airfoil* in *Computers and Fluids*

## 4.1 Introduction

Many experimental and computational studies are dedicated to the investigation of the unsteady flow over streamlined bodies, particularly airfoils. Oscillating and translating airfoils with their resulting fluctuating aerodynamic loads constitute a very important category of these flow problems. The loads result from fluctuations (or unsteadiness) of the surrounding flow or the movement of the airfoil itself. Our study has been motivated by applications of wind turbines and helicopters, where turbulent wind conditions lead to such situations.

Unsteady flow conditions are generally associated with very interesting, complex, non-linear phenomena such as flutter, vortex-induced vibrations, and dynamic stall. The understanding and prediction of the dynamic stall phenomenon was the motivation of more than three decades of theoretical, computational and experimental work [25, 26]. Unsteady flows over an airfoil include heaving, pitching and flapping airfoils.

In their experimental work *Ohmi et al.* [30] conducted water tank experimental studies of the incompressible and viscous flow around an elliptic airfoil oscillating and translating at large incidences, using solid and electrochemical tracers. They also performed 2D numerical simulations, which were based on a finite-difference approximation of the unsteady two-dimensional Navier-Stokes equations. They investigated the variation of the following parameters, Reynolds number:  $1500 \leq Re \leq 10^4$  (where  $Re = U_0 c \nu$ ,  $c$  is the airfoil chord length, and  $U_0$  is the free-stream velocity), reduced frequency  $f^* = fc/U_0$ :  $0.2 \leq f^* \leq 2$ , mean incidence  $\bar{\alpha}$ :  $15^\circ \leq \bar{\alpha} \leq 30^\circ$  and angular amplitude of the oscillations  $\Delta\alpha$ :  $7^\circ \leq \Delta\alpha \leq 15^\circ$ . The authors found that the effects of  $f^*$  and the product  $f^* \Delta\alpha$  were more significant than changing the Reynolds number. They extended their work in [31], where the effects of the pitching axis and of a non-elliptic cross-section airfoil (NACA0012) were included. They concluded that the aerodynamic characteristics of an unsteady airfoil oscillating at large incidences are rather sensitive to any variation of the flow conditions.

In a computational study *Akbari & Price* [2] investigated the incompressible and viscous flow over a 2D elliptic airfoil translating and oscillating in pitch at large angles of attack, with mean angles of attack up to  $30^\circ$ . They solved the Navier-Stokes equations in a vorticity-stream-function form using a time-marching approach. They also investigated the effects of the reduced frequency of oscillation, the mean angle of attack, the pitch-axis location, and the thickness of the airfoil at  $Re = 3000$ . The authors observed that the frequency of oscillation has a significant effect on the flow structure at higher reduced frequencies  $1 \leq f^* \leq 2$ . At these reduced frequencies the vortices are shed from the upper surface rather than from the trailing-edge and this shedding is controlled by the rotational motion. Furthermore, the formation of alternate vortices at the trailing-edge is observed during both the up and downstroke of the elliptic airfoil. The mean angle of attack was found to have an effect on both the vortex formation and the

wake pattern. Moving the pitch-axis from the mid- to the quarter-chord, did not influence the flow characteristics, although it causes the vortices to be stronger, at both the leading and trailing edge.

Hovering (simultaneously pitching and heaving airfoils) is considered by *Gustafson & Leben* in [16] in an attempt to compare computational results to the experimental results of *Freymuth* [13]. The governing equations are formulated in terms of the stream-function and the vorticity, where a Poisson equation is solved for the stream function by a covariant multigrid solver, and the vorticity transport equation is solved by an ADI time-marching scheme. Three hovering modes are classified with respect to the average angle of attack and the phase difference between the pitching and the heaving. Excellent spatial and temporal correlation was found with the experimental results in [13]. The authors concluded that high-thrust and high-lift vortical signatures can be obtained using a single hovering airfoil, therefore there is no need to involve more complicated phasing of multiple wing beats in dragonflies. The explanation for these results is attributed by the authors to the right *tuning* of the airfoil, which means executing short plunge combined with large pitch.

An interesting configuration of an immersed plunging and heaving airfoil is studied by *Spagnolie & al.* in a recent contribution [35]. The authors studied through experiments and computational simulations a freely moving wing which can pitch passively as it is actively heaved in a fluid in order to investigate the locomotion regimes and capabilities of such flows common in aquatic animals propulsion [32]. Numerical simulations were performed by coupling the Navier-Stokes equations in two dimensions to the equations for lateral and rotational accelerations of an elliptical airfoil. The passive pitch motion is represented by the restoring force of a spring mounted system. The governing parameters are the Reynolds number based on the heaving frequency ( $Re_f = \rho UL/\mu = \rho afL/\mu$ , of the order of  $10^5$  for the experiments and 50 for the computations.  $f$  is the imposed heaving frequency and  $L$  is the half chord of the airfoil), the heaving amplitude  $a$ , the elliptic aspect ratio  $e = b/a$  (equal to the ratio of the minor and the major axes of the elliptical airfoil), the spring constant  $\kappa$  and the mass ratio  $M$ . The results revealed different dynamical regimes with respect to the heaving frequency, among which two are novel. First, a reversal in the direction of lateral motion as the heaving increases beyond a critical frequency. Second, a bistable, hysteretic regime where the airfoil can move either backward or forward depending on its history. These new regimes were also verified experimentally by the authors.

For the case of a pure heaving (flapping or plunging) motion there exist numerous experimental and computational studies [21, 37]. Due to the fact that an airfoil forced to oscillate in heave can produce thrust at certain combinations of the heaving amplitude and frequency, most of the research is dedicated to the determination of these combinations [12, 36]. As applications areas for flapping airfoils we cite the investigation of animal propulsion techniques [18], Micro-Air

Vehicles (MAV) industry [24] and wind turbine rotor loading and dynamics [17]. Our aim in implementing pure heaving motion in this study is however not motivated by thrust production optimization, but mainly to investigate the effects of varying the governing parameters on the flow structure.

*Levin & Haj-Hariri* presented in [22] a numerical model for the two-dimensional and viscous flow around an elliptic airfoil subjected to a prescribed heaving motion. The viscous term of the vorticity transport equation is discretized using a fourth-order centered differencing and a third-order upwind scheme is used for the advection terms. Time stepping is achieved using a second-order Runge-Kutta scheme. Vortex patterns, flow characteristics and power coefficients are examined over a range of reduced frequencies ( $2.0 \leq k \leq 10.0$ , where  $k = 2\pi fc/U_0$ ) and amplitudes ( $0.8 \leq h^* \leq 1.5$ , where  $h^* = h/c$ ) at a mean angle of attack  $\bar{\alpha} = 0$  and  $Re = 500$ . The authors found that the wake patterns depend on whether the leading-edge vortex (or LEV) is shed or not and on how it interacts with the trailing-edge vortex (TEV). When the LEV is shed, it can either strengthen the TEV, resulting in a pair of vortices shed per oscillation cycle, or pair up with the TEV, resulting in two pairs of vortices shed per oscillation cycle. The LEV dynamics are also correlated to the heaving efficiency of the airfoil, as significant gain in efficiency occurs when the LEV remains attached during the duration of each stroke. The authors pointed out that high thrust coefficients and propulsion efficiencies are achieved as a result of the positive reinforcement of the TEV by the LEV as found in [5].

The motion of the airfoil can be coupled to the flow, thus the motion of the flow is not prescribed, but is instead determined by the fluid forces acting on it. In [3] an implicit method is proposed for computing coupled airfoil-flow dynamics using a plunging and rising elliptical airfoil in order to probe its instability to horizontal motions. For both airfoil motions (plunging and rising), it is found that a linear instability to the horizontal motion is present at a critical Reynolds number, which leads to a stable oscillatory state. The pressure forces are found to have a destabilizing role, while the viscous forces have a stabilizing role. The oscillatory state time scales are set either by the external plunge motion or by the intrinsic flow-airfoil coupling.

With the interest shifted towards numerical solutions of the Navier-Stokes equations around aerodynamic configurations, it has been recognized that higher-order accurate approximations significantly enhance the quality of simulation results and improve the predictive simulation capability for many applications [7, 19]. Computational Fluid Dynamics (CFD) methods are commonly second-order accurate in both time and space, so the increase of the accuracy levels requires the use of higher-order methods. The idea behind using high-order numerical methods is to achieve high accuracy, resolving all the flow length scales at a reduced cost and avoiding the extra costs of remeshing or excessive grid resolution [29].

Global spectral methods have been extended to multi-domains (spectral el-

ements) to provide a better geometric flexibility. Spectral/ $hp$  Element Methods combine the characteristics and the advantages of both finite elements and spectral methods. Unlike pure spectral methods and finite elements methods, Spectral/ $hp$  Element Methods allow the use of two refinement techniques simultaneously: the  $h$ -refinement, denoting the increase of the number of elements, and the  $p$ -refinement, denoting the increase of the polynomial order of the approximation [19].

We use for the first time the Spectral/ $hp$  Element Methods combined with a moving-frame of reference technique to investigate the problem of the flow around an oscillating airfoil in an attempt to achieve a better accuracy than that obtained using lower-order numerical methods. In this scope all the simulations presented in this work are Direct Numerical Simulations (DNS), in order to capture all the flow details and particularly the spatio-temporal flow evolution. Our choice of the numerical method is also based on the possibility to obtain highly accurate temporal and spatial data that can be used in applications such as turbulence characterization and non-linear analysis of the airfoil response to forced oscillations. To the authors knowledge this is the first time where the boundary-layer temporal development is investigated for a heaving airfoil using a numerical approach, as most of the studies for this type of motion were concerned with the wake configuration [38], [4], [11].

In this paper, we study the particular case of an incompressible viscous flow over a two-dimensional NACA0012 airfoil forced to oscillate in a sinusoidal heave motion. In Section 4.2 the numerical method is presented and validated, the results of the spatio-temporal flow pattern generated by a motionless airfoil are presented in Section 4.3.1 and Section 4.3.2. In Section 4.4 a heaving airfoil is considered at different mean incidences and Reynolds numbers. The parameters were chosen to exhibit the effects of varying the mean angle of attack and the Reynolds number on the flow pattern and on the aerodynamical coefficients.

## 4.2 The numerical method

The governing Navier-Stokes equations of the viscous incompressible flow studied in this investigation are written in terms of the following nondimensional quantities:

$$x^* = \frac{x}{c} \quad , \quad y^* = \frac{y}{c}, \quad (4.1)$$

$$t^* = \frac{tU_0}{c} \quad , \quad u^* = \frac{u}{U_0}, \quad (4.2)$$

$$v^* = \frac{v}{U_0} \quad , \quad p^* = \frac{p}{\rho U_0^2}, \quad (4.3)$$

where the airfoil chord length  $c$  and the free-stream velocity  $U_0$  are used to obtain

the nondimensional velocity  $u^* = (u, v)$ . The static pressure  $p$  is scaled by the fluid density  $\rho$ .  $t$  is the time,  $Re = \rho U_0 c / \mu$  is the Reynolds number, and  $\mu$  is the dynamic viscosity of the fluid. For simplicity, the sign  $*$  is dropped during the remainder of this paper.

In the framework of the Spectral /hp Element Method the physical domain and the governing equations have to be spatially and temporally discretized. The spatial discretization involves the division of the physical domain into triangular and/or quadrilateral subdomains for 2D configurations. Within each subdomain/element a spectral expansion in the form of Jacobi polynomials of mixed weight and of order  $p$ , is used to represent the solution variable [19]. The temporal discretization is achieved using a splitting scheme [20]. In the following, the polynomial expansions and the temporal splitting scheme are introduced.

## Polynomial bases/expansions

For a polynomial expansion a basis  $u_{m,n}(r, s)$  needs to be defined in order to approximate the function  $f(x, y)$  over  $i$  triangular subdomains by a  $C^0$  continuous expansion of the form (for rectangular subdomains see [19])

$$f(x, y) = \sum_i^N \sum_m^{N_1} \sum_n^{N_2} u_{m,n}^i u_{m,n}(r(x, y), s(x, y)). \quad (4.4)$$

$u_{m,n}^i$  are the expansion coefficients in the  $i^{th}$  subdomain,  $(x, y)$  are the spatial coordinates and  $(r, s)$  are the local coordinates within the subdomains.  $N$  is the total number of subdomains,  $N_1, N_2$  are the number of the quadrature points in the  $r$  and  $s$  directions respectively. The space spanned by the local coordinates system is defined as

$$L^2 = \{(r, s) | -1 \leq r, s; r + s \leq 0\} \quad (4.5)$$

and the orthogonal expansion bases used are Dubiner's modified bases, defined as

$$u_{m,n} = P_m^{0,0} \left( 2 \frac{(1+r)}{(1-s)} - 1 \right) (1-s)^m P_n^{2m+1,0}(s). \quad (4.6)$$

$P_n^{\alpha,\beta}(x)$  is the  $n^{th}$ -order Jacobi polynomial in the  $[-1, 1]$  interval, which satisfies the orthogonality relationship:

$$\int_{-1}^1 P_m^{\alpha,\beta}(x) P_n^{\alpha,\beta}(x) (1-x)^\alpha (1+x)^\beta dx = \delta_n^m, \quad (4.7)$$

where  $\delta_n^m$  is the Kronecker-delta. The Jacobi polynomial is expressed as follows [1, 15] :

$$P_n^{\alpha,\beta}(x) = \frac{(-1)^n}{2^n n!} (1-x)^{-\alpha} \frac{d^n}{dx^n} [(1-x)^{\alpha+n} (1+x)^{\beta+n}], \alpha, \beta > -1. \quad (4.8)$$

The bases are decomposed into boundary and interior modes (thus allowing the construction of a global  $C^0$  expansion). Integration and differentiation are performed at elemental level, and an elemental mapping which allows the generalisation of the local operations in a standard region to elements of general shapes is defined. To extend these techniques to a  $C^0$  multi-dimensional basis, global operations such as matrix numbering, connectivity and assembly are introduced. The spatial discretisation thereby introduced is independent of the Navier-Stokes solver which will be introduced later in the next Section.

## Temporal discretization

The temporal discretization of the Navier-Stokes equations is achieved via a time-splitting scheme [20], where three steps are required to determine the fields for the next time step using the velocity at the previous time step. This is achieved by writing the Navier-Stokes equation in the form:

$$\frac{\partial \mathbf{u}}{\partial t} = -\nabla p + \nu \mathbb{L}(\mathbf{u}) + \mathbb{N}(\mathbf{u}) \quad (4.9)$$

where  $\mathbb{L}(\mathbf{u}) \equiv \nabla^2 \mathbf{u}$  and  $\mathbb{N}(\mathbf{u}) \equiv -\mathbf{u} \cdot \nabla \mathbf{u}$  are the linear and non-linear operators; respectively. The temporal discretization is achieved via the propagation of  $\mathbf{u}^n$  and  $p^n$  at a time step  $n$ , with a time discretization  $\Delta t$ , to determine  $\mathbf{u}^{n+1}$  and  $p^{n+1}$  at the next time step  $n+1$ . This is expressed as follows

$$\frac{\tilde{\mathbf{u}} - \sum_{q=0}^{J_i-1} \alpha_q \mathbf{u}^{n-q}}{\Delta t} = \sum_{q=0}^{J_e-1} \beta_q \mathbb{N}(\mathbf{u}^{n-q}) \quad (4.10)$$

$$\nabla^2 \bar{p}^{n+1} = \nabla \cdot \left( \frac{\tilde{\mathbf{u}}}{\Delta t} \right) \quad (4.11)$$

$$\frac{\gamma_0 \mathbf{u}^{n+1} - \tilde{\mathbf{u}}}{\Delta t} + \nabla \bar{p}^{n+1} = \frac{1}{Re} \nabla^2 \mathbf{u}^{n+1}, \quad (4.12)$$

where in the first step, the non-linear terms are advanced using a convective form which is integrated in time via a multilevel explicit Adams-Bashforth scheme, represented by the coefficient  $\beta_q$ . An implicit time scheme is used for the integration of the linear terms.  $J_e$  and  $J_i$  are the integration orders of the explicit and implicit schemes; respectively. In the second step, the time-averaged pressure term  $\bar{p}^{n+1}$  is calculated using the divergence of Eq. (4.10). In the third step, the viscous term is treated implicitly via an Euler backwards scheme, where  $\gamma_q$  are appropriately chosen weights. The coefficients  $\alpha_q$ ,  $\beta_q$ , and  $\omega_0$  take different values depending on the integration order [8, 20]. This time integration numerical

scheme requires both velocity and pressure boundary conditions to be defined. High-order Neumann boundary conditions are imposed for the pressure (to ensure that the splitting error is consistent with the overall temporal discretization) as follows:

$$\frac{\partial \bar{p}^{n+1}}{\partial \mathbf{n}} = n \cdot \left\{ \sum_{q=0}^{J_e-1} \beta_q \left[ \mathbb{N}(\mathbf{u}^{n-q}) - \frac{1}{\text{Re}} (\nabla \times (\nabla \times \mathbf{u}^{n-q})) \right] \right\}. \quad (4.13)$$

## Airfoil motion

To implement the airfoil motion the Navier-Stokes equations and the boundary conditions are written in a moving frame of reference. The resulting system is then solved. The method is briefly described here. For further details of the solution procedure we refer the reader to [23].

Let's consider that the body is performing a translational motion  $d$  defined in the fixed or absolute frame of reference  $(X_a, Y_a)$  as  $d = (a(t), b(t))^T$ . A moving frame of reference  $(x_m, y_m)$ , attached to the airfoil is defined as a function of the absolute frame as:

$$X_a = a(t) + x_m \cos \theta + y_m \sin \theta \quad (4.14)$$

$$Y_a = b(t) - x_m \sin \theta + y_m \cos \theta, \quad (4.15)$$

where  $\theta$  is the rotational angle in the moving frame of reference and  $a(t)$  and  $b(t)$  represent the coordinates of the origin of the moving frame of reference in the absolute frame of reference (see Fig. 4.1). In the case of a plunging (non-rotating) airfoil  $\theta$  and  $a(t)$  are constant. Using matrix notation one obtains the transformation from the coordinates in the absolute frame of reference to the moving frame of reference as:

$$\mathbf{X}_a = \mathbf{d} + \mathbf{A} \mathbf{x}_m, \quad (4.16)$$

and the inverse transformation as:

$$\mathbf{x}_m = \mathbf{A}^T (\mathbf{X}_a - \mathbf{d}), \quad (4.17)$$

where  $d = (a(t), b(t))^T$  and  $A$  is the matrix defined as :

$$\begin{pmatrix} \cos \theta & \sin \theta \\ -\sin \theta & \cos \theta \end{pmatrix}$$

Using the definition of the coordinates  $(x_m, y_m)$  given by the equation (4.14), the Navier-Stokes equations are re-written in the moving frame of reference as follows:

$$\nabla \cdot \mathbf{u} = 0, \quad (4.18)$$

$$\frac{\partial \mathbf{u}}{\partial t} + (\mathbf{u} \cdot \nabla) \mathbf{u} = -\nabla \mathbf{p} + \frac{1}{\text{Re}} \nabla^2 \mathbf{u} + \mathbf{Q}(t), \quad (4.19)$$

$$Q(t) = -A^T \ddot{d}, \quad (4.20)$$

where the term  $A^T \ddot{d}$  is the result of the unsteady translational motion, in our case a plunging motion. The boundary conditions are also transformed in the moving frame of reference, and expressions are derived for Neumann and Dirichlet boundary conditions [23].

For the present simulations we have considered the body as being rigid (non-deformable) and forced to oscillate in heave (plunge) motion as illustrated in Figure 4.1. The heave motion is defined as

$$d = y(t) = a \cos(2\omega t). \quad (4.21)$$

where  $y(t)$  is the time-dependent vertical motion,  $a^* = a/c$  is the non-dimensional heaving frequency,  $\omega = 2\pi f$  is the angular frequency, and  $f^* = fc/U_0$  is the non-dimensional heaving frequency (for simplicity, the superscript  $*$  will be dropped in the remainder of this investigation). The airfoil is set at a constant initial angle of attack  $\bar{\alpha} = \theta$  (or mean incidence) and is forced to oscillate vertically in a sinusoidal fashion.

## Aerodynamic forces

The forces and moments are evaluated by calculating their viscous and pressure contributions. The aerodynamic force applied by the flow on the body can be expressed as the integration of local stress as:

$$F = \int_{\omega} \sigma n_A ds_A = - \int_{\omega} p n_A ds_A + \int_{\omega} \tau n_A ds_A = F_{press,A} + F_{visc,A}. \quad (4.22)$$

where  $\sigma = -p\mathbf{I} + \tau$  is the stress tensor,  $\omega$  is the airfoil surface,  $n_A$  is the unit normal on the airfoil,  $F_{press,A}$  are the pressure forces and  $F_{visc,A}$  are the viscous forces. The subscript  $A$  indicates that the quantities are expressed in the absolute frame of reference. The forces in Equation (4.22) are expressed in the moving frame of reference as follows:

$$F = F_{press,A} + F_{visc,A} = A(F_{press,m} + F_{visc,m}). \quad (4.23)$$

where  $A$  is the matrix introduced in Equation (4.17).

The boundary conditions are  $u = 1, v = 0$  on the left, upper, and lower mesh boundaries on Fig. 4.2. On the right boundary  $\partial u/\partial x = 0, \partial v/\partial x = 0$  are employed, and  $u = v = 0$  on the airfoil surfaces (or walls). The pressure boundary-conditions are high-order conditions on all boundaries [20] except at the outflow boundary where  $p = 0$  is considered. The external boundary is located at 17 chord lengths from the trailing-edge of the airfoil.

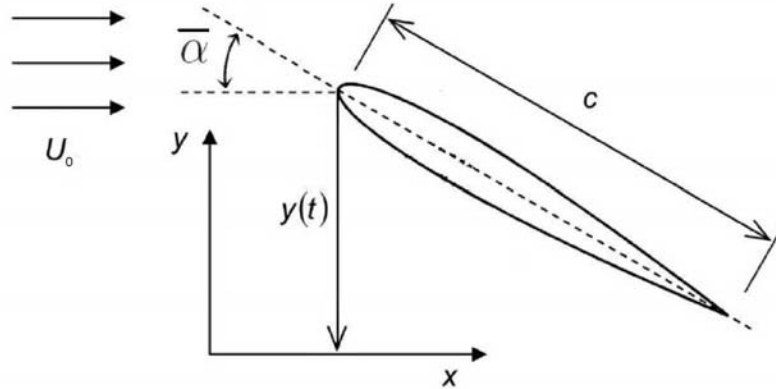


Figure 4.1: Schematic representation of the airfoil for the heave motion, where the vertical displacement  $y(t)$  varies sinusoidally.  $\bar{\alpha}$  is the mean incidence (initial angle of attack),  $U_0$  is the free-stream velocity and  $c$  the chord length.

### The *Nεκταρ* solver

*Nεκταρ* is a general purpose Navier-Stokes solver for simulating incompressible and compressible flows, based on the Spectral/*hp* Element Method [34]. The code was validated for many flow geometries, among those cylindrical [9], helical [10] and rectangular [23].

We validate our simulations for a steady and an unsteady flow over a NACA0012 airfoil against the results obtained by *A.V. Shatalov* and reported in [33]. *Shatalov* used a numerical method based on decomposing the velocity (as a sum of irrotational and rotational components) and on the viscous-inviscid interaction method. We simulate several flow cases at constant angles of attack  $\bar{\alpha}$  as in [33]. All our simulations agree well with *Shatalov*'s results [33]. For brevity we will present here only the results at  $\bar{\alpha} = 20^\circ$  and  $Re = 800$ .

The numerical grid used for the *Nεκταρ* solver is composed of 4220 triangular and quadrilateral elements, the elements density is increased around the airfoil profile and in the wake. A polynomial order of 9 and a time step of  $\Delta t = 10^{-4}$  are used for the validation. Figure 4.2 shows the numerical mesh and Fig. 4.3 shows close-ups of the grid around the leading and trailing edges, respectively.

The unsteady results are compared in terms of the surface pressure distribution (see Figure 4.4) and  $u$ -velocity contours (see Figure 4.5). Comparison has also been done for the  $v$ -velocity and the iso-pressure contours. For the surface pressure distribution, a very good qualitative and quantitative agreement is found between our simulations and the reference. This agreement is confirmed by the  $u$ -velocity contours, where our results reproduced the vortices and the flow details.

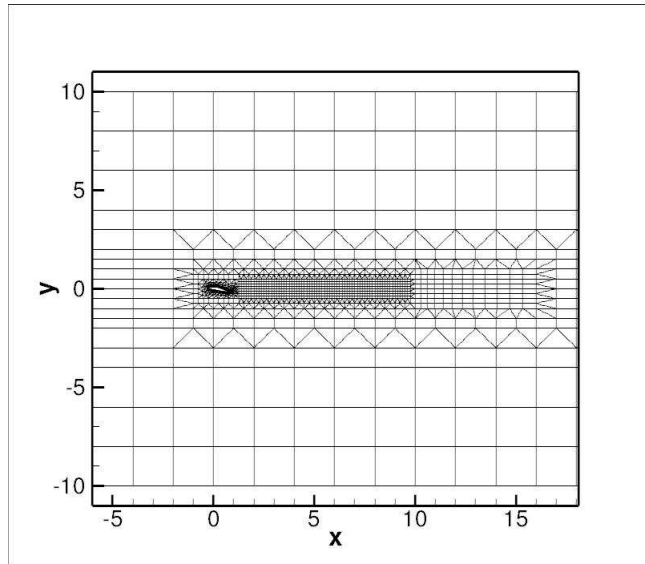


Figure 4.2: The numerical grid used in this investigation. The resolution is increased around the airfoil surface (the boundary-layer region) and in the near wake. The mesh is composed of triangular and quadrilateral elements and the total number of the elements is 4220.

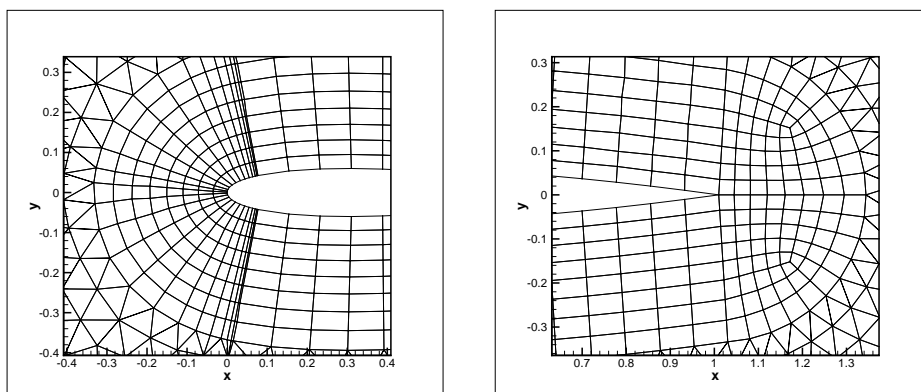


Figure 4.3: Leading- and trailing-edge meshing details.

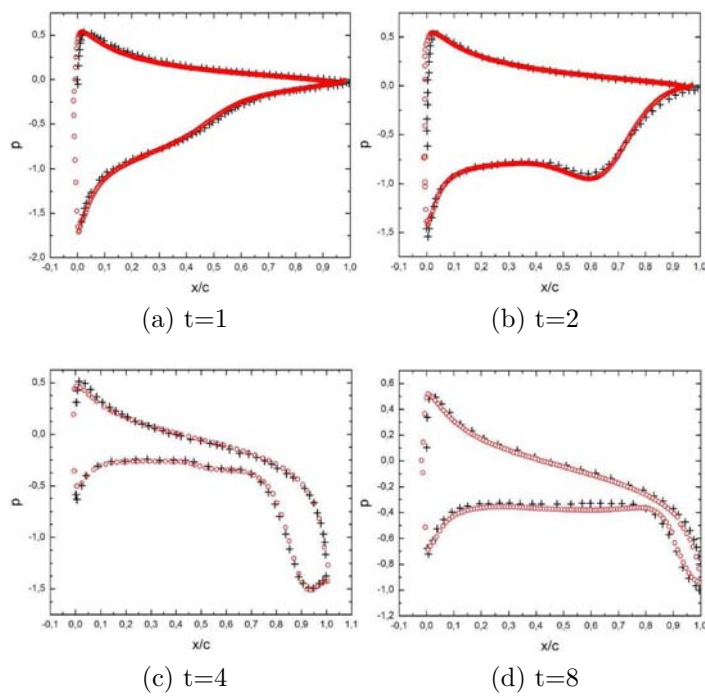


Figure 4.4: Surface pressure distribution at selected time steps for the fixed airfoil at  $\bar{\alpha} = 20^\circ$ ,  $Re = 800$ . The red circles represent the output of the  $N\epsilon\kappa\tau\alpha r$  solver and the crosses are data extracted from reference [33].

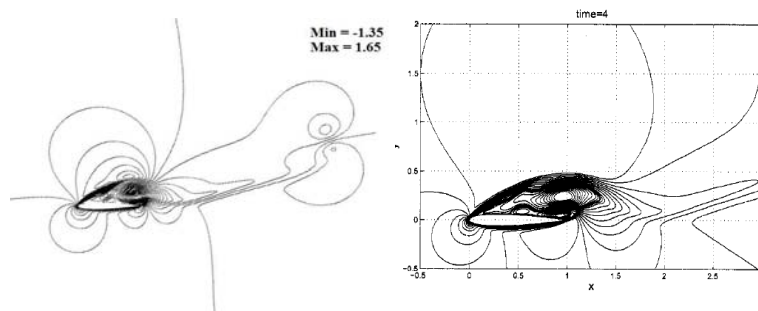
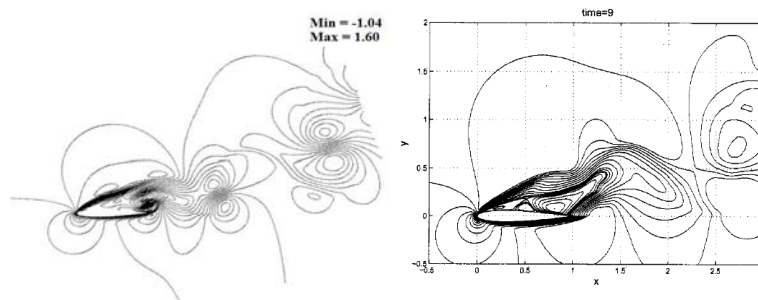
(a)  $t=4$ (b)  $t=9$ 

Figure 4.5:  $u$ -velocity contours at selected times from [33] (right) and with the  $N\epsilon\kappa\tau\alpha r$  solver (left), at  $Re = 800$  and  $\bar{\alpha} = 20^\circ$ . For clarity, our figures are rotated to the same orientation as in [33].

## 4.3 Simulations for a motionless airfoil

### 4.3.1 Fixed airfoil at $\bar{\alpha} = 12^\circ$

The vorticity contours of the flow over a stationary airfoil at the fixed angle of attack  $\bar{\alpha} = 12^\circ$  and  $Re = 4500$  are presented in Figure 4.6. At  $t = 0.6$  (Figure 4.6a) the flow is attached over all the upper surface and at the trailing-edge, an anti-clockwise vortex has already been shed and convected in the near-wake region. A separation bubble (counter-rotating) is formed on the airfoil upper-surface, it grows in size and detaches further as the simulation is advanced to  $t = 2.4$  (Figure 4.6b) under the action of a positive vorticity region that forms under it. In Figure 4.6c, the recirculation region interacts further with the positive vorticity. This results in the creation of clockwise rotating vortices. At  $t = 6$  (Figure 4.6d) the first clockwise vortex is shed in the wake at the trailing-edge, along with an anti-clockwise vortex. At the upper-surface the recirculation region (counter-rotating) continues to interact with the positive vortices and this interaction results in a periodic shedding of a pair of counter-rotating vortices (see Figure 4.6d). We define this periodicity to be spatial, i.e. the spatial distribution of the flow will be the same for each period. The vortex shedding period is found to be  $T_s \approx 1.4$ .

The periodicity is confirmed when plotting the lift and drag coefficients time series (Figure 4.7a). After a short initial transient period, the lift and the drag coefficients vary periodically with time, reaching a stable oscillatory state at  $t \approx 9$ . The mean values of the lift and drag coefficients (excluding the initial transients) are 1 and 0.25; respectively. Thus, the force coefficients time evolution exhibit a periodic behaviour that is in synchronization with the flow temporal development and with the vortex shedding.

The Reynolds number is increased to  $Re = 8000$  and the vorticity contours are the same as at  $Re = 4500$  for  $t < 2.4$  (see Figure 4.8). At  $t = 2.4$  (Figure 4.8a) the recirculating region interaction with the upper-surface separation bubble results in the creation of a pair of clockwise vortices. As the simulation is advanced the vortices are convected downstream over the airfoil (Figures 4.8a, 4.8c), where they interact again with a recirculation region which is rolling-up at the airfoil trailing-edge. This results in opposed signs vortices to be shed in the wake (Figure 4.8d). A new flow feature, which is not observed for  $Re = 4500$ , is the shedding of small scale vortices at the airfoil trailing-edge (Figure 4.8c).

The time series of the lift and the drag coefficients at  $Re = 8000$  exhibit an unsteady behaviour (Figure 4.7b) which can be attributed to the increase of the Reynolds number and thus to the acceleration of the flow over the airfoil.

Here we analyse the effects of increasing the Reynolds number on the aerodynamical coefficients and the flow configuration. First, the lift and the drag coefficients at  $Re = 4500$  are compared to the simulation at  $Re = 8000$  in Figure 4.7, where for  $Re = 4500$  the time evolution is periodic and aperiodic/unsteady

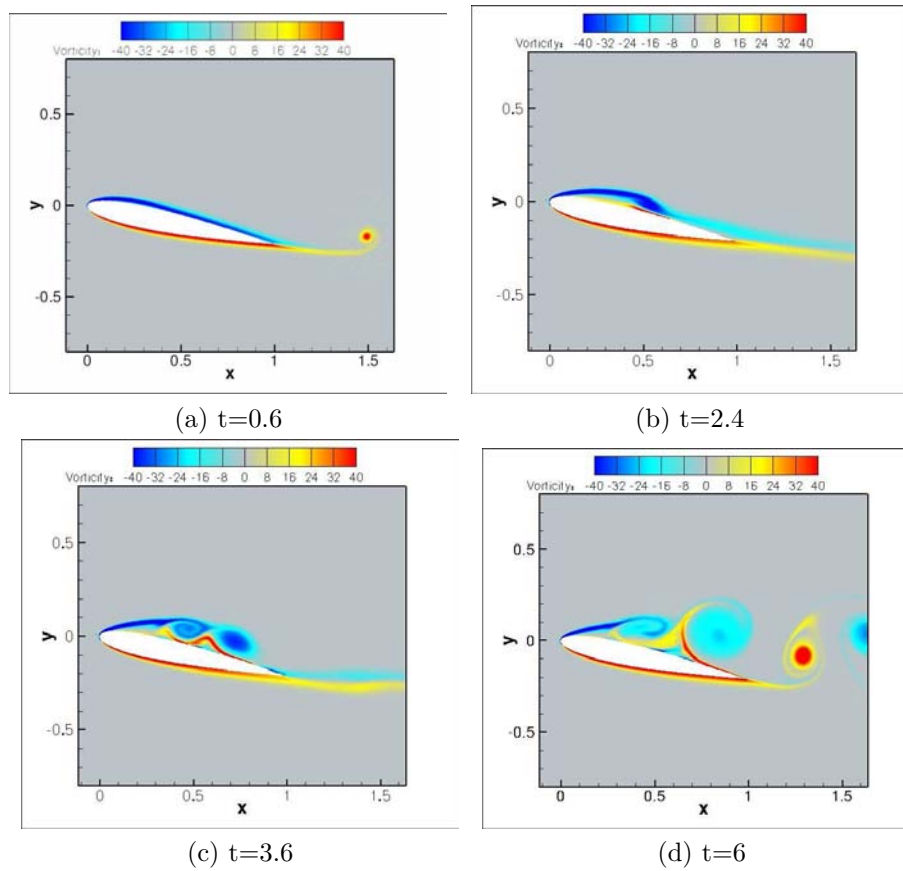


Figure 4.6: Vorticity contours at successive times for a fixed airfoil at  $\bar{\alpha} = 12^\circ$  and  $Re = 4500$ .

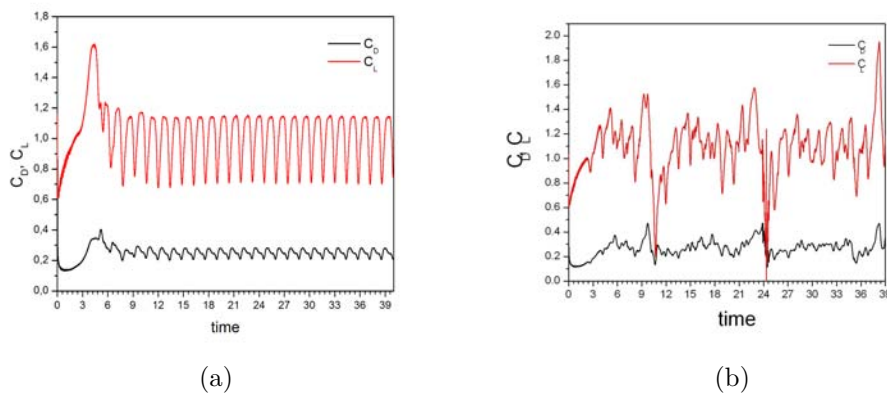


Figure 4.7: Time series of the lift and drag coefficients for a fixed airfoil at  $\bar{\alpha} = 12^\circ$  and (a)  $Re = 4500$  (b)  $Re = 8000$ .

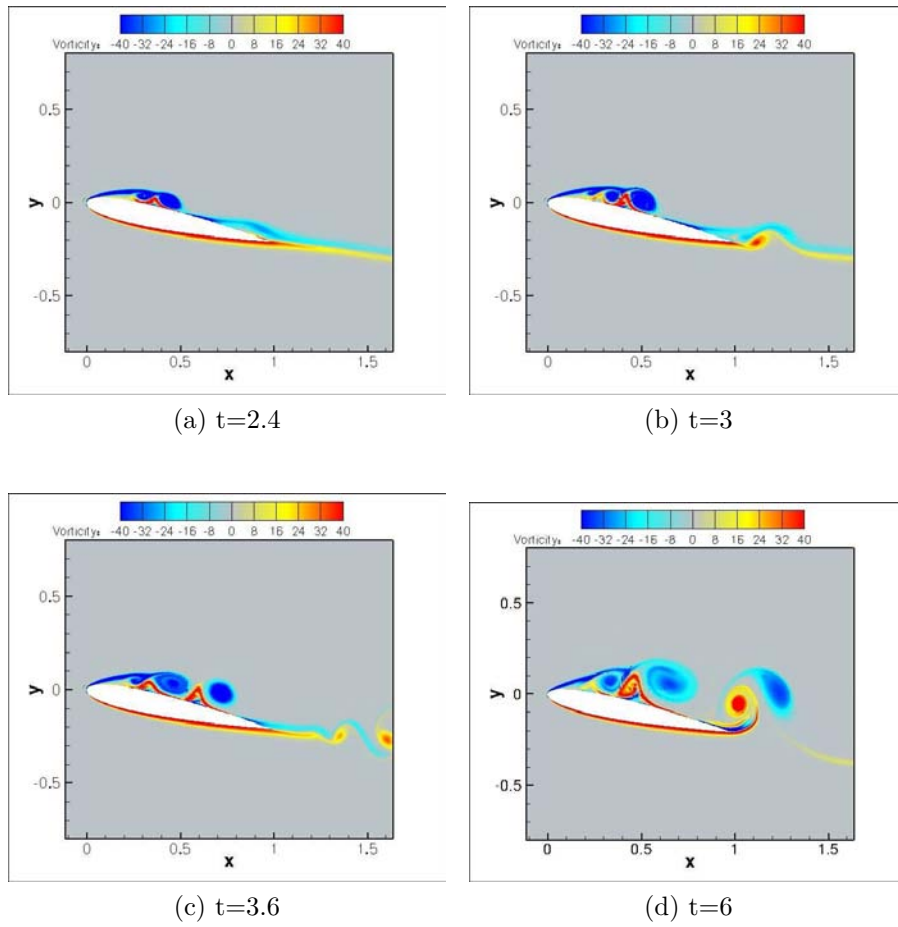


Figure 4.8: Vorticity contours at successive times for a fixed airfoil at  $\bar{\alpha} = 12^\circ$  and  $Re = 8000$ .

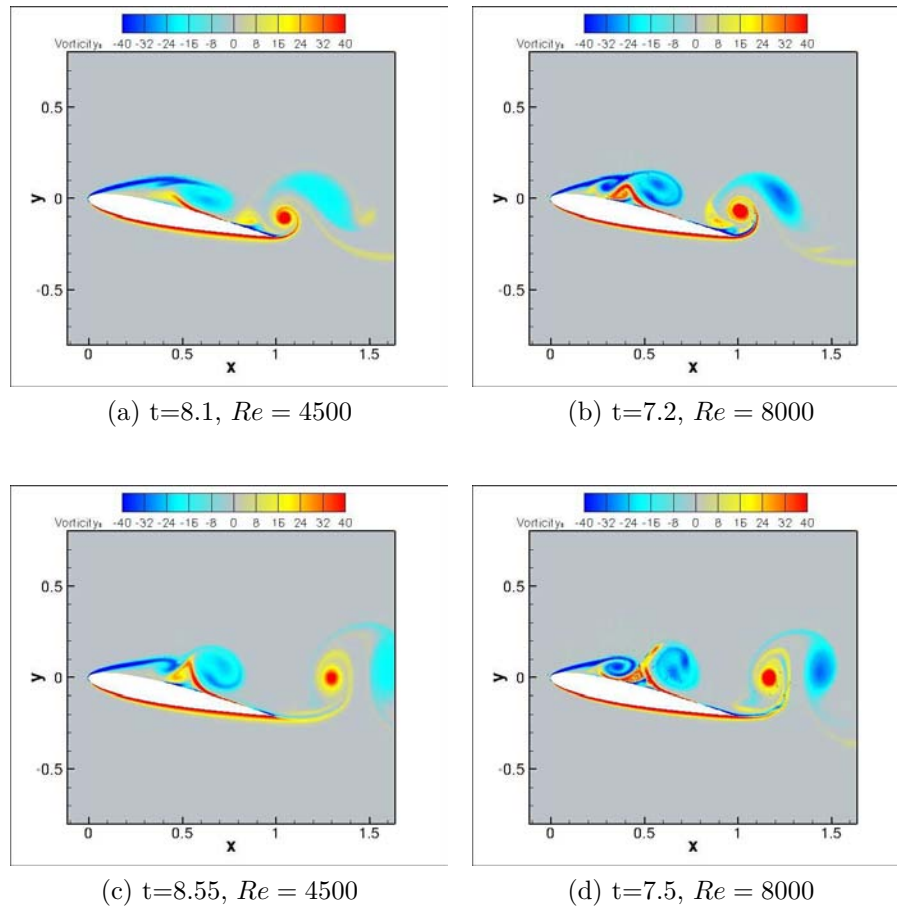


Figure 4.9: Vorticity contours at different times for a fixed airfoil at  $\alpha = 12^\circ$ ,  $Re = 4500$  and  $Re = 8000$ ; respectively. The flow configuration is the same at the two Reynolds numbers, which confirms the spatial periodicity of the flow. The flow patterns shown were selected at similar lift and drag values.

at  $Re = 8000$ . However, if we compare the vorticity contours of the flow at the two Reynolds numbers, we find that the flow configurations resemble each other (see Figure 4.9) if we condition the states on similar  $c_D$  and  $c_L$  values. This indicates that at  $Re = 8000$  there are still remains of the spatial periodicity observed at  $Re = 4500$ . The mean values of the lift and drag coefficients at  $Re = 8000$  are 1.06 and 0.28; respectively. This represents an increase by 7% for the lift and 3% for the drag as a response of increasing the Reynolds number. Simulations performed at  $Re = 800$  and  $Re = 1600$  at the same mean incidence ( $\bar{\alpha} = 12^\circ$ ) confirm this trend of the increase in the mean values when increasing the Reynolds number. Second, increasing the Reynolds number shifts the separation point upstream by 50% (Figure 4.10).

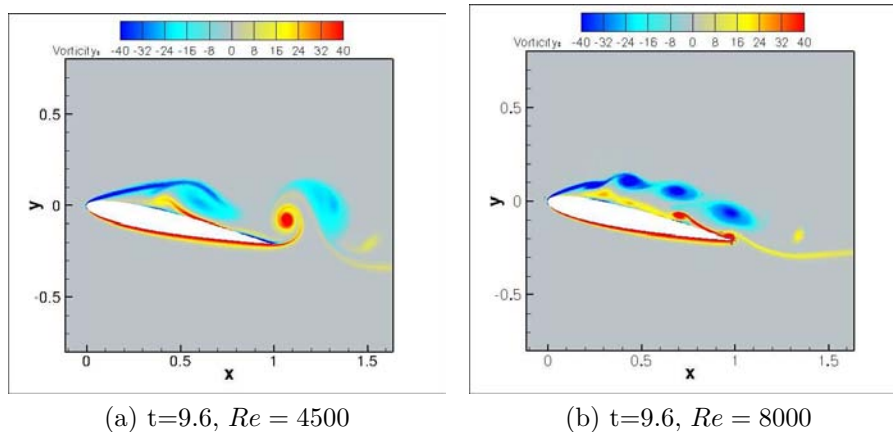


Figure 4.10: Vorticity contours at  $t = 9.6$  for a fixed airfoil at  $\alpha = 12^\circ$ ,  $Re = 4500$  and  $Re = 8000$ ; respectively. The separation point is shifted upwards for the simulation at  $Re = 8000$ .

### 4.3.2 Fixed airfoil at $\bar{\alpha} = 20^\circ$

The initial angle of attack is increased to  $20^\circ$  and two Reynolds numbers,  $Re = 800$  and  $Re = 1600$ , are considered. At  $\bar{\alpha} = 20^\circ$  and  $Re = 800$  the flow detaches from the airfoil upper surface and an anti-clockwise vortex is shed at the airfoil trailing-edge (see Figure 4.11a). The separated boundary-layer (or separation bubble) region grows under the impulse of the recirculating region which is beneath it, this results in the growth and the shedding of opposite sign vortices at the trailing-edge (Figures 4.11b – 4.11d). Due to the high mean incidence the boundary layer detaches massively and directly at the leading-edge. It reaches a bigger size compared to the simulation at  $\bar{\alpha} = 12^\circ$  (compare Figure 4.6c with Figure 4.11c). Nevertheless, there are less interactions between the positive and negative vorticity on the upper-surface. This is due to the high incidence angle which decelerates the flow over the airfoil [30, 31], and to the relatively small Reynolds number.

The time-histories of the forces are periodic (see Figure 4.12). The mean values for the drag and the lift coefficients (without the transient fluctuations) at  $Re = 800$  are 0.45 and 0.9; respectively.

Increasing the Reynolds number from 800 to 1600 exhibits no new flow features. The time series of the aerodynamical forces at  $Re = 1600$  are reported in Figure 4.12. The mean values are 0.46 for the drag coefficient and 0.96 for the lift coefficient.

To expose the effects of increasing the initial angle of attack  $\bar{\alpha}$ , a simulation was carried out at  $Re = 1600$  and  $\bar{\alpha} = 12^\circ$ . The corresponding drag and lift times series are shown in Figure 4.13. Note that the values of the drag and lift

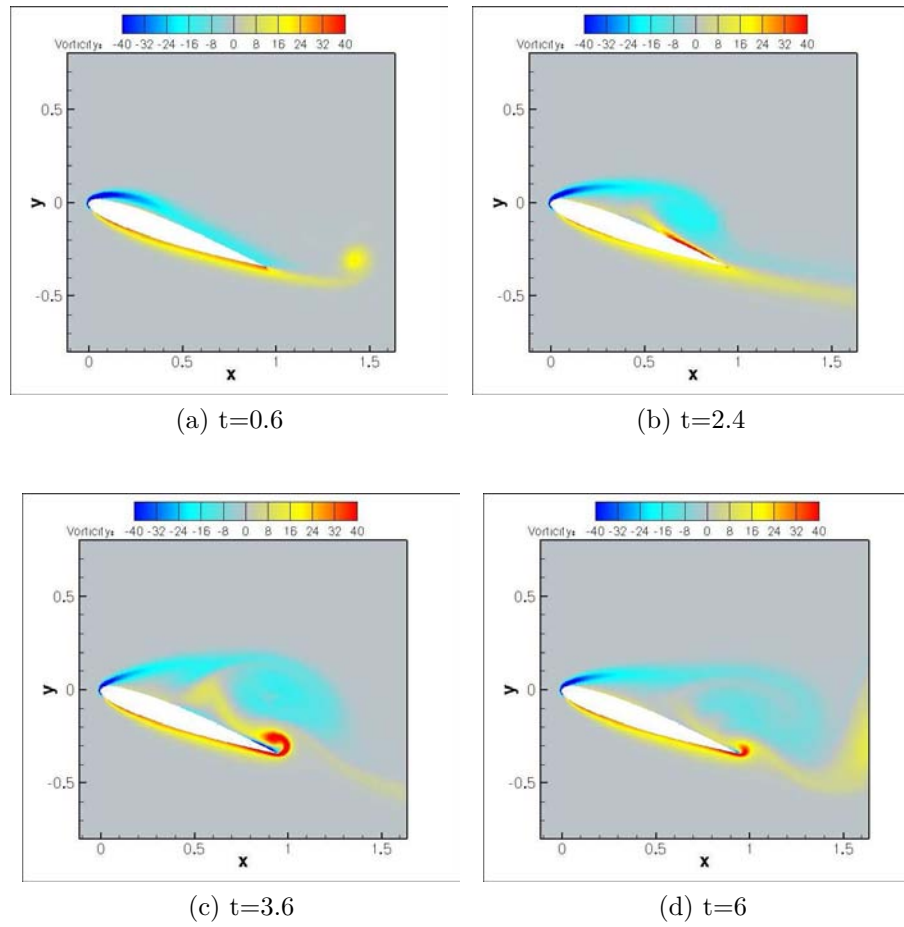


Figure 4.11: Vorticity contours at successive times for a fixed airfoil at  $\bar{\alpha} = 20^\circ$  and  $Re = 800$ .

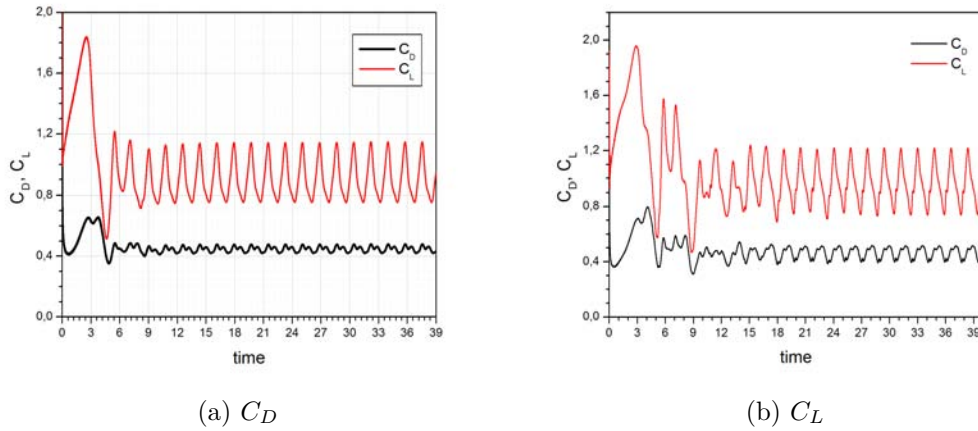


Figure 4.12: Time series of the drag and the lift coefficients for a fixed airfoil at  $\alpha = 12^\circ$ , (a)  $Re = 800$  and (b)  $Re = 1600$ .

coefficients are greater for the highest incidence case. The mean values of the drag and lift coefficients at  $\bar{\alpha} = 12^\circ$  are 0.54 and 0.19; respectively. At  $\bar{\alpha} = 20^\circ$  the mean values of the lift and drag coefficients increase by 36% and 27%; respectively. This increase, which is due to the increase in the mean incidence was observed and reported in the literature for low and moderate Reynolds numbers [2], where increasing the mean incidence from  $0^\circ$  to  $30^\circ$  at  $Re = 3000$  resulted in a dramatic increase of the lift and drag coefficients, especially the latter, which increased by one order of magnitude. One can conclude here that the effect of the Reynolds number is much less important than the mean incidence.

## 4.4 Simulations for a heaving airfoil

In this section the simulations of the flow around an airfoil forced to oscillate sinusoidally in heave are presented in terms of vorticity contours and aerodynamical coefficients time series. The airfoil motion is implemented using the moving frame of reference technique introduced in section 4.2. The values of the frequency and amplitude of oscillation are chosen to be in accordance with the range of values from simulations found in the literature. The same values are used in the investigation of the wakes of plunging airfoils [27] and the lock-in phenomenon and frequency selection in flows over oscillating airfoils [28].

### 4.4.1 Heaving airfoil at $\bar{\alpha} = 12^\circ$

Figure 4.15 illustrates the vorticity contours at selected time steps for an airfoil forced to oscillate in the  $y$  direction (heave motion) at  $Re = 4500$  and at a fre-

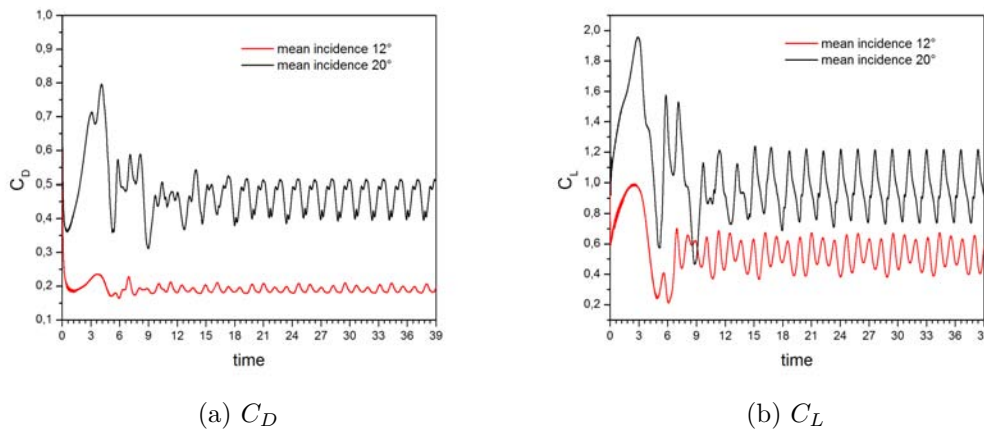


Figure 4.13: Drag and lift coefficients for fixed airfoils at  $Re = 1600$  and  $\bar{\alpha} = 12^\circ$ ,  $\alpha = 20^\circ$ .

quency and amplitude of oscillation of  $f = 0.3184$  and  $a = 0.1047$ ; respectively. Also indicated on the Figures is the ratio  $t/T^*$ , where  $T^* = 3.14$  is the period of the forced oscillations. The vorticity contours are illustrated for 2 oscillation cycles and the vertical position of the airfoil during the oscillation cycle is indicated on Figure 4.14. At  $t = 0.6$  (Figure 4.15a) the flow is already separated at the leading-edge, and a first anti-clockwise vortex is shed from the trailing-edge. At  $t = 2.4$  (Figure 4.15b) the counter-rotating recirculation region is created beneath the separation bubble and clockwise vortices are created and convected by the flow towards the trailing-edge. The lower-surface vorticity rolls up at the trailing-edge to form a clockwise vortex (Figure 4.15c). This vortex is shed along with a clockwise vortex (Figure 4.15d). This vortex shedding continues periodically as the simulation advances in time (Figure 4.15e).

The flow periodicity is confirmed by the time series of the lift and drag coefficients (see Figure 4.16). The period of the vortex shedding is  $T_s = 3.17$ , which is close to the period of the forced oscillation motion ( $T_h = 3.14$ ). The lift and drag coefficients reach a periodic state with mean values 1.07 and 0.28; respectively. This represents an increase in the mean values compared to the motionless simulation at the same Reynolds number and mean incidence. This increase is due to two main reasons triggered by the imposed airfoil heaving motion. First, the leading-edge vortex is created at a position more afore the airfoil than in the motionless case, which creates a depression zone which enhances the lift. This can be observed on Figure 4.17, depicting the vorticity and the pressure distributions at the vertical positions corresponding to the mid-downstroke and mid-upstroke, during which the lift reaches its peak values. This phenomenon holds only for sufficiently small heaving frequencies (less than 0.5) [6]. Second, the leading-edge vortex convection contributes to the increase of the lift. As the inverse of the

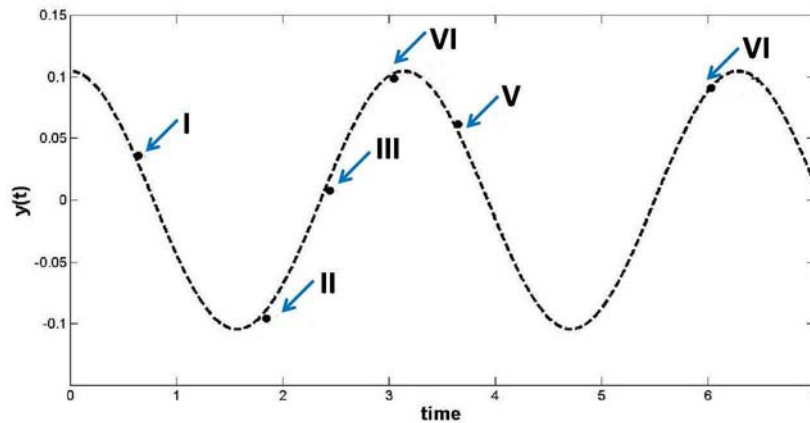


Figure 4.14: Schematic representation of the vertical positions occupied by the airfoil during the oscillation cycle at  $f = 0.3184$  and  $a = 0.1047$ . Position I:  $t = 0.6$ , position II:  $t = 1.8$ , position III:  $t = 2.4$ , position IV:  $t = 3$ , position V:  $t = 3.6$  and position VI:  $t = 6$ .

heaving frequency indicates the time left for the vortices to form, grow, separate and travel along the airfoil to be shed, a small value of  $f$  results in the vortices staying longer on the airfoil surface. Moreover, subjecting the airfoil to the heave motion contributes to an increase in the acceleration and thus an increase in the vortex circulation (which can also be observed in our simulations when comparing the Figures 4.6 of the vorticity distributions of the motionless airfoil and Figures 4.15 for the heaving airfoil). The longer time spent by the vortices on the airfoil surface and the increase in their circulation contributes to the increase in the lift observed in Figure 4.16. This result is also reported by *Andro & Jacquin* for simulations with  $0.05 < f < 0.4$  [6].

Compared to the fixed airfoil simulations, the flow phenomenology is the same, in the sense that there are no new flow features. Those results are to be expected, since the frequency of the forced oscillations ( $f = 0.3184$ ) is less than 1. For this particular case it was reported for various experimental and computational studies that the flow features for the oscillating airfoil are the same as for the fixed (static) airfoil at the same incidence angle [2, 14, 30, 31]. However, the motion of the airfoil reduces the strength of the recirculation zone and restricts its effect at the trailing-edge. Another effect of the airfoil motion on the flow is that the shed vortices are lifted to a higher vertical position (compared to Figure 4.6d).

Moreover, the upward motion delays the flow separation and favours a more stable flow creating smaller leading-edge vortices. Compare Figure 4.6d and 4.15e, where the flow is clearly more separated for the motionless simulation. On the other hand, the downward motion promotes the leading-edge separation (Figure 4.15d). These previous results have been also reported in the literature for the

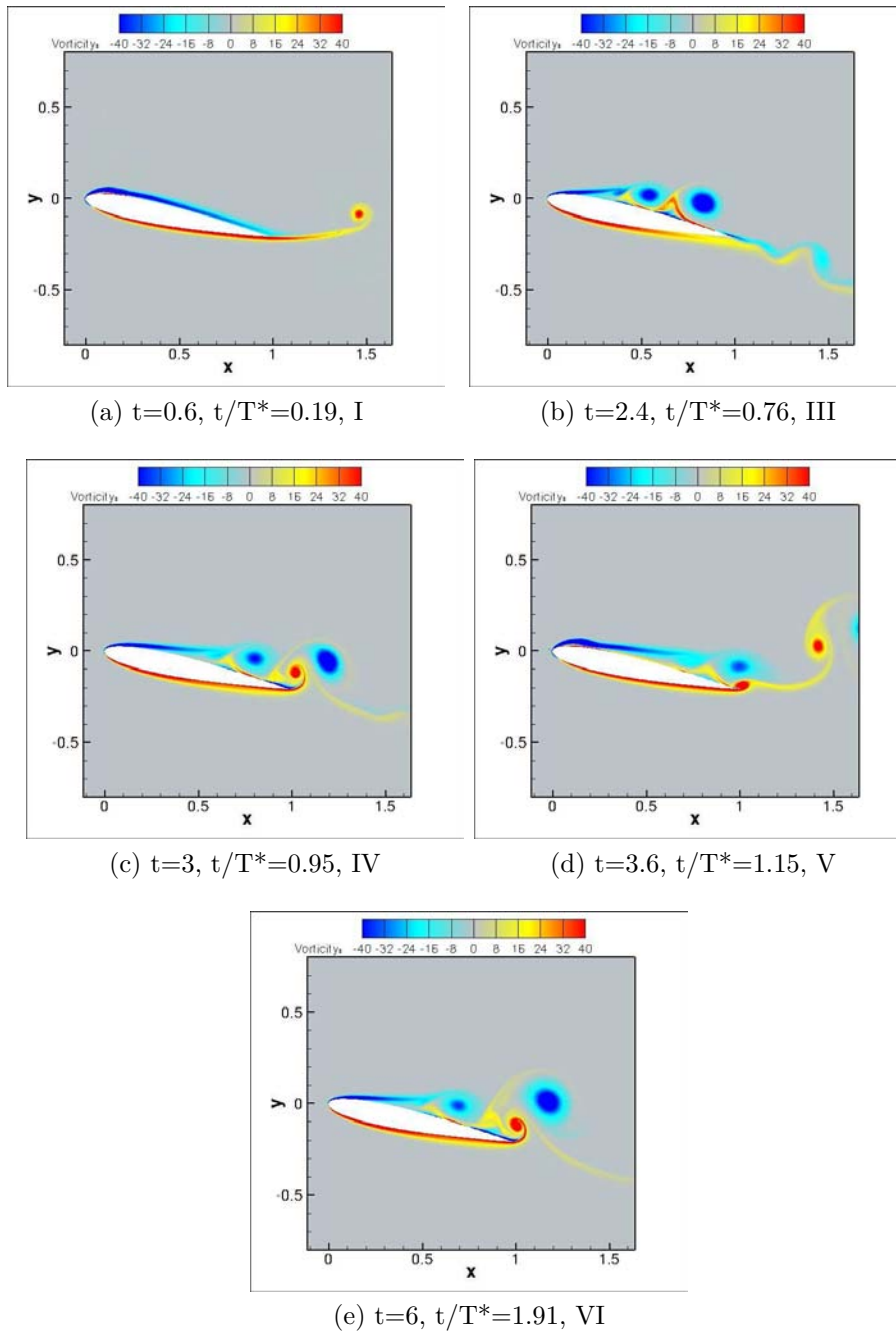


Figure 4.15: Vorticity contours at successive times for a heaving airfoil at  $\bar{\alpha} = 12^\circ$ ,  $Re = 4500$ ,  $f = 0.3184$  and  $a = 0.1047$ . The roman numbers indicate the horizontal position of the airfoil as on Figure 4.14.

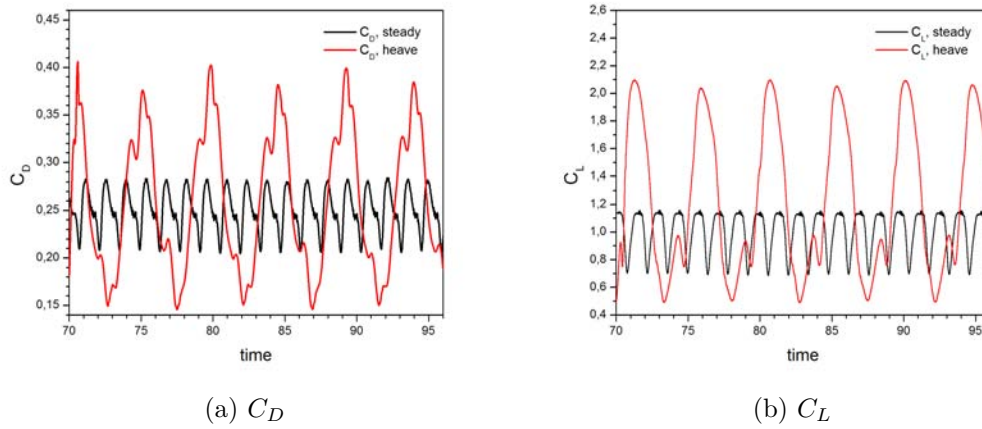


Figure 4.16: Time series of (a) drag and (b) lift coefficients for the fixed airfoil at  $\alpha = 12^\circ$  and  $Re = 4500$  and the heaving airfoil at  $\bar{\alpha} = 12^\circ$ ,  $Re = 4500$ ,  $f = 0.3184$  and  $a = 0.1047$ .

pitching case [2, 30] and will be confirmed by the next simulation at a higher Reynolds number.

Increasing the Reynolds number to  $Re = 8000$  accentuates the effects of the airfoil motion due to the flow acceleration. As for the simulation at  $Re = 4500$ , the upward motion of the airfoil delays the separation and the size of the vortices is smaller (compare 4.18d with 4.8b and Figure 4.18f with 4.8d). During the downward motion of the airfoil the separation of the main leading-edge vortex is promoted and small-scale clockwise vortices form in the wake. An example of this can be seen at  $t = 2.4$  (Figure 4.8a) where for the motionless airfoil the separation-bubbles are small and are not completely detached from the upper-surface, and the leading-edge vortex is small. While for the forced airfoil (at the same simulation time,  $t = 2.4$ , Figure 4.15b) the separation-bubbles are detached from the upper-surface and the leading-edge vortex has already reached an important size and is about to be shed. Small clockwise vortices are shed in the near wake for the forced simulation. Moreover, the downward motion shifts the shed vortices at a higher vertical position. As previously mentioned these results have been also reported for the pitching case [2, 30], but the small scale vortices are anti-clockwise for the pitch case.

The lift and drag coefficient mean values at  $Re = 4500$  are 1.05 and 0.23; respectively. At  $Re = 8000$  the drag coefficient mean value is 0.20 and the mean value of the lift coefficient is 1.09.

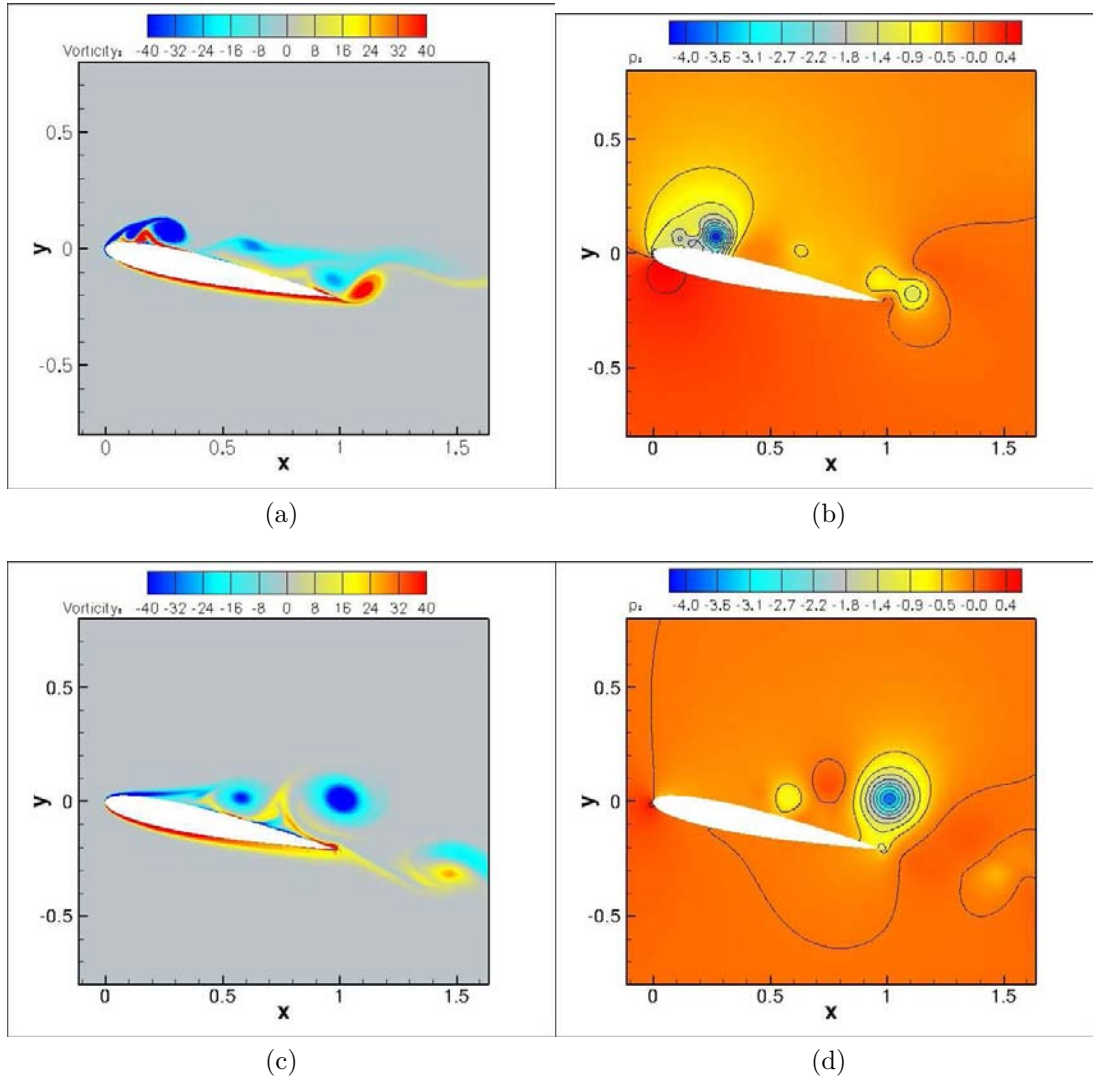


Figure 4.17: Vorticity (left) and pressure contours (right) during a heaving cycle (a)-(b) mid-downstroke, (c)-(d) mid-upstroke at  $Re = 4500$ ,  $f = 0.3184$  and  $a = 0.1047$ .

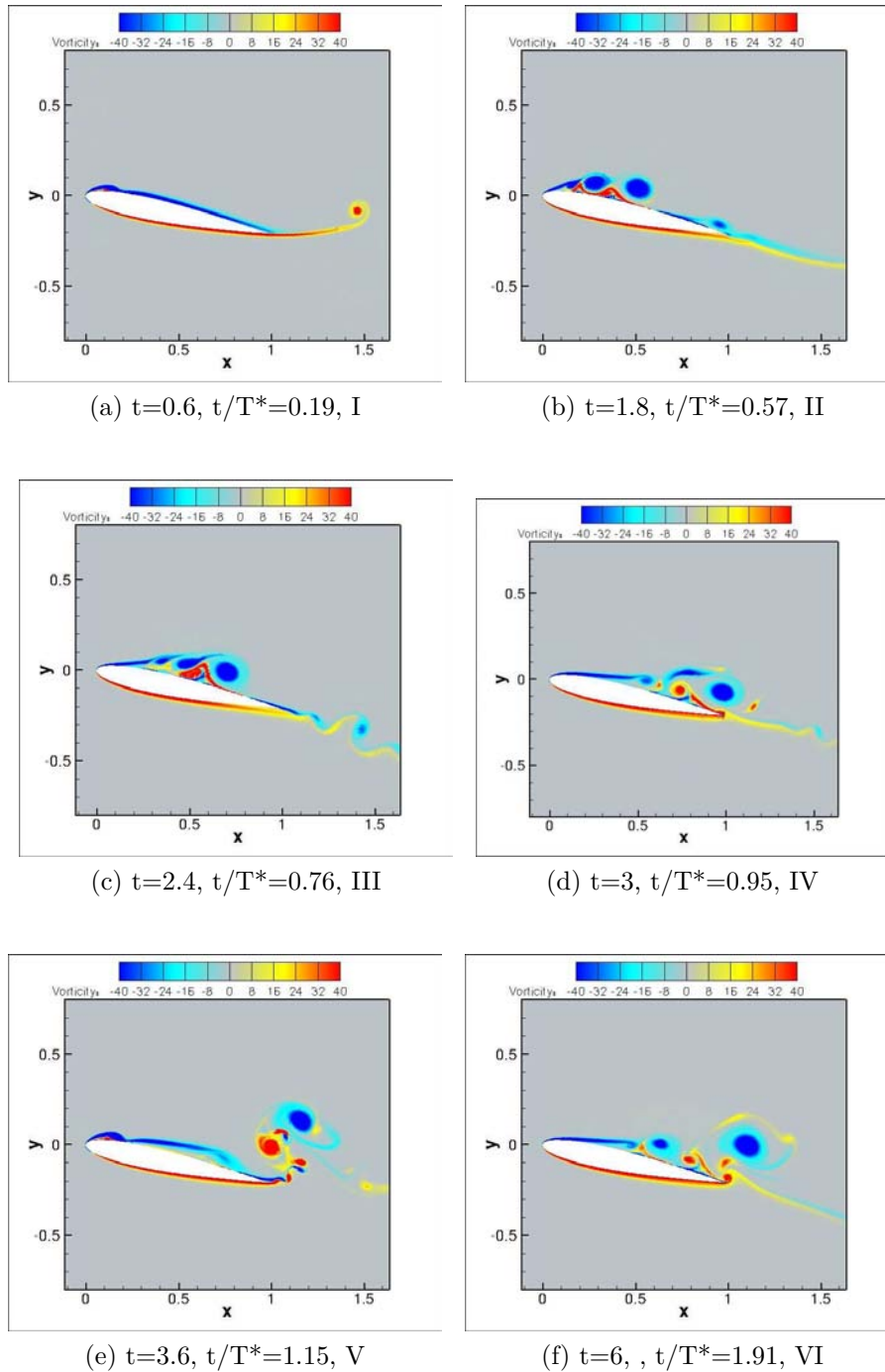


Figure 4.18: Vorticity contours at successive times for the heaving airfoil at  $\bar{\alpha} = 12^\circ$ ,  $Re = 8000$ ,  $f = 0.3184$  and  $a = 0.1047$ . The roman numerals indicate the horizontal position of the airfoil as on Figure 4.14.

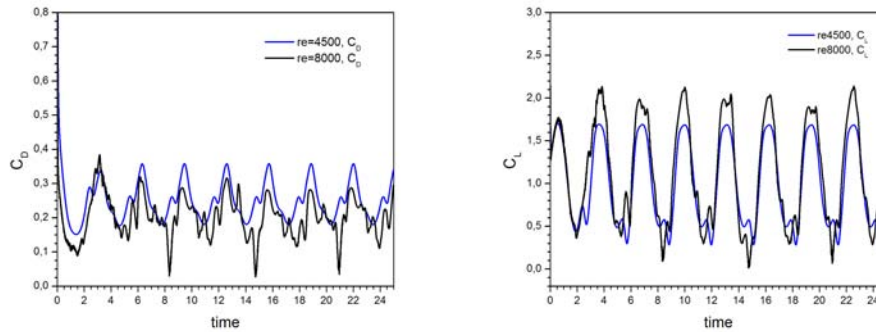


Figure 4.19: Time series of the drag and lift coefficients for the heaving airfoil at  $\bar{\alpha} = 12^\circ$  for  $Re = 4500$  and  $Re = 8000$  both forced to oscillate at a frequency and amplitude of oscillations of  $f = 0.3184$  and  $a = 0.1047$ ; respectively.

#### 4.4.2 Heaving airfoil at $\alpha = 20^\circ$

The mean incidence of the heaving airfoil is increased to  $\bar{\alpha} = 20^\circ$ . Even for the relatively low Reynolds number considered different flow and wake structures are observed. These wake structures were not observed in the previous simulations.

The simulation is first conducted for a motionless airfoil at  $Re = 800$ , and after reaching the steady state the airfoil is forced to oscillate in heave at a frequency and amplitude of  $f = 0.25$  and  $a = 0.7958$  respectively. Figure 4.21 illustrates the vorticity contours at successive times covering one cycle of the airfoil oscillation. Also indicated on the Figures is the ratio  $t/T^*$ , where  $T^* = 3.14$  is the period of the forced oscillations. The vorticity contours are illustrated for one oscillation cycle and the vertical position of the airfoil during the oscillation cycle is indicated on Figure 4.20. In Figure 4.21a the flow is separated at the upper-surface. A leading-edge vortex is formed at  $t = 116.5$  and it detaches partially under the action of the counter-rotating separation zone that develops underneath it (see Figure 4.21b). Note that unlike the previous simulations, the action region of the counter-rotating separation zone is shifted in the upstream direction. At the same time counter clockwise vorticity continues to be shed from the trailing-edge (see Figure 4.21b) and it has an elongated shape under the downward motion of the airfoil. As the simulation advances, the leading-edge vortex reaches an important size (almost 80% of the chord length) and is shed directly at the leading-edge, while negative vorticity continues to be shed at the trailing-edge (Figure 4.21c). Note again that the anti-clockwise vortex is convected upstream as a result of the airfoil motion, and of the suction effect of the clockwise vortex. In Figure 4.21d the clockwise rotating vortex is convected towards the trailing-edge and interacts with the anti-clockwise vorticity. The fact that the leading-edge vortex returns on the airfoil upper-surface (after being shed at  $t = 116.5$ ) is due to the

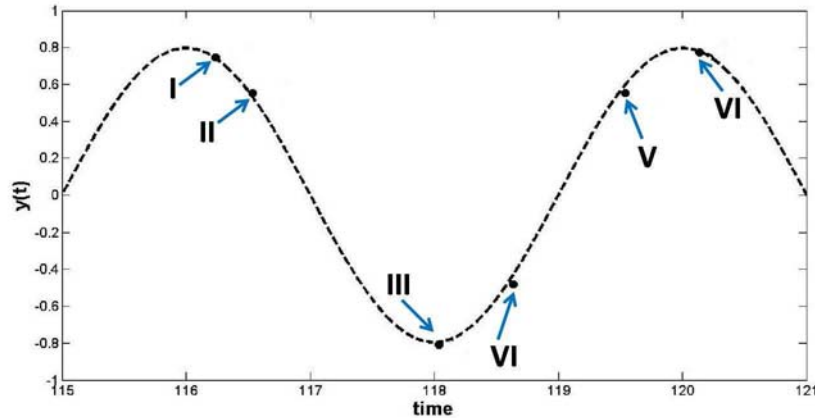


Figure 4.20: Schematic representation of the vertical positions occupied by the airfoil during the oscillation cycle at  $f = 0.25$  and  $a = 0.7958$ . Position I:  $t = 0.6$ , position II:  $t = 1.8$ , position III:  $t = 2.4$ , position IV:  $t = 3$ , position V:  $t = 3.6$  and position VI:  $t = 6$ .

airfoil motion, as the airfoil is moving upwards at this time. The clockwise and anti-clockwise vortices are both shed in the near wake (Figure 4.21e-4.21f) in a jet-like flow. The scenario described is repeated periodically. The high mean incidence coupled to the airfoil motion at a high frequency and amplitude triggers much stronger interactions between the vortices and generates a new wake type, which is different from the one for the low mean incidence combined with a fixed airfoil. To isolate the effect of the mean incidence a simulation was carried for a lower heaving amplitude and frequency at  $\bar{\alpha} = 20^\circ$ ,  $f = 0.0796$ ,  $h = 0.1047$  and  $Re = 1200$ . The results of this simulation (not presented here for brevity) indicate that the detachment of the leading-edge vortex at an advanced position on the airfoil surface is due to the increase in the mean incidence. The same applies to the increase in the circulation of the trailing-edge and its detachment at the rear of the airfoil. These two phenomena were not observed for simulations performed at  $\bar{\alpha} = 12^\circ$ ,  $f = 0.3184$ ,  $h = 0.1047$  (not presented here for brevity). The high heaving amplitude of the simulation presented in Figure 4.21 may trigger high circulation vortices, the detachment of vorticity from both surfaces of the airfoil and the arm-like vorticity shedding.

The periodical behavior is confirmed when plotting the forces coefficients time series (Figure 4.22). The values of the drag and lift are very high compared to the previous simulations. This may be due to the high frequency and amplitude of oscillations and to the high mean incidence considered. The mean value of the lift and drag coefficients are 3.19 and 0.91 respectively. Compared to a motionless case, the lift coefficient increased by a factor of 3.5 and the drag by a factor of 2. This dramatic increase in the values of the aerodynamical coefficients is representative of the increase in the loads that the airfoil is subjected to when it is

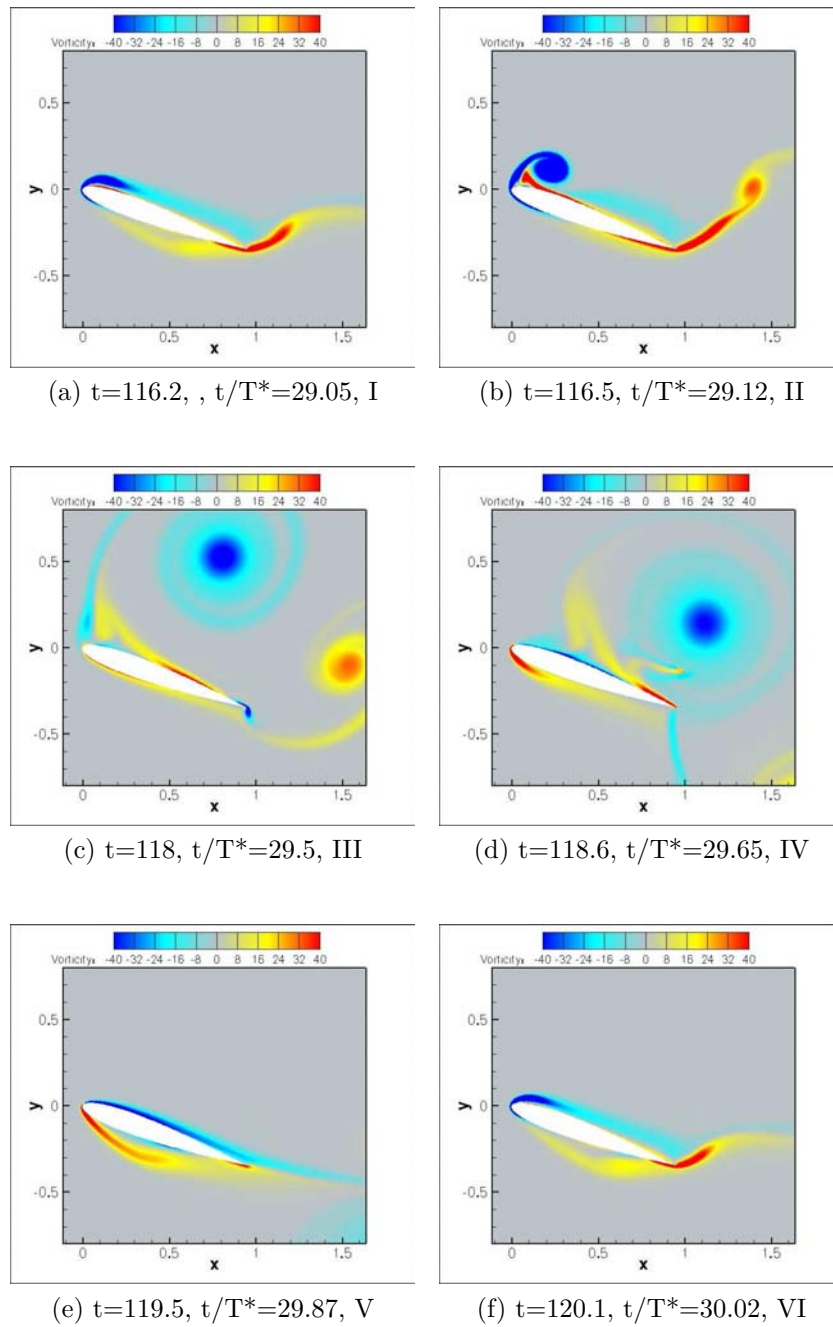


Figure 4.21: Vorticity contours at selected times for the heaving airfoil at  $\bar{\alpha} = 20^\circ$ ,  $Re = 800$ ,  $f = 0.25$  and  $a = 0.7958$ . The roman numbers indicates the horizontal position of the airfoil as on Figure 4.20.

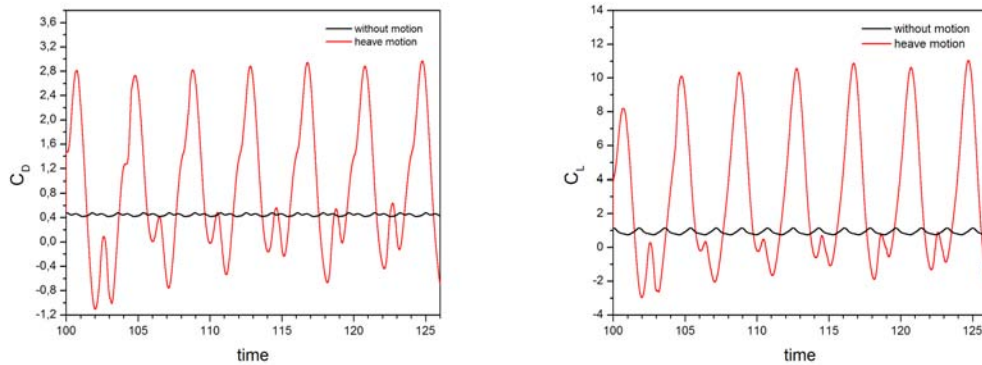


Figure 4.22: Time series of the drag and lift coefficients for the motionless airfoil at  $Re = 800$  and the heaving airfoil at  $\bar{\alpha} = 20^\circ$ ,  $Re = 800$ ,  $f = 0.25$  and  $a = 0.7958$ . For the heaving simulation, the mean values are 3.19 and 0.91 for the lift and drag coefficients; respectively.

forced to oscillate at high incidences. It is also an indication of the much stronger interactions taking place in the boundary-layer. The periods of oscillation of the lift and drag coefficients are approximately equal to the imposed oscillation period.

## 4.5 Conclusion

The flow field around a NACA0012 airfoil forced to oscillate in heave has been simulated for a combination of mean incidences and Reynolds numbers.

The Spectral/ $hp$  Element Method was used to simulate steady and unsteady flows over fixed airfoils and the results were validated against published studies. The method was also used for the first time in combination with the moving frame of reference technique to simulate an oscillating airfoil in heave and describe the boundary-layer temporal development, for different values of the mean incidence, the Reynolds number and the amplitude and frequency of oscillations.

For the fixed airfoil it was observed that increasing the Reynolds number slightly increases the mean value of the aerodynamic coefficients. The flow development is faster due to its acceleration but in general it has the same phenomenological development as that at a lower Reynolds number. The mean incidence is found to have more effects on the flow development. The flow is delayed in response to the increase in the mean incidence and the force coefficients increase, like it was previously reported in the literature.

For the oscillating airfoil at a reduced frequency less than 1 the fixed airfoil and the heaving airfoil exhibit similar flow fields, thus confirming previous ex-

perimental and computational findings. Nevertheless, the mean values of the lift and drag coefficients increase.

Increasing the Reynolds number while keeping the same frequency and amplitude of oscillations has no major effects neither on the flow structure nor on the aerodynamical loads. However, increasing the mean incidence has a dramatic influence on the flow field and the wake which is characterized by vortices of greater size and strength. The values of the lift and drag increase dramatically even if the Reynolds number considered is low.

Setting the airfoil in motion has the same effect as for increasing the mean incidence for motionless airfoils.

## 4.6 Acknowledgments

We gratefully acknowledge the computer time provided by the Regionales Rechenzentrum fuer Niedersachsen (RRZN). We also thank Prof. S. Sherwin for providing the *Nektar* solver. W.M. gratefully acknowledges the hospitality of Prof. Sherwin group at the Department of Aeronautics at Imperial College, London. This research was supported by a DAAD scholarship. W.M. thanks Carlos Peralta for his valuable comments and contributions to this paper.

## Bibliography

- [1] M. Abramowitz and I. A. Stegun. *Handbook of Mathematical Functions*. Dover Publications, New York, 1972.
- [2] M. H. Akbari and S. J. Price. Simulation of the Flow Over Elliptic Airfoils Oscillating at Large Angles of Attack. *J. Fluid Struct.*, 14:757–777, 2000.
- [3] S. Alben. An implicit method for coupled flow-body dynamics. *Journal of Computational Physics*, 227:4912–4933, 2008.
- [4] J. M. Anderson, k. Streitlien, D. S. Barrett, and M. S. Triantafyllou. Oscillating foils of high propulsive efficiency. *J. Fluid Mech.*, 360:41–72, 1998.
- [5] J. M. Anderson, K. Streitlien, K. S. Barrett, and M. S. Triantafyllou. Oscillating foils of high propulsive efficiency. *Journal of Fluid Mechanics*, 360: 41–72, 1998.
- [6] J. Y. Andro and L. Jacquin. Frequency effects on the aerodynamic mechanisms of a heaving airfoil in a forward flight configuration. *Aerospace Science and Technology*, 13:71–80, 2009.
- [7] J. P. Boyd. *Chebyshev and Fourier Spectral Methods*. Dover Publications, 2001.
- [8] J. Butcher. *Numerical Methods for Ordinary Differential Equations*. John Wiley, 2003.
- [9] B. S. Carmo, S. J. Sherwin, P. W. Bearman, and R. H. J. Willden. Wake transition in the flow around two circular cylinders in staggered arrangements. *J. Fluid Mech.*, 597(1):1–29, 2008.
- [10] A. N. Cookson, D. J. Doorly, and S. J. Sherwin. Mixing Through Stirring of Steady Flow in Small Amplitude Helical Tubes. *Ann. Biomed. Eng.*, 37: 710–721, 2009.
- [11] K. D. Ellenrieder, K. R. Parker, and J. Soria. Flow structures behind a heaving and pitching finite-span wing. *J. Fluid Mech.*, 490:129–138, 2003.
- [12] P. Freymuth. Propulsive vortical signature of plunging and pitching airfoils. *AIAA J.*, 26:881–883, 1988.
- [13] P. Freymuth. Thrust generation by an airfoil in hover modes. *Experiments in Fluids*, 9(1-2):17–24, 1990.
- [14] P. Freymuth, M. Palmer, and W. Bank. Comparative visualization of accelerating flow around various bodies, starting from rest. In *AFOSR Proceedings of the Workshop on Unsteady Separated Flow*, pages 52–57, 1984.

- [15] A. Ghizzetti and A. Ossicini. *Quadrature Formulae*. Academic Press, New York, 1970.
- [16] K. Gustafson and R. Leben. Computation of dragonfly aerodynamics. *Computer Physics Communications*, 65:121–132, 1991.
- [17] Zhu W. J., W. Z. Shen, N. N. Sørensen, J. N. Sørensen, and J. J. Wedel-Heinen. Calculations of Flow around an Airfoil with a Trailing Edge Flap by Use of an Immersed Boundary Method. In *European Wind Energy Conference, EWEC, Marseille, France, 16-19 March 2009*, 2009.
- [18] K. Jones and M. Platzer. Design and development considerations for biologically inspired flapping-wing micro air vehicles. *Experiments in Fluids*, 46:199–810, 2009.
- [19] G. E. Karniadakis and S. Sherwin. *Spectral/hp Element Methods for Computational Fluid Dynamics*. Oxford University Press, 2005.
- [20] G. E. Karniadakis, S. A. Orszag, and M. Israeli. High-order splitting methods for the incompressible Navier-Stokes equations. *J. Comp. Phys.*, 97:414–443, 1991.
- [21] M. M. Koochesfahani. Vortical patterns in the wake of an oscillating airfoil. *AIAA J.*, 27:1200–1205, 1989.
- [22] G. C. Lewin and H. Haj-Hariri. Modelling thrust generation of a two-dimensional heaving airfoil in a viscous flow. *Journal of Fluid Mechanics*, 492:339–362, 2003.
- [23] L. Li, S. J. Sherwin, and P. W. Bearman. A moving frame of reference algorithm for fluid/structure interaction of rotating and translating bodies. *Int. J. Numer. Meth. Fl.*, 38:187–206, 2002.
- [24] Y. Lian, W. Shyy, D. Viieru, and B. Zhang. Membrane wing aerodynamics for micro air vehicles. *Progress in Aerospace Sciences*, 39(6-7):425–465, 2003.
- [25] W.J. McCroskey. Some current research in unsteady fluid dynamics - The 1976 Freeman Scholar Lecture. *Trans. ASME I: J. Fluids Engng.*, 99:8–39, 1977.
- [26] W.J. McCroskey. Unsteady airfoils. *Ann. Rev. Fluid Mech.*, 14:285–311, 1982.
- [27] W. Medjroubi, B. Stoevesandt, and J. Peinke. Direct numerical simulations of plunging airfoil wakes using spectral/hp element method. Submitted for publication in *Journal of Computational and Applied Mathematics*, 2010.

- [28] W. Medjroubi, B. Stoevesandt, and J. Peinke. Frequency selection in plunging airfoil wakes using a high-order numerical method. Submitted for publication in *Journal of Physics*, 2011.
- [29] C. R. Nastase and D. J. Mavriplis. High-order discontinuous Galerkin methods using an hp-multigrid approach. *J. Comp. Phys.*, 213(1):330–357, 2006.
- [30] K. Ohmi, M. Coutanceau, T. P. Loc, and A. Dulieu. Vortex formation around an oscillating and translating airfoil at large incidences. *J. Fluid Mech.*, 211:37–60, 1990.
- [31] K. Ohmi, M. Coutanceau, O. Daube, and T. P. Loc. Further experiments on vortex formation around an oscillating and translating airfoil at large incidences. *J. Fluid Mech.*, 225:607–630, 1991.
- [32] M. Sfakiotakis, D. M. Lane, and J. B. C. Davies. Review of fish swimming modes for aquatic locomotion. *IEEE J. Ocean. Eng.*, 24:237–252, 1999.
- [33] A. V. Shatalov. *Numerical Simulation of Incompressible Laminar Flows Using Viscous-Inviscid Interaction Procedure*. PhD thesis, University of California, Division Mechanical and Aeronautical Engineering, 2006.
- [34] S. J. Sherwin. <http://www3.imperial.ac.uk/spectralhp>, 2010.
- [35] E. S. Spagnolie, L. Moret, M. J. Shelley, and J. Zhang. Surprising behaviours in flapping locomotion with passive pitching. *Physics of Fluids*, 22:041903–1:20, 2010.
- [36] Z. J. Wang. Vortex shedding and frequency selection in flapping flight. *J. Fluid Mech.*, 410:323–341, 2000.
- [37] M. J. Wolfgang, M. S. Triantafyllou, and D. K. P. Yue. Visualization of Complex Near-body Transport Processes in Flexible-body Propulsion. *Journal of Visualization*, 2(2):143–151, 1999.
- [38] J. Young. *Numerical simulation of the unsteady aerodynamics of flapping airfoils*. PhD thesis, School of Aerospace, Civil and Mechanical Engineering. The University of New South Wales. Australian Defence Force Academy, May 2005.



# Chapter 5

## Plunging Airfoil Wakes classification Using Spectral/hp Element Method <sup>1</sup>

In this contribution the two dimensional unsteady flow over a plunging NACA0012 airfoil is simulated using a high-order numerical method associated with a moving frame of reference technique, in order to obtain more accurate and high resolution data. This data can be used to characterize oscillating airfoil wakes with very fine temporal and spatial detail. The mean incidence investigated is  $\bar{\alpha} = 0^\circ$  and Reynolds number  $Re = 10^4$ . The transition from a drag-producing wake, to a neutral, and a thrust-producing wake is observed and analyzed. The results obtained are in accordance with previously published experimental and computational investigations. Furthermore, a more detailed wake classification is presented, where two more wake configurations are captured. The role of the trailing-edge, and the interaction of the natural shedding frequency of the airfoil and the imposed forcing frequency in the creation of multiple-vortices-per-half-cycle shedding mode is investigated. These results clarify the role of the interaction of the natural shedding frequency of the airfoil and the shedding frequency of the imposed motion into the appearance of the multiple-vortices-per-half-cycle mode. The relation between the interaction of the two aforementioned frequencies and the observed shedding modes is established.

---

<sup>1</sup>Submitted to publication as W. MEDJROUBI, B. STOEVE SANDT and J. PEINKE: *Plunging Airfoil Wakes classification Using Spectral/hp Element Method* in Journal of Computational and Applied Mathematics

## 5.1 Introduction

Thrust generation by plunging airfoils is highly dependent on the qualitative wake structure behind the trailing-edge of the airfoil [12]. It has been proven theoretically [1, 4, 10] and experimentally [9] [11] that plunging airfoils produce thrust at certain values of frequency and amplitude of oscillations. The wake structure depends on the Reynolds number, the reduced frequency, the mean angle of attack and the amplitude of oscillations. At low reduced frequencies the wake is a Karman vortex street with one pair of opposite vortices shed during each oscillation cycle. This wake is a drag-producing wake. At high reduced frequencies the wake becomes an opposite or reversed Karman vortex street, with one pair of opposite vortices shed per oscillation cycle. The sense of rotation of the vortices is inverted compared to the Karman street. This latter configuration produces thrust. During the transition from drag to thrust-producing wakes, a neutral mode appears where the produced thrust equals the inherent drag, thus the name neutral. This mode is in some cases accompanied by the shedding of more than one vortex pair per oscillation cycle and is thus referred to as the multiple-vortex-per-half-cycle mode. This wake is not well understood and *Young* in [18] attributes its origin to the interaction between the natural shedding of the airfoil and the imposed plunging frequency.

The transition from a drag-producing to a thrust-producing wake can be achieved by varying either the frequency or the amplitude of the imposed oscillations. The approximate boundaries defining the different wake types, which were determined experimentally [17], do not coincide with either the lines of constant thrust coefficient (as predicted by the Garrick model in [4]), nor with lines of constant  $kh$  or the Strouhal number (as in [5]). This observation is more pronounced at low values of  $h$ .

In this contribution plunging airfoils are investigated for different applications such as Micro-Air Vehicles (MAVs), bird and fish-like propulsion, airfoils in flutter or gusts and turbomachinery. The two dimensional unsteady flow over a plunging NACA0012 airfoil is simulated using a high-order numerical method associated with a moving frame of reference technique introduced in Section 5.2. The region of low amplitude of oscillations, where the borders between the different wake types are not well defined experimentally and computationally, is explored in order to obtain a more accurate wake classification. In Section 5.3 the transition from a drag to a thrust producing wake is observed when increasing the plunge frequency (at constant amplitude) and when increasing the amplitude of oscillations (at constant frequency). Furthermore, the different simulated wakes are classified and the formation and the origin of the multiple-vortex-per-cycle mode is presented and analyzed. The role of the trailing-edge and the natural and forcing frequency interactions are also investigated.

## 5.2 Numerical Method

The Navier-Stokes equations for an incompressible, unsteady and viscous flow are written as:

$$\frac{\partial \mathbf{u}}{\partial t} + (\mathbf{u} \cdot \nabla) \mathbf{u} = -\nabla p + \frac{\nabla^2 \mathbf{u}}{Re}, \quad (5.1)$$

where  $\mathbf{u}$  is the velocity vector that satisfies the incompressibility condition ( $\nabla \cdot \mathbf{u} = 0$ ) where  $p$  is the pressure,  $Re = U_0 c / \nu$  is the Reynolds number based on the airfoil chord length  $c$ ,  $\nu$  is the kinematic viscosity and  $U_0$  is the free-stream velocity.

In the Spectral /hp Element Method the physical domain is divided into triangular and/or quadrilateral subdomains. Within each subdomain a spectral expansion in the form of Jacobi polynomials of mixed weight and order  $n$  is used to represent the solution variable. The temporal discretization of the Navier-Stokes equations is achieved via a time-splitting scheme [8], where three steps are required to determine the fields for the next time step using the velocity at the previous time step. This is achieved by forcing the incompressibility constraint over an intermediate velocity field and a Poisson equation is solved for the pressure. The final velocity field is obtained by solving a Helmholtz equation. Equation (5.1) is discretized in 2D with the linear term treated implicitly and the nonlinear term treated explicitly. For further details about the the derivation of the method see [6].

To implement the airfoil motion, the Navier-Stokes equations and the boundary conditions are re-written in a moving frame of reference. The resulting system is then solved [13]. For the present simulations we have considered the body as being rigid (non-deformable) and forced to oscillate in plunge, with  $y(t) = h \cos(2\pi f t)$ , where  $y(t)$  is the time dependent vertical motion,  $f^* = f c / U_0$  and  $h^* = h / c$  are the dimensionless frequency and amplitude of oscillations, respectively. Commonly, the reduced frequency defined as  $k = 2\pi f c / 2U_\infty$  is used to characterize the flow. The geometrical angle of attack is set in this investigation to  $\bar{\alpha} = 0^\circ$ . The thrust coefficient is defined as  $C_T = -1/T \int_0^T C_D(t) dt$ , where  $T = 1/f$  is the oscillation period and  $C_D$  is the drag coefficient. For simplification, during the remainder of this investigation the non-dimensional frequency and amplitude of oscillation will be noted as  $f$  and  $h$ ; respectively.

In this paper a general purpose Navier-Stokes solver is used where the aforementioned numerical method is implemented. The solver called *Nεκταρ* [16] was validated for many flow geometries, among those cylindrical [2], helical [3] and rectangular [13]. We have also validated the solver for the airfoil geometry for steady and unsteady flows [14] and found a very good agreement with previously published numerical results [15]. All the simulations of oscillating airfoils were started from fully converged motionless airfoil solutions.

## 5.3 Results

The results presented here were obtained using a 2D unstructured grid composed of 4220 elements [14]. The polynomial order  $n$  has been varied from 9 to 15. The boundary conditions at the domain surfaces are inflow conditions at the entry and outflow conditions at the exit. Periodic boundary conditions were used for the upper and lower part of the domain. At the airfoil surface no-slip conditions are considered.

### 5.3.1 Constant amplitude transition

In this section the amplitude of oscillations is kept constant at  $h = 0.02$  and the frequency is increased in order to exhibit a drag- to thrust-producing wake. For a motionless airfoil at  $\bar{\alpha} = 0^\circ$  and  $Re = 10^4$ , the wake exhibits a typical drag-production configuration (see Fig. 5.1a). The vortex wake in this case is a Karman street, which consists of alternating rows of clockwise vortices (at the top of the centerline) and anticlockwise vortices (at the bottom of the centerline). This configuration results from the shedding of one pair of counter-rotating vortices during each oscillation cycle (one vortex is shed in each half oscillation cycle). Note here that the cores of the vortices are not aligned with the centerline, but that the wake vortices present a mushroom-like structure tilted upstream. This is the signature of a drag-producing wake [12, 18], and it is confirmed by the time-averaged velocity profile, which is clearly a momentum deficit one (Fig. 5.2a). This means that the mean velocity in the wake is lower than the free-stream velocity.

The airfoil is then forced to oscillate in heave at a frequency  $k = 4.52$  and amplitude  $h = 0.02$ . Fig. 5.1b shows the vorticity contours, where the two rows of vortices are now separated vertically. The time-averaged horizontal velocity profile (Fig. 5.2b) exhibits what is labelled as a neutral wake [18], and the velocity presents both a deficit and a jet around the free-stream velocity. This means that the mean velocity in the wake is almost equal to the free-stream velocity. The total momentum is close to zero, as the inherent drag is balanced by the produced thrust. In the present case the total momentum is slightly less than zero, which can explain the slightly upstream tilted vortices near the trailing-edge. The presence of a double peak on each side of the horizontal velocity profile is due to the presence of the two vortex rows, which are now clearly separated horizontally. It is important to note that in this case two pairs of vortices are shed per oscillation cycle in opposition to the motionless case where only one pair of vortices is shed per cycle. Thus this mode is labelled multiple-vortices-per-half-cycle mode. In the vicinity of the trailing-edge the vortex structure appears to be tilted upstream as in a drag-producing wake, however this is *adjusted* further downstream. Such a behaviour was also reported in [18].

The plunging frequency is further increased to  $k = 7.85$ , which results in

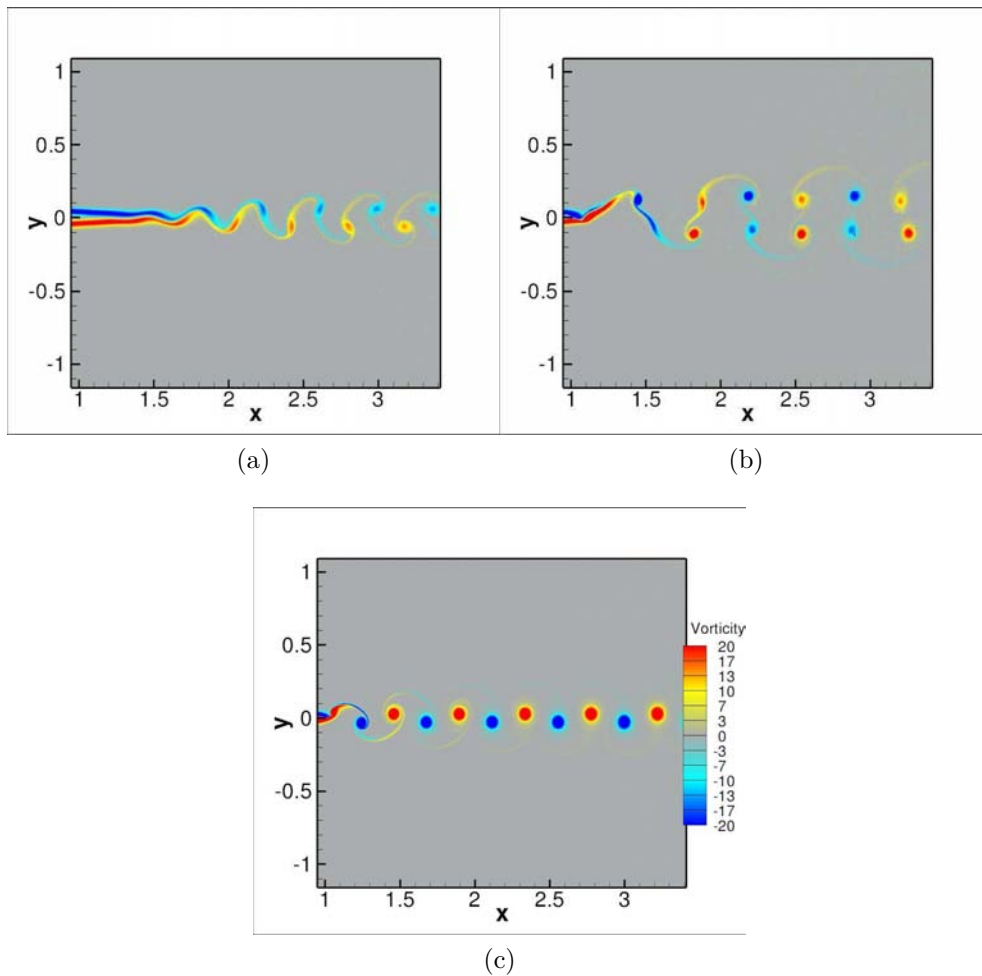


Figure 5.1: (a) Vorticity contours for a motionless airfoil representing a drag-producing wake at  $Re = 10^4$  and  $\bar{\alpha} = 0^\circ$ . (b) Vorticity contours for a plunging airfoil at  $k = 4.52$ ,  $h = 0.02$ ,  $Re = 10^4$  and  $\bar{\alpha} = 0^\circ$ ; representing a neutral wake. (c) Vorticity contours for a plunging airfoil at  $k = 7.85$ ,  $h = 0.02$ ,  $Re = 10^4$  and  $\bar{\alpha} = 0^\circ$ ; representing a thrust-producing wake.

another wake transition. The wake obtained is labelled the reverse or inverted Karman street, and consists of alternating rows of anticlockwise vortices (on the top of the centerline) and clockwise vortices (on the bottom of the centerline). Again only one pair of counter-rotating vortices is shed per oscillation cycle. This transition is from a neutral to a thrust-producing wake. The thrust-producing wake is characterized by mushroom-like vortex structures tilted downstream (see Fig. 5.1c). The time-averaged horizontal velocity profile is a jet-like (or momentum surfeit) profile indicating a net thrust production (see Fig. 5.2c). This means that the mean velocity in the wake is higher than the free-stream velocity.

When plotting close-ups of the trailing-edge region in the vorticity contour

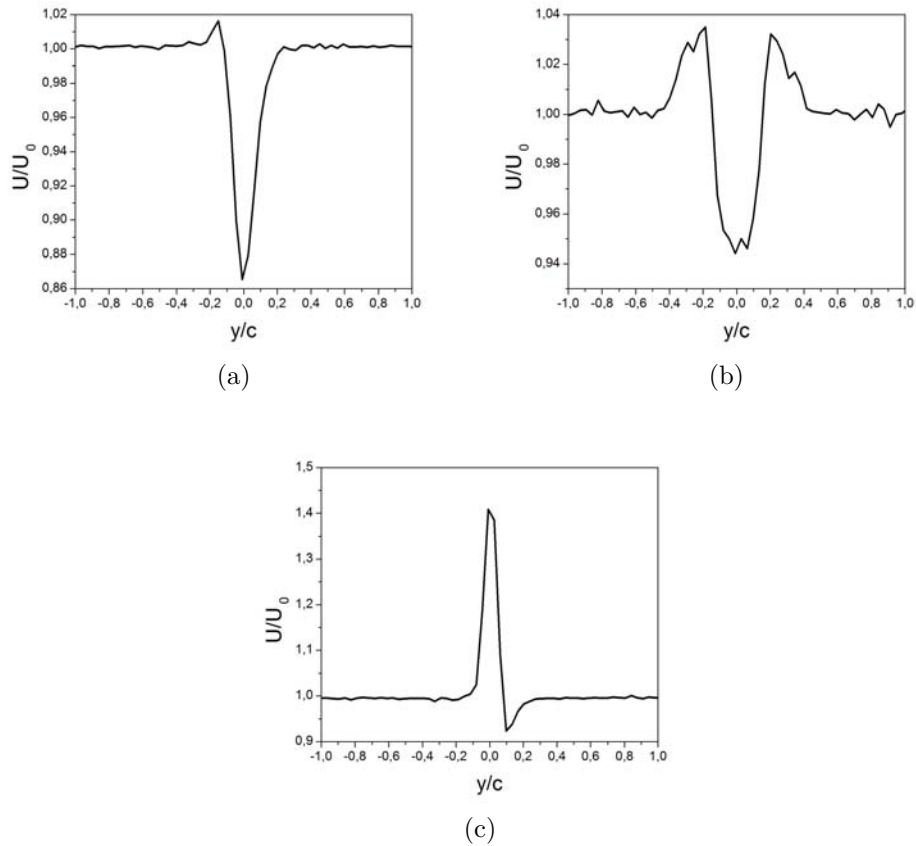


Figure 5.2: Time averaged horizontal velocity profiles at  $\bar{\alpha} = 0^\circ$  and  $Re = 10^4$  for (a) a motionless airfoil (drag-producing wake), (b) a plunging airfoil at  $k = 4.52$ ,  $h = 0.02$  (neutral wake) and (c) for a plunging airfoil at  $k = 7.85$ ,  $h = 0.02$  (thrust-producing wake).

distributions for the previous simulations (not presented here for brevity) the transition cited above can be followed with very good detail. The main observation for the simulations at constant amplitude  $h = 0.02$  and  $4.52 \leq k \leq 7.85$  is that the transition from a neutral to a thrust producing wake has two distinct phases, namely the rolling-up of the vorticity and its shedding at each side of the trailing-edge tip. The vorticity is shed when the airfoil is at its upper- and lowermost vertical position. The rolling-up of the vorticity at the trailing-edge occurs when the airfoil is at the vertical position  $y = 0$ .

Note that different vortex configurations, corresponding to different combinations of the frequency and amplitude of oscillations, can give rise to different neutral wakes [12, 18]. The latter can exhibit one vortex pair shedding per cycle or a multiple-vortices-per-half-cycle shedding [18].

### 5.3.2 Constant frequency transition

In this Section the frequency of oscillation is kept constant at  $k = 3.92$  and the amplitude is increased in order to obtain a transition from a drag- to a thrust-producing wake. Fig. 5.3a shows the vorticity contours of the flow at  $h = 0.001$ . Although the mushroom-like vortices are tilted upstream, the pairs of vortices are not equidistant and of the same size as observed for the drag-producing wake for the motionless airfoil (see Fig. 5.1a). The drag-nature of the wake is confirmed by the time-average velocity profile, which is a deficit one (Fig. 5.4a). This configuration was observed in [18] too and will be discussed in this investigation.

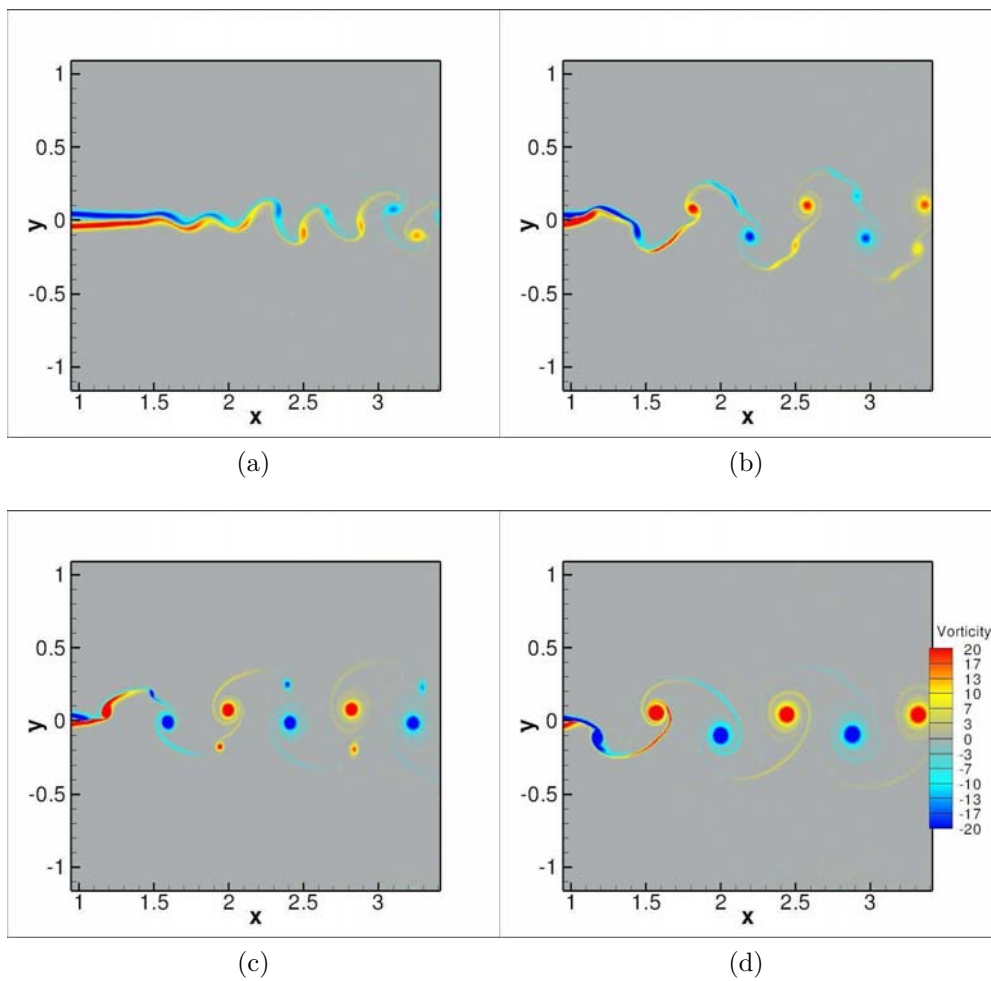


Figure 5.3: Vorticity contours snapshots at  $Re = 10^4$ ,  $\bar{\alpha} = 0^\circ$ ,  $k = 3.92$ . The amplitude of oscillation is (a)  $h = 0.001$ , (b)  $h = 0.02$ , (c)  $h = 0.035$  and (d)  $h = 0.05$ .

Increasing the amplitude to  $h = 0.02$  results in a wake transition (see Fig. 5.3b) as more than a vortex pair is shed per oscillation period. The vortices

are slightly tilted downstream, which is confirmed by the non-alignment of the vortices cores on the centerline. The time-averaged velocity profile shows that a transition occurred as the profile at the center of the wake points upward although the mean value of the drag coefficients is still negative (indicating drag production, see Fig. 5.4b). On the border of the bell shaped velocity profile the deficit in the mean velocity increased, which can be explained by the fact that the rows of vortices in the wake are more horizontally separated. This also explains that although the profile is pointing upwards there is an overall drag production. At  $h = 0.035$ , the multiple-vortices-per-half-cycle shedding persists, although the wake nature changed from drag to a neutral wake, as confirmed by the time averaged horizontal profile (see Fig. 5.3c). This is also reflected in the alignment of the vortices cores on the centerline and the vortices becoming untilted (the average horizontal velocity profiles which are symmetric around  $y = 0$ ). A thrust-producing wake is obtained at  $h = 0.05$  (see Fig. 5.3d), with the vortices now tilted downstream and the cores are again non-aligned on the centerline. This is again confirmed by the average velocity profile on Fig. 5.4d. Fig. 5.4 summarizes the drag to thrust transition when increasing the amplitude of the forced oscillations. This transition was observed experimentally in [12] at  $k = 7.85$ ,  $Re = 2 \times 10^4$  and  $0.0125 \leq h \leq 0.075$ , and computationally in [18]. The variation of the thrust coefficient for the constant frequency transition (not shown here for brevity reason) indicates an increase in the thrust coefficient value as the amplitude of oscillations is increased.

When plotting close-ups of the trailing-edge region in the vorticity contour distributions at  $k = 3.92$  and  $0.001 \leq h \leq 0.05$  (not presented here for brevity), and as for the constant amplitude drag/thrust transition, the transition has two distinct phases. These phases are the rolling-up of the vorticity and its shedding at each side of the trailing-edge region as well. The vertical position corresponding to the rolling-up and the shedding of the vorticity is *switched* along the transition process. This can be attributed to the variation in the amplitude of the oscillations.

### 5.3.3 Wake structures classification

The approximate boundaries defining different wakes types, determined experimentally, do not coincide with either the lines of constant thrust coefficient (as predicted by the Garrick model in [4]), or lines of constant  $kh$  (as concluded in [5]). This behaviour is more pronounced at low values of  $h$  which motivated the simulation of this configuration in the present investigation. *Young* in [18] classified plunging airfoils wake types based on several computational and experimental investigations (see Fig. 5.19 from [18]). Fig. 5.5 shows the wake classification for the simulations conducted in the present investigation. In Fig. 5.5 the three wakes, namely the drag-, thrust-producing and neutral wakes are simulated. As discussed above, the neutral wake zone is a transition between the

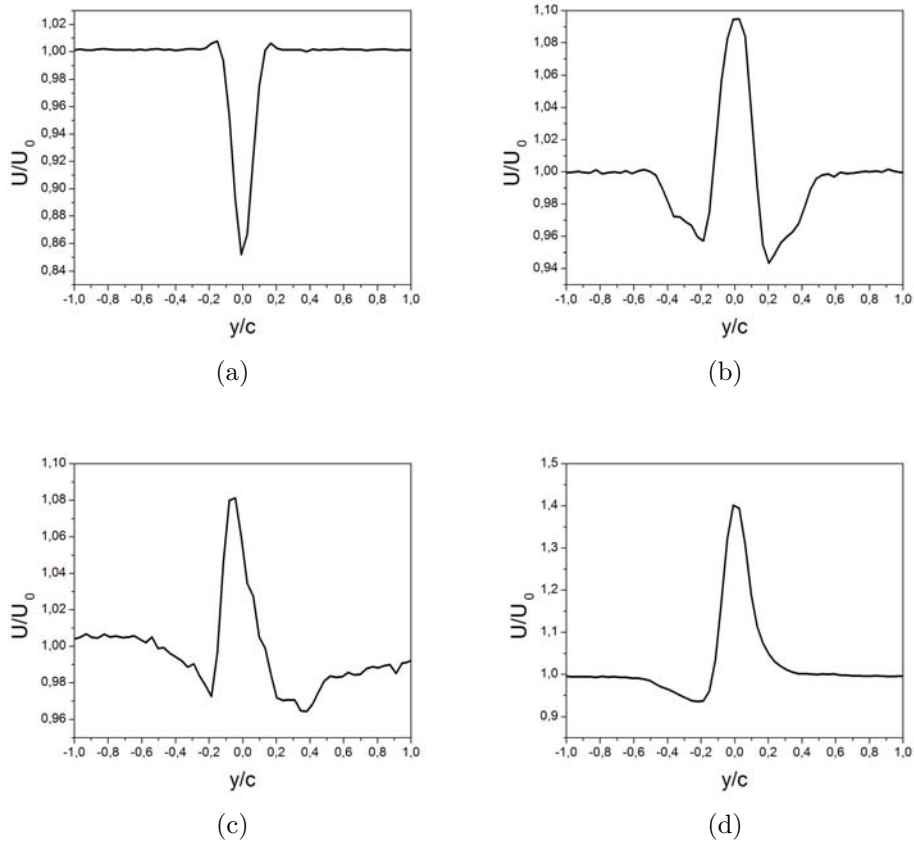


Figure 5.4: Time averaged horizontal velocity profiles at  $\bar{\alpha} = 0^\circ$ ,  $Re = 10^4$  and  $k = 3.92$ . The amplitudes of oscillations simulated are (a)  $h = 0.001$ , (b)  $h = 0.02$ , (c)  $h = 0.035$  and (d)  $h = 0.05$ .

drag- and thrust-producing wakes.

Comparing the results obtained by the present investigation to the ones obtained in [18] new features are present. The wakes described in [18] are well captured in the present investigations. Interestingly, two wake modes appear, which were not reported by [18] in his schematic wake classification. The first mode consists of multiple-vortices-per-cycle shedding with a thrust-producing wake. This mode is represented by the black circles on Fig. 5.5 for the combinations  $k = 1.96$  ( $h = 0.1$ ) and  $k = 1.96$  ( $h = 0.08$ ). The vorticity contours distribution for these two combinations are shown on Fig. 5.6. The second mode consists of a single pair of vortices per cycle shedding with a neutral wake. This mode appears as the open circles on Fig. 5.5 for the combinations  $k = 4.14$  ( $h = 0.025$ ) and  $k = 5.18$  ( $h = 0.02$ ). The vorticity contours distribution for these two combinations are shown on Fig. 5.7.

The use of the Spectral /hp Element Method (SEM) permits a better spatial

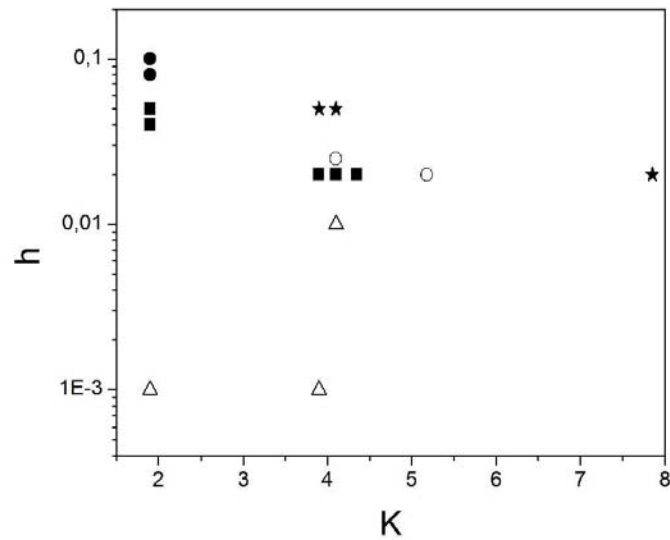


Figure 5.5: Wakes classification as function of the amplitude and frequency of the forced oscillations. The triangles are for drag-producing wakes with one vortex pair shedding per oscillation cycle. The stars represent thrust-producing wakes with one pair of vortices shed per oscillation cycle. The squares are for neutral wakes with multiple-vortices-per-cycle shedding. The open circles represent neutral wakes with one pair of vortices shed per oscillation cycle and the black circles are for thrust-producing wakes with multiple-vortices-per-cycle shedding.

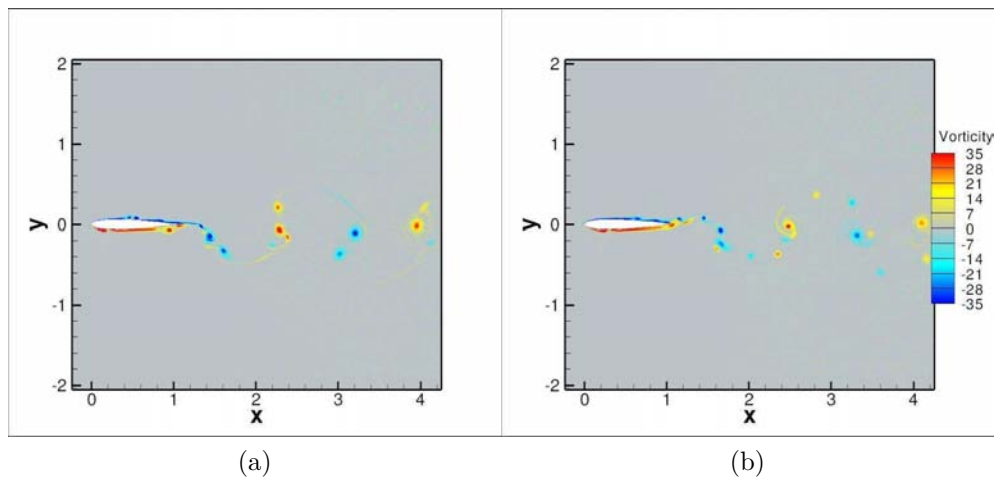


Figure 5.6: Vorticity contours snapshots at  $Re = 10^4$  and  $\bar{\alpha} = 0^\circ$ . (a)  $k = 1.96$  and  $h = 0.1$ , (b)  $k = 1.96$  and  $h = 0.08$ .

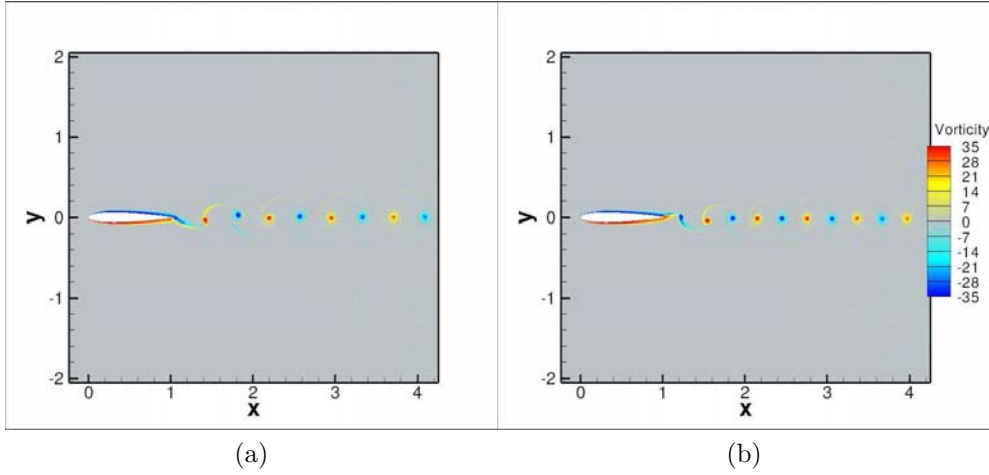


Figure 5.7: Vorticity contours snapshots at  $Re = 10^4$  and  $\bar{\alpha} = 0^\circ$ . (a)  $k = 4.14$  and  $h = 0.025$ , (b)  $k = 5.18$  and  $h = 0.02$ .

and temporal resolution and therefore made the appearance of the aforementioned modes possible. This contributes to a more accurate wake visualization and classification, in the sense that SEM captures more flow and transition details. As it can be seen in Fig. 5.5, SEM allows the distinction between the airfoil wakes even at the border of the different mode regions.

As mentioned above, neither the value  $kh$  (also referred to as the plunge velocity) nor the thrust coefficient are sufficient to characterize the different plunging airfoil wakes. In the following, two different wakes are simulated at the same  $kh$  value and the thrust coefficient is calculated. In Fig. 5.8 two wakes at  $kh = 0.08$  are simulated using two different combinations of the amplitude and the frequency of oscillations. In Fig. 5.8a the wake is a drag-producing wake ( $C_T = -2.61 \times 10^{-2}$ ) and more than a vortex pair is shed per oscillation cycle. In Fig. 5.8b the wake is a complex wake where 3 pairs of counter-rotating vortices and a positive vortex are shed per oscillation cycle. This complex shedding behaviour will be discussed in Section 5.3.4. Nevertheless, this wake is also a drag-producing wake ( $C_T = -2.36 \times 10^{-2}$ ), but it has a fundamentally different structure as the one in Figure 5.8a. Note that these two simulations have approximately the same thrust coefficient value, indicating that the thrust coefficient can also be discarded as the only wake classification parameter. To further assess this trend another simulation is performed at  $kh = 0.1$  using again two different combinations of the amplitude and the frequency of oscillations. In this case the wakes produced are not only different in their shape and the number of vortices shed per cycle of oscillation but also in their nature as one is drag-producing and the other is thrust-producing (see Fig. 5.9). In Fig. 5.9a the wake is drag-producing ( $C_T = -1.48 \times 10^{-2}$ ) and is a multiple-vortex-per-half-cycle wake. On the other hand, in Fig. (5.9b) only one pair of counter-rotating vortices is shed

per cycle and the wake produced thrust ( $C_T = 6.44 \times 10^{-2}$ ).

This confirms that neither  $kh$  or the thrust coefficient can be considered as the only parameters characterizing the plunging airfoils wakes. Rather the amplitude and the frequency (or reduced frequency) of oscillations have to be considered as separate control parameters. This is a further indication of the complicated nature of the unsteady flow produced by plunging (oscillating) airfoils.

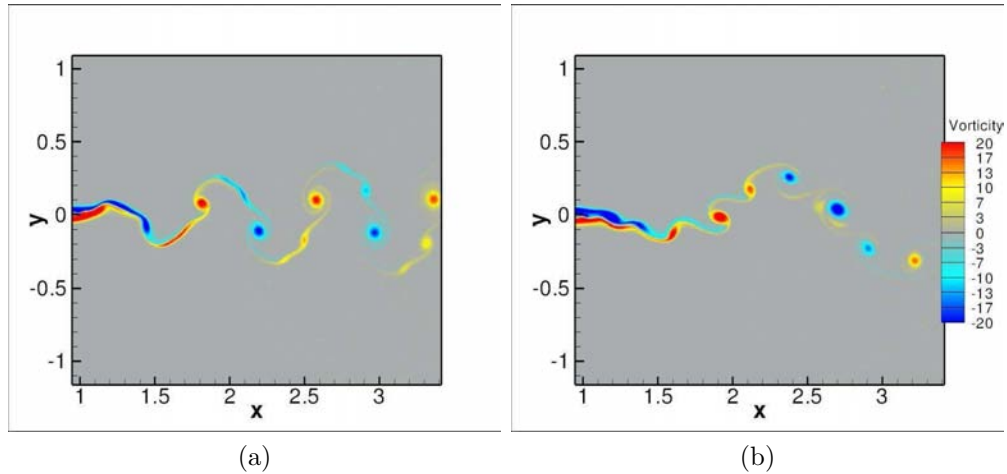


Figure 5.8: Vorticity contours snapshots at  $Re = 10^4$ ,  $\bar{\alpha} = 0^\circ$  and  $kh = 0.08$ . (a)  $h = 0.02$  and  $k = 3.92$ , (b)  $h = 0.04$  and  $k = 1.96$ .

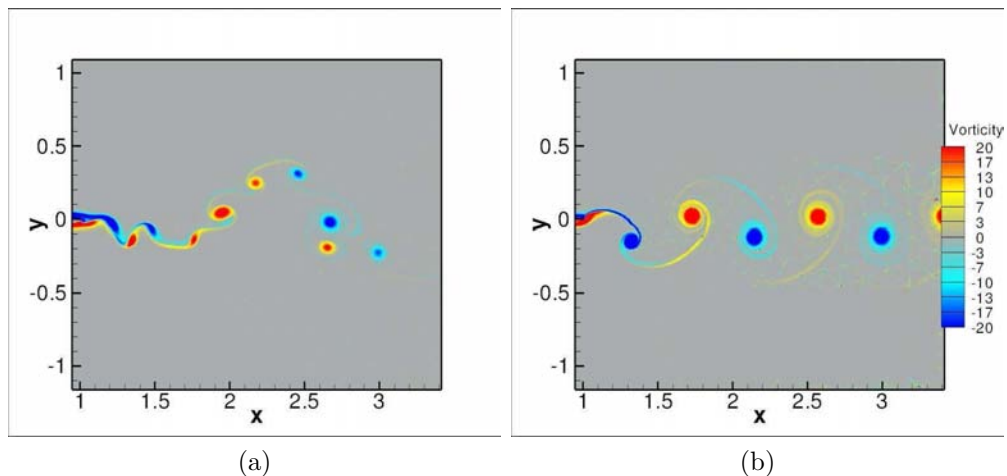


Figure 5.9: Vorticity contours snapshots at  $Re = 10^4$ ,  $\bar{\alpha} = 0^\circ$  and  $kh = 0.1$ . (a)  $h = 0.05$  and  $k = 1.96$ , (b)  $h = 0.05$  and  $k = 4.14$ .

### 5.3.4 The multiple-vortices-per-half cycle mode

Investigating the multiple-vortex-per-cycle mode, the leading-edge shedding can be dismissed as the only reason for the appearance of this mode. Although the leading-edge becomes more important at high amplitudes of oscillations and participate to the creation of more than a vortex pair per oscillation cycle, multiple-vortices-per-cycle mode exist even when there is no leading-edge shedding. It is important to point out the presence of a second frequency associated with the natural shedding at the trailing-edge and a frequency associated with the shedding resulting from the forced airfoil motion. These two frequencies are likely to interact over the oscillation cycle. This interaction offers a more plausible explanation for the origin of the multiple-vortex-per-cycle mode [18, 19]. In this investigation, a relation between the interaction of the two aforementioned frequencies and the observed shedding modes is established.

Fig. 5.10 is a close-up of the trailing-edge region for the case of the neutral wake (at  $k = 3.92$  and  $h = 0.02$ ) with plotted streamlines, for one oscillation cycle. In Fig. 5.10a there is a separation region on the upper side of the airfoil trailing-edge. During a cycle of plunging motion (see Fig. 5.3.4) the separation region develops on both sides of the airfoil and its shape and size changes. This separation region induces an effective blunt-edge-like body configuration and will have a natural shedding associated with it.

It has been established for the forced wakes of cylinders, that the wake can be in three possible states. These states are dominated either by the natural frequency shedding, or by the forcing frequency shedding (this mode is called the lock-in mode) or by a harmonic shedding (which is the interaction region of the natural and the forced shedding frequency) [7]. This is well captured on a plot representing the forcing frequency over the natural frequency as a function of the oscillations amplitude. This plot is called the lock-in boundary graph and is shown in [7] (Fig. 24). A similar conclusion can be made for the forced wakes of airfoils, although the presence of the sharp trailing-edge makes that the shape of the lock-in boundary is different from the one for a cylinder. The main difference is that the lock-in boundary is not symmetric and that the harmonic boundary meets the lock-in boundary at  $k/k_{nat} = 0.5$  (where  $k_{nat}$  is the natural shedding frequency). This is due to the fact that any harmonic (multiple) of the forcing frequency will be greater than the natural shedding frequency.

Indeed we observed, when examining a number of simulations, that at certain regimes there is an interaction between the natural and the forcing frequency resulting in a *harmonic* response, where the dominant frequency in the wake is the combination of these two frequencies. This state results in the shedding of more than one pair of counter-rotating vortices. In other regimes, where either the natural or the forcing frequency is the dominant response frequency, only one pair of vortices is shed. At high values of  $k$  and  $h$  multiple vortices pairs can be shed in one cycle, indicating the presence of a threshold value for  $h$  and  $k$ , at

which value the leading-edge shedding becomes important and participates in the shedding of more than a pair of vortices per oscillation cycle. This phenomenon of frequency interactions may also be the origin of the different wake behaviour observed for flows with the same  $kh$  obtained with different combinations of  $k$  and  $h$ .

These findings are of great importance when considering flow control issues. The identification of the flow states is closely related to flow control as the forcing imposed on the airfoil can be considered as an active control system and its performance can be determined from the state of the airfoil wake [7]. This determination can provide valuable information as to which control strategy is better to achieve the purpose sought from using the control device.

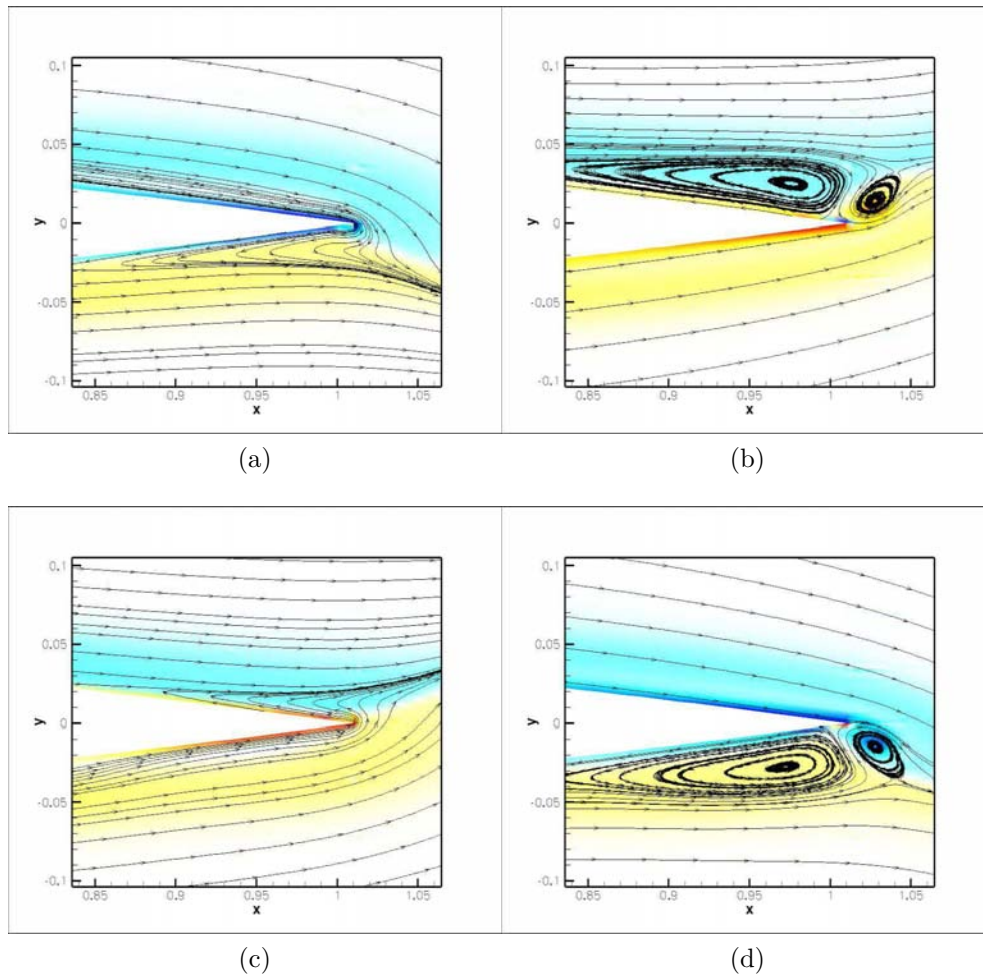


Figure 5.10: Close-up of the vorticity contours at the trailing-edge region with streamlines at  $\bar{\alpha} = 0^\circ$ ,  $Re = 10^4$ ,  $k = 4.52$  and  $h = 0.02$ . The four close-ups correspond to one cycle of oscillation: (a) lowermost  $y$  position, (b)  $y = 0$ , (c) uppermost  $y$  position, and (d)  $y = 0$ , thus covering one cycle of oscillation.

## 5.4 Conclusion

We successfully simulated the two dimensional unsteady flow on both a motionless and a heaving airfoil using a high order CFD method. The high spatial and temporal resolution achieved by the Spectral Element Method permits a detailed analysis of the flow over the airfoil and the near wake. This enables the description of the shedding process through which the wake undergoes a transition from a Karman street to a reversed Karman street. We could successfully simulate drag, neutral and thrust wakes and the transition between these wakes. We were able to reproduce previous results obtained in the literature. New and interesting results are presented concerning the interaction of the natural shedding frequency of the airfoil and the imposed forcing frequency and their role in the formation of more than a vortex per oscillation cycle. These results confirm for the first time for the airfoil geometry that it is in the harmonic regime (resulting from the interaction of the natural shedding frequency of the airfoil and the shedding frequency of the imposed motion) that the multiple-vortices-per-half-cycle mode appears. Moreover, more shedding modes are captured, which assess the ability of the computational method to produce more accurate wake classification and wake transitions. Two more modes are observed here and added to the wake classification are a multiple-vortex-per-half-cycle in a thrust producing wake and one pair of vortex shedding in a neutral wake.

## Bibliography

- [1] A. Betz. Ein Beitrag zur Erkl drung des Segelflufes. *Zeitschrift f r Flugtechnik und Motorluftschiffahrt*, 3:269–272, 1912.
- [2] B. S. Carmo, S. J. Sherwin, P. W. Bearman, and R. H. J. Willden. Wake transition in the flow around two circular cylinders in staggered arrangements. *J. Fluid Mech.*, 597(1):1–29, 2008.
- [3] A. N. Cookson, D. J. Doorly, and S. J. Sherwin. Mixing Through Stirring of Steady Flow in Small Amplitude Helical Tubes. *Ann. Biomed. Eng.*, 37:710–721, 2009.
- [4] I. E. Garrick. Propulsion of a Flapping and Oscillating Airfoil. Report 567, NACA, 1937.
- [5] K. D. Jones, C. M. Dohring, and M. F. Platzer. Wake Structures Behind Plunging Airfoils: A Comparison of Numerical and Experimental Results. In *34th AIAA Aerospace Sciences Meeting and Exhibit*, Reno-Nevada, 15-18 January 1996. American Institute of Aeronautics and Astronautics.
- [6] G. E. Karniadakis and S. Sherwin. *Spectral/hp Element Methods for Computational Fluid Dynamics*. Oxford University Press, 2005.
- [7] G. E. Karniadakis and G. S. Triantafyllou. Frequency selection and asymptotic states in laminar wakes. *J. Fluid Mech.*, 199(1):441–469, 1989.
- [8] G. E. Karniadakis, S. A. Orszag, and M. Israeli. High-order splitting methods for the incompressible Navier-Stokes equations. *J. Comp. Phys.*, 97:414–443, 1991.
- [9] R. Katzmayr. Effect of Periodic Changes of Angle of Attack on Behaviour of Airfoils. Technical Report TM-147, NACA, 1992.
- [10] R. Knoller. Die Gesetze des Luftwiderstandes. *Flug- und Motortechnik*, 3(21):1–7, 1909. Wien.
- [11] M. M. Koochesfahani. Vortical patterns in the wake of an oscillating airfoil. *AIAA J.*, 27:1200–1205, 1989.
- [12] J. C. S. Lai and M.F. Platzer. Jet Characteristics of a Plunging Airfoil. *AIAA J.*, 37(12):1529–1537, 1999.
- [13] L. Li, S. J. Sherwin, and P. W. Bearman. A moving frame of reference algorithm for fluid/structure interaction of rotating and translating bodies. *Int. J. Numer. Meth. Fl.*, 38:187–206, 2002.

- 
- [14] W. Medjroubi, B. Stoevesandt, B. Carmo, and J. Peinke. Direct numerical simulations of the flow around a heaving airfoil. Submitted for publication in *Computers and Fluids*, 2010.
- [15] A. V. Shatalov. *Numerical Simulation of Incompressible Laminar Flows Using Viscous-Inviscid Interaction Procedure*. PhD thesis, University of California, Division Mechanical and Aeronautical Engineering, 2006.
- [16] S. J. Sherwin. <http://www3.imperial.ac.uk/spectralhp>, 2010.
- [17] G. S. Triantafyllou, M. S. Triantafyllou, and M. A. Grosenbaugh. Optimal Thrust Development in Oscillating Foils with Application to Fish Propulsion. *J. Fluid Struct.*, 7:205–224, 1993.
- [18] J. Young. *Numerical simulation of the unsteady aerodynamics of flapping airfoils*. PhD thesis, School of Aerospace, Civil and Mechanical Engineering. The University of New South Wales. Australian Defence Force Academy, May 2005.
- [19] J. Young and J. C. S. Lai. Oscillation Frequency and Amplitude Effects on the Wake of a Plunging Airfoil. *AIAA Journal*, 42(10):2042–2052, 2004.



## Chapter 6

# Frequency Selection in Plunging Airfoil Wakes Using a High-Order Method <sup>1</sup>

In this contribution the two dimensional unsteady flow over a plunging NACA0012 airfoil is simulated using a high-order numerical method associated with a moving frame of reference technique. The goal of using a high-order numerical method is to characterize heaving airfoil wakes with very fine temporal and spatial resolution. This characterization is essential in understanding the transition process which oscillating airfoils undergo, and can enable more control on the transition. The response of motionless and periodically forced airfoils is considered separately. The flow is investigated at a mean incidence  $\bar{\alpha} = 0^\circ$ , Reynolds number  $Re = 10^4$ , and over a range of heaving frequencies and amplitudes. The airfoil wakes are analyzed with respect to their frequency response and to their type. It is shown that for forced airfoils three regimes of frequency response exist: (a) a natural regime where the response frequency is equal to the natural frequency, (b) a lock-in regime where the response frequency is equal to the forcing frequency, and (c) a harmonic regime where the response frequency is a mixture of the natural frequency and the forcing frequency. The transition between these regimes is presented at constant frequency and constant amplitude of the forcing oscillations. The frequency regimes are then explored in detail and related to the wake types and to the wake-types transition. The results obtained are in accordance with previously published experimental and computational investigations. Furthermore, a more detailed wake classifica-

---

<sup>1</sup>Submitted to publication as W. MEDJROUBI, B. STOEVE SANDT and J. PEINKE: *Frequency Selection in Plunging Airfoil Wakes Using a High-Order Method* in Physics of Fluids.

tion is presented, where two more wake configurations are captured. The role of the trailing-edge and the interaction of the natural shedding frequency of the airfoil with the imposed forcing frequency in the creation of multiple-vortices-per-half-cycle shedding mode is investigated. These results show that the frequencies interaction can be related to the appearance of the multiple-vortices-per-half-cycle mode.

## 6.1 Introduction

Oscillating airfoils have received much attention and interest in the framework of different contexts and applications. This attention is due to the unsteadiness and the complex nature of these flows, rendering their numerical simulation a challenging task. Unsteadiness and its consequences are fundamentally important problems which concern a broad range of applications. These undesirable consequences can range from flutter [37], vortex-induced-vibrations (VIV) [44], and flow-induced-vibrations (FIV) [5, 31], which can be the cause of buffeting and material fatigue [3, 45]. Other areas of interest for unsteadiness are turbomachinery and, recently, the field of wind turbines design and manufacturing. On the other hand, unsteadiness can be used in a beneficial way, as oscillating airfoils can generate propulsion. This latter application motivated research on Micro Air Vehicles (or MAVs) and Unmanned Aerial Vehicles (UAVs) [29, 41]. MAVs have a broad range of applications, ranging from military to civil applications, as monitoring, remote sensing, forestry and wildlife surveys. Some work is also dedicated to the use of *smart control systems*, which use the unsteadiness in an efficient way to actively or passively control airfoils to reduce vibrations [15, 27], acoustic signature or achieve higher energy efficiency [32, 40]. Other beneficial aspects of unsteadiness are stall delay to higher incidences, controlled vortex generation and controlling the unsteady forces in some effective way as to permit improvements of performance.

The most studied aspect of oscillating airfoils is the ability to generate thrust and/or lift using such simple motions. And it is well established that flapping (or oscillating) airfoils are more efficient than their fixed counterparts when the size and thus the Reynolds number are decreased [16, 22]. The thrust production is achieved at certain combinations of frequency and amplitude of oscillations. This production results from the fact that flapping airfoils create an effective angle of attack, so that an aerodynamic force is generated which decomposes into lift and thrust forces during both the up and down strokes of the flapping motion. This effect is called the *Knoller-Betz* effect. This effect was confirmed experimentally by *Katzmayr* [21] and it motivated research in the areas of animal-like propulsion and the development of insect-like and MAVs. Therefore, there is a need to understand flapping wings/airfoils mechanisms which are used in nature and to

adopt or change these mechanisms for the purpose of designing better and more efficient MAVs. For this purpose, it is necessary to predict the flow over and in the wake of these airfoils as well as the forces and loads they experience.

Oscillating airfoils include: Heaving (or plunging), pitching and flapping airfoils. Pure heaving airfoils have received less attention compared to pitching airfoils. This is mainly due to the applications involving dynamic stall on helicopters, which are more concerned by the pitching motion. Nevertheless, heaving airfoils exhibit a rich variety of wakes, which are classified into three types as drag-producing, neutral and thrust-producing wakes [11, 23, 46]. This classification depends on the frequency and amplitude of the heaving oscillations. At low reduced frequencies the wake is a Karman vortex street with one pair of opposite vortices shed during each oscillation cycle. The vortex pairs for *mushroom-like* structures which are tilted upstream and the wake produces drag. At high reduced frequencies the wake becomes an opposite or reversed Karman vortex street, with one pair of opposite vortices shed per oscillation cycle tilted downstream. The sense of rotation of the vortices is inverted compared to the Karman street and this configuration produces thrust. During the transition from drag to thrust-producing wakes, a neutral mode appears where the produced thrust equals the inherent drag (thus the name *neutral* wake). The vortex pairs are untilted and in some cases this mode is characterized by the shedding of more than one vortex pair per oscillation cycle and is thus referred to as the multiple-vortex-per-half-cycle mode. The details of the wake structure formation, and the lift and drag production are not well understood, especially the multiple-vortex-per-half-cycle mode [46, 47]. The multiple-vortex-per-half-cycle mode origin is thought to be the result of the interaction between the natural shedding of the airfoil and the imposed heaving frequency [26, 46].

*Freytmuth* [11], showed experimentally that an airfoil subjected to oscillations either in pitch or in heave can produce thrust. *Koochesfahani* [22], studied the flow patterns of a pitching NACA0012 profile experimentally using water tunnel measurements. The airfoil was pitching around its quarter chord at Reynolds number  $Re = 12 \times 10^3$  and two different amplitudes ( $2^\circ$  and  $4^\circ$ ). The results also demonstrated that pitching airfoils can generate thrust and that the flow dynamics are solely described by the Strouhal number  $St$  ( $St = fA U_0$ , where  $f$  is the forcing frequency,  $A$  is defined as twice the forcing amplitude  $h$ , and  $U_0$  is the mean-stream velocity). These findings are confirmed by the experimental work of *Jones & Dohring* [16]. The authors used Laser-Doppler Velocimetry (LDV) and an unsteady potential-flow code. The experiments and the simulations covered a wide range of heaving frequencies and amplitudes,  $0 < k < 15$ ,  $0 < h < 0.8$ , where  $k$  is the reduced frequency ( $k = 2\pi fc/U_0$ ). The authors found that a line of constant heave velocity  $V_p = kh$ , which is equivalent to the strouhal number, separates the different flow regimes where thrust or drag is produced. These results confirmed the analytical results previously obtained by *Triantafyllou & al.* [42]. Nevertheless, the experimental work in [4, 36] challenged the validity of the

single-parameter characterisation of oscillating airfoils propulsive efficiency, wake patterns, and thrust production. *Young* conducted several numerical studies over a wide range of heaving amplitudes and frequencies at  $Re = 2 \times 10^4$  [35, 46–48] and compiled the results of several experimental results [23] and found that the  $St$  number can not be considered as the only parameter controlling the aerodynamics of heaving airfoil flows. He found that the aerodynamics depends on both the  $St$  number and the flapping frequency independently. In this paper we challenge the assumption of a unique control-parameter characterizing the oscillating airfoils thrust production. We also challenge the assumption that the Strouhal number is sufficient in characterizing the oscillating airfoils wake types.

The forced wake of the airfoil can undergo three different regimes, depending on the forcing frequency and the forcing amplitude and the relation between the forcing frequency and the natural frequency of the airfoil. The natural frequency (or Strouhal frequency) is defined as the frequency of shedding of vortices of the unforced airfoil [19, 46]. The three regimes exhibited are called natural, harmonic, and lock-in regimes. In the natural regime the vortex shedding frequency is equal to the natural frequency. In the harmonic regime, the vortex shedding frequency is a mixture or a combination of the natural and the forcing frequency. Finally, in the lock-in regime, the vortex shedding frequency is locked to the forcing frequency. These regimes have been extensively studied and observed for oscillating cylinders [9, 19, 33, 34, 49] and less explored for oscillating airfoils [46, 48]. The objective of this paper is to explore these flow regimes and to determine the relation between the flow frequency regimes and the wake types.

Most of the numerical methods used to model the flow around and in the wake of oscillating airfoils employ low-order spatial and temporal discretizations. These methods are unable to capture the flow details unless a very large number of grid points is used and therefore are computationally cost-ineffective, especially if highly resolved data is to be extracted. This cost is further increased if adaptivity is to be implemented. The use of high-order numerical methods offers on the other hand the advantage of higher spatial and temporal discretization using less grid points and the possibility of more advantageous adaptivity techniques [6, 18].

We use Spectral/*hp* Element Methods combined with a moving-frame of reference technique to investigate the problem of the flow around an oscillating airfoil in an attempt to achieve a better accuracy than that obtained using lower-order numerical methods. In this scope all the simulations presented in this work are Direct Numerical Simulations (DNS), in order to capture all the flow details and particularly the spatio-temporal flow evolution. Our choice of the numerical method is also based on the possibility to obtain highly accurate temporal and spatial data that can be used in applications such as turbulence characterization and non-linear analysis of the airfoil response to forced oscillations. To the authors knowledge, this is the first time where the frequency-regimes are investigated for a heaving airfoil using a high-order numerical approach, as most of the studies for this type of motion were concerned with the wake configuration [46],

[2], [10].

In this paper the incompressible, 2D and unsteady flow over a stationary and a heaving NACA0012 airfoil is simulated. The Reynolds numbers considered are moderate ( $Re = 10^4 - 3 \times 10^4$ ), which corresponds to MAVs applications. A range of heaving amplitudes and frequencies of oscillation is simulated in order to expose the frequency regimes introduced earlier and to achieve a transition between these regimes. This transition is simulated by varying the amplitude of oscillation (at constant frequency) and by varying the frequency of oscillation (at constant amplitude). The dependency of the frequency regimes on the relation between the natural and forcing frequency is explored as the origin of the multiple-vortex-per-half-cycle shedding mode. The Spectral /hp Element Method and the moving-frame of reference technique are introduced in Section 6.2. The characterisation of the wake modes in function of the interaction of the natural shedding frequency and the imposed heaving frequency interaction are presented in Section 6.3. Finally, Section 6.4 contains a summary of the findings of this paper.

## 6.2 The Numerical Method

The main idea behind using high-order numerical methods is to achieve high accuracy, resolving all the flow length scales at a reduced cost and avoiding the extra costs of remeshing or excessive grid resolution [30]. In this context, global spectral methods have been extended to multi-domains (spectral elements) to provide a better geometric flexibility. Spectral/hp Element Methods combine the characteristics and the advantages of both finite elements and spectral methods. Unlike pure spectral methods and finite elements methods, Spectral/hp Element Methods allow the use of two refinement techniques simultaneously: the  $h$ -refinement, denoting the increase of the number of elements, and the  $p$ -refinement, denoting the increase of the polynomial order of the approximation [18]. The  $p$ -refinement is a powerful tool, as it offers the possibility of increasing the simulations accuracy without any remeshing by increasing the order of the approximation in all or parts of the computational domain, which can be considered as a way of implementing adaptivity.

In the framework of the Spectral /hp Element Method the physical domain and the governing equations have to be spatially and temporally discretized. The method used in this paper was developed by *Sherwin & Karniadakis* [17, 18, 20] and is shortly introduced in this Section.

The incompressible, unsteady and viscous flow over an airfoil is governed by the Navier-Stokes equations, written as follows

$$\frac{\partial \mathbf{u}}{\partial t} + (\mathbf{u} \cdot \nabla) \mathbf{u} = -\nabla p + \frac{\nabla^2 \mathbf{u}}{Re}, \quad (6.1)$$

where  $\mathbf{u}$  is the velocity vector that satisfies the incompressibility condition ( $\nabla \cdot \mathbf{u} = 0$ ),  $p$  is the pressure,  $Re = U_0 c / \nu$  is the Reynolds number based on the airfoil chord length  $c$ ,  $\nu$  is the kinematic viscosity, and  $U_0$  is the free-stream velocity.

### Spatial discretization

For 2D problems, the physical domain discretization is achieved through its division into triangular and/or quadrilateral subdomains. Within each subdomain a spectral expansion in the form of a high-order polynomial is used to represent the solution variable, as follows

$$u(x, y) = \sum_i^N \sum_m^{N_1} \sum_n^{N_2} u_{m,n}^i u_{m,n}(r(x, y), s(x, y)), \quad (6.2)$$

where  $u_{m,n}(r, s)$  is a polynomial expansion basis used to approximate  $u$  over  $i$  triangular subdomains by a  $C^0$  continuous expansion (for rectangular subdomains see [18]),  $u_{m,n}^i$  are the expansion coefficients in the  $i^{th}$  subdomain,  $(x, y)$  are the cartesian spatial coordinates and  $(r, s)$  are the local coordinates within the subdomains.  $N$  is the total number of subdomains, and  $N_1, N_2$  are the number of the quadrature points in the  $r$  and  $s$  directions, respectively. The space spanned by the local coordinates system is defined as

$$L^2 = \{(r, s) | -1 \leq r, s; r + s \leq 0\}, \quad (6.3)$$

and the orthogonal expansion bases used are Dubiner's modified bases, defined as

$$u_{m,n} = P_m^{0,0} \left( 2 \frac{(1+r)}{(1-s)} - 1 \right) (1-s)^m P_n^{2m+1,0}(s), \quad (6.4)$$

$P_n^{\alpha,\beta}(x)$  is the  $n^{th}$ -order Jacobi polynomial in the  $[-1, 1]$  interval, which satisfies the orthogonality relationship

$$\int_{-1}^1 P_m^{\alpha,\beta}(x) P_n^{\alpha,\beta}(x) (1-x)^\alpha (1+x)^\beta dx = \delta_n^m, \quad (6.5)$$

$\delta_n^m$  is the Kronecker-delta. The Jacobi polynomial is expressed as follows [1, 12]

$$P_n^{\alpha,\beta}(x) = \frac{(-1)^n}{2^n n!} (1-x)^{-\alpha} \frac{d^n}{dx^n} [(1-x)^{\alpha+n} (1+x)^{\beta+n}], \alpha, \beta > -1. \quad (6.6)$$

The bases are decomposed into boundary and interior modes (thus allowing the construction of a global  $C^0$  expansion). Integration and differentiation are performed at elemental level, and an elemental mapping which allows the generalisation of the local operations in a standard region to elements of general shapes is defined. To extend these techniques to a  $C^0$  multi-dimensional basis, global

operations such as matrix numbering, connectivity and assembly are introduced [17, 18].

## Temporal discretization

The temporal discretization of the Navier-Stokes equations is achieved via a time-splitting scheme [20], where three steps are required to determine the fields for the next time step using the velocity at the previous time step. This is achieved by writing the Navier-Stokes equation in the form:

$$\frac{\partial \mathbf{u}}{\partial t} = -\nabla p + \nu \mathbb{L}(\mathbf{u}) + \mathbb{N}(\mathbf{u}), \quad (6.7)$$

where  $\mathbb{L}(\mathbf{u}) \equiv \nabla^2 \mathbf{u}$  and  $\mathbb{N}(\mathbf{u}) \equiv -\mathbf{u} \cdot \nabla \mathbf{u}$  are the linear and non-linear operators; respectively. The temporal discretization is achieved via the propagation of  $\mathbf{u}^n$  and  $p^n$  at a time step  $n$ , over a time step  $\Delta t$ , to determine  $\mathbf{u}^{n+1}$  and  $p^{n+1}$  at the next time step  $n + 1$ . This is expressed as follows

$$\frac{\tilde{\mathbf{u}} - \sum_{q=0}^{J_i-1} \alpha_q \mathbf{u}^{n-q}}{\Delta t} = \sum_{q=0}^{J_e-1} \beta_q \mathbb{N}(\mathbf{u}^{n-q}), \quad (6.8)$$

$$\nabla^2 \bar{p}^{n+1} = \frac{\nabla \cdot \tilde{\mathbf{u}}}{\Delta t}, \quad (6.9)$$

$$\frac{\gamma_0 \mathbf{u}^{n+1} - \tilde{\mathbf{u}}}{\Delta t} + \nabla \bar{p}^{n+1} = \frac{1}{Re} \nabla^2 \mathbf{u}^{n+1}, \quad (6.10)$$

where in the first step, the non-linear terms are advanced using a convective form which is integrated in time via a multilevel explicit Adams-Bashforth scheme, represented by the coefficient  $\beta_q$ . An implicit time scheme is used for the integration of the linear terms.  $J_e$  and  $J_i$  are the integration orders of the explicit and implicit schemes; respectively. In the second step, the time-averaged pressure term  $\bar{p}^{n+1}$  is calculated using the divergence of Eq. (6.8). In the third step, the viscous term is treated implicitly via an Euler backwards scheme, where  $\gamma_q$  are appropriately chosen weights. The coefficients  $\alpha_q$ ,  $\beta_q$ , and  $\omega_0$  take different values depending on the integration order [7, 20]. This time integration numerical scheme requires both velocity and pressure boundary conditions to be defined. High-order Neumann boundary conditions are imposed for the pressure (to ensure that the splitting error is consistent with the overall temporal discretization) as follows

$$\frac{\partial \bar{p}^{n+1}}{\partial \mathbf{n}} = n \cdot \left\{ \sum_{q=0}^{J_e-1} \beta_q \left[ \mathbb{N}(\mathbf{u}^{n-q}) - \frac{1}{Re} (\nabla \times (\nabla \times \mathbf{u}^{n-q})) \right] \right\}. \quad (6.11)$$

## Airfoil motion

To implement the airfoil motion the Navier-Stokes equations and the boundary conditions are written in a moving frame of reference. The method is briefly described here. For further details of the solution procedure we refer the reader to [24].

Let's consider that the body is performing a translational motion  $d$  defined in the fixed or absolute frame of reference  $(X_a, Y_a)$  as  $d = (a(t), b(t))^T$ . A moving frame of reference  $(x_m, y_m)$  attached to the airfoil is defined as a function of the absolute frame as:

$$X_a = a(t) + x_m \cos\theta + y_m \sin\theta, \quad (6.12)$$

$$Y_a = b(t) - x_m \sin\theta + y_m \cos\theta, \quad (6.13)$$

where  $\theta$  is the rotational angle in the moving frame of reference and  $a(t)$  and  $b(t)$  represent the coordinates of the origin of the moving frame of reference in the absolute frame of reference (see Fig. 6.1). In the case of a heaving (non-rotating) airfoil  $\theta$  and  $a(t)$  are constant. Using matrix notation one obtains the transformation from the coordinates in the absolute frame of reference to the moving frame of reference as:

$$\mathbf{X}_a = \mathbf{d} + \mathbf{A}\mathbf{x}_m, \quad (6.14)$$

and the inverse transformation as:

$$\mathbf{x}_m = \mathbf{A}^T(\mathbf{X}_a - \mathbf{d}), \quad (6.15)$$

where  $d = (a(t), b(t))^T$  and  $A$  is the matrix defined as :

$$\begin{pmatrix} \cos\theta & \sin\theta \\ -\sin\theta & \cos\theta \end{pmatrix}$$

Using the definition of the coordinates  $(x_m, y_m)$  given by the equation (6.12), the Navier-Stokes equations are re-written in the moving frame of reference as follows:

$$\nabla \cdot \mathbf{u} = 0, \quad (6.16)$$

$$\frac{\partial \mathbf{u}}{\partial t} + (\mathbf{u} \cdot \nabla) \mathbf{u} = -\nabla p + \frac{1}{\text{Re}} \nabla^2 \mathbf{u} + \mathbf{Q}(t), \quad (6.17)$$

$$Q(t) = -A^T \ddot{d}, \quad (6.18)$$

where the term  $A^T \ddot{d}$  is the result of the unsteady translational motion, in our case a heaving motion. The boundary conditions are also transformed in the

moving frame of reference, and expressions are derived for Neumann and Dirichlet boundary conditions [24].

For the present simulations we have considered the body as being rigid (non-deformable) and forced to oscillate in heave (plunge) motion, as illustrated in Figure 6.1. The heave motion is defined as

$$d = y(t) = h \cos(2\pi ft), \quad (6.19)$$

where  $y(t)$  is the time-dependent vertical motion,  $h^* = h/c$  is the non-dimensional heaving frequency, and  $f^* = f/c/U_0$  is the non-dimensional heaving frequency (for simplicity, the superscript  $*$  will be dropped in the remainder of this paper). The airfoil is set at a constant initial angle of attack  $\bar{\alpha} = \theta$  (or mean incidence) and is forced to oscillate vertically in a sinusoidal fashion.

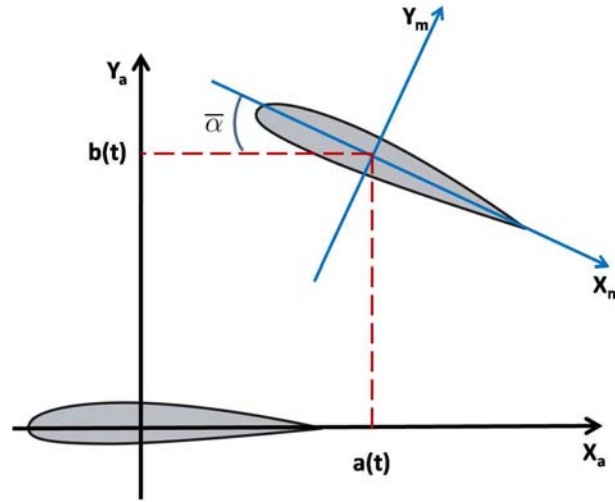


Figure 6.1: Schematic representation of the absolute and moving frame of references. The subscript  $a$  refers to the absolute frame of reference and  $m$  to the moving frame of reference.  $\theta$  is the angle at which the airfoil is set, it can be considered as the mean angle of attack  $\bar{\alpha}$

## Aerodynamic forces

The forces and moments are evaluated by calculating their viscous and pressure contributions. The aerodynamic force applied by the flow on the body can be expressed as the integration of local stresses as:

$$F = \int_{\Omega} \sigma n_A ds_A = - \int_{\Omega} p n_A ds_A + \int_{\Omega} \tau n_A ds_A = F_{press,A} + F_{visc,A}. \quad (6.20)$$

where  $\sigma = -p\mathbf{I} + \tau$  is the stress tensor,  $\Omega$  is the airfoil surface,  $n_A$  is the unit normal on the airfoil,  $F_{press,A}$  are the pressure forces and  $F_{visc,A}$  are the viscous forces. The subscript  $A$  indicates that the quantities are expressed in the absolute frame of reference. The forces in Equation (6.20) are expressed in the moving frame of reference as follows:

$$F = F_{press,A} + F_{visc,A} = A(F_{press,m} + F_{visc,m}), \quad (6.21)$$

where  $A$  is the matrix introduced in Equation (6.15).

The geometrical angle of attack is set in this paper to  $\bar{\alpha} = 0^\circ$ . The viscous and pressure contributions of the aerodynamical forces are calculated to obtain the lift and drag forces and coefficients ( $C_L$  and  $C_D$ ). Commonly, the reduced frequency defined as  $k = \pi fc/U_0$  is used to characterize the flow. The Strouhal number for the heaving oscillatory motion is defined as  $St = 2kh/\pi$ . For simplification, during the remainder of this paper the flow will be characterized by the reduced frequency  $k$  instead of the frequency  $f$ .

The general purpose Navier-Stokes solver  $N\epsilon\kappa\tau\alpha r$  is used, based on the Spectral /hp Element Method. The solver was validated for many flow geometries, among those cylindrical [8] and rectangular [24]. We have also validated the solver for the airfoil geometry for steady and unsteady flows [26] and found a very good agreement with previously published numerical results [13, 25, 39]. All the simulations of oscillating airfoils were started from fully converged motionless airfoil solutions.

### 6.3 Results

The results presented here were obtained using a 2D unstructured grid composed of 4220 elements, illustrated on Fig. 6.2 (with details of the spatial resolution at the leading- and trailing-edge regions on Fig. 6.3). The mesh is refined around the airfoil surface and the near wake region, as they are regions of interest where the most important fluid phenomena occur. The polynomial order  $n$  has been varied from 9 to 15, and the time step  $\Delta t$  is of the order of  $10^{-4}$ . The boundary conditions are  $u = 1, v = 0$  on the left, upper, and lower mesh boundaries (see Fig. 6.2). On the right boundaries  $\partial u/\partial x = 0, \partial v/\partial x = 0$  and  $u = v = 0$  are employed, and  $u = v = 0$  on the airfoil surfaces (or walls). The pressure boundary conditions are high-order conditions on all boundaries (Eq. 6.11) except at the outflow boundary, where  $p = 0$  is considered.

In this Section the wake of a stationary airfoil is simulated. This flow is used as a reference in analyzing the flow topology when considering heaving airfoils. This flow also serves to obtain the frequency at which the vortices are shed from the motionless airfoil. Heaving airfoils are also simulated at different frequencies and amplitude of oscillations. This is performed in order to exhibit the different frequency regimes experienced by oscillating airfoils and the transition between

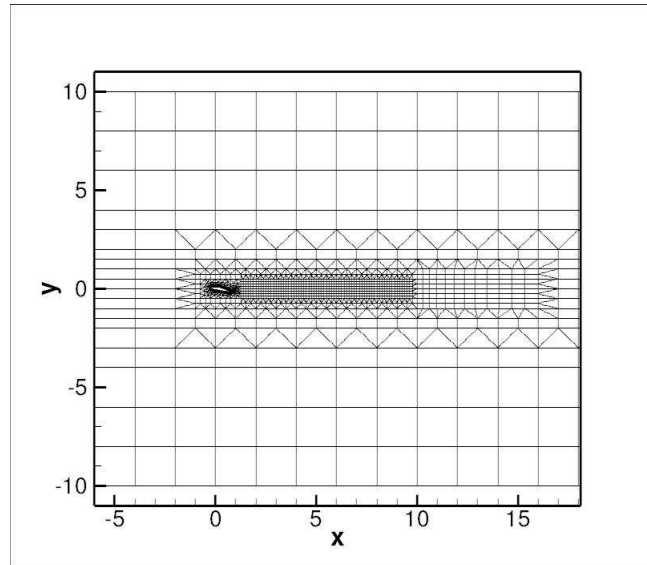


Figure 6.2: The numerical grid used in this paper. The resolution is increased around the airfoil surface (the boundary-layer region) and in the near wake. The mesh is composed of triangular and quadrilateral elements.

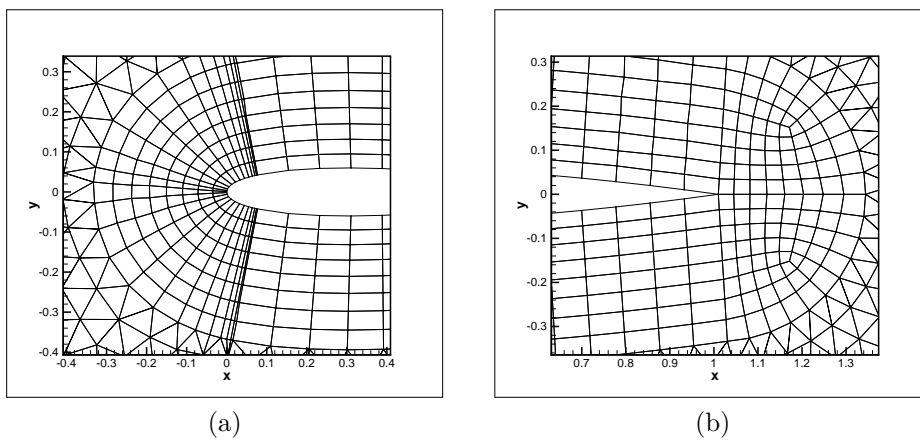


Figure 6.3: (a) Leading- and (b) trailing-edge meshing details. The coordinates system has its origin at the leading-edge of the airfoil.

these regimes. These transitions are achieved at constant frequency (and varying amplitude) and constant amplitude (and varying frequency) of oscillations. The shedding frequencies of these regimes are extracted and compared to the shedding frequency of motionless airfoils.

### 6.3.1 Unforced airfoil wakes

The flow is simulated at  $\bar{\alpha} = 0^\circ$  and at three Reynolds numbers  $Re = 10^4$ ,  $= 2 \times 10^4$  and  $3 \times 10^4$ . Fig. 6.4 illustrate the vorticity distribution for these simulations. At the three simulated Reynolds numbers the flow exhibits a typical Karman vortex-street configuration. The upper-row of vortices rotates clockwise and the lower-row of vortices rotates anti-clockwise. The flow is attached over all the surface of the airfoil and leaves the airfoil parallel to the trailing-edge (see Fig. 6.5 for a close-up of the trailing-edge region for the simulations at  $Re = 10^4$  and  $Re = 3 \times 10^4$ ). The vortices are shed at a certain distance from the trailing-edge due to the wake instability [38] and this distance decreases as the Reynolds number is increased as does the rolling-up of the shed vortices. The wakes observed for the simulated Reynolds numbers are drag-producing wakes (confirmed by the values of the thrust coefficient), where the vortices are tilted upstream. The thrust coefficient increases with increasing Reynolds number as the drag decreases.

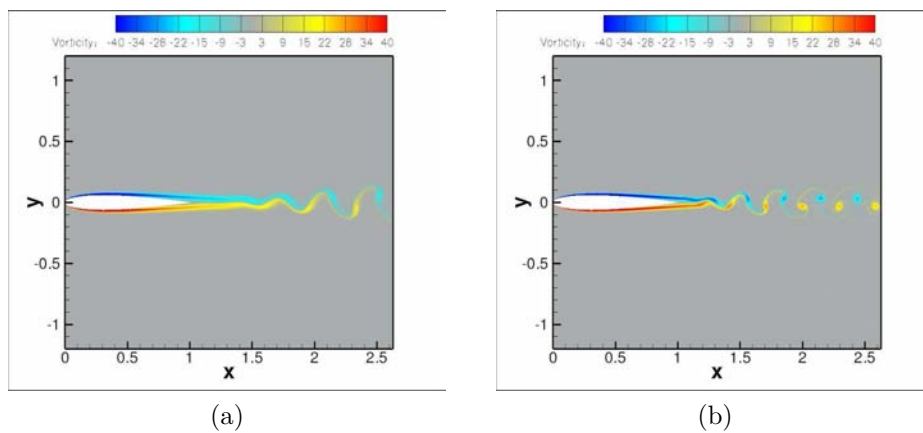


Figure 6.4: Vorticity distribution at  $\bar{\alpha} = 0^\circ$  (a)  $Re = 10^4$  and (b)  $Re = 2 \times 10^4$ .

The time trace of the horizontal velocity  $u$  is shown on Fig. 6.6a at  $Re = 10^4$  and  $\bar{\alpha} = 0^\circ$ . Note that the temporal variation of  $u$  is periodic. A Fast Fourier Transform (FFT) is performed on the  $u(t)$  in order to obtain its frequency content. This technique is used to characterize the frequency content of the airfoil response either for the motionless airfoil or for the oscillating (heaving) airfoil. Fig. 6.6b illustrates the FFT of the time trace plotted in Fig. 6.6a. The peak frequency  $k = k_{nat} = 7.85$  is called the natural shedding frequency and it characterizes the frequency response of the motionless airfoil to the incoming inflow at a certain Reynolds number [14]. This is the frequency at which the vortices are shed into the wake of the airfoil. The frequency response contains also some other weaker peaks at the superharmonics of the natural shedding frequency. This behaviour is typical for a motionless object response to an incoming inflow [5, 19, 28, 43].

The same behaviour is observed at  $Re = 2 \times 10^4$ .  $u(t)$  varies periodically (see

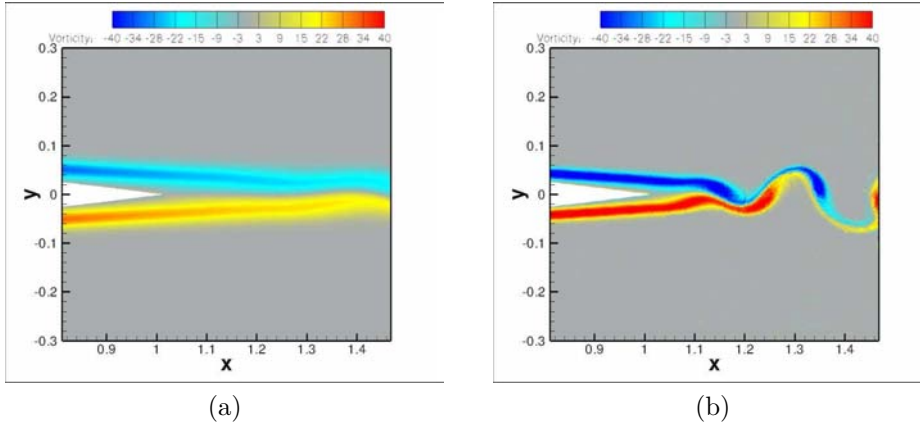


Figure 6.5: Vorticity distribution close-up view of the trailing-edge region at  $\bar{\alpha} = 0^\circ$  (a)  $Re = 10^4$  and (b)  $Re = 3 \times 10^4$ . The horizontal distance at which the shed flow begins to roll in the wake decreases when the Reynolds number increases.

Fig. 6.6c) and the FFT exhibits a strong peak at the natural shedding frequency and weaker peaks at its superharmonics (see Fig. 6.6d). The FFT of the time signal of the horizontal velocity  $U$  at  $Re = 2 \times 10^4$  is  $k = k_{nat} = 10.15$ .

At  $Re = 3 \times 10^4$ ,  $u(t)$  is less periodic due to the acceleration of the flow in response to the increase in the Reynolds number (see Fig. 6.6e). The peak frequency at this Reynolds number is  $k = K_{nat} = 12.91$  (see Fig. 6.6f).

### 6.3.2 Forced airfoil wakes

The response of the airfoil wake to a harmonic forcing is presented in this Section. The airfoil is forced to oscillate in heave at a prescribed frequency and amplitude at  $Re = 10^4$  and a mean angle of attack  $\bar{\alpha} = 0^\circ$ . The frequency of the imposed motion is called the forcing frequency and is labelled  $k_f$ . The frequency response of the flow to the imposed heave oscillation is obtained by analyzing the frequency content of the temporal signal of the horizontal velocity  $u(t)$  by means of a Fast Fourier Transform (FFT). The dominant frequency in the response signal is labelled  $k_r$  and it characterizes the response of the airfoil. The frequency and amplitude values considered in this simulation are chosen to exhibit the heaving airfoil wake in different response regimes. These regimes are defined as follows: the *natural* regime, where the response frequency is equal to the natural shedding frequency of the motionless airfoil, also called the Strouhal frequency. The *lock-in* regime corresponds to the response frequency being *locked* to the forcing frequency. Finally, the *harmonic* regime corresponds to the response frequency being a mixture of the natural and the forcing frequency.

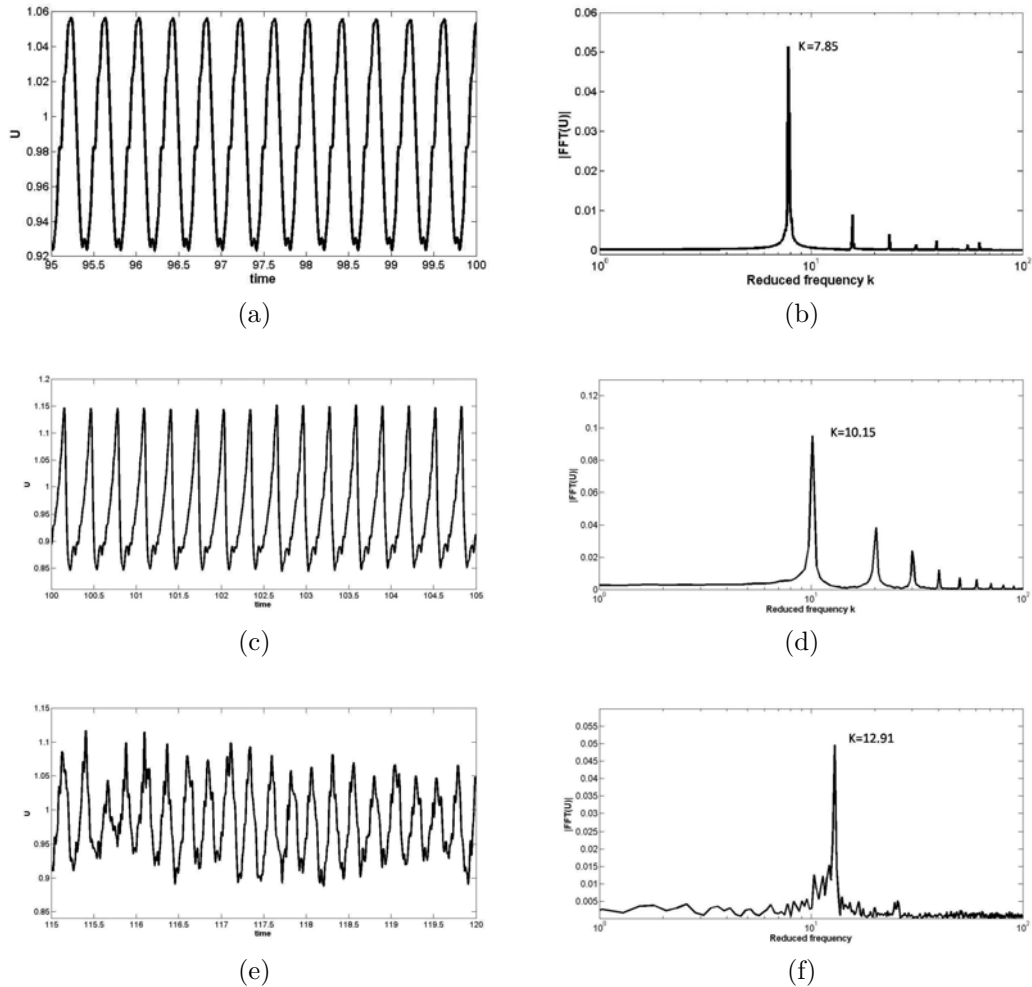


Figure 6.6: (a) Time trace of the horizontal velocity  $u$  for a motionless airfoil at  $Re = 10^4$ . (b) The Fast Fourier Transform of  $u(t)$  for a motionless airfoil at  $Re = 10^4$ . (c) Time trace of the horizontal velocity  $u$  for a motionless airfoil at  $Re = 2 \times 10^4$ . (d) The Fast Fourier Transform of  $u(t)$  for a motionless airfoil at  $Re = 2 \times 10^4$ . (e) Time trace of the horizontal velocity  $u$  for a motionless airfoil at  $Re = 3 \times 10^4$ . (f) The Fast Fourier Transform of  $u(t)$  for a motionless airfoil at  $Re = 3 \times 10^4$ . All the cases above are for  $\bar{\alpha} = 0^\circ$  and  $u(t)$  is extracted at the location ( $x = 1.62, y = 0.09$ ).

## Constant frequency regime transition

In this section the forcing frequency is kept constant and the forcing amplitude is varied. The amplitude is increased in order to identify the possible response states (or modes) exhibited by the forced airfoil. Note that for each case the unforced flow response is used as an initial flow and the computation is performed until an asymptotic state is reached. The frequency content of the horizontal velocity time signal at a location in the near wake ( $x = 1.63, y = 0.09$ ) is then determined by performing an FFT analysis. This location is chosen according to the assumption that it is in the near wake that the forcing and natural frequency are competing with each other. The result of this frequency competition or interaction determines the final state of the wake [19].

The time trace of the horizontal velocity and the FFT analysis of the natural regime (or mode) are shown in Fig. 6.7a and Fig. 6.7b. Note that  $u(t)$  is quasi-periodic in time. This regime is obtained at  $k = 1.96$  (corresponding to  $k/k_{nat} = 1/4$ ) and  $h = 0.001$ . The dominant peak occurs at the natural shedding frequency  $k_{nat} = 7.85$  and its first superharmonic. Another peak occurs at the forcing frequency but it is weaker than the ones at  $k_{nat}$  and its superharmonic. Some other weak peaks are present around the dominant peaks, this behaviour was also observed for a cylinder in a non-lock-in state and reported in [19].

Increasing the amplitude to  $h = 0.04$  and keeping the frequency of oscillation constant results in a dramatic change in the frequency response of the flow. Fig. 6.7c shows the time-series of  $u$  (which are now periodic in time) and Fig. 6.7d shows its FFT analysis. The peak frequency is  $k_r = 5.93$  and it can be written as a linear combination of the natural shedding frequency and the forcing frequency ( $k_r = k_{nat}/2 + k_f$ ). This indicates that we are in the harmonic regime where  $k_n$  and  $k_f$  are interacting together. The result of this interaction is that the peak frequency is some mixture of the natural shedding frequency and the imposed forcing frequency. Other weaker peaks are present at some other combinations of these two frequencies ( $k_{nat} + k_f, 1/4k_{nat} + k_f$ ). Compared to the frequency response of the natural regime it is important to note that the  $k_f$  peak becomes more important and the peak corresponding to the natural shedding frequency  $k_{nat}$  is less prominent. This indicates that the forcing frequency is gaining importance at the expense of the natural shedding frequency. This is also visible in the time trace of  $u$ , where two distinct frequencies can be identified. These frequencies correspond to  $k_r$  and  $k_{nat}$ .

A further increase in the amplitude of oscillation to  $h = 0.1$  results in a lock-in regime where the response frequency is *locked* to the forcing frequency. Fig. 6.7e (where  $u(t)$  is again quasi-periodic in time) illustrates the time trace of the horizontal velocity  $u$ . Fig. 6.7f shows the FFT of the time trace of  $u$  where the peak frequency now corresponds to the forcing frequency  $k_f = k_r = 1.96$ . There are less important peaks at the superharmonics of the forcing frequency. This is typical for a lock-in regime, as this regime is similar to the non-forced case in its

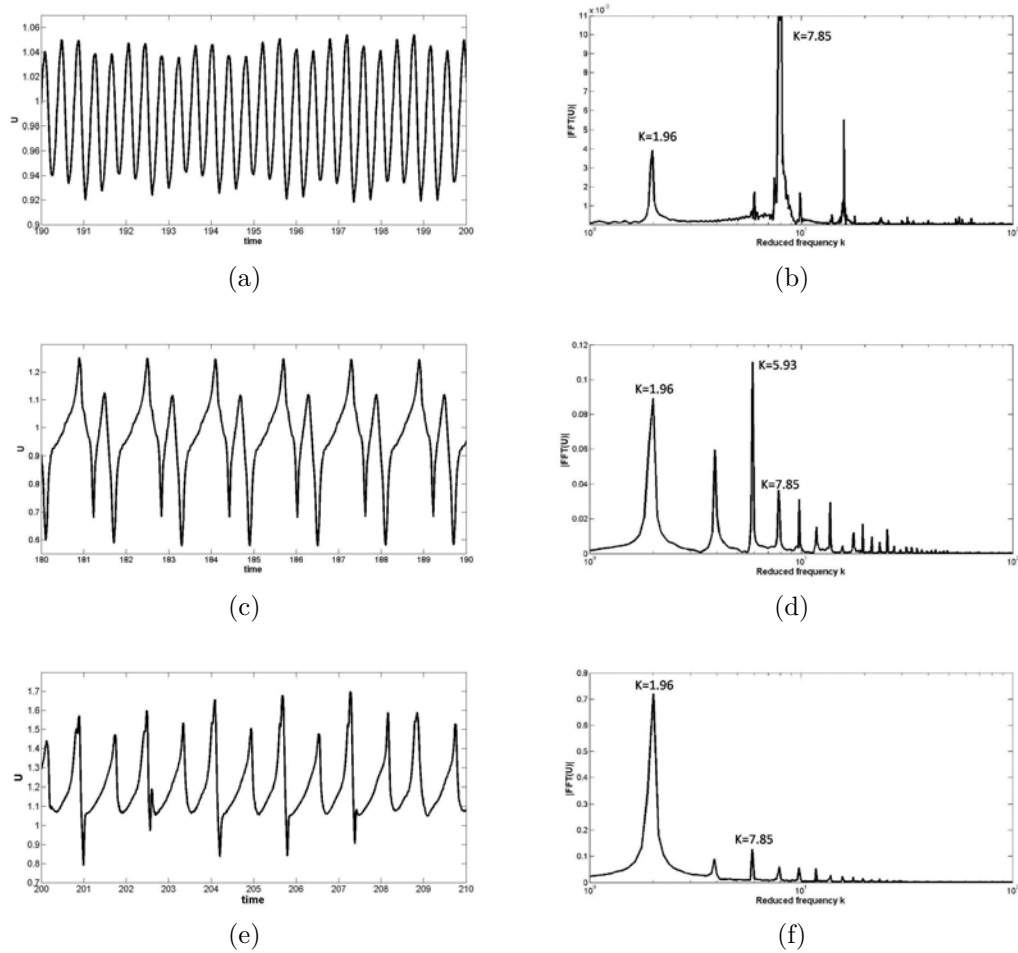


Figure 6.7: (a) Time trace of the horizontal velocity  $u$  and its (b) Fast Fourier Transform  $h = 0.001$ ,  $k = 1.96$ . (c) Time trace of  $u$  and its (d) Fast Fourier Transform at  $h = 0.04$ ,  $k = 1.96$ . (e) Time trace of  $u$  and its (f) Fast Fourier Transform at  $h = 0.1$ ,  $k = 1.96$ . All precedent simulations are at  $Re = 10^4$ ,  $\bar{\alpha} = 0^\circ$ , and  $u(t)$  is plotted at the location  $(x = 1.63, y = 0.09)$ .

frequency response (see Fig. 6.6b) [19].

The frequency regime transition described embodies another transition in the wake type (or pattern). This transition is from a drag-producing wake to a thrust-producing wake via a neutral wake at constant frequency. Fig. 6.8 shows the vorticity distributions of the simulations described above. These wake types are typical of heaving airfoils and the transition between them has been reported in the literature [23, 26, 35, 46, 48]. On Fig. 6.8a the wake exhibits a Karman vortex-street, where the upper-vortices are clockwise and the lower-vortices are anti-clockwise. A pair of counter-rotating vortices is shed per oscillation cycle. These vortices are mushroom-like structures which are tilted upstream and are typical of a drag-producing wake. The wake type changes as the amplitude of the heaving oscillation increases. The vortices are now untilted and more than a pair of counter-rotating vortices is shed per oscillation cycle (see Fig. 6.8c). This wake type is called a neutral wake (also labeled multiple-vortices-per-half-cycle mode), as the inherent drag balances the produced thrust. This mode is not well understood. The mechanism by which more than a vortex is shed per half-cycle is not well known [46]. We propose here that this mode (or wake type) results from the interaction between the shedding frequency and the imposed frequency, as already explained earlier in this Section by means of FFT analysis. This result will be further confirmed by the simulations of the frequency transition at constant amplitude in the next Section. This explanation for the multiple-vortices-per-half-cycle regime was also provided by *Young* [46]. The author briefly discussed this mode and did not provide any frequency analysis. His conclusions were only based on observing the time trace of  $u$  for one cycle of oscillations.

A further increase of the amplitude results in a transition to a thrust-producing wake (see Fig. 6.8e). This wake type is characterized by mushroom-like structures tilted downstream. Note here that more than one pair of counter-rotating vortices is shed per oscillation-cycle. This thrust-producing wake is different from the *typical* thrust-producing wake, as the latter looks like the drag-producing wake in Fig. 6.8a (but with the vortices structures tilted downstream). This *new* thrust-producing wake is due to the increase in the amplitude of the heaving oscillation. The increase in the amplitude triggers the shedding of more vortices per oscillation cycle [48]. This is mainly due to the fact that at higher amplitudes the leading-edge also contributes to the vortices shed at the trailing-edge. This is confirmed by the presence of vortices on the upper and lower airfoil surface. Note that for the multiple-vortices-per-half-cycle for the neutral regime (see Fig. 6.8c) there are no contributions from the leading-edge, although the flow is slightly detached close to the trailing-edge region. The rolling-up and the vorticity increase with the amplitude and the thrust coefficient also increases. This increase is due to the increase in the heaving velocity.

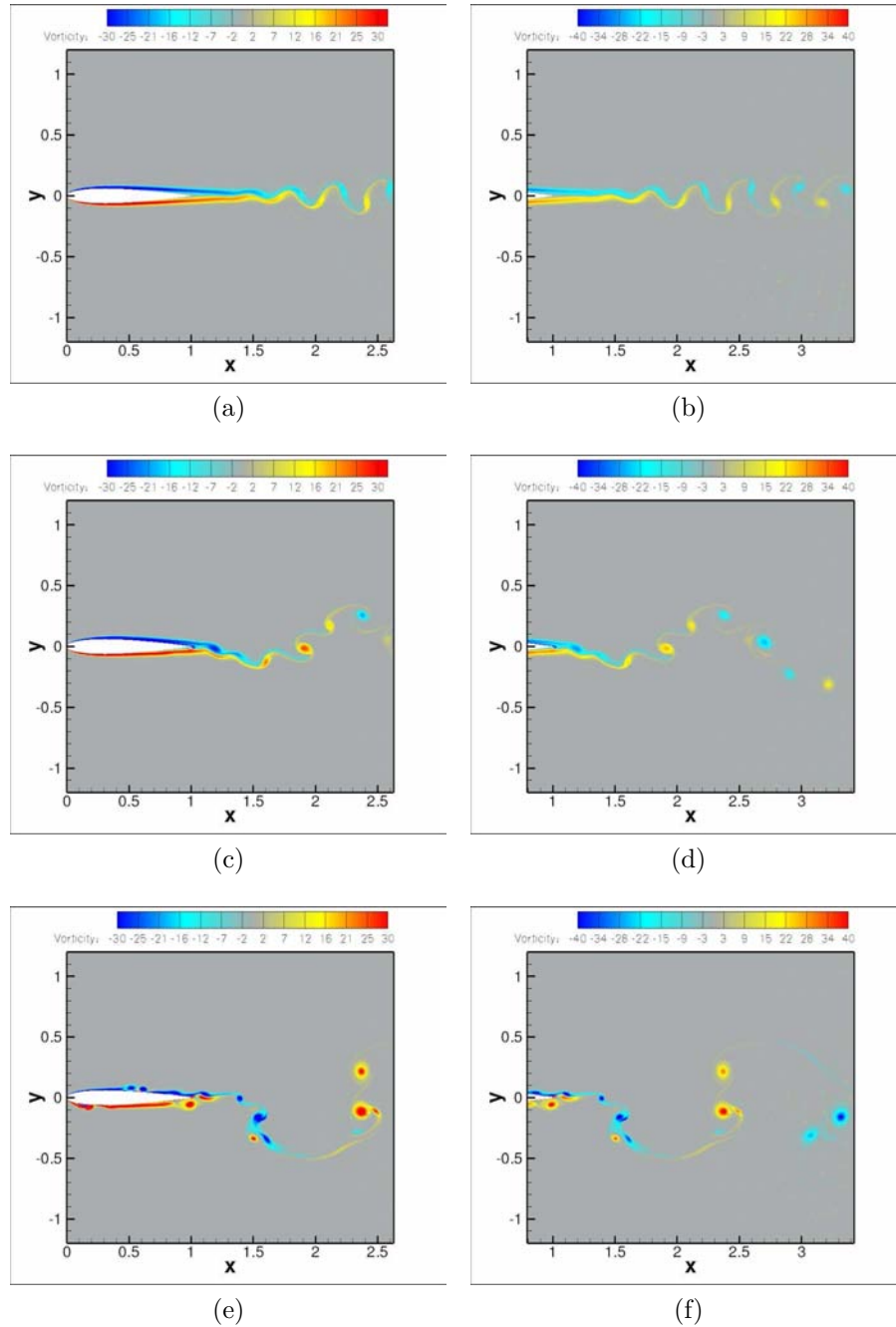


Figure 6.8: Vorticity distribution at  $\bar{\alpha} = 0^\circ$ ,  $Re = 10^4$  for (a) a drag-producing wake ( $k = 1.96$ ,  $h = 0.001$ ), (b) view of the near wake region. (c) A neutral wake ( $k = 1.96$ ,  $h = 0.04$ ), (d) view of the near wake region. (e) A thrust-producing wake ( $k = 1.96$ ,  $h = 0.1$ ), (f) view of the near wake region.

### Constant amplitude regime transition

In this Section the forcing amplitude is kept constant at  $h = 0.05$  and the forcing frequency is increased to achieve a frequency regime transition. As for the case

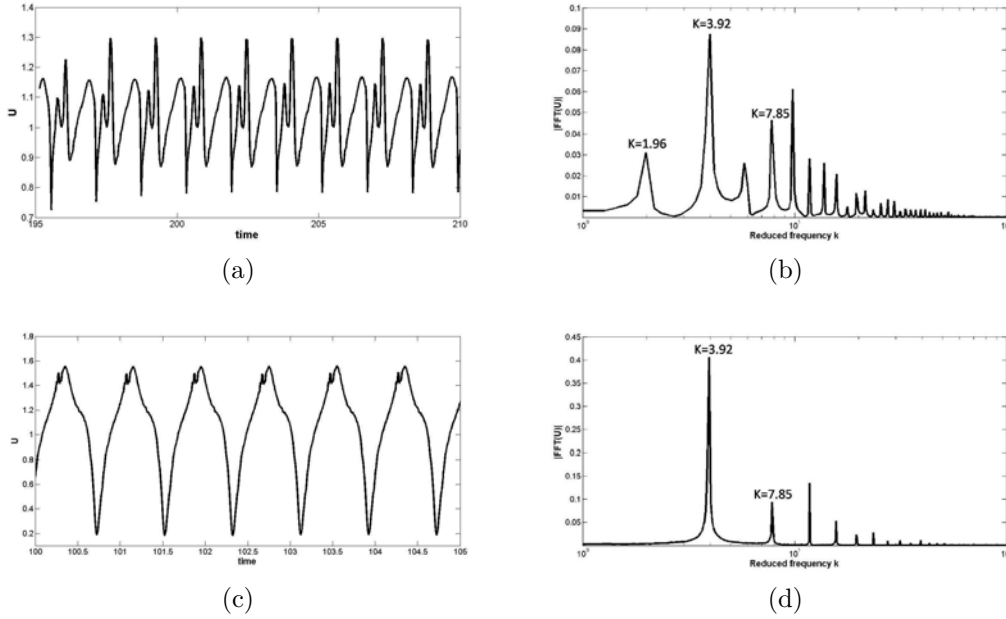


Figure 6.9: (a) Time trace of the horizontal velocity  $u$  and its (b) Fast Fourier Transform at  $k = 1.96$ ,  $h = 0.05$ . (c) Time trace of the horizontal velocity  $u$  and its (d) Fast Fourier Transform at  $k = 3.92$ ,  $h = 0.05$ . All precedent simulations are at  $Re = 10^4$ ,  $\bar{\alpha} = 0^\circ$ , and  $u(t)$  is plotted at the location  $(x = 1.63, y = 0.09)$ .

of a constant-frequency-regime transition the unforced flow response is used as an initial flow and the computation is performed until an asymptotic state is reached. The frequency content of  $u(t)$  is analyzed at the same location as for the constant frequency regime transition.

The time trace of  $u$  at  $h = 0.05$  and  $k = 1.96$  (see Fig. 6.9a) is periodic. The peak frequency of the time trace of  $u$  corresponds to a mixture of the natural shedding frequency and the forcing frequency ( $k_r = 1/4K_{nat} + k_f = 3.92$ ). A second frequency peak corresponds to another combination of these frequencies ( $k = 1/2K_{nat} + k_f = 5.88$ ) (see Fig. 6.9). There are weaker peaks at the natural shedding frequency and the forcing frequency and their sum ( $k = k_{nat} + k_f = 9.81$ ). This response is typical of a harmonic regime, as shown earlier in this paper for the simulation at  $k = 1.96$ ,  $h = 0.04$ . However, it is important to note that for the present simulation ( $k = 1.96$ ,  $h = 0.05$ ) the peak at the natural frequency  $k_{nat} = 7.85$  is more important than the one at the forcing frequency  $k_f = 1.96$ , while this is inverted for the simulation at  $k = 1.96$  and  $h = 0.05$ . This may indicate that the response of the airfoil to the forcing motion depends on the amplitude of the oscillations.

Increasing the frequency to  $k_f = 3.92$  results in a transition to a lock-in regime (see Fig. 6.9d), where the dominant frequency peak is equal to the forcing

frequency  $k_r = 3.92$ . The time trace of the velocity is periodic (see Fig. 6.9c).

During the transition from the harmonic to the lock-in regime a wake transition occurs from a neutral to a thrust producing wake. The vorticity contours of the neutral wake are shown in Fig. 6.10a, where the wake presents a multiple-vortices-per-half-cycle regime. Again for a neutral multiple-vortices-per-half-cycle regime there is no vortices contribution from the leading-edge and the flow is attached over all the airfoil surface. Increasing the frequency of oscillations results in a wake transition to a thrust-producing wake (see Fig. 6.10c), where one pair of counter-rotating vortices is shed per oscillation cycle. The wake configuration is typical of a thrust-producing wake [46, 47], and although there is a slight contribution of leading-edge to the shed vortices this does not create a multiple-vortices-per-half-cycle configuration. This phenomenon is discussed in the next Section.

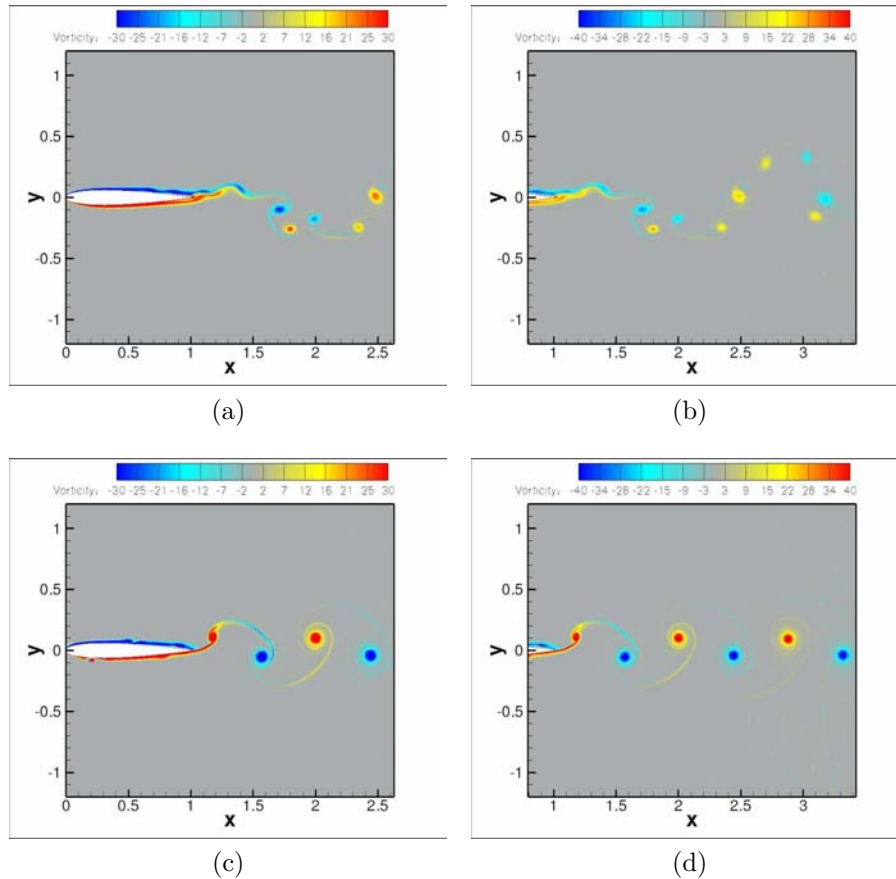


Figure 6.10: Vorticity contours at  $\bar{\alpha} = 0^\circ$ ,  $Re = 10^4$  for (a) a neutral wake ( $k = 1.96$ ,  $h = 0.05$ ), (b) view of the near wake region. (c) A thrust-producing wake ( $k = 3.92$ ,  $h = 0.05$ ), (d) view of the near wake region.

### 6.3.3 Frequency regimes classifications - a frequency pattern

Several simulations are conducted at different combinations of frequency and amplitude of the forcing oscillations in order to obtain a phase diagram of the frequency regimes. The simulations are conducted at low heaving amplitudes and at moderate to high heaving frequencies. This region of the  $k/k_{nat}$  vs  $h$  plot is associated with aeroelastic and aeroacoustic phenomena and is not well explored in the literature. Moreover, the boundaries of the wake-types in this region are not well defined [46]. This phase diagram is obtained by identifying the different frequency regimes using the FFT analysis and expressing it in function of the amplitude and frequency of oscillation, more precisely the oscillation frequency normalized by the natural frequency of vortex shedding ( $k/k_{nat}$ ).

On Fig. 6.11 a schematic representation is shown, based on the simulations performed in this paper of the natural, harmonic, and lock-regimes as a function of  $h$  and  $k/k_{nat}$ . At low forcing frequencies ( $h < 10^{-2}$ ) an increase in the frequency at a constant amplitude triggers a transition from the natural regime to the lock-in regime without going through a harmonic regime. This is also valid for a transition varying the amplitude at a constant forcing frequency for  $k/k_{nat} > 0.5$ . This is because above  $k/k_{nat} = 0.5$ , any harmonic of the forcing frequency will be higher than the natural shedding frequency and the flow will lock to the forcing frequency value. This is mainly due to the trailing-edge of the airfoil which dictates the separation point for  $k/k_{nat} > 0.5$  and enforces the dominance of the forcing frequency (lock-in) even in the presence of leading-edge vortex shedding (as in Fig. 6.10c). On Fig. 6.12 the vorticity contours at  $h = 0.05$  and  $k = 3.92$  (corresponding to  $k/k_{nat} = 0.5$ , represented on Fig. 6.11 with a star pointed to by a red arrow) are shown for one forced-oscillation cycle for a simulation belonging to the lock-in region. Note that the vortices are shed at the trailing-edge when the airfoil is at its maximum (minimum) vertical position; respectively (see Fig. 6.12). This confirms that in this case the trailing-edge motion imposes the shedding process. And this even if vortices are shed from the both the upper and lower airfoil surface.

On the other hand, Fig. 6.13 shows the vorticity countours at  $h = 0.1$  and  $k = 1.96$  ( $k/k_{nat} = 0.25$ , represented by a square pointed to by a red arrow on Fig. 6.11). These values of  $k$  and  $h$  correspond to a wake in the harmonic regime region. The shedding of vortices occurs not only when the airfoil is at its maximum (minimum) vertical position but also when the airfoil is at  $y = 0$ . This explains how more than one vortex-pair is shed per oscillation cycle. These vortices are stronger than the ones at  $h = 0.05, k = 3.92$ . This is an indication that the trailing-edge motion does not control the shedding process at this stage. Additionally, the frequency resulting from the interaction between the imposed motion and the natural shedding of the airfoil is responsible for this particular mode. The frequency at which the vortices are shed is  $k = 1.24$ , not  $k_f$  but

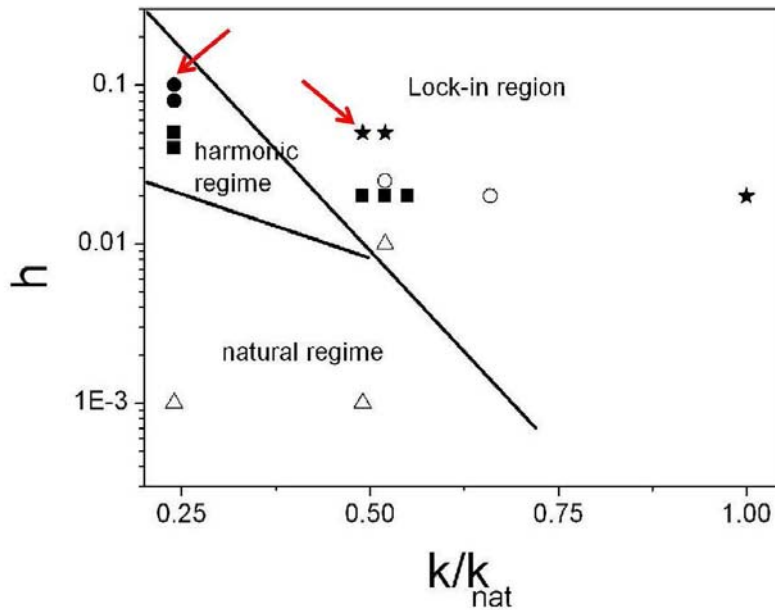


Figure 6.11: Phase diagram of the wake-types classification as a function of the amplitude  $h$  and the normalized forcing frequency  $k/k_{nat}$ . The triangles are for drag-producing wakes with one vortex pair shedding per oscillation cycle. The stars represent thrust-producing wakes with one pair of vortices shed per oscillation cycle. The squares are for neutral wakes with multiple-vortices-per-cycle shedding. The open circles represent neutral wakes with one pair of vortices shed per oscillation cycle and the black circles are for thrust-producing wakes with multiple-vortices-per-cycle shedding. The frequency regimes boundaries are approximately indicated based on the simulations performed in this paper.

a combination of both  $k_{nat}$  and  $k_f$ . When plotting the streamlines around the trailing-edge region (see Fig. 6.14) a recirculation region is observed on both sides of the trailing-edge, thus creating a blunt-like body. The bluntness of the trailing-edge varies with the heaving cycle and has a frequency associated with it. This results in the shedding frequency being neither the natural nor the forcing frequency but a mixture of both frequencies.

In the region defined by  $h > 10^{-2}$  and  $k/k_{nat} < 0.5$  the transition at constant frequency or amplitude from the natural to the lock-in regime passes via the harmonic regime, as observed in the previous Section.

The phase diagram of the frequency regimes provides an idea of the complexity of the frequency regimes transition and the frequencies interplay in the case of a heaving airfoil. There is a rich variety of wake-types and frequency regimes.

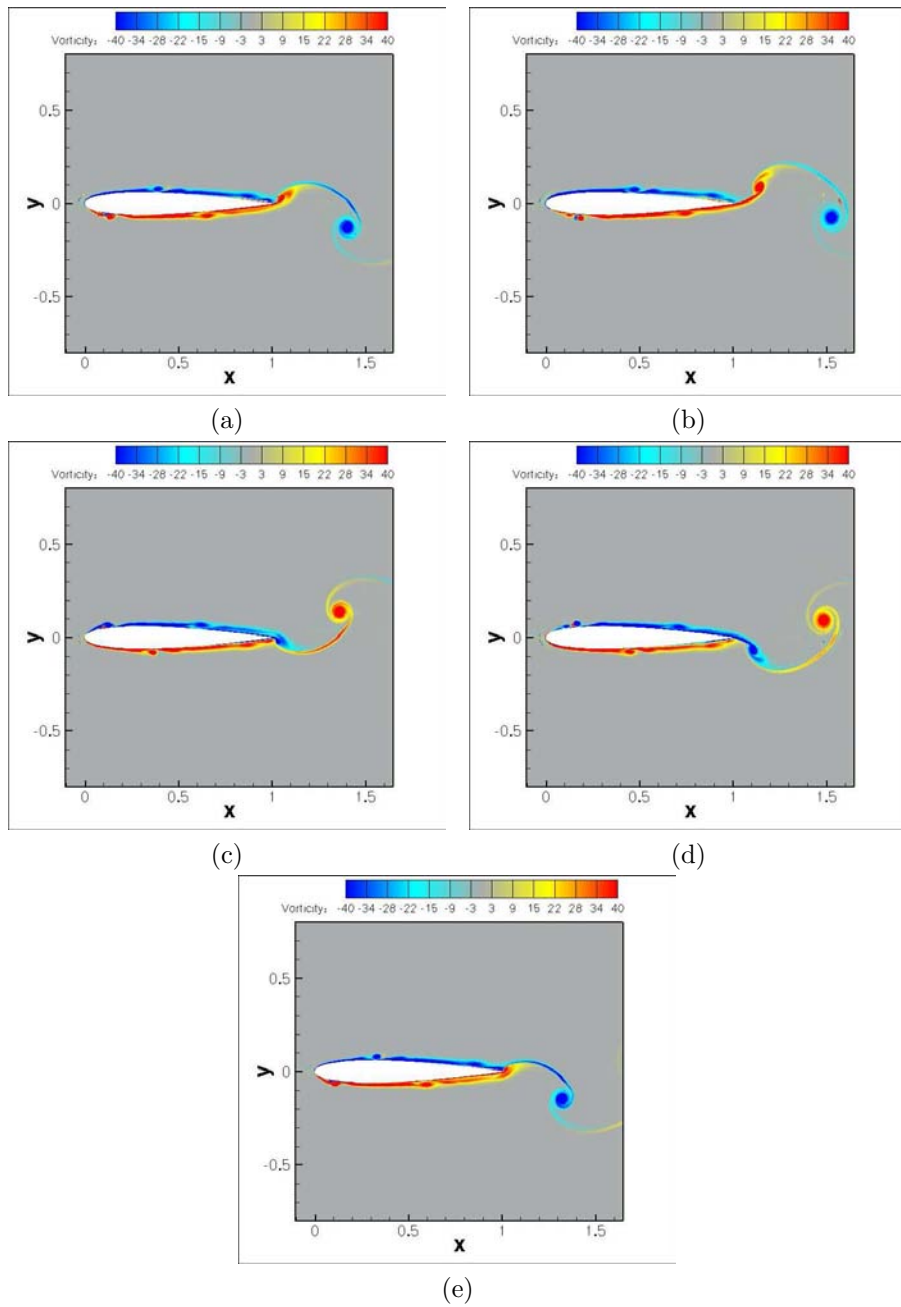


Figure 6.12: Vorticity contours at  $\bar{\alpha} = 0^\circ$ ,  $Re = 10^4$ ,  $h = 0.05$  and  $k = 3.92$  ( $k/k_{nat} = 0.5$ ) during one oscillation cycle.  $y$  is the vertical position of the airfoil. (a)  $y$  is at its maximum vertical position, (b)  $y=0$ , (c)  $y$  is at its minimum vertical position, (d)  $y=0$ , and (e)  $y$  is at its maximum vertical position.

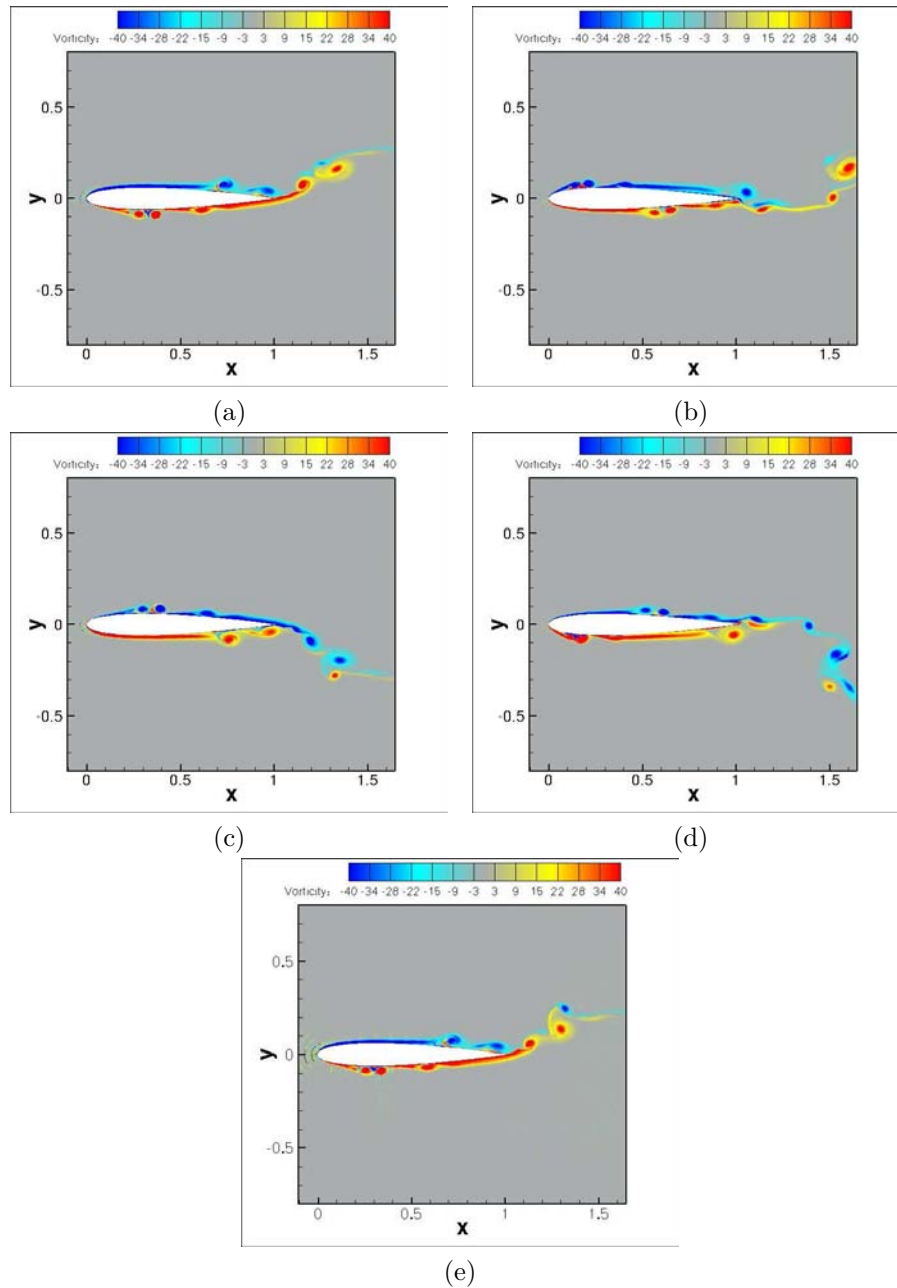


Figure 6.13: Vorticity contours at  $\bar{\alpha} = 0^\circ$ ,  $Re = 10^4$ ,  $h = 0.1$  and  $k = 1.96$  during one oscillation cycle. (a)  $y=0$ , (b)  $y$  at its minimum vertical position, (c)  $y=0$ , (d)  $y$  is at its maximum vertical position, (e)  $y=0$ .

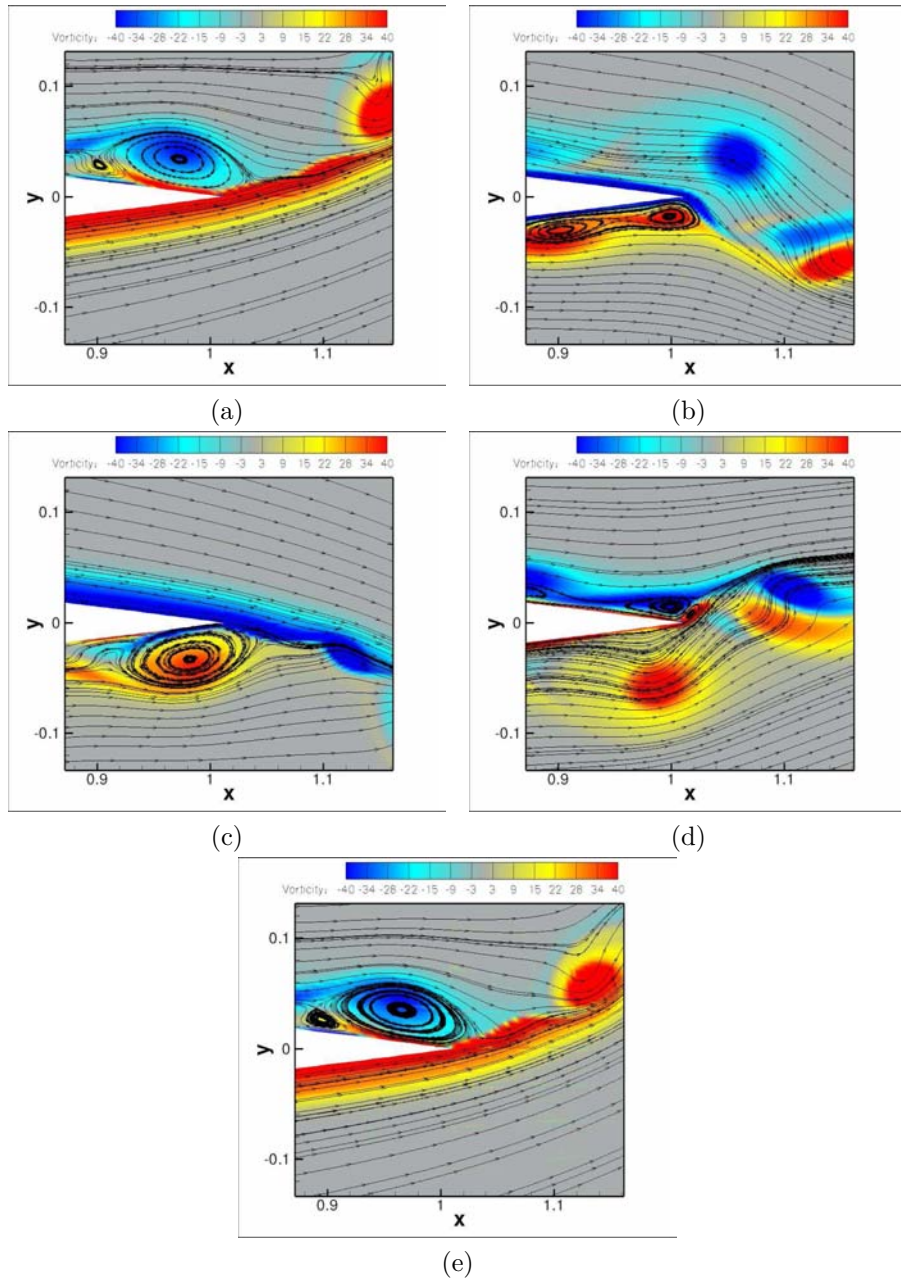


Figure 6.14: Streamlines at  $\bar{\alpha} = 0^\circ$ ,  $Re = 10^4$ ,  $h = 0.1$  and  $k = 1.96$  during one oscillation cycle. (a)  $y=0$ , (b)  $y$  at its minimum vertical position, (c)  $y=0$ , (d)  $y$  is at its maximum vertical position, (e)  $y=0$ .

One can conclude that the wake-type is strongly related to the frequency regime. For example, wake-types with multiple-vortices-per-half-cycle of oscillation are in a region where the forcing and the natural frequency of vortex shedding are interacting together (the harmonic regime). Wake-types with one vortex-pair shed per cycle are in the region where one distinct frequency is in control. Note that the phase diagram is not symmetric as it is the case for the cylinder [19, 46]. This can be attributed to the presence of the sharp trailing-edge of the airfoil and to the fact that at certain values of the control parameters, the airfoil sheds vortices from both the leading- and trailing-edge, for example at  $k = 1.96$  and  $h = 0.1$  (see Fig. 6.8).

The phase diagram presented in this paper agrees very well with the one presented by *J. Young* in [46] at  $Re = 2 \times 10^4$ , although the author noted the presence of only three wake types in his diagram and no frequency analysis was presented to confirm the nature of the frequency regimes. A less similar diagram for the pitching airfoil is shown by *T. Schnipper et al.* (see [38], Fig.2). Although it is important to note that for both the pitching and heaving cases there exist a region where the shedding of more than a vortex pair per oscillation occurs and that this region is confined at high amplitudes and low frequencies of oscillations.

## 6.4 Conclusion

We successfully simulated the two dimensional unsteady flow on both a motionless and a heaving airfoil using a high-order spectral CFD method. The high spatial and temporal resolution achieved by the Spectral /hp Element Method permits a detailed analysis of the flow over the airfoil and the near wake. The high-order numerical methods enabled the simulation and the characterization of the frequency response regimes. These regimes are: (a) the natural regime, (b) the lock-in regime, and (c) the harmonic regime. These frequency response regime are related to the shedding process through which the wake undergoes a transition from a Karman street (a drag-producing wake) to a reversed Karman street (a thrust-producing wake). The transition between the different frequency regimes is simulated at both constant frequency and constant amplitude. This transition is successfully related to the wake-types regimes and the transition between them. It is found that the frequency regimes are strongly related to the wake type exhibited. Wake-types with multiple-vortices-per-half-cycle of oscillation are found in harmonic regimes and wake-types with one vortex-pair shed per cycle are in the region where one distinct frequency is in control (lock-in and natural regimes). Regimes where the leading-edge vortices contribute to the shedding process were also simulated.

## Bibliography

- [1] M. Abramowitz and I. A. Stegun. *Handbook of Mathematical Functions*. Dover Publications, New York, 1972.
- [2] J. M. Anderson, k. Streitlien, D. S. Barrett, and M. S. Triantafyllou. Oscillating foils of high propulsive efficiency. *J. Fluid Mech.*, 360:41–72, 1998.
- [3] Corporate Authors. Aircraft Stalling and Buffeting, Lecture series. Technical report, Advisory Group for Aerospace Research and Development, Paris, France, 1975.
- [4] P. R. Bandyopadhyay, J. M. Castano, W.H. Nedderman, and M. J. Donnelly. Experimental Simulation of Fish-Inspired Unsteady Vortex Dynamics on a Rigid Cylinder. *J. Fluid Eng.-T. ASME*, 122(2):219–238, 2000.
- [5] R. D. Blevins. *Flow-induced vibration*. New York, Van Nostrand Reinhold Co., 1977. 377 p., 1977.
- [6] J. P. Boyd. *Chebyshev and Fourier Spectral Methods*. Dover Publications, 2001.
- [7] J. Butcher. *Numerical Methods for Ordinary Differential Equations*. John Wiley, 2003.
- [8] B. S. Carmo, S. J. Sherwin, P. W. Bearman, and R. H. J. Willden. Wake transition in the flow around two circular cylinders in staggered arrangements. *J. Fluid Mech.*, 597(1):1–29, 2008.
- [9] M. Cheng, Y. T. Chew, and S. C. Luo. Numerical Investigation of a Rotationally Oscillating Cylinder in Mean Flow. *J. Fluid Struct.*, 15(7):981–1007, 2001.
- [10] K. D. Ellenrieder, K. R. Parker, and J. Soria. Flow structures behind a heaving and pitching finite-span wing. *J. Fluid Mech.*, 490:129–138, 2003.
- [11] P. Freymuth. Propulsive vortical signature of plunging and pitching airfoils. *AIAA J.*, 26:881–883, 1988.
- [12] A. Ghizzetti and A. Ossicini. *Quadrature Formulae*. Academic Press, New York, 1970.
- [13] H. Gopalan. *Numerical Modeling of Aerodynamics of Airfoils of Micro Air Vehicles in Gusty Environment*. PhD thesis, University of Akron, 2008.
- [14] S. I. Green. *Fluid Vortices*. Kluwer Academic Publishers, 1995.

- [15] D. G. Infield, J. B. Feuchtwang, and P. Fitches. Development and Testing of a Novel Self-Twisting Wind Turbine Rotor. In *European Wind Energy Conference*, pages 329–332, Nice-France, May 1999.
- [16] K. D. Jones, C. M. Dohring, and M. F. Platzer. Wake Structures Behind Plunging Airfoils: A Comparison of Numerical and Experimental Results. In *34th AIAA Aerospace Sciences Meeting and Exhibit*, Reno-Nevada, 15-18 January 1996. American Institute of Aeronautics and Astronautics.
- [17] G. E. Karniadakis. Spectral element-Fourier methods for incompressible turbulent flows. *Comput. Method Appl. M.*, 80(1-3):367–380, 1990.
- [18] G. E. Karniadakis and S. Sherwin. *Spectral/hp Element Methods for Computational Fluid Dynamics*. Oxford University Press, 2005.
- [19] G. E. Karniadakis and G. S. Triantafyllou. Frequency selection and asymptotic states in laminar wakes. *J. Fluid Mech.*, 199(1):441–469, 1989.
- [20] G. E. Karniadakis, S. A. Orszag, and M. Israeli. High-order splitting methods for the incompressible Navier-Stokes equations. *J. Comp. Phys.*, 97:414–443, 1991.
- [21] R. Katzmayr. Effect of Periodic Changes of Angle of Attack on Behaviour of Airfoils. Technical Report TM-147, NACA, 1992.
- [22] M. M. Koochesfahani. Vortical patterns in the wake of an oscillating airfoil. *AIAA J.*, 27:1200–1205, 1989.
- [23] J. C. S. Lai and M.F. Platzer. Jet Characteristics of a Plunging Airfoil. *AIAA J.*, 37(12):1529–1537, 1999.
- [24] L. Li, S. J. Sherwin, and P. W. Bearman. A moving frame of reference algorithm for fluid/structure interaction of rotating and translating bodies. *Int. J. Numer. Meth. Fl.*, 38:187–206, 2002.
- [25] Y. Lian and W. Shyy. Aerodynamics of Low Reynolds Number Plunging Airfoil Under Gusty Environment. In *45th AIAA Aerospace Sciences Meeting and Exhibit. 8-11 January 2007, Reno, Nevada*, volume AIAA-2007-71, 2007.
- [26] W. Medjroubi, B. Stoevesandt, B. Carmo, and J. Peinke. Direct numerical simulations of the flow around a heaving airfoil. Submitted for publication in *Computers and Fluids*, 2010.
- [27] V. Middleton, P. Fitches, J. Jeronimidis, and J. B. Feuchtwang. Passive Blade Pitching for Overspeed Control of an HAWT. In *20th British Wind Energy Association Conference*, Cardiff University of Wales, September 2-4 1998.

- [28] R. Mittal and F. M. Najjar. Vortex Dynamics in the Sphere Wake. In *29th AIAA Fluid Dynamics Conference and Exhibit, Norfolk, Virginia*, volume 99-3806, 1999.
- [29] T. J. Mueller and J. D. DeLaurier. Aerodynamics of Small Vehicles. *Ann. Rev. Fluid Mech.*, 35:89–111, 2003.
- [30] C. R. Nastase and D. J. Mavriplis. High-order discontinuous Galerkin methods using an hp-multigrid approach. *J. Comp. Phys.*, 213(1):330–357, 2006.
- [31] E. Naudascher and D. Rockwell. *Flow-Induced Vibrations: An Engineering Guide*. Rotterdam, Netherlands: Balkema, 1994.
- [32] R. C. Nelson, T. C. Corke, and H. Othman. A Smart Wind Turbine Blade Using distributed Plasma Actuators for Improved Performance. In *46th Aerospace Sciences Meeting*, Reno, Nevada, January 7-10 2008. AIAA.
- [33] A. Ongoren and D. Rockwell. Flow structure from an oscillating cylinder Part 1. Mechanisms of phase shift and recovery in the near wake. *J. Fluid Mech.*, 191(1):197–223, 1988.
- [34] A. Ongoren and D. Rockwell. Flow structure from an oscillating cylinder Part 2. Mode competition in the near wake. *J. Fluid Mech.*, 191(1):225–245, 1988.
- [35] M. F. Platzer, K. D. Jones, J. Young, and J. C. S. Lai. Flapping-Wing Aerodynamics: Progress and Challenges. *AIAA Journal*, 46(9):2136–2149, 2008.
- [36] J. J. Rohr and F. E. Fish. Strouhal numbers and optimization of swimming by odontocete cetaceans. *J. Exp. Biol.*, 207(10):1633–1642, 2004.
- [37] R. H. Scanlan and J. J. Tomko. Airfoil and Bridge Deck Flutter Derivatives. *Journal of the Engineering Mechanics Division ASCE*, 97:1717, 1971.
- [38] T. Schnipper, A. Andersen, and T. Bohr. Vortex Wakes of a Flapping Foil. *J. Fluid Mech.*, 633:411–423, 2009.
- [39] A. V. Shatalov. *Numerical Simulation of Incompressible Laminar Flows Using Viscous-Inviscid Interaction Procedure*. PhD thesis, University of California, Division Mechanical and Aeronautical Engineering, 2006.
- [40] Y. Shimizu and Y. Kamada. Studies on a Horizontal Axis Wind Turbine With Passive Pitch-Flap Mechanism: Performance and Flow Analysis Around Wind Turbine. *J. Fluid Eng.-T. ASME*, 123(3):516–522, 2001.

- [41] W. Shyy, M Berg, and D. Ljungqvist. Flapping and Flexible Wings for Biological and Mico Air Vehicles. *Prog. Aerosp. Sci.*, 35:455–506, 1999.
- [42] G. S. Triantafyllou, M. S. Triantafyllou, and M. A. Grosenbaugh. Optimal Thrust Development in Oscillating Foils with Application to Fish Propulsion. *J. Fluid Struct.*, 7:205–224, 1993.
- [43] C. H. K. Williamson. *Fluid Vortices: Vortex Dynamics in the Wake of a Cylinder*, chapter 5, pages 155–277. Kluwer Academic Publishers, 1995.
- [44] C. H. K. Williamson and R. Govardhan. Vortex-Induced Vibrations. *Annu. Rev. Fluid Mech.*, 36:413–55, 2004.
- [45] J. R. Wright and J. E. Cooper. *Introduction to Aircraft Aeroelasticity and Loads*. Wiley, 2007.
- [46] J. Young. *Numerical simulation of the unsteady aerodynamics of flapping airfoils*. PhD thesis, School of Aerospace, Civil and Mechanical Engineering. The University of New South Wales. Australian Defence Force Academy, May 2005.
- [47] J. Young and J. C. S. Lai. Frequency and Amplitude Effects in the Wake of a Plunging Airfoil. In *14th Australasian Fluid Mechanics Conferences, Adelaide University, Adelaide, Australia. 10-14 December, 2001*.
- [48] J. Young and J. C. S. Lai. Oscillation Frequency and Amplitude Effects on the Wake of a Plunging Airfoil. *American Institute of Aeronautics and Astronautics*, 42(10):2042–2052, 2004.
- [49] Z. C. Zheng and N. Zhang. Frequency effects on lift and drag for flow past an oscillating cylinder. *J. Fluid Struct.*, 24(3):382–399, 2008.



# Chapter 7

## Conclusions and Outlook

### 7.1 Synopsis of motivation and results

In this thesis we have studied numerically the unsteady flow over oscillating (heaving and plunging) airfoils using a high resolution method for the first time.

In Chapter 1 we presented a review of the literature on unsteady flows over airfoils, dynamic stall, oscillating airfoils and their wakes, the generation of thrust by plunging (heaving) airfoils, and the frequency regimes exhibited by forced airfoil wakes. This Section also included a presentation of Direct Numerical Simulations (CFD) and the use of high-order methods.

The literature review revealed that unsteadiness is a phenomenon which can not be avoided when dealing with flows over airfoils. Although unsteadiness presents serious challenges for their numerical simulation, high resolution spectral numerical studies can be used to improve and/or control airfoils performance. It is also important to point out that oscillating airfoils generate thrust and lift. Moreover, at low Reynolds numbers and for small-size airfoils, oscillating airfoils produced more thrust than their motionless counterparts and therefore achieved a better propulsive efficiency. This was one of the main motivations for the simulation of motionless and oscillating airfoils in the present investigation.

In Chapter 2 we introduced the Spectral /hp Element Method, the framework of the weighted residuals and the Galerkin formulation. The discretization for 2D problems was discussed along with the elemental operations on standard and general-shaped elements. The solution procedure of the global system and the global assembly method were described, as the extension to 3D cases. We also discussed the time advancement scheme and the implementation of the airfoil motion using the moving frame of reference.

In Chapter 3 the *Nεκταρ*-solver was validated against the experimental and computational results published in the literature for the steady and unsteady flow over motionless cylinders and motionless and heaving airfoils. The *Nεκταρ*-solver was able to reproduce the flow configuration and both qualitatively and

quantitatively agreement was achieved.

In Chapter 4 the simulation of steady and unsteady flows over a fixed airfoil were conducted and the results were validated against previously published experimental and computational studies. Heaving airfoils were also simulated for different values of the mean incidence, Reynolds number and amplitude and frequency of oscillations and a detailed description of the the boundary-layer temporal development was achieved. The main results of this Chapter are the following:

- For the fixed airfoil it was observed that increasing the Reynolds number slightly increases the mean value of the aerodynamic coefficients. Moreover, the flow development is faster due to its acceleration but in general it has the same phenomenological development as that at a lower Reynolds number. The mean incidence is found to have more effects on the flow development. The flow is delayed in response to the increase in the mean incidence and the force coefficients increase, as it was previously reported in the literature.
- For the oscillating airfoil at a reduced frequency less than 1 the fixed airfoil and the heaving airfoil exhibit similar flow fields, thus confirming previous experimental and computational findings. Nevertheless, the mean values of the lift and drag coefficients increase.
- Increasing the Reynolds number while keeping the same frequency and amplitude of oscillations has no major effects neither on the flow structure nor on the aerodynamical loads. However, increasing the mean incidence has a dramatic influence on the flow field and the wake which is characterized by vortices of greater size and strength. The values of the lift and drag increase dramatically even at low Reynolds numbers.
- It can be concluded that setting the airfoil in motion has the same effect as for increasing the mean incidence for motionless airfoils.

Plunging (or heaving) airfoil wakes shed vortices as they oscillate, and these wakes are classified into *drag-*, *neutral* and *thrust-producing* wakes, depending on the nature of the force produced by the airfoil. A typical drag-producing wake exhibits a Karman vortex street which consists of two alternating rows of clockwise (upper row of vortices) and anticlockwise vortices (lower row of vortices). The vortex pairs are shaped as mushroom-like structures tilted downstream, and the time-averaged horizontal velocity exhibits a momentum-deficit. A typical thrust-producing wake exhibits a *reversed* Karman vortex street, where the vortices sense of rotation is reversed compared to the Karman vortex street. The vortex pairs are also shaped as mushroom-like structures but tilted upstream, and the time-averaged horizontal velocity presents a momentum-surfeit. Finally, for a typical neutral wake the vortex-pairs shed are untilted and are on the same

horizontal line (on one row). Nevertheless, some studies show that the wake pattern is weakly correlated to the produced thrust as many wake configurations can exist for drag-, neutral or thrust-producing wakes.

To explore plunging airfoils wakes we conducted a parametrical study in Chapter 5, which enabled the description of the shedding process through which the wake undergoes a transition from a Karman street to a reversed Karman street. Drag, neutral and thrust wakes were successfully simulated, and also the transition from one wake to another. Furthermore, new and interesting results were presented concerning the interaction of the natural shedding frequency of the airfoil and the imposed forcing frequency. The role of this interaction in the formation of more than one vortex per oscillation cycle was also investigated. These results confirm for the first time for the airfoil geometry that it is in the harmonic regime that the multiple-vortices-per-half-cycle mode appears. The harmonic regime is a regime characterized by the dominant frequency being a mixture of the natural shedding frequency and the forcing frequency.

More shedding modes are captured when using the  $N\epsilon\kappa\tau\alpha r$ -solver, which assess the ability of the computational method to produce more accurate wake classification and wake transitions. Two more modes are observed here and added to the wake classification. These modes are: (1) a multiple-vortex-per-half-cycle wake producing thrust and (2) a neutral wake with one pair of vortices shed per cycle.

The assumption that the *Strouhal number* is the main and only parameter to characterize the wake configurations and thus the nature of the forces produced for oscillating airfoils was questioned in this investigation. To characterize such flows one needs to consider the amplitude and frequency of oscillations as independent parameters, and that the Strouhal number alone is not sufficient to characterize oscillating airfoil wakes.

The forced wake of the airfoil presents several frequency regimes. These regimes depend on the forcing frequency and the forcing amplitude. They also depend on the relation between the forcing frequency and the natural frequency of the airfoil. Three frequency regimes are defined in the literature: the natural regime, the harmonic regime and the lock-in regime. In the natural regime the vortex shedding frequency is equal to the natural frequency. In the harmonic regime, the vortex shedding frequency is a mixture or a combination of the natural and the forcing frequency. Finally, in the lock-in regime, the vortex shedding frequency is locked to the forcing frequency. In the published literature the frequency regimes have been studied for oscillating cylinders. The case of oscillating airfoils is less investigated. In this investigation we study heaving airfoils in an attempt to shed more light on the mechanisms behind the different wakes observed experimentally and computationally. We also establish a preliminary phase diagram to explain some aspects of the frequency regimes observed for heaving airfoils.

In Chapter 6 we explored the frequency regimes for oscillating airfoils. These

different frequency regimes were successfully simulated and were also related to the shedding process through which the wake undergoes a transition from a Karman street (a drag-producing wake) to a reversed Karman street (a thrust-producing wake). The transition between the different frequency regimes was simulated at both constant frequency and constant amplitude. It was found that the frequency regimes are strongly related to the wake type exhibited. Wake-types with multiple-vortices-per-half-cycle of oscillation are found in harmonic regimes and wake-types with one vortex-pair shed per cycle are in the region where one distinct frequency is in control (lock-in and natural regimes). Wakes where the leading-edge vortices contribute to the shedding process were also simulated.

## 7.2 Future Work

Based on the encouraging results obtained using the Spectral /hp Element Method, this study can be extended in several ways. A large number of parameters govern the flow over oscillating airfoils, even for the simple 2D plunging/heaving motion. Thus, further parametric studies are necessary in order to grasp the importance of each parameter and the interplay between them. In the same spirit, the study can be extended to other oscillatory motions and even non-oscillatory ones. Additionally, one can also combine two oscillatory motions (for example pitch and heave motions).

The Reynolds numbers considered in this investigation are relatively low (of the order of  $10^4$ ) and it can be interesting to consider higher Reynolds numbers, in the range  $2 \times 10^4 \leq Re \leq 5 \times 10^4$ . These Reynolds number correspond to the conditions at which Micro Air Vehicles (MAVs) operate.

Another interesting aspect of oscillating airfoils research is the investigation of flexible airfoils (or membranes), as opposed to rigid airfoils. Bird- and fish-like propulsion is achieved by oscillating flexible wings/fins, and it is essential to investigate these airfoils in order to gain more understanding of the animal-like propulsion to be implemented in MAVs and other insect-like robotic applications. The extension of this investigation to non-symmetric airfoil profiles and other airfoil shapes will permit the understanding of the role played by the airfoil geometry on the flow configuration and the forces production and will permit improvements in airfoils design for propulsive purposes.

A very important aspect of studying oscillating airfoils is the extension of the simulations to 3D flows. This can include the study of 3D effects on the wake structure, the frequency regimes and on the aerodynamical forces. This study will permit the understanding of more realistic flow configurations and will provide a valuable input to airfoils and MAVs design.



# Danksagung

I would like to thank Prof. Joachim Peinke for supervising and advising me in this work, yet leaving me a lot of freedom for own ideas and creativity. I also would like to thank Bruno Carmo for being the co-author of one of my papers, for helping me during my stay at Imperial College London, and for keeping my version of the Nektar code up to date. I also thank Prof. Spencer Sherwin for all the support during my stay at Imperial College London. I finally dedicate this work to all the colleagues and friends with whom I have worked and met along my PhD studies...thank you all for your support and help ... thank you for all the football games we shared, the BBQ's, the group meetings ... and simply for making my daily life richer with your presence. A special thank to my friend without whom I will not be here today presenting this work ... Bernhard Stoevesand (Danke für alles !) a special thanks goes also to my female friends Tanja and Aga ... A big thank you to Hendrik, Matthias, Pat, Thomas, Allan, Mike, Philip, Andreas, Edgar, Julia ... and in general the Hydro/Twist/Forwind group ... sorry if I forgot any of you ...

Je dédie ce travail à mes supportrices de la première heure, aux êtres qui ont aidé à façonner la personne que je suis devenue, aux êtres qui m'ont toujours aidé, supporté, encouragé et qui n'ont jamais douté de moi même (ou plutôt surtout) pendant mes moments de doute ... je dédie ce travail aux êtres qui comptent le plus pour moi, à ma mère Nadra (zozo) et à mes deux sœurs Anissa (nousty) et Nawel (loupy). Merci pour tout et j'espère qu'un jour je serai capable de vous rendre un tant soit peu de ce que vous m'avez donné tout au long de ces années. Je dédie ce travail à mes deux grand-mères que j'ai perdues dernièrement, qu'elles reposent en paix.

I also dedicate this work to my best friend, companion and dear husband. For all the sacrifices you did for us, for all the unconditional support you provided, for your help with my work, for reading and correcting countless drafts of my work...and for simply being always there for me...I will never be able to express my love and affection for you... Gracias mi amor ... mi Carlitos.

# Lebenslauf

## Persönliche Daten:

Name                Wided Medjroubi  
Geburtsdatum    11.10.1979  
Geburtsort        Constantine, Algerien

## Schulbildung:

1985 - 1991    Boublat Salah Grundschule in Constantine (Algerien)  
1991 - 1994    Khoualdia Salah Mittelschule Constantine (Algeiren)  
1994 - 1997    Zighoud Youcef Gymnasium in Constantine (Algerien)  
Abschluss mit Abitur im Bereich Naturwissenschaft

## Studium:

1998 - 2002    Studium der Physik  
                  an der Mentouri Universität in Constantine (Algerien)  
                  Abschluss mit Oberstudien Diplom in Energetische Physik  
2002            Aufnahmeprüfung für die Zulassung  
                  des Postgraduales Studiums in Physik  
                  an der Mentouri Universität in Constantine (Algerien)  
2002 - 2003    Postgraduales Studium der Energetische Physik  
                  an der der Mentouri Universität in Constantine (Algerien)  
2003 - 2005    Masterstudium der Physik Diplomarbeit  
                  an der der Mentouri Universität in Constantine (Algerien)  
                  Thema: Flow regimes between two concentric and rotating spheres  
seit 2006        Promotion an der Universität Carl von Ossietzky, Oldenburg

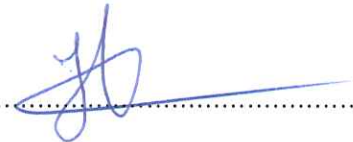
**Berufstätigkeit:**

2008 Tätigkeit als wissenschaftliche Hilfskraft bei TÜV-Nord, Hamburg  
10/2010 - 01/2011 Wissenschaftliche Hilfskraft  
an der Universität Carl von Ossietzky, Oldenburg  
seit 02/2011 Wissenschaftlicher Mitarbeiter  
an der Universität Carl von Ossietzky, Oldenburg

# Erklärung

Ich erkläre hiermit, dass ich diese Arbeit selbstständig verfasst und nur die angegebenen Hilfsmittel benutzt habe.

Oldenburg, den 10. Juli 2007

A handwritten signature in blue ink, consisting of stylized initials and a long horizontal stroke extending to the right, positioned above a dotted line.

(Wided Medjroubi)

## Publikationsliste

der in dieser Arbeit enthaltenen Veröffentlichungen

W. MEDJROUBI, B. STOEVE SANDT, B. CARMO AND J. PEINKE Direct Numerical Simulations of the Flow Around a Heaving Airfoil, *Submitted for publication in Computers and Fluids, 2010.*

J. Peinke hatte bei dieser Arbeit eine betreuende Funktion. B. Stoevesandt und B. Carmo haben mit Rat und Ideen bei der Ausarbeitung mit sprachlicher Überarbeitung unterstützt. Die wesentlichen Ideen und die wissenschaftliche Ausarbeitung stammen von W. Medjroubi.

W. MEDJROUBI, B. STOEVE SANDT AND J. PEINKE Direct Numerical Simulations of Plunging Airfoil Wakes Using Spectral/hp Element Method, *Submitted for publication in Journal of Computational and Applied Mathematics, 2010.*

J. Peinke hatte bei dieser Arbeit eine betreuende Funktion. B. Stoevesandt hatte mit Rat und Ideen bei der Ausarbeitung mit sprachlicher Überarbeitung unterstützt. Die wesentlichen Ideen und die wissenschaftliche Ausarbeitung stammen von W. Medjroubi.

W. MEDJROUBI, B. STOEVE SANDT AND J. PEINKE Frequency Selection in Plunging Airfoil Wakes Using a High-Order Numerical Method, *In preparation to be submitted for publication in Physics of Fluids.*

J. Peinke hatte bei dieser Arbeit eine betreuende Funktion. B. Stoevesandt hatte mit Rat und Ideen bei der Ausarbeitung mit sprachlicher Überarbeitung unterstützt. Die wesentlichen Ideen und die wissenschaftliche Ausarbeitung stammen von W. Medjroubi.

Die Anteile der aufgeführten Autoren entsprechen den Angaben.

Oldenburg, den 10. März 2011

(Prof. Dr. J. Peinke)

## Conferences where my work was published

- Summer School Complex Motion in Fluids. Lyngby, Denmark, Danish Technical University, Department of Fluid Dynamics. 19-25 August 2007. [Poster]
- From fast cars to slow flows over bluff bodies: translating knowledge on separated fluid mechanics. Imperial College, London, UK. 29-30 June 2009. [Poster and talk]
- 4<sup>th</sup> PhD Seminar on Wind Energy in Europe, Magdeburg, Germany. 1-2 October 2008. [Poster, talk and Proceeding paper]
- Deutsche Wind Energy Konferenz (DEWEK), Bremen, Germany. 26-27 November 2008. [Poster and Proceeding paper]
- 5<sup>th</sup> PhD Seminar on Wind Energy in Europe, Durham, UK. 29 September, 2 October 2009. [Talk and Proceeding paper]
- International Congress on Computational and Applied Mathematics, Leuven, Belgium. 05-09 July 2010. [Talk and Proceeding paper]
- Conference in Numerical Analysis (NumAn2010): recent approaches to numerical analysis: Theory, Methods and Applications. Chania, Crete, Greece. 15-18 September 2010. [Talk and Proceeding paper]